

**Vibration of Rotor–Stator Systems  
Coupled by Viscous Liquids**  
Theory, Experiment and Simulation

A thesis submitted to attain the degree of  
DOCTOR OF SCIENCES of ETH ZURICH  
(Dr. sc. ETH Zurich)

presented by

**Mario Weder**

MSc ETH ME, ETH Zurich  
born on November 7, 1981  
citizen of Diepoldsau-Schmitter SG

accepted on the recommendation of  
Prof. Dr. Jürg Dual, examiner  
Dr. Mirjam Sick, co-examiner  
Prof. Dr. Thomas Staubli, co-examiner



# Acknowledgments

The work presented in this thesis documents the research project which I carried out at ETH Zurich during my doctorate in the past four years. In the course of this project, I was supported by several people to whom I would like to express my gratitude.

First of all, I am very grateful to *Prof. Dr. Jürg Dual* for giving me the opportunity to conduct research at the Institute for Mechanical Systems and for the confidence he placed in me. He has created a fruitful environment by providing academic liberties on one hand and by a strong interest and support on the other.

Likewise, I am very thankful to *Dr. Mirjam Sick* for her enduring encouragement for the project inside Andritz Hydro. Without her persistence in the approval stage, this project would not even have been started. I also appreciate her commitment to act as co-examiner. Furthermore, I wish to thank *Prof. Dr. Thomas Staubli* for accepting the responsibility as co-examiner.

This project was carried out in collaboration with Andritz Hydro, to which I would also like to address my thanks. Foremost, I am especially grateful to *Beat Horisberger* for the fruitful and friendly cooperation. His reliable, efficient and well documented way of working was a key in the successful outcome of this project. I very much appreciate *Christian Oram's* contribution in the initial stage of the project. Many thanks go to *Pius Bucher* and his team of the *Lehrwerkstatt*, who machined most of the parts of the experimental test bench. Moreover, I thank the teams in Kriens, Vevey and Montreal for their expertise and their interest in this work.

Further, I wish to thank *Prof. Dr. Karl Schöllhorn*. He not only taught me the joy of dynamics in my early years at the Fachhochschule Aargau, but also advised me during the present project in the modal analysis of rotating structures. I would like to take this opportunity to express my gratitude to *Prof. Dr. Christoph Gossweiler* for teaching me the systematic approach in

scientific and applied research. I am also very thankful to *Rainer Hochspach* for the fundamentals in engineering design and the numerous discussions we had. Many thanks to *Dr. Simon Eugster* for sharing his expertise in the variational treatment of continuum mechanics. I would also like to thank *Prof. Dr. Christoph Glocker* for his excellent lectures and the exciting discussions about the foundations of mechanics.

Thanks also go to the students who contributed to this project, most notably the work of *Markus Specker*, which provided the basis for the finite element implementation in COMSOL Multiphysics.

I am much obligated to the staff and colleagues at the Institute for Mechanical Systems. Particularly, I would like to mention *Beate Fonfé*, *Raphael Frei*, *Raoul Hopf*, *Dr. Stephan Kaufmann*, *Andreas Lamprecht*, *Ivo Leibacher*, *Gabriel Nützi*, *Gabriela Squindo*, *Jean-Claude Tomasina* and *Bernhard Zybach*. Further, I thank *Thierry Baasch*, *Michael Schindlberger* and *Valentin van Gemmeren* for reviewing the manuscript. I am very grateful to *Ueli Marti* for the rotating electronics on the test bench and the lively discussions. Special thanks go to *Robert Ernst* and *Mathis Trachsel*, with whom I share the enthusiasm for bicycles.

I am especially thankful to *Michael Baumann* for the nice atmosphere in our office and the interesting discussions about mathematics, mechanics, sports and everyday topics.

Finally, I owe my deepest gratitude to my lovely wife, *Yvonne*, for all her love, support and patience—in any situation. Thank you very much!

*Zurich, Switzerland*  
*March 2018*

Mario Weder



# Contents

<b>Abstract</b>	<b>VII</b>
<b>Zusammenfassung</b>	<b>IX</b>
<b>Nomenclature</b>	<b>XI</b>
<b>1 Introduction</b>	<b>1</b>
1.1 Background and Motivation . . . . .	1
1.2 Literature Survey . . . . .	4
1.3 Aim and Scope . . . . .	10
1.4 General Methods and Assumptions . . . . .	11
1.5 Outline . . . . .	12
<b>2 Theoretical Background</b>	<b>15</b>
2.1 Governing Equations of the Solid . . . . .	16
2.1.1 System and Kinematics . . . . .	16
2.1.2 Principle of Virtual Work . . . . .	19
2.1.3 Perfect Bilateral Constraints . . . . .	23
2.1.4 Linearization . . . . .	25
2.1.5 Boundary Value Problem . . . . .	27
2.2 Governing Equations of the Fluid . . . . .	28
2.2.1 System and Kinematics . . . . .	28
2.2.2 Principle of Virtual Power . . . . .	30
2.2.3 Perfect Bilateral Constraints . . . . .	32
2.2.4 Linearization . . . . .	35
2.2.5 Boundary Value Problem . . . . .	37
2.3 Coupling of Solid with Fluid . . . . .	37
2.3.1 Total System . . . . .	37

2.3.2	Interface Condition . . . . .	39
2.3.3	Linearization . . . . .	41
<b>3</b>	<b>Semi-analytical Model</b>	<b>43</b>
3.1	Sandwich Model . . . . .	43
3.1.1	Model and Assumptions . . . . .	43
3.1.2	Governing Equations . . . . .	44
3.1.3	Implementation . . . . .	45
3.2	Results . . . . .	48
3.2.1	Modal Parameters without Bias Motion . . . . .	48
3.2.2	Modal Parameters with Bias Motion . . . . .	49
<b>4</b>	<b>Experimental Test Bench</b>	<b>55</b>
4.1	Functional Requirements . . . . .	55
4.2	Design Concept and Realization . . . . .	56
4.2.1	Design Concept . . . . .	56
4.2.2	Test Bench Design . . . . .	58
4.2.3	Kinematics . . . . .	62
4.3	Vibration Excitation and Measurement . . . . .	63
4.3.1	Measuring Layout and Overview . . . . .	63
4.3.2	Main Motor . . . . .	63
4.3.3	Electromagnetic Excitation . . . . .	64
4.3.4	Laser Doppler Velocimetry on Stator . . . . .	65
4.3.5	Self-tracking Laser Doppler Velocimetry on Rotor . . . . .	67
4.3.6	Signal Processing and Data Acquisition . . . . .	71
4.3.7	Test Bench Control . . . . .	72
4.3.8	Data Storage . . . . .	75
<b>5</b>	<b>Measurements and Modal Analysis</b>	<b>77</b>
5.1	Measuring Procedure . . . . .	77
5.1.1	Sample Preparation . . . . .	77
5.1.2	Reference Measurements and Verification . . . . .	79
5.1.3	Test Bench Preparation . . . . .	83
5.1.4	Scan Measurement . . . . .	84
5.1.5	Series of Measurements . . . . .	87
5.2	Modal Analysis . . . . .	88
5.2.1	Theory . . . . .	89
5.2.2	Adaption to Test Bench Measurements . . . . .	94

5.2.3	Numerical Implementation . . . . .	97
5.3	Experimental Results . . . . .	100
5.3.1	Eigenfrequency Spectrum and Mode Shapes . . . . .	100
5.3.2	Modal Parameters without Bias Motion . . . . .	104
5.3.3	Modal Parameters with Bias Motion . . . . .	110
<b>6</b>	<b>Finite Element Simulations</b>	<b>115</b>
6.1	Test Bench Model . . . . .	115
6.1.1	Model and Assumptions . . . . .	115
6.1.2	Perturbation Equations . . . . .	117
6.1.3	Cylindrical Coordinates and Rotational Symmetry . . . . .	120
6.1.4	Modal Ansatz . . . . .	122
6.2	Implementation in COMSOL Multiphysics . . . . .	123
6.2.1	Fluid Bias Motion . . . . .	123
6.2.2	Solid Bias Motion . . . . .	125
6.2.3	Perturbation Motions of Solid–Fluid System . . . . .	125
6.2.4	Computational Grid . . . . .	126
6.3	Simulation Results . . . . .	128
6.3.1	Bias Motion . . . . .	128
6.3.2	Modes Shapes . . . . .	130
6.3.3	Features of Perturbation Motion . . . . .	130
<b>7</b>	<b>Comparison of Experiment with Simulation</b>	<b>137</b>
7.1	Modal Parameters without Bias Motion . . . . .	137
7.2	Modal Parameters with Bias Motion . . . . .	143
<b>8</b>	<b>Conclusions and Outlook</b>	<b>147</b>
8.1	Conclusions . . . . .	147
8.2	Outlook . . . . .	151
<b>A</b>	<b>Mathematical Tools and Evaluations</b>	<b>155</b>
A.1	Gâteaux Derivative . . . . .	155
A.2	Tensor Analysis . . . . .	156
A.2.1	Tensors in Curvilinear Coordinates . . . . .	156
A.2.2	Tensors in Cartesian Coordinates . . . . .	157
A.2.3	Tensors in Cylindrical Coordinates . . . . .	159
A.2.4	Evaluations for General Curvilinear Coordinates . . . . .	161
A.2.5	Evaluations for Plane Periodic Plate . . . . .	161

A.2.6	Evaluations for Axisymmetric Disk . . . . .	163
A.3	Implementation of Semi-analytical Model . . . . .	165
A.4	Bi-orthogonality of Eigenvectors . . . . .	166
<b>B</b>	<b>Measurement Data</b>	<b>169</b>
B.1	Measured Modal Parameters . . . . .	169
	<b>References</b>	<b>203</b>
	<b>Curriculum Vitae</b>	<b>215</b>

# Abstract

This thesis examines the vibration behavior of rotor–stator systems coupled by intermediate viscous liquids. This problem is of particular importance in the design of pump-turbines, where the runner (rotor) is coupled to the head cover (stator) via the surrounding water. The elasticity of the rotor and the stator, their relative rotational motion and the various damping mechanisms contribute to the complexity of the vibration problem. We study this rotor–stator coupling on a simplified model, consisting of a circular stator disc (clamped at the outer circumference) and a ring-shaped rotor disc (clamped at the inner circumference) separated by an axial gap.

In a first part, we present a concise theory of the dynamics of small perturbations (first order) which are superimposed on a stationary bias motion (zero order). The theory is systematically deduced from fundamental principles of continuum mechanics and presented in weak variational form, which is best suited for its implementation in the finite element framework. Special attention is paid to the correct linearization of the governing equations and the coupling condition between solid and liquid.

The second part of the work is devoted to the experimental modal analysis of the rotor–stator system with the use of a specially engineered test bench. The test bench enables the measurement of eigenfrequencies, damping factors and mode shapes of rotor and stator. We have applied the laser interferometer technique to precisely measure the vibrations and therefore have developed a special mechanism for the vibration measurements on rotating parts. The measurements collected over a wide range of parameters form a substantial and unique experimental database for the verification of current and future simulation models.

In the third part, we describe a new physically-based simulation technique for the prediction of modal parameters of fluid-coupled rotor–stator systems. We discretize the derived perturbation equations with the finite element

method and solve the resulting eigenvalue problem numerically using the simulation software COMSOL Multiphysics. Both the stationary bias motion and the viscosity of the liquid are included in the model. As solutions we directly obtain the angular eigenfrequencies, the damping factors and the complex eigenforms of the respective vibration modes. The simulation model not only predicts the vibrational behavior of the system, but also provides valuable insights into the underlying mechanisms.

The vibration modes can be characterized by an azimuthal wave number, a radial index as well as the relative motion between rotor and stator (varicose or sinuous). Modes with a non-zero azimuthal wave number appear in pairs of co- and counter-rotating modes (relative to the rotation of the rotor). In the inertial frame of reference, a higher frequency is observed for the co-rotating mode compared to the counter-rotating mode. The difference in frequency is approximately proportional to the rotor speed and the mode's azimuthal wave number. This frequency split effect, caused by the stationary bias motion, is excellently mapped by the simulation model. For the more challenging characterization of the damping, we have also found a good agreement between simulation and experiment over a wide range of parameters.

# Zusammenfassung

Die vorliegende Arbeit untersucht das Schwingungsverhalten von Rotor–Stator-Systemen, die über viskose Flüssigkeiten gekoppelt sind. Mit dieser Problemstellung ist man insbesondere bei der Auslegung von Pumpsturbinen konfrontiert, bei denen der Läufer (Rotor) über das umgebende Wasser mit der Turbinenrückwand (Stator) gekoppelt ist. Die Nachgiebigkeit von Rotor und Stator, deren rotative Relativbewegung, sowie die verschiedenen Dämpfungsmechanismen, tragen zur Komplexität dieses Schwingungsproblems bei. Wir studieren die Grundlagen dieser Rotor–Stator-Kopplung an einem vereinfachten Modell, bestehend aus einer kreisförmigen Statorscheibe (aussen eingespannt) und einer ringförmigen Rotorscheibe (innen eingespannt), getrennt über einen axialem Fluidspalt.

Im ersten Teil erarbeiten wir die theoretischen Grundlagen zur Dynamik kleiner Störungen erster Ordnung, die einer stationären Grundbewegung nullter Ordnung überlagert sind. Die Formulierung der Störungsgleichungen in variationeller Form, direkt abgeleitet aus dem Prinzip der virtuellen Arbeit/Leistung, bietet die Grundlage für die folgende Implementierung mittels der Finite-Elemente-Methode. Der korrekten Linearisierung der Grundgleichungen und der Kopplungsbedingung zwischen Festkörper und Flüssigkeit kommt dabei eine besondere Aufmerksamkeit zu.

Der zweite Teil der Arbeit widmet sich der experimentellen Modalanalyse des Rotor–Stator-Systems mit einem eigens dazu entwickelten Versuchsstand. Dieser Versuchsstand ermöglicht eine hochgenaue Bestimmung der Eigenfrequenz, des Abklingfaktors sowie der (komplexen) Eigenformen von Rotor und Stator. Die Schwingungen werden elektromagnetisch angeregt und, sowohl beim Stator als auch beim Rotor, interferometrisch gemessen. Um die Messung mit dem Laservibrometer auch rotorseitig zu realisieren, wurde ein spezieller Mechanismus entwickelt, bei dem der messende Laserstrahl körperfest auf dem Rotor mitgeführt wird. Der grosse Umfang der

gewonnenen Daten bildet eine einzigartige Grundlage für die Verifikation von aktuellen und zukünftigen Simulationsmodellen.

Im dritten Teil beschreiben wir eine neuartige Simulationsmethode für die Vorhersage von modalen Parametern flüssigkeitsgekoppelter Rotor–Stator-Systeme. In der Simulationssoftware COMSOL Multiphysics werden die hergeleiteten Störungsgleichungen mittels Finite-Elemente-Methode diskretisiert und das resultierende Eigenwertproblem numerisch gelöst. Hierbei gehen sowohl die stationäre Grundbewegung wie auch die Viskosität der Flüssigkeit in die Modellierung ein. Als Lösungen erhalten wir direkt die Eigenfrequenzen, die Abklingfaktoren sowie die komplexen Eigenformen der entsprechenden Schwingungsmoden. Mit diesem Simulationsmodell erhält man nicht nur eine Vorhersage des Schwingungsverhaltens, sondern gewinnt auch wertvolle Einblicke in die zu Grunde liegenden Mechanismen.

Die gefundenen Schwingungsformen können über eine Umfangswellenzahl, einen radialen Index sowie über die Relativbewegung zwischen Rotor und Stator charakterisiert werden (varicose oder sinuous). Moden mit nicht verschwindender Umfangswellenzahl treten paarweise als mit- und gegenrotierende Moden auf (relativ zur Drehrichtung des Rotors). Dabei misst man im Inertialsystem bei der mitrotierenden Mode eine höhere Frequenz als bei der gegenrotierenden. Diese Frequenzdifferenz ist näherungsweise proportional zur Drehzahl des Rotors und der Umfangswellenzahl des Modes. Der Effekt, hervorgerufen durch die stationäre Grundbewegung, wird mit dem Simulationsmodell sehr gut abgebildet. Auch bei der herausfordernden Modellierung der Dämpfung, finden wir über einen grossen Parameterbereich eine gute Übereinstimmung zwischen Simulation und Experiment.



# Nomenclature

*Symbols used in the text are listed in the first column and its description can be found in the second column. The optional third and fourth column specify the units, and the page of prominent appearance, respectively. First-order tensors or vectors are typed in bold italic serif letters (e.g.,  $\mathbf{v}$ ,  $\mathbf{A}$ ) and second-order tensors in bold roman serif letters (e.g.,  $\mathbf{d}$ ,  $\mathbf{E}$ ). Vectors or tuples are typed in bold oblique sans-serif letters (e.g.,  $\mathbf{u}$ ,  $\mathbf{F}$ ) and matrices in bold roman sans-serif letters (e.g.,  $\mathbf{M}$ ).*

## Latin Letter Variables

$a, A$	area in deformed and reference configuration	$\text{m}^2$	23
$\mathbf{a}, \mathbf{A}$	acceleration vector in deformed and reference configuration	$\text{m}/\text{s}^2$	16, 29
$\mathbf{A}$	system matrix of first-order system	–	90
$\mathbf{b}, \mathbf{B}$	body force vector in deformed and reference configuration	$\text{N}/\text{m}^3$	19
$\mathbf{B}$	system matrix of first-order system	–	90
$c_1$	dilatational wave speed	$\text{m}/\text{s}$	45
$c_2$	distortional wave speed	$\text{m}/\text{s}$	45
$d, D$	diameters	$\text{m}$	57, 116
$\mathbf{d}$	spatial strain rate tensor (symmetric)	$1/\text{s}$	29
$\mathbf{D}$	damping matrix (symmetric)	$\text{N}/(\text{m s})$	89

$e = 2.71828\dots$	Euler's number	—	43, 90, 120
$e_1^I, e_2^I, e_3^I$	unit base vectors in the $I$ -system	—	16
$E$	Young's modulus of solid	Pa	22, 124
$\mathbf{E}$	Green–Lagrange strain tensor (symmetric)	—	19
$d\mathbf{f}, d\mathbf{F}$	generalized force measure (vector) in deformed and reference configuration	N	19
$df, d\mathbf{F}$	generalized force measure (tensor) in deformed and reference configuration	Nm	19
$\tilde{\mathbf{f}}, \tilde{\mathbf{F}}$	force vector of first- and second-order system	N	89, 90
$g$	gap width	m	43, 57, 116
$g(\mathbf{u}), G(\mathbf{H})$	strong constraint function on displacement or displacement gradient	—	23, 24
$\mathbf{g}_i, \mathbf{g}^i$	basis vectors of natural and reciprocal basis	—	156
$\tilde{\mathbf{g}}$	generalized force vector	N	92
$\mathbf{G}$	deformation gradient	—	19
$\mathbf{G}$	gyroscopic matrix (skew-symmetric)	N/(m.s)	89
$h_R, h_S$	plate thicknesses of rotor and stator	m	57, 116
$\mathbf{H}$	displacement gradient	—	19
$\mathbf{H}$	frequency response matrix	—	93
$\mathbf{I}, \mathbf{I}$	identity tensor and matrix	—	19, 92
$j := \sqrt{-1}$	imaginary unit	—	43, 90, 120
$J$	volume ratio	—	19

$k$	longitudinal wave number	rad/m	43
$\mathbf{K}(\mathcal{X}, t) = \mathbf{X}$	motion in the reference configuration	m	17
$\mathbf{K}$	stiffness matrix (symmetric)	N/m	89
$l$	radial index	—	100
$\mathbf{l}$	spatial velocity gradient tensor	1/s	29
$\mathbf{l}, \mathbf{l}$	left eigenvector of first- and second-order system	—	90, 91
$\mathfrak{L}, \mathbf{L}$	matrix of left eigenvectors of first- and second-order system	—	90, 91
$\mathbf{M}$	mass matrix (symmetric)	kg	89
$n$	azimuthal wave number	—	95
$\mathbf{n}, \mathbf{N}$	normal unit vector in the deformed and reference configuration	—	27, 37
$\mathbf{N}$	matrix of circulating forces (skew-symmetric)	N/m	89
$p$	mechanical pressure	Pa	34
$\delta p$	virtual power measure or density	W/m <sup>3</sup>	33
$\delta P$	virtual power	W	31
$\mathbf{P}$	first Piola–Kirchhoff stress tensor	Pa	21
$\tilde{\mathbf{q}}$	generalized coordinate vector	m	92
$r$	radial coordinate in cylindrical coordinate system	m	120, 159
$\mathbf{r}_{QP}$	position vector of point $P$ with respect to point $Q$	m	18
$\mathbf{t}, \mathbf{r}$	right eigenvector of first- and second-order system	—	90, 91

**XIV**

Nomenclature

$\mathfrak{R}, \mathbf{R}$	matrix of right eigenvectors of first- and second-order system	—	90, 91
$\mathbf{S}$	second Piola–Kirchhoff stress tensor (symmetric)	Pa	21
$t$	time	s	16
$T$	absolute temperature	K	124
$\mathbf{t}, \mathbf{T}$	surface traction vector in the deformed and reference configuration	Pa	23, 32
$\mathbf{u}$	displacement vector	m	18
$\tilde{\mathbf{u}}$	displacement vector of second-order system	m	89
$v, V$	volume in deformed and reference configuration	m <sup>3</sup>	17, 28
$\mathbf{v}, \mathbf{V}$	velocity vector in deformed and reference configuration	m/s	16, 29
$\delta w$	virtual work measure or density	N/m <sup>2</sup>	24, 120
$\delta W$	virtual work	Nm	20
$\mathbf{w}$	spatial spin tensor (skew-symmetric)	1/s	29
$x$	longitudinal coordinate in Cartesian coordinate system	m	157, 29
$\mathbf{x}, \mathbf{X}$	position vector in deformed and reference configuration	m	16
$\tilde{\mathbf{x}}$	state vector	—	90
$\mathfrak{X}$	particle	—	16
$y$	spanwise coordinate in Cartesian coordinate system	m	157

$z$	transversal coordinate in Cartesian coordinate system, axial coordinate in cylindrical coordinate system	m	120, 157, 159
-----	--	---	---------------

## Greek Letter Variables

$\alpha$	rotation angle of $H$ -system with respect to $S$ -system	rad	62
$\beta$	rotation angle of $R$ -system with respect to $S$ -system	rad	62
$\gamma(\mathbf{v}), \Gamma(\mathbf{l})$	strong constraint function on velocity or velocity gradient	—	32, 34, 39
$\delta_{ij}, \delta_j^i$	Kronecker delta	—	156
$\delta^f$	thickness of viscous boundary layer	m	48, 126
$\delta^r = \omega^i$	damping factor	1/s	43, 88, 122
$\varepsilon$	variational or expansion variable	—	20, 25, 155
$\boldsymbol{\eta}$	vorticity vector	rad/s	30
$\vartheta$	modal rotation angle	rad	95
$\boldsymbol{\kappa}(\boldsymbol{\mathcal{X}}, t) = \boldsymbol{x}$	motion in the deformed configuration	m	16
$\lambda = j\omega$	complex eigenvalue	1/s	88, 122
$\lambda^f$	second viscosity of fluid	Pa s	34
$\lambda^s$	first Lamé constant of solid	Pa	22
$\mathbf{\Lambda}$	diagonal eigenvalue matrix	1/s	92
$\mu^f$	first viscosity of fluid	Pa s	34, 124
$\mu^s$	second Lamé constant of solid or shear modulus	Pa	22
$\mu$	Lagrange multiplier	—	24, 33

$\nu$	Poisson's ratio of solid	—	22, 124
$\xi(\mathbf{X}, t) = \mathbf{x}$	deformation from the reference configuration	m	18
$\pi = 3.14159\dots$	ratio of a circle's circumference to its diameter	—	44, 95, 121
$\varpi$	excitation angular frequency	rad/s	85, 93
$\delta\Pi$	weak constraint function at velocity level	W	34, 39
$\Pi$	coordinate mapping	—	156
$\rho^f, \rho^s$	mass density of fluid and solid	kg/m <sup>3</sup>	124
$\sigma$	Cauchy stress tensor (symmetric)	Pa	21, 31
$\varsigma$	constraint stress tensor (symmetric)	Pa	34
$\tau$	group delay	s	100
$\tau$	time constant	s	119
$\tau$	impressed shear stress tensor (symmetric)	Pa	34
$\varphi$	azimuthal coordinate in cylindrical coordinate system	rad	62, 120, 159
$\varphi$	constraint traction vector	N/m <sup>2</sup>	41
$\Phi(\varphi)$	azimuthal mode shape	—	95
$\Psi(r)$	radial mode shape	m	95
$\omega$	complex angular eigenfrequency	rad/s	43
$\omega^r$	real angular eigenfrequency	rad/s	43, 88, 122
$\Omega_R$	angular rotor speed	rad/s	62, 117
$\Omega$	angular velocity vector	rad/s	18, 117

## Sets

$\mathbb{N}$	natural numbers
$\mathbb{Z}$	integers
$\mathbb{R}$	real numbers
$\mathbb{C}$	complex numbers
$\mathcal{R}$	rotor domain
$\mathcal{S}$	stator domain
$\mathcal{F}$	fluid domain
$\mathcal{B} \in \{\mathcal{R}, \mathcal{S}\}$	general solid domain
$\mathcal{T}$	total system
$\mathcal{K}$	subsystem

## Coordinate Systems

$I$	inertial system $(\mathbf{e}_x^I, \mathbf{e}_y^I, \mathbf{e}_z^I)$
$H$	measuring head system $(\mathbf{e}_x^H, \mathbf{e}_y^H, \mathbf{e}_z^H)$
$R$	rotor system $(\mathbf{e}_x^R, \mathbf{e}_y^R, \mathbf{e}_z^R)$
$S$	(inertial) stator system $(\mathbf{e}_x^S, \mathbf{e}_y^S, \mathbf{e}_z^S)$
$C$	cylindrical system $(\mathbf{e}_r^C, \mathbf{e}_\varphi^C, \mathbf{e}_z^C)$

## Operators

$ \bullet $	absolute value of (complex) $\bullet$
$\ \bullet\ $	Euclidian norm of vector $\bullet$
$\bullet^r := \Re\{\bullet\}$	real part of complex $\bullet$

$\bullet^i := \Im\{\bullet\}$	imaginary part of complex $\bullet$
$\bullet^*$	complex conjugate of complex $\bullet$
$\dot{\bullet}$	total time derivative of $\bullet$
$Df(\bullet)[\circ]$	Gâteaux derivative of $f$ at $\bullet$ in the direction of $\circ$
$\partial_\circ \bullet$	partial derivative of $\bullet$ with respect to $\circ$
$\mathcal{D}_t \bullet$	material time derivative of $\bullet$
$\mathcal{D}_z \bullet := d\bullet/dz$	derivative of $\bullet(z)$ with respect to $z$
$\circ_\bullet$	coordinates of tensor $\bullet$ expressed in coordinate system $\circ$
$\bullet^T$	transpose of matrix or second order tensor $\bullet$
$\text{sym } \bullet$	symmetric part of matrix or second order tensor $\bullet$
$\text{skw } \bullet$	skew-symmetric part of matrix or second order tensor $\bullet$
$\bullet \cdot \circ$	scalar product of vectors $\bullet$ and $\circ$
$\bullet : \circ$	double contraction of second-order tensors $\bullet$ and $\circ$
$\bullet \times \circ$	cross product of vector $\bullet$ with vector $\circ$
$\partial_x \bullet$	spatial gradient of $\bullet$
$\partial_X \bullet$	material gradient of $\bullet$
$(\partial_x \bullet) : \mathbf{I}$	spatial divergence of $\bullet$
$(\partial_X \bullet) : \mathbf{I}$	material divergence of $\bullet$
$\delta \bullet$	first variation of $\bullet$ on position level
$\underline{\delta} \bullet$	first variation of $\bullet$ on velocity level
$\bar{\bullet}$	closure of set $\bullet$
$\partial \bullet$	boundary of set $\bullet$



## Sub- and Superscripts

- <sup>f</sup>                    related to fluid
- <sup>s</sup>                    related to solid
- <sub>R</sub>                   related to rotor
- <sub>S</sub>                   related to stator
- <sup>↑↑</sup>                  sinuous mode
- <sup>↑↓</sup>                  varicose mode
- <sup>→</sup>, •<sup>↔</sup>            longitudinal modes
- $\bar{\bullet}(\boldsymbol{x})$             bias or zero-order motion
- $\tilde{\bullet}(\boldsymbol{x}, t)$             first-order perturbation
- $\hat{\bullet}(\boldsymbol{x}, \omega)$            complex first-order perturbation amplitude
- <sup>int</sup>                  contributions of internal forces
- <sup>ext</sup>                  contributions of external forces
- <sup>dyn</sup>                  contributions of inertia forces
- <sub>tot</sub>                  totality of all contributions



# Introduction

# 1

## 1.1 Background and Motivation

The worldwide production and storage of electric energy faces substantial challenges. To avert global warming, a major reduction of the greenhouse gas emissions is inevitably required. Substitution of fossil energy with renewable energy (e.g., from wind, water and solar power) can contribute to a reduction in carbon dioxide emissions. In addition, we see a stagnation—or in some countries even a phase out—of the nuclear power production. This is due to the disposal problematic and the inherent risks of this technology; especially in the light of the catastrophic accident on the Fukushima Daiichi power plant in 2011.

Unfortunately, a drawback of many renewable energy technologies is the intermittent power production. This volatility limits their potential to substitute nonrenewable energies that produce continuous base-load power. A common approach to balance the loads is the use of *pumped-storage hydroelectricity*. Such pumped-storage power plants mainly consist of two water reservoirs at different elevations, connected by intermediate pumps and turbines. When the electrical supply is high, the plant obtains electricity *from* the grid and pumps water from the lower to the higher reservoir. In case of electrical demand, the plant releases the stored water (and thus energy) in turbine operation and supplies electricity *to* the grid.

Pumped-storage systems are now operational for over a century, but the emerging transition to renewable energies changes their requirements. For example, to compensate the load volatility, the market demands systems with an extended operating range (e.g., variable rotation speeds) and with the capability for faster and more frequent changes of the operating points (e.g., from pump to turbine operation). To meet these enhanced require-

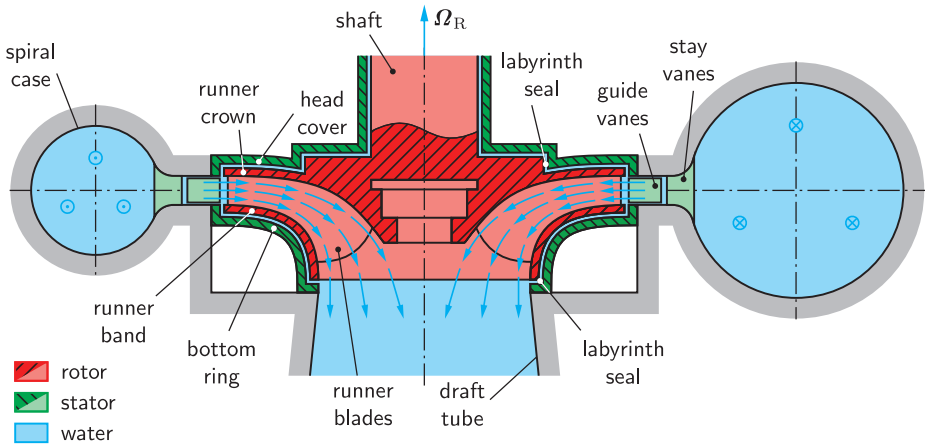


**Fig. 1.1:** Cross section of a vertical pump-turbine. The blue arrows indicate the direction of rotation and of fluid flow in turbine operation.

ments, an increased knowledge of the underlying physics and the limiting factors is necessary.

The most common hydraulic machines used for pumped-storage applications are of *Francis* type. Fig. 1.1 shows a cross section of a pump-turbine with the most important components labeled. The function of this radial machine is described for turbine operation as follows: Swirling water flow enters the turbine radially through a *spiral case* and exits axially through the centric *draft tube*. During the flow through the turbine, the fluid generates work on the rotating *runner* by the change of angular momentum between the inlet and the outlet flow. The runner drives an electric generator that transforms the mechanical power into electrical power. The *guide vanes* between the spiral casing and the runner are used for turbine control. Large hydraulic turbines generate an output up to 800 MW using runners with diameters of approximately 10 m. A special feature of the pump-turbine is that same machine can run in both pump *and* turbine operation. In pump operation, the direction of rotation and flow is reversed, and as a consequence, the runner must generate work on the fluid.

A key factor in the design of the hydraulic machines is their vibrational behavior. Various mechanisms can excite resonances which lead to an amplification of vibration amplitudes (e.g., the rotor–stator interaction of guide vanes and runner blades (Dubas, 1984)). It is evident to suppress resonance, as it leads to fatigue, shortens the lifetime, or even endangers the structural integrity of the system. Therefore, a prediction of resonance frequencies and corresponding damping factors, as well as an understanding of the underlying mechanisms is of capital importance. This knowledge may then be used to develop designs that meet the increased requirements.

However, the detailed characterization of the vibrational behaviour of pump-turbines is still a challenging topic. The complexity arises from the specific design of the hydraulic machine. From a detailed inspection of Fig. 1.1, we notice that the runner is submerged in water, and consequently, this water couples the flexible rotor with the adjacent flexible stator structures. Particularly, we recognize a small clearance between *runner crown* (rotor) and *head cover* (stator) as well as between *runner band* (rotor) and *bottom ring* (stator). As a result, the rotor and stator cannot be analysed independently but must rather be considered in the combined rotor–stator system.

The present thesis investigates the complex coupling mechanism between rotor and stator caused by an intermediate viscous liquid. The sources of complexity of the coupling problem are multifarious. We may name the following challenges:

- The rotor–stator system consists of both *rotating* and *non-rotating* parts.
- Both rotor and stator are *elastic* structures that influence the vibration of the system.
- The intermediate liquid that couples the rotor and the stator is governed by *nonlinear equations* of motion (Navier–Stokes equations).
- Besides the resonance frequency, the *characterization of the damping* is also of great interest.

## 1.2 Literature Survey

### Vibration of Elastic Structures in Contact with Fluid

Early works on the vibration of elastic structures in contact with liquids date back to Lamb (1920). He has investigated the flexural vibration of a thin circular plate which is clamped at its circumference and in contact with a half space of water. The derived analytical model estimates the vibration frequency of the first axisymmetrical mode as well as the damping due to the radiation of sound into the far field. He argues that the frequency of the fluid-loaded plate is lower compared to the unloaded plate because of the additional mass of the water. Later, McLachlan (1932) has considered flexural vibrations of a free circular plate submerged in a fluid. He has found that the frequency reduction, compared to the vibration in vacuum, may be marginal for air but is significant for water.

More recently, research has focused on the analytical treatment of special cases or on numerical methods, such as the Ritz and Galerkin methods. For example, Amabili and Kwak (1996) have reconsidered Lamb's problem by applying the Rayleigh–Ritz solution to additionally compute the change of the mode shape of the fluid-loaded plate. The analytical treatment of special cases includes, for instance, annular plates (Amabili et al., 1996), circular plates on a sloshing liquid (Kwak and Kim, 1991; Amabili, 2001), cylindrical shells partially filled with liquid (Chiba, 1996) or infinite plates (Hagedorn, 1994; Grosh and Pinsky, 1994).

Jeong and Kim (2005) have investigated the vibration of a confined problem, where a circular plate is clamped at its circumference and partitions a water-filled rigid cylindrical cavity in two halves. They have formulated an analytical model with an incompressible fluid and derived a finite element model with a compressible fluid. These two formulations are in good agreement for the non-axisymmetrical modes in the low-frequency range. The analytical model overestimates the frequency of the higher-order modes and the axisymmetrical modes, because it neglects the compressibility of the fluid.

The works cited above all describe the solid–fluid interaction from a solid-mechanics perspective. This means that the authors mainly focus on the elastic structure and the change in frequency caused by the fluid loading. The quiescent fluid (no bias motion) is assumed to be inviscid (irrotational flow), where the motion can be described by a velocity potential obeying

the Laplace equation (incompressible) or the wave equation (compressible). These works do neither consider the damping due to fluid's viscosity nor the influence of a bias motion of the fluid or solid.

Using the same methodology, the coupling of multiple elastic structures by an intermediate inviscid liquid has been studied. For instance, Jeong (2003) and Jhung et al. (2003) have examined the vibration of a system consisting of a lower and an upper circular plate coupled by the intermediate fluid. In the investigated low-frequency range, the mode shapes of the lower and upper plates are of the same form, which is characterized by an azimuthal wave number (number of nodal diameters) and a radial index (number of nodal circles). For a given pair of azimuthal wave number and radial index, the coupled system comprises two different modes: (i) a *sinuous* mode, where the motions of the two plates are in the *same* direction, and (ii) a *varicose* mode, where the motions of the plates are in *opposite* directions. The fluid motion of these two mode types is rather different: Whereas the fluid motion of the sinuous mode is mainly in axial direction, the varicose mode shows large radial velocity components. The squeezing flow for the varicose mode is caused by the opposing movement of the plates, leads to an increased apparent mass, and, as a result, has a lower eigenfrequency compared to the sinuous mode. A similar phenomena has also been reported by Jeong (1998), who has investigated the fluid coupling between two coaxial cylindrical shells.

### **Hydrodynamic Stability of Flows with Compliant Walls**

Another perspective to the solid–fluid interaction problem is provided by the hydrodynamic stability theory. This field of fluid dynamics studies the stability of laminar flows, which are governed by the nonlinear Navier–Stokes equations. For example, the dynamics of small perturbations superimposed on a plane, viscous, stationary, parallel bias flow is described by the celebrated Orr–Sommerfeld equation (see, e.g., Drazin and Reid (2004, p. 156), Criminale et al. (2003, p. 13) and Schmid and Henningson (2001, p. 57)). Even though the hydrodynamic stability theory is mainly concerned with the conditions for the onset of instability (because linear instability is an important path to turbulence), the dedicated tools and methods may also be used to study the damping in sub-critical conditions.

As an example, Davis and Carpenter (1997) and Larose and Grotberg (1997) have incorporated an elastic wall model into the Orr–Sommerfeld

equation to investigate the stability of a plane channel flow with compliant walls. Among other types of instability, they describe a flutter instability which is characteristic to a flow with compliant walls. More complex geometries have also been examined, such as the effect of wall compliance to the stability of Taylor–Couette flow in the gap between rotating cylinders (Guaus et al., 2009), or the stability of a rotating-disk boundary-layer flow over a compliant wall (Cooper and Carpenter, 1997a,b).

### **Vibrational Analysis of Hydraulic Turbines**

Dubas and Schuch (1987) have initiated the numerical modeling of the vibrational behaviour of real turbines using the finite element method. They have modeled a Francis runner with shell elements to compute its eigenfrequencies in vacuum. At that time, computing power was limited and a realistic modeling of the surrounding water not realizable. Instead, the frequency of the submerged structure was estimated from the frequency in vacuum by empirical correction factors.

A landmark in the computation of eigenfrequencies of runners including added-mass effects is the work by Jacquet-Richardet and Dal-Ferro (1996). They have modeled both fluid and structure domains with finite elements, where the fluid has been assumed to be inviscid, incompressible and at rest (Laplace equation). The computational effort could be reduced by exploiting cyclic symmetries of the investigated centrifugal pump runner.

With increasing computational power, larger and more detailed models have become feasible. For instance, Liang et al. (2007) have computed eigenfrequencies of a complete, non-rotating Francis runner submerged in water. They included the compressibility of water by using acoustic elements (wave equation). The eigenfrequencies of the numerical modal analysis shows a good agreement with the experimental study performed by Rodriguez et al. (2006). Additionally, Lais et al. (2009) have described a harmonic response analysis of an immersed runner with the excitation pattern computed by computational fluid dynamics (CFD).

Coutu et al. (2008) have performed a root cause analysis of a Francis runner, which failed within two weeks of operation. The reason for the failure was high cycle fatigue due to resonance, because the eigenfrequency of the built-in runner surrounded by water was too close to the excitation frequency resulting from the rotor–stator interaction pattern. The authors concluded (i) that the method with empirical correction factors (the method available



at the time of development of the machine) is not sufficient to predict the eigenfrequencies of the built-in runner and (ii) that an eigenfrequency analysis with acoustic elements would have averted the problem. As a result, the eigenfrequency analysis—with acoustic elements modeling the quiescent liquid—has become the state-of-the-art method to predict the vibrational behavior of hydraulic machines during its design stage.

More recently, several attempts were made to enhance models for a better prediction of the vibrational behavior. The attempts were aimed to take further, probably relevant, effects into account, such as the rotation of the runner, the bias fluid motion, large vibration amplitudes, the damping of the vibration or the coupling of rotor and stator. For instance, Dompierre and Sabourin (2010) described a transient two-way solid–fluid coupled simulation of Francis turbine to study the resonance of the system. Therefore, a computational fluid dynamics solver and a structural finite element code were coupled to simulate the fluid and solid motion in the time domain. Basically, such a simulation takes many relevant effects directly into account (e.g., rotation of runner, bias fluid motion, large vibration amplitudes). But it is not feasible for the design of a machine, because the simulation is extremely laborious and computationally expensive. For example, to resolve one single vibration mode in a time frame of 0.286 s in physical time, a computational time of 95 days was necessary. Furthermore, Krey et al. (2011) have investigated the coupling of runner and head cover of a Francis type pump-turbine with a transient finite element simulation. The intermediate liquid was modeled using acoustic elements by neglecting viscosity and advection terms due to bias fluid motion. To include the rotation of the runner, a rotating frame of reference was defined together with an acoustic rotor–stator interface.

### Simplified Disk Models

Real water turbines are large and complex systems which makes them not suitable to study fundamental vibration phenomena. A promising approach for basic research is to reduce the (geometric) complexity of the model, where, for example, rotor and stator parts are represented as circular disks.

Hengstler (2013) has followed this approach and experimentally investigated the vibration of a stator disk submerged in swirling flow of water. He has observed that degenerated disk modes show a *frequency split* roughly proportional to the swirling speed of the water. This means that a pair of

modes, for which the frequencies coincide for the quiescent fluid, have different frequencies in the case of fluid motion. Additionally, the mode shapes of the non-rotating disk are no longer stationary but rotate in the two different directions. In the inertial reference frame, the mode shape with the higher frequency rotates with the direction of fluid flow (co-rotating) and the one with lower frequency against the fluid flow (counter-rotating). The influence of the gap width between stator disk and the rigid stator wall on the eigenfrequencies was also investigated in this work.

Later on, the vibration of a rotating disk submerged in a confined water cavity has been examined. Presas et al. (2014) have presented an experimental test bench, where the vibration on the rotating disk is excited using patches of piezoelectric transducers (Presas et al., 2015c, 2017) and measured with accelerometers placed at selected locations. Measurements with this setting also show a frequency split of mode pairs with non-zero azimuthal wave number, which are related to co- and counter-rotating mode shapes (Presas et al., 2015a). As they measured the vibration in the rotor-fixed reference frame, the lower frequency is now related to the co-rotating mode and the higher frequency to the counter-rotating mode. Valentín et al. (2016) presented a simple simulation approach to predict the eigenfrequency split measured in the test bench. They formulated the finite element model in a rotating frame of reference related to an averaged motion of the liquid. The liquid is modeled with acoustic elements, albeit without including the necessary gyroscopic terms (e.g., centrifugal and Coriolis terms). Additionally, they only considered the *relative* angular velocity between the rotor and liquid, which also leads to incorrect gyroscopic terms for the solid motion. These oversimplifications are a consequence of the limitations of the commercial finite element software used for the study. Further investigations on the same test bench have addressed the influence of the axial gap (Presas et al., 2016) and the coupling of the rotor disk with the elastic casing (Presas et al., 2015b).

Recently, Valentín et al. (2015, 2017) did an experimental study of a stator disk vibrating in a cylindrical cavity filled with quiescent liquid and covered with a compliant plate. The focus of the study was on the coupling of the stator disk with the elastic cover plate by the intermediate liquid. They have observed that the stator disk and cover plate build a system with a common eigenfrequency and that the eigenfrequency of the system with a compliant cover is larger compared to the one with a stiff cover. Bassio et al. (2017) have performed a numerical study of the same setup using

acoustic elements to model the water. They investigated the influence of the eigenfrequency on several parameters such as the radial gap width, the axial gap width or the liquid's speed of sound.

### **Vibration of Rotating Disks**

The transverse vibrations of unconstrained rotating disks has been theoretically studied by Lamb and Southwell (1921). They have provided an approximation of the vibration frequency which is derived from the two extreme cases, namely (i) a flexural plate at rest (by neglecting membrane forces) and (ii) a thin membrane rotating (by neglecting flexural forces). Their model predicts an increase of the eigenfrequency with the rotation speed due to the stress stiffening effect. Later, Southwell (1922) considered the rotating disk clamped at the center and Tobias and Arnold (1957) studied rotating disks with imperfections.

### **Fluid Flow Near Rotating Disks**

In his famous work, von Kármán (1921) has found the similarity solution for the laminar flow in a fluid half space in contact with an infinitely extended rotating wall. The rotating disk acts as centrifugal pump with an radial outflow and an axial inflow. The work also provides the driving torque of a disk with finite radius as well as an approximation for the turbulent flow regime. The stability and transition of this flow has been investigated by Kobayashi et al. (1980) with a linear stability analysis together with experiments. At the onset of instability, the experiments showed a regular pattern of spiral vortices appearing around the circumference. Batchelor (1951) generalized Kármán's similarity solutions for the flow confined between a rotor and a stator disk. This torsional Couette flow is characterized by a secondary flow which is superposed to the primary flow in azimuthal direction. Schouveiler et al. (2001) experimentally studied the laminar-turbulent transition of this flow and observed different types of instability which evolve as circular or spiral rolls. Subsequently, Cros et al. (2003) additionally investigated the effect of wall compliance on this transition.

### 1.3 Aim and Scope

The long-term objectives of the project are validated tools and methods that allow a reliable prediction of the vibrational characteristics of real turbines at the design stage. To take a stride towards this goal, a comprehensive knowledge about the *fundamentals* of the rotor–stator coupling is crucial. In the present thesis, we focus on the rotor–stator coupling with an *axial clearance*, such as between the runner crown and the head cover. To study the fundamentals, we work on strongly *simplified models*, where the runner crown (rotor) and head cover (stator) are represented as circular disks. The abstraction from a real turbine to the simplified disk model is illustrated in Fig. 1.2.

It is the idea to gain knowledge about the coupling phenomena on the simplified model, where the geometrical aspect of the complexity is eliminated but other substantial aspects are still part of the model. The complexity of the disk model particularly includes (i) a combination of rotating and non-rotating parts, (ii) deformability of rotor and stator, and (iii) a viscous liquid which couples rotor and stator. The disk model therefore allows to study the coupling phenomena on simpler experimental setups and simulation models. It is the aim, to afterwards transfer the derived concepts into the development process of real turbines. This important process of

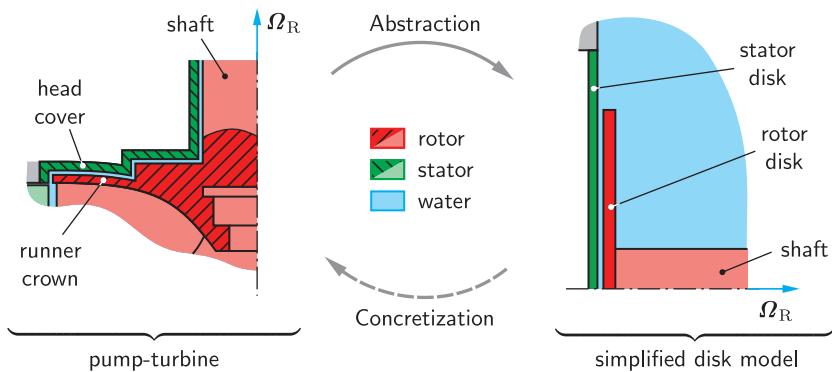


**Fig. 1.2:** Abstraction of the complex pump-turbine with a simplified disk model.

concretization is challenging, but will not be part of the present thesis. In an overall view, we are confident that the approach with the ‘detour’ via the simplified model is faster, more robust and provides more reliable concepts.

The literature survey has revealed various gaps in knowledge of liquid-coupled vibration problems. For example, there is an insufficient experimental data base that covers liquid-coupled systems with rotation and/or investigates its damping mechanisms. Additionally, there are no simulation tools available to efficiently compute the influence of the bias motion on the vibration frequency or the damping due to the viscous liquid. The present work addresses these topics and tries to bridge the lack of understanding. With regard to the state of the art and the comments about our focus on simplified disk models, we formulate the following *research questions*:

- What are the fundamental mechanisms and features that characterize the vibration of elastic rotor–stator systems coupled by viscous liquids?
- How do important parameters such as the stiffness of rotor and stator, the gap width between rotor and stator, and the rotor speed influence the resonance frequency and damping of the system?
- How can rotor–stator systems coupled by viscous liquids be modeled to predict the resonance frequency and damping characteristics?

## 1.4 General Methods and Assumptions

We anchor the work on the three pillars of science, namely *theory*, *experiment* and *simulation*. Fig. 1.3 illustrates their interplay and emphasizes that these methods are not disjoint but overlap. For example, a comparison of experiment with simulation reveals the quality of the derived model and gives a feedback about the assumptions made (validation). In addition, a validated simulation model can provide insights, which would not have been accessible with experimental techniques. In the present thesis we will intensively make use of this interplay.

In the following, we state general assumptions for the rotor–stator coupling with viscous liquids that we apply to the entire thesis:

- We study the rotor–stator coupling by liquids on a strongly simplified model, where the rotor and the stator are modelled as elastic disks.

- We assume small vibration amplitudes which are governed by linearized equations of motions (perturbation theory).
- We neglect nonlinear effects such as streaming (second-order effect) or large deformations.
- The fluid flow is assumed to be incompressible (bias flow and first-order perturbation).
- The solid structures are assumed to behave linearly elastic.

## 1.5 Outline

The present thesis is outlined as follows: Chapter 2 provides the *theoretical background* of the thesis. The governing equations for the solid and fluid are derived in the weak variational form, which build the basis for the simulation models in Chapter 3 and 6. Special attention is paid on the formulation of the fluid–solid interaction as well as on the linearization of the equations about the bias motion. Chapter 3 describes a *semi-analytical model* consisting of two parallel plates with an intermediate viscous liquid. This is

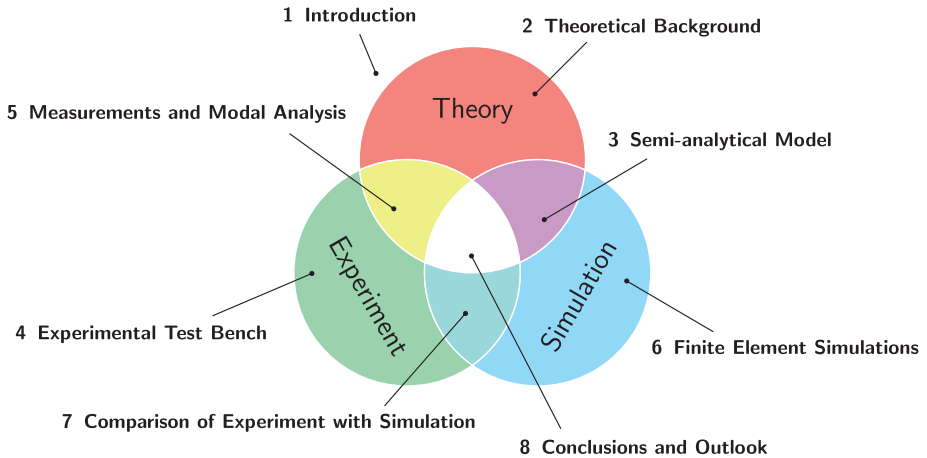


**Fig. 1.3:** The interplay between theory, experiment and simulation with references to the individual chapters of this thesis.

probably the simplest model to study the coupling of elastic structures by a liquid. With this sandwich model, we investigate fundamental phenomena of the coupled vibration, such as characteristic mode shapes, added mass effects and damping mechanisms.

Chapter 4 documents the *experimental test bench* for the characterization of the rotor–stator coupling by liquids. We discuss the general design concept and the specific realization of the test bench, which mainly consists of a rigid casing filled with liquid, a stator disk clamped to the casing and a rotor disk clamped to a driven rotor shaft. The control of the test bench, the excitation and measurement of the vibrations, the signal processing, the data acquisition as well as the data storage are discussed in detail. Chapter 5 presents test bench *measurements and modal analysis* theory. We describe the preparation of the samples and of the test bench, a single scan measurement as well as the series of measurements performed with the test bench. Additionally, the theoretical basics of the modal analysis with rotating components are reviewed and the adaptations to our symmetric problem are discussed. In the same chapter, we show the measured mode shapes as well as the experimental results for the eigenfrequency and damping.

The *finite element simulations* of the simplified disk model are covered in Chapter 6. This includes a description of the finite element model and its implementation in COMSOL Multiphysics. The chapter also presents simulation results of the bias motion, mode shapes of the vibration and some features of the perturbation motion. In Chapter 7 we show the *comparison of experiment with simulation* and discuss the results. Finally, in Chapter 8 we provide the *conclusions and outlook* of the work.





# Theoretical Background

# 2

This chapter provides the theoretical foundations of the dynamics of solid–fluid coupled systems. This includes the governing equations of the solid and the fluid as well as a description of the coupling between these two. The equations are derived in a general form, from which the specific forms of Chapter 3 (semi-analytical model) and Chapter 6 (finite element model) are deduced.

We assume small vibration amplitudes and hence apply the perturbation method, where the total motion is decomposed into a *bias motion* (zero order) and a *linear perturbation* (first order). This method is widely used in engineering, for instance, to investigate the generation and propagation of sound (Howe, 2003), or to study the linear stability of fluid flows (Drazin and Reid, 2004; Schmid and Henningson, 2001; Criminale et al., 2003). Special consideration is required when linearizing the governing equations: For the solid equations, the general non-linear framework is necessary prior to the linearization to take the effect of bias-stress effects into account (Bonet and Wood, 2008, pp. 218; Bremer, 2008, pp. 159). For the fluid equations in Eulerian representation, the material time derivative of the velocity field needs to be linearized. Moreover, at the solid–fluid interface, the linearization of the boundary conditions leads to an interaction between fluid bias motion and solid perturbation (Benjamin, 1960).

We formulate the mechanical principles of the continua in variational form based on the work by Hellinger (1914) (see Eugster and dell’Isola (2017, 2018a,b) for a commented English translation thereof). This is motivated by the later implementation of the equations in the finite element framework COMSOL Multiphysics, where the physics can be described directly in the weak form. Additionally, the variational principles are more descriptive than the classical balance laws. Note that many derivations in this chapter make use of the Gâteaux derivative which is defined in Appendix A.1.

## 2.1 Governing Equations of the Solid

### 2.1.1 System and Kinematics

This section introduces the system and the kinematics to describe the solid body motion according to Fig. 2.1. We follow the textbooks by Chadwick (1976, pp. 50); Odgen (1984, pp. 73); Haupt (2002, pp. 7) as well as the work by Eugster and Glocker (2017) and adopt their terminology. However, in contrast to these publications—and other standard works in continuum mechanics—we explicitly allow the reference configuration to be time dependent. This leads to additional terms in the expressions for the particle velocity and acceleration that take rotodynamic effects of rotating structures into account. We typeset quantities in the deformed configuration in lower case letters and those in the reference configuration in upper case letters, or, alternatively, we tag them with a subscript or superscript ‘0’.

A *solid body*  $\mathfrak{B}$  is a set of particles that can be bijectively placed into a subset of a *physical space*, here represented by the three-dimensional Euclidean vector space  $\mathbb{E}^3$ . The Euclidean vector space is inertial and equipped with an orthonormal base  $(e_1^I, e_2^I, e_3^I)$  and an origin  $O$ , forming the  $I$ -system.

The time parameter family of *placements* into the *deformed configuration*  $\bar{\mathcal{B}}_t \subset \mathbb{E}^3$  is defined as the function  $\kappa : \mathfrak{B} \times \mathbb{R} \rightarrow \bar{\mathcal{B}}_t$  together with its inverse

$$\mathbf{x} = \kappa(\mathfrak{X}, t), \quad \mathfrak{X} = \kappa^{-1}(\mathbf{x}, t), \quad (2.1)$$

where  $\mathfrak{X} \in \mathfrak{B}$  denotes a specific *particle* and  $\mathbf{x}$  its *position vector* in the deformed configuration with respect to  $O$ . This time evolution of placements is called the *motion* of  $\mathfrak{B}$  in the deformed configuration. The *trajectory*, *velocity* and *acceleration* of a particle  $\mathfrak{X}$  in the deformed configuration then are, respectively,

$$\mathbf{x}(t) = \kappa(\mathfrak{X}, t), \quad \dot{\mathbf{x}}(t) = \partial_t \kappa(\mathfrak{X}, t), \quad \ddot{\mathbf{x}}(t) = \partial_t^2 \kappa(\mathfrak{X}, t), \quad (2.2)$$

where we use partial time derivatives since the particle  $\mathfrak{X}$  remains fixed. In Eulerian representation, the velocity and acceleration fields read,

$$\dot{\mathbf{x}} = \mathbf{v}^s(\mathbf{x}, t) := \partial_t \kappa \underbrace{(\kappa^{-1}(\mathbf{x}, t), t)}_{\mathfrak{X}}, \quad \ddot{\mathbf{x}} = \mathbf{a}^s(\mathbf{x}, t) := \partial_t^2 \kappa \underbrace{(\kappa^{-1}(\mathbf{x}, t), t)}_{\mathfrak{X}}, \quad (2.3)$$

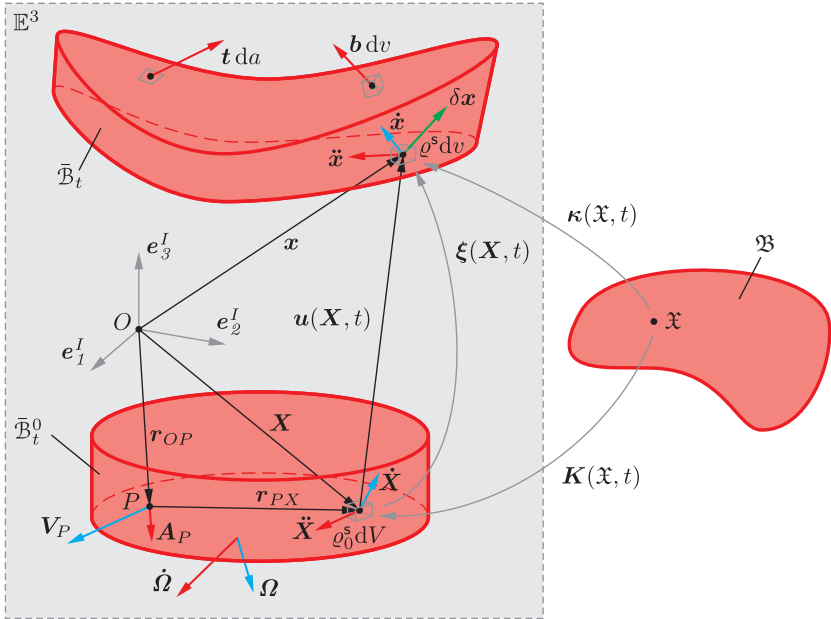


**Fig. 2.1:** Placements of solid body  $\mathfrak{B}$  into the deformed configuration  $\bar{\mathcal{B}}_t$  and the reference configuration  $\bar{\mathcal{B}}_t^0$  of Euclidean vector space  $\mathbb{E}^3$ .

where we eliminated  $\mathfrak{X}$  using (2.1)<sub>2</sub>. The region occupied by the image  $\bar{\mathcal{B}}_t = \kappa(\mathfrak{B}, t)$  can be written as the disjoint union  $\bar{\mathcal{B}}_t = \mathcal{B}_t \cup \partial\mathcal{B}_t$  of the *interior*  $\mathcal{B}_t$  and the *boundary*  $\partial\mathcal{B}_t$  of the deformed configuration, respectively.

As we will formulate constitutive equations later on, we rely on a strain free reference configuration. We therefore define a time parameter family of placements into the *reference configuration*  $\bar{\mathcal{B}}_t^0 \subset \mathbb{E}^3$  as the function  $\mathbf{K} : \mathfrak{B} \times \mathbb{R} \rightarrow \bar{\mathcal{B}}_t^0$  together with its inverse

$$\mathbf{X} = \mathbf{K}(\mathfrak{x}, t), \quad \mathfrak{x} = \mathbf{K}^{-1}(\mathbf{X}, t), \quad (2.4)$$

where  $\mathbf{X}$  denotes the position vector in the reference configuration with respect to  $O$ . Here, we explicitly include the time dependence and call the time evolution of placements the motion of  $\mathfrak{B}$  in the reference configuration. The particle trajectory, velocity and acceleration of a particle  $\mathfrak{x}$  in the

reference configuration then write as, respectively,

$$\mathbf{X}(t) = \mathbf{K}(\mathfrak{x}, t), \quad \dot{\mathbf{X}}(t) = \partial_t \mathbf{K}(\mathfrak{x}, t), \quad \ddot{\mathbf{X}}(t) = \partial_t^2 \mathbf{K}(\mathfrak{x}, t). \quad (2.5)$$

The motion in the reference configuration shall be strain free for all times. We therefore restrict the motion (2.5) to that of a rigid body with particle velocity and acceleration fields

$$\dot{\mathbf{X}} = \mathbf{V}_P + \boldsymbol{\Omega} \times \mathbf{r}_{PX}, \quad \ddot{\mathbf{X}} = \mathbf{A}_P + \dot{\boldsymbol{\Omega}} \times \mathbf{r}_{PX} + \boldsymbol{\Omega} \times (\boldsymbol{\Omega} \times \mathbf{r}_{PX}), \quad (2.6)$$

where  $\mathbf{V}_P$  and  $\mathbf{A}_P$  denote the particle velocity and acceleration of an arbitrary reference point  $P$ ,  $\boldsymbol{\Omega}$  the angular velocity of the rigid body motion, and  $\mathbf{r}_{PX}$  the particle position vector with respect to  $P$ .

It is convenient to express the motion in the deformed configuration in terms of the reference position  $\mathbf{X}$  rather than the particle  $\mathfrak{x}$ . Using (2.4)<sub>2</sub> together with (2.1)<sub>1</sub>, we eliminate  $\mathfrak{x}$  and define the *deformation* as the function  $\boldsymbol{\xi} : \bar{\mathcal{B}}_t^0 \times \mathbb{R} \rightarrow \bar{\mathcal{B}}_t$  together with its inverse

$$\mathbf{x} = \boldsymbol{\xi}(\mathbf{X}, t) := \underbrace{\kappa(\mathbf{K}^{-1}(\mathbf{X}, t), t)}_{\mathfrak{x}}, \quad \mathbf{X} = \boldsymbol{\xi}^{-1}(\mathbf{x}, t) := \underbrace{\mathbf{K}(\kappa^{-1}(\mathbf{x}, t), t)}_{\mathfrak{x}}. \quad (2.7)$$

The relative motion between deformed and reference configuration is called *displacement* and is defined as the function  $\mathbf{u} : \bar{\mathcal{B}}_t^0 \times \mathbb{R} \rightarrow \mathbb{E}^3$  with

$$\mathbf{u}(\mathbf{X}, t) := \boldsymbol{\xi}(\mathbf{X}, t) - \mathbf{X}. \quad (2.8)$$

We now express the kinematic quantities of (2.2) in Lagrangian representation, this is, in terms of  $\mathbf{X}$  and  $\mathbf{u}$ . By applying the chain rule, with  $\mathfrak{x}$  remaining fixed, the velocity and acceleration fields become

$$\begin{aligned} \dot{\mathbf{x}} &= \mathbf{V}^s(\mathbf{X}, t) := \mathcal{D}_t^s \mathbf{u} = \underbrace{\dot{\mathbf{X}}}_{=: \mathbf{V}^I} + \underbrace{\partial_t \mathbf{u}}_{=: \mathbf{V}^{II}} + \underbrace{(\partial_X \mathbf{u}) \dot{\mathbf{X}}}_{=: \mathbf{V}^{III}}, \end{aligned} \quad (2.9)$$

$$\begin{aligned} \ddot{\mathbf{x}} &= \mathbf{A}^s(\mathbf{X}, t) := \mathcal{D}_t^{s^2} \mathbf{u} := \underbrace{\ddot{\mathbf{X}}}_{=: \mathbf{A}^I} + \underbrace{\partial_t^2 \mathbf{u}}_{=: \mathbf{A}^{II}} + \underbrace{2\partial_t(\partial_X \mathbf{u}) \dot{\mathbf{X}}}_{=: \mathbf{A}^{III}} \\ &\quad + \underbrace{[(\partial_X \partial_X \mathbf{u}) \dot{\mathbf{X}}] \dot{\mathbf{X}}}_{=: \mathbf{A}^{IV}} + \underbrace{(\partial_X \mathbf{u}) \ddot{\mathbf{X}}}_{=: \mathbf{A}^V}, \end{aligned} \quad (2.10)$$

where  $(\partial_{\mathbf{X}}\mathbf{u})\dot{\mathbf{X}} = D\mathbf{u}(\mathbf{X})[\dot{\mathbf{X}}]$  and  $[(\partial_{\mathbf{X}}\partial_{\mathbf{X}}\mathbf{u})\dot{\mathbf{X}}]\dot{\mathbf{X}} = D^2\mathbf{u}(\mathbf{X})[\dot{\mathbf{X}}]$  are geometrically defined by the Gâteaux derivative (A.1). The operators  $\mathcal{D}_t^s$  and  $\mathcal{D}_t^{s^2}$  operate on  $\mathbf{u}$  and formally define the material time derivative for the solid body.

The deformation in the vicinity of  $\mathbf{x} = \boldsymbol{\xi}(\mathbf{X}, t)$  is described by the *deformation gradient*, defined by the two-point tensor

$$\mathbf{G}(\mathbf{X}, t) := \partial_{\mathbf{X}}\boldsymbol{\xi}(\mathbf{X}, t), \quad (2.11)$$

which linearly maps tangent vectors in the reference configuration  $d\mathbf{X}$  to tangent vectors in the deformed configuration  $d\mathbf{x} = \mathbf{G} d\mathbf{X}$ . We assume a positive *volume ratio*

$$J(\mathbf{X}, t) := \det \mathbf{G}(\mathbf{X}, t) > 0 \quad \forall \mathbf{X} \in \mathcal{B}_t^0, \forall t, \quad (2.12)$$

so that  $\mathbf{G}$  is invertible. The *displacement gradient* is the two-point tensor given by

$$\mathbf{H}(\mathbf{X}, t) := \partial_{\mathbf{X}}\mathbf{u}(\mathbf{X}, t) \equiv \mathbf{G}(\mathbf{X}, t) - \mathbf{I}. \quad (2.13)$$

We define the *Green–Lagrange strain tensor* as

$$\mathbf{E}(\mathbf{X}, t) := \frac{1}{2}(\mathbf{G}^T\mathbf{G} - \mathbf{I}) \equiv \frac{1}{2}(\mathbf{H}^T + \mathbf{H} + \mathbf{H}^T\mathbf{H}), \quad (2.14)$$

which measures the difference of squared lengths of tangent vectors in the deformed and reference configuration by  $\|d\mathbf{x}\|^2 - \|d\mathbf{X}\|^2 = 2(\mathbf{E} d\mathbf{X}) \cdot d\mathbf{X}$ .

Generalized forces measures acting on the solid body  $\mathfrak{B}$  are denoted by

$$d\mathbf{f}(\mathbf{x}, t), d\mathbf{f}(\mathbf{x}, t), \quad \text{or} \quad d\mathbf{F}(\mathbf{X}, t), d\mathbf{F}(\mathbf{X}, t), \quad (2.15)$$

depending on whether expressed in the deformed or reference configuration. Note that generalized forces can either be represented by vector quantities ( $d\mathbf{f}$ ,  $d\mathbf{F}$ ) in  $\mathbb{N}$  or by tensor quantities ( $d\mathbf{f}$ ,  $d\mathbf{F}$ ) in  $\mathbb{N}\mathbb{m}$ . We further distinguish between *volume body forces*  $\mathbf{b} dv$  or  $\mathbf{B} dV$ , *surface traction forces*  $\mathbf{t} da$  or  $\mathbf{T} dA$ , *inertia forces*  $(-\rho^s \mathbf{a}^s) dv$  or  $(-\rho_0^s \mathbf{A}^s) dV$  and *internal forces*, which we subsequently express in terms of stress contributions  $-\boldsymbol{\sigma} dv$  or  $-\mathbf{P} dV$ .

## 2.1.2 Principle of Virtual Work

In the present section we introduce the governing equation for the motion of the solid body  $\mathfrak{B}$ . For this, we apply the principle of virtual work, from which

the scalar equation of motion in variational form results. For a comprehensive analysis of this topic, we refer to the fundamental works by Eugster (2015) and Eugster and Glocker (2017).

First, we define the *variational family of virtual placements*  $\bar{\kappa} : \mathfrak{B} \times \mathbb{R} \times \mathbb{R} \rightarrow \bar{\mathfrak{B}}_t^\varepsilon$  with the variational parameter  $\varepsilon$ . These virtual placements are *arbitrary* besides the prerequisite that the actual placement  $\kappa(\mathfrak{X}, t)$  is revealed by setting  $\varepsilon = \varepsilon_0$ , that is,  $\bar{\kappa}(\mathfrak{X}, t, \varepsilon_0) \equiv \kappa(\mathfrak{X}, t)$ . The Gâteaux derivative (A.1) then defines the *virtual displacement* of particle  $\mathfrak{X}$

$$\delta\kappa(\mathfrak{X}, t) := D\bar{\kappa}(\varepsilon_0)[\delta\varepsilon] = \partial_\varepsilon\bar{\kappa}(\mathfrak{X}, t, \varepsilon_0) \cdot \delta\varepsilon, \quad (2.16)$$

where  $\delta\varepsilon := \varepsilon - \varepsilon_0$  denotes the variation of  $\varepsilon$ . As a result of the arbitrariness of the virtual placements, the virtual displacements become arbitrary in direction—a fact that is used in the principle of virtual work to test the force contributions. We express the virtual displacement fields in terms of the position fields in the deformed and the reference configuration, respectively, as

$$\delta\mathbf{x}(\mathbf{x}, t) := \delta\kappa(\underbrace{\kappa^{-1}(\mathbf{x}, t)}_{\mathfrak{x}}, t), \quad \delta\xi(\mathbf{X}, t) := \delta\kappa(\underbrace{\mathbf{K}^{-1}(\mathbf{X}, t)}_{\mathfrak{x}}, t). \quad (2.17)$$

The variation of the displacement field (2.8) is

$$\delta\mathbf{u}(\mathbf{X}, t) := D\mathbf{u}[\delta\xi] = \lim_{\varepsilon \rightarrow 0} \frac{(\xi + \varepsilon\delta\xi - \mathbf{X}) - (\xi - \mathbf{X})}{\varepsilon} \equiv \delta\xi(\mathbf{X}, t), \quad (2.18)$$

and thus equals the virtual displacement (2.17)<sub>2</sub>.

Now, we state the *principle of virtual work* according to Eugster and Glocker (2017): Let  $d\mathbf{f}_{\text{tot}}, d\mathbf{f}_{\text{tot}}, \dots$  be the totality of forces acting on the body expressed in the deformed configuration  $\bar{\mathfrak{B}}_t$  and  $d\mathbf{F}_{\text{tot}}, d\mathbf{F}_{\text{tot}}, \dots$  be the same expressed in the reference configuration  $\bar{\mathfrak{B}}_t^0$ . In order that the solid body  $\mathfrak{B}$  is in dynamical equilibrium, the overall virtual work  $\delta W_{\text{tot}}$  performed by  $(d\mathbf{f}_{\text{tot}}, d\mathbf{f}_{\text{tot}}, \dots)$  or  $(d\mathbf{F}_{\text{tot}}, d\mathbf{F}_{\text{tot}}, \dots)$ , must vanish for all virtual displacement fields  $\delta\mathbf{x}$  or  $\delta\mathbf{u}$  and gradients thereof, that is,

$$\boxed{\begin{aligned} 0 = \delta W_{\text{tot}} &= \int_{\bar{\mathfrak{B}}_t} \delta\mathbf{x} \cdot d\mathbf{f}_{\text{tot}} + \int_{\bar{\mathfrak{B}}_t} (\partial_x \delta\mathbf{x}) : d\mathbf{f}_{\text{tot}} && \forall \delta\mathbf{x}, \forall t \\ &= \int_{\bar{\mathfrak{B}}_t^0} \delta\mathbf{u} \cdot d\mathbf{F}_{\text{tot}} + \int_{\bar{\mathfrak{B}}_t^0} (\partial_X \delta\mathbf{u}) : d\mathbf{F}_{\text{tot}} && \forall \delta\mathbf{u}, \forall t. \end{aligned}} \quad (2.19)$$

The totality of forces must include all forces, namely the inertia forces, the internal forces, and the external forces. Accordingly, we can write the total virtual work as

$$\delta W_{\text{tot}} = \delta W^{\text{dyn}} + \delta W^{\text{int}} + \delta W^{\text{ext}}, \quad (2.20)$$

with the virtual work contributions further specified in the following paragraphs.

### Virtual Work Contribution of Inertia Forces

The inertia forces contribute to the virtual work by

$$\begin{aligned} \delta W^{\text{dyn}} &:= \int_{\mathfrak{B}_t} \delta \mathbf{x} \cdot (-\varrho^s \mathbf{a}^s) \, dv \\ &:= \int_{\mathfrak{B}_t^0} \delta \mathbf{u} \cdot (-\varrho_0^s \mathbf{A}^s) \, dV, \end{aligned} \quad (2.21)$$

where the first line is expressed in the deformed configuration and the second line in the reference configuration, using the acceleration terms defined in (2.3)<sub>2</sub> and (2.10).

### Virtual Work Contribution of Internal Forces

We call a force *internal* with respect to the body  $\mathfrak{B}$ , if the force only interacts with particles of the body itself and not with the environment. According to Eugster and Glocker (2017), we consider *stress* as the internal forces modeling the small range interactions. The virtual work contribution by the internal forces is then given by

$$\begin{aligned} \delta W^{\text{int}} &:= \int_{\mathfrak{B}_t} -(\partial_x \delta \mathbf{x}) : \boldsymbol{\sigma} \, dv \\ &:= \int_{\mathfrak{B}_t^0} -(\partial_X \delta \mathbf{u}) : \mathbf{P} \, dV = \int_{\mathfrak{B}_t^0} -\delta \mathbf{E} : \mathbf{S} \, dV, \end{aligned} \quad (2.22)$$

where, in the deformed configuration,  $\partial_x \delta \mathbf{x}$  denotes the *spatial gradient of the virtual displacement field* and  $\boldsymbol{\sigma}$  the symmetric *Cauchy stress tensor*; and in the reference configuration,  $\partial_X \delta \mathbf{u}$  denotes *material gradient of the virtual displacement field*,  $\mathbf{P}$  the *first Piola–Kirchhoff stress tensor*,  $\delta \mathbf{E}$  the *variation of the Green–Lagrange strain tensor* and  $\mathbf{S}$  the symmetric *second*

*Piola–Kirchhoff stress tensor.* The variation of the Green–Lagrange strain tensor is obtained by

$$\begin{aligned}\delta\mathbf{E}(\mathbf{X}, t) &:= DE[\delta\mathbf{G}] = \frac{1}{2}(\mathbf{G}^\top\delta\mathbf{G} + \delta\mathbf{G}^\top\mathbf{G}) \\ &:= DE[\delta\mathbf{H}] = \frac{1}{2}(\delta\mathbf{H}^\top + \delta\mathbf{H} + \mathbf{H}^\top\delta\mathbf{H} + \delta\mathbf{H}^\top\mathbf{H}),\end{aligned}\tag{2.23}$$

either using the *variation of the deformation gradient*

$$\delta\mathbf{G}(\mathbf{X}, t) := DG[\delta\xi] = \partial_{\mathbf{X}}\delta\xi(\mathbf{X}, t),\tag{2.24}$$

or the *variation of the displacement gradient*

$$\delta\mathbf{H}(\mathbf{X}, t) := DH[\delta\mathbf{u}] = \partial_{\mathbf{X}}\delta\mathbf{u}(\mathbf{X}, t) \equiv \delta\mathbf{G}(\mathbf{X}, t).\tag{2.25}$$

Now, we specify the constitutive equations describing the material behaviour of the solid body. Following Haupt (2002, p. 346), we assume the material to be *Green elastic* or *hyperelastic*, so that we can state a scalar-valued *strain energy function*  $W_{\mathbf{E}}(\mathbf{E})$  to deduce the second Piola–Kirchhoff stress from

$$\mathbf{S}(\mathbf{E}) = \frac{dW_{\mathbf{E}}}{d\mathbf{E}}.\tag{2.26}$$

We further assume the material to be *isotropic* and *linear-elastic*, for which the strain energy function is expressed by

$$W_{\mathbf{E}}(\mathbf{E}) := \mu^s \mathbf{E} : \mathbf{E} + \frac{\lambda^s}{2} (\mathbf{E} : \mathbf{I})^2,\tag{2.27}$$

with  $\lambda^s$  defining the *first Lamé constant* and  $\mu^s$  the *second Lamé constant*, also known as *shear modulus* (Haupt, 2002, p. 365). If we evaluate (2.26) using (2.27), we find the second Piola–Kirchhoff stress for an isotropic, linear-elastic material by

$$\mathbf{S} = 2\mu^s \mathbf{E} + \lambda^s (\mathbf{E} : \mathbf{I}) \mathbf{I}.\tag{2.28}$$

The relations between the *Young’s modulus*  $E$  and the *Poisson’s ratio*  $\nu$  to the Lamé constants read

$$\mu^s = \frac{E}{2(1+\nu)}, \quad \lambda^s = \frac{\nu E}{(1+\nu)(1-2\nu)}.\tag{2.29}$$



### Virtual Work Contribution of External Forces

We call a force *external* with respect to the solid body  $\mathfrak{B}$ , if the force interacts with the environment and not with particles of the body itself. The virtual work contribution of these external forces then write as

$$\begin{aligned}\delta W^{\text{ext}} &:= \int_{\mathfrak{B}_t} \delta \mathbf{x} \cdot \mathbf{b} \, dv + \int_{\partial \mathfrak{B}_t} \delta \mathbf{x} \cdot \mathbf{t} \, da \\ &:= \int_{\mathfrak{B}_t^0} \delta \mathbf{u} \cdot \mathbf{B} \, dV + \int_{\partial \mathfrak{B}_t^0} \delta \mathbf{u} \cdot \mathbf{T} \, dA,\end{aligned}\tag{2.30}$$

where the body volume forces  $\mathbf{b}$  or  $\mathbf{B}$  act on the interior and the surface traction forces  $\mathbf{t}$  or  $\mathbf{T}$  at the boundary of the solid body  $\mathfrak{B}$ . Again, in the first line, the forces are represented in the deformed configuration, and in the second line, the same forces are given in the reference configuration.

As a summary, we assemble the contributions of the inertia forces (2.21), the internal forces (2.22) and external forces (2.30) and write out the principle of virtual work in the reference configuration as

$$\begin{aligned}0 = \delta W_{\text{tot}} &= \int_{\bar{\mathfrak{B}}_t^0} \delta \mathbf{u} \cdot (-\varrho_0^s \mathbf{A}^s) \, dV \\ &\quad + \int_{\mathfrak{B}_t^0} -\delta \mathbf{E} : \mathbf{S} \, dV \\ &\quad + \int_{\mathfrak{B}_t^0} \delta \mathbf{u} \cdot \mathbf{B} \, dV + \int_{\partial \mathfrak{B}_t^0} \delta \mathbf{u} \cdot \mathbf{T} \, dA \quad \forall \delta \mathbf{u}, \forall t.\end{aligned}\tag{2.31}$$

### 2.1.3 Perfect Bilateral Constraints

So far we have not considered any kinematic constraints on the motion of the solid body. In the present section we discuss perfect bilateral constraints on the displacement field which may be equivalently represented in local strong form or in the weak variational form, namely,

$$0 = g^\mu(\mathbf{u}) \quad \Leftrightarrow \quad 0 = \delta \Omega^\mu := \int_{\bar{\mathfrak{B}}_t^0} \delta \mu \cdot g^\mu(\mathbf{u}) \, dV \quad \forall \delta \mu.\tag{2.32}$$

Therein,  $g^\mu(\mathbf{u})$  is a scalar-valued *constraint function* at the displacement level and  $\delta \mu$  an arbitrary test function called *virtual force*. The forces which

ensure the constraint (2.32) are called constrained forces and denoted as  $d\mathbf{F}^{\text{con}}$ .

We now formulate the *principle of d'Alembert–Lagrange*, which is the constitutive law for the constraint forces of the perfect bilateral constraint at position level: The virtual work  $\delta W_{\text{adm}}^{\text{con}}$  generated by constraint forces  $d\mathbf{F}^{\text{con}}$  vanishes for all virtual displacements  $\delta \mathbf{u}_{\text{adm}}$  admissible with the constraint, that is

$$0 = \delta W_{\text{adm}}^{\text{con}} = \int_{\bar{\mathcal{B}}_t^0} \delta \mathbf{u}_{\text{adm}} \cdot d\mathbf{F}^{\text{con}} \quad \forall \delta \mathbf{u}_{\text{adm}}, \forall t, \quad (2.33)$$

or in local form

$$0 = \delta w_{\text{adm}}^{\text{con}} = \delta \mathbf{u}_{\text{adm}} \cdot d\mathbf{F}^{\text{con}} \quad \forall \delta \mathbf{u}_{\text{adm}}, \forall t. \quad (2.34)$$

Furthermore, we find the admissible variations of (2.32) using the Gâteaux derivative (A.1) as

$$\begin{aligned} 0 = \delta g_{\text{adm}}^{\mu}(\mathbf{u}) &= Dg^{\mu}(\mathbf{u})[\delta \mathbf{u}_{\text{adm}}] = [\partial_{\mathbf{u}} g^{\mu}(\mathbf{u})] \cdot \delta \mathbf{u}_{\text{adm}} \\ &= \delta \mathbf{u}_{\text{adm}} \cdot [\partial_{\mathbf{u}} g^{\mu}(\mathbf{u})] \quad \forall \delta \mathbf{u}_{\text{adm}}. \end{aligned} \quad (2.35)$$

A comparison of (2.34) and (2.35), with the fact that both equations hold for all  $\delta \mathbf{u}_{\text{adm}}$ , reveals the form of the constraint force

$$d\mathbf{F}^{\text{con}} = \mu [\partial_{\mathbf{u}} g^{\mu}(\mathbf{u})] dV, \quad (2.36)$$

where  $\partial_{\mathbf{u}} g^{\mu}(\mathbf{u})$  represents the generalized force direction and  $\mu$  is a scalar Lagrange multiplier. The vector-valued force direction, defined as the gradient  $\partial_{\mathbf{u}} g^{\mu}(\mathbf{u})$ , may be found, again, by applying the Gâteaux derivative (A.1) on the constraint function (2.32), that is

$$0 = Dg^{\mu}(\mathbf{u})[\tilde{\mathbf{u}}] = [\partial_{\mathbf{u}} g^{\mu}(\mathbf{u})] \cdot \tilde{\mathbf{u}} \quad \forall \tilde{\mathbf{u}}. \quad (2.37)$$

Instead of (2.32) we could also define constraints on the field of the displacement gradient  $\mathbf{H} = \partial_X \mathbf{u}$ , again equivalently in local strong form or in the weak variational form, by

$$0 = G^{\mu}(\mathbf{H}) \quad \Leftrightarrow \quad 0 = \delta \Omega^{\mu} := \int_{\mathcal{B}_t^0} \delta \mu \cdot G^{\mu}(\mathbf{H}) dV \quad \forall \delta \mu. \quad (2.38)$$

The formalism is the same as sketched out above and leads to constraint stresses of the form

$$d\mathbf{F}^{\text{con}} = \mu [\partial_{\mathbf{H}} G^{\mu}(\mathbf{H})] dV, \quad (2.39)$$

where the gradient  $\partial_{\mathbf{H}} G^{\mu}(\mathbf{H})$  represents the tensor-valued stress direction.

### 2.1.4 Linearization

The governing equation (2.31) derived above is non-linear. For the perturbation method, we separate the total process  $\mathbf{q}$  into a bias process  $\bar{\mathbf{q}}$  (zero order) and linear perturbation process  $\tilde{\mathbf{q}}$  (first order), that is,

$$\mathbf{q} = \bar{\mathbf{q}} + \varepsilon \tilde{\mathbf{q}} + \mathcal{O}(\varepsilon^2), \quad \mathbf{q} \in \{\mathbf{u}, \mathbf{B}, \mathbf{T}\}. \quad (2.40)$$

We derive the equation for the linear perturbations  $\tilde{\mathbf{q}}$  by linearizing the governing equations about the bias solution  $\bar{\mathbf{q}}$ . The procedure of linearization by applying the Gâteaux derivative (A.1), is described by Bonet and Wood (2008, pp. 218). Accordingly, linearization is a strict use of the Gâteaux derivative on the non-linear equations at the bias solution  $\bar{\mathbf{q}}$  into the direction of the disturbances  $\tilde{\mathbf{q}}$ .

We apply the linearization procedure to (2.31) and derive the *linearized principle of virtual work*

$$0 = \delta \tilde{W}_{\text{tot}} = \delta \tilde{W}^{\text{dyn}} + \delta \tilde{W}^{\text{int}} + \delta \tilde{W}^{\text{ext}} \quad \forall \delta \mathbf{u}, \forall t, \quad (2.41)$$

with the different contributions given in the following. Firstly, we deduce the *linearized virtual work contribution of the inertia forces*

$$\begin{aligned} \delta \tilde{W}^{\text{dyn}} &:= D\delta W^{\text{dyn}}(\bar{\mathbf{u}})[\tilde{\mathbf{u}}] = \int_{\mathbb{B}_t^0} D\{\delta \mathbf{u} \cdot (-\varrho_0^s \mathbf{A}^s)\}(\bar{\mathbf{u}})[\tilde{\mathbf{u}}] dV \\ &= \int_{\mathbb{B}_t^0} -\delta \mathbf{u} \cdot \varrho_0^s \{\partial_t^2 \tilde{\mathbf{u}} + 2\partial_t(\partial_X \tilde{\mathbf{u}}) \dot{\mathbf{X}} \\ &\quad + [(\partial_X \partial_X \tilde{\mathbf{u}}) \dot{\mathbf{X}}] \dot{\mathbf{X}} + (\partial_X \tilde{\mathbf{u}}) \ddot{\mathbf{X}}\} dV. \end{aligned} \quad (2.42)$$

from (2.21) using (2.10). Secondly, we derive the *linearized virtual work contribution of the internal forces* from (2.22)

$$\begin{aligned} \delta \tilde{W}^{\text{int}} &:= D\delta W^{\text{int}}(\bar{\mathbf{u}})[\tilde{\mathbf{u}}] = \int_{\mathbb{B}_t^0} D\{-\delta \mathbf{E} : \mathbf{S}\}(\bar{\mathbf{u}})[\tilde{\mathbf{u}}] dV \\ &= \int_{\mathbb{B}_t^0} -\delta \bar{\mathbf{E}} : D\mathbf{S}(\bar{\mathbf{u}})[\tilde{\mathbf{u}}] dV + \int_{\mathbb{B}_t^0} -D\delta \mathbf{E}(\bar{\mathbf{u}})[\tilde{\mathbf{u}}] : \bar{\mathbf{S}} dV \\ &= \int_{\mathbb{B}_t^0} -\delta \bar{\mathbf{E}} : \bar{\mathbf{S}} dV + \int_{\mathbb{B}_t^0} -\delta \bar{\mathbf{E}} : \bar{\mathbf{S}} dV, \end{aligned} \quad (2.43)$$

by using the Gâteaux derivative together with the product rule. The second integral in the last line describes the influence of bias forces that arise from

the gross body motion of the reference configuration or other prestressing effects (Bremer, 1988, pp. 194); (Bremer and Pfeiffer, 1992, pp. 103); (Bremer, 2008, pp. 159). It remains to provide the missing quantities: The *bias variation of the Green–Lagrange strain* is given by

$$\delta \bar{\mathbf{E}} := \delta \mathbf{E}(\bar{\mathbf{u}}) = \frac{1}{2}(\delta \mathbf{H}^T + \delta \mathbf{H} + \bar{\mathbf{H}}^T \delta \mathbf{H} + \delta \mathbf{H}^T \bar{\mathbf{H}}) = \text{sym}[\overbrace{(\mathbf{I} + \bar{\mathbf{H}})}^{\bar{\mathbf{G}}}]^T \delta \mathbf{H}, \quad (2.44)$$

and the *perturbation variation of the Green–Lagrange strain* by

$$\delta \tilde{\mathbf{E}} := D\delta \mathbf{E}(\bar{\mathbf{u}})[\tilde{\mathbf{u}}] = \frac{1}{2}(\tilde{\mathbf{H}}^T \delta \mathbf{H} + \delta \mathbf{H}^T \tilde{\mathbf{H}}) = \text{sym}(\tilde{\mathbf{H}}^T \delta \mathbf{H}), \quad (2.45)$$

where *bias* and *perturbation displacement gradients* are defined as

$$\bar{\mathbf{H}} := \partial_{\mathbf{X}} \bar{\mathbf{u}}(\mathbf{X}, t), \quad \tilde{\mathbf{H}} := \partial_{\mathbf{X}} \tilde{\mathbf{u}}(\mathbf{X}, t). \quad (2.46)$$

The *bias stress* and the *bias Green–Lagrange strain* read

$$\bar{\mathbf{S}} := \mathbf{S}(\bar{\mathbf{u}}) = 2\mu \bar{\mathbf{E}} + \lambda(\bar{\mathbf{E}} : \mathbf{I})\mathbf{I}, \quad \bar{\mathbf{E}} := \mathbf{E}(\bar{\mathbf{u}}) = \frac{1}{2}(\bar{\mathbf{H}}^T + \bar{\mathbf{H}} + \bar{\mathbf{H}}^T \bar{\mathbf{H}}). \quad (2.47)$$

The *perturbation stress* writes as

$$\tilde{\mathbf{S}} := D\mathbf{S}(\bar{\mathbf{u}})[\tilde{\mathbf{u}}] = 2\mu \tilde{\mathbf{E}} + \lambda(\tilde{\mathbf{E}} : \mathbf{I})\mathbf{I} \quad (2.48)$$

using the linear *perturbation Green–Lagrange strain*

$$\tilde{\mathbf{E}} := D\mathbf{E}(\bar{\mathbf{u}})[\tilde{\mathbf{u}}] = \frac{1}{2}(\tilde{\mathbf{H}}^T + \tilde{\mathbf{H}} + \bar{\mathbf{H}}^T \tilde{\mathbf{H}} + \tilde{\mathbf{H}}^T \bar{\mathbf{H}}) = \text{sym}[\overbrace{(\mathbf{I} + \bar{\mathbf{H}})}^{\bar{\mathbf{G}}}]^T \tilde{\mathbf{H}}. \quad (2.49)$$

Finally, the *linearized virtual work contribution of the external forces*

$$\begin{aligned} \delta \tilde{W}^{\text{ext}} &:= D\delta W^{\text{ext}}(\bar{\mathbf{B}}, \bar{\mathbf{T}})[\tilde{\mathbf{B}}, \tilde{\mathbf{T}}] \\ &= \int_{\mathcal{B}_t^0} D\{\delta \mathbf{u} \cdot \mathbf{B}\}(\bar{\mathbf{B}})[\tilde{\mathbf{B}}] dV + \int_{\partial \mathcal{B}_t^0} D\{\delta \mathbf{u} \cdot \mathbf{T}\}(\bar{\mathbf{T}})[\tilde{\mathbf{T}}] dA \\ &= \int_{\mathcal{B}_t^0} \delta \mathbf{u} \cdot \tilde{\mathbf{B}} dV + \int_{\partial \mathcal{B}_t^0} \delta \mathbf{u} \cdot \tilde{\mathbf{T}} dA. \end{aligned} \quad (2.50)$$

is deduced from (2.30).

To summarize, we combine the linearized contributions (2.42), (2.43) and (2.50) and write the linearized principle of virtual work for the solid body as

$$\begin{aligned}
 0 = \delta \tilde{W}_{\text{tot}} = & \int_{\tilde{\mathcal{B}}_t^0} -\delta \mathbf{u} \cdot \varrho_0^s \{ \partial_t^2 \tilde{\mathbf{u}} + 2\partial_t (\partial_X \tilde{\mathbf{u}}) \dot{\mathbf{X}} \\
 & + [(\partial_X \partial_X \tilde{\mathbf{u}}) \dot{\mathbf{X}}] \dot{\mathbf{X}} + (\partial_X \tilde{\mathbf{u}}) \ddot{\mathbf{X}} \} dV \\
 & + \int_{\mathcal{B}_t^0} -\delta \tilde{\mathbf{E}} : \tilde{\mathbf{S}} dV + \int_{\mathcal{B}_t^0} -\delta \tilde{\mathbf{E}} : \bar{\mathbf{S}} dV \\
 & + \int_{\mathcal{B}_t^0} \delta \mathbf{u} \cdot \tilde{\mathbf{B}} dV + \int_{\partial \mathcal{B}_t^0} \delta \mathbf{u} \cdot \tilde{\mathbf{T}} dA \quad \forall \delta \mathbf{u}, \forall t.
 \end{aligned} \tag{2.51}$$

### 2.1.5 Boundary Value Problem

In the present section we derive the boundary value problem corresponding to the equation of motion (2.31) given in weak variational form. This is mainly an exercise in integration by parts in the three-dimensional domain. Using the general relation for the contraction of tensors

$$(\mathbf{AB}) : \mathbf{C} = \text{tr}[(\mathbf{AB})^T \mathbf{C}] = \text{tr}[\mathbf{B}^T (\mathbf{A}^T \mathbf{C})] = \mathbf{B} : (\mathbf{A}^T \mathbf{C}), \tag{2.52}$$

we can rewrite the virtual work contribution of the internal force (2.22) as

$$\begin{aligned}
 \delta \mathbf{E} : \mathbf{S} &= \frac{1}{2} (\mathbf{G}^T \delta \mathbf{G} + \delta \mathbf{G}^T \mathbf{G}) : \mathbf{S} = \text{sym}(\mathbf{G}^T \delta \mathbf{G}) : \mathbf{S} = (\mathbf{G}^T \delta \mathbf{G}) : \mathbf{S} \\
 &= \delta \mathbf{G} : (\mathbf{GS}) = (\partial_X \delta \mathbf{u}) : (\mathbf{GS}).
 \end{aligned} \tag{2.53}$$

Additionally, we find from Gauss's divergence theorem that

$$\int_{\mathcal{B}_t^0} -(\partial_X \mathbf{c}) : \mathbf{B} dV = \int_{\mathcal{B}_t^0} \mathbf{c} \cdot [(\partial_X \mathbf{B}) : \mathbf{I}] dV - \int_{\partial \mathcal{B}_t^0} \mathbf{c} \cdot (\mathbf{BN}) dA \quad \forall \mathbf{c}, \forall \mathbf{B}, \tag{2.54}$$

where  $\mathbf{N}$  denotes the outward unit vector normal to the boundary surface  $\partial \mathcal{B}_t^0$ . By combining (2.53) and (2.54) we rewrite (2.31) as

$$\begin{aligned}
 0 = \delta W_{\text{tot}} = & \int_{\mathcal{B}_t^0} \delta \mathbf{u} \cdot \{ [\partial_X (\mathbf{GS})] : \mathbf{I} + \mathbf{B} - \varrho_0^s \mathbf{A}^s \} dV \\
 & + \int_{\partial \mathcal{B}_t^0} \delta \mathbf{u} \cdot [\mathbf{T} - (\mathbf{GS})\mathbf{N}] dA \quad \forall \delta \mathbf{u}.
 \end{aligned} \tag{2.55}$$

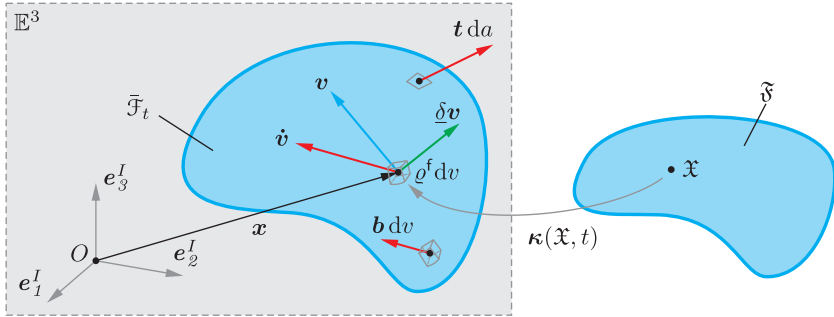


**Fig. 2.2:** Placement of fluid body  $\mathfrak{F}$  in the current configuration  $\bar{\mathcal{F}}_t$  of Euclidean vector space  $\mathbb{E}^3$ .

As this equation must hold for all  $\delta u$ , we can state the boundary value problem

$$\begin{cases} \varrho_0^s \mathbf{A}^s = [\partial_{\mathbf{x}}(\mathbf{GS})] : \mathbf{I} + \mathbf{B} & \text{in } \mathcal{B}_t^0 \\ \mathbf{T} = (\mathbf{GS})\mathbf{N} & \text{on } \partial\mathcal{B}_t^0. \end{cases} \quad (2.56)$$

## 2.2 Governing Equations of the Fluid

### 2.2.1 System and Kinematics

Similar to definitions for the solid body motion in §2.1.1, we introduce the system and kinematics for the fluid body motion according to Fig. 2.2. In contrast to the solid body, we do not rely on a reference configuration to describe the constitutive equations. Furthermore, we choose an Eulerian representation of the kinematics, where the velocity field in the current configuration is the primary variable.

A *fluid body*  $\mathfrak{F}$  is a set of particles that can be bijectively placed into a subset of a *physical space*, again represented by the three-dimensional Euclidean vector space  $\mathbb{E}^3$ . The Euclidean vector space is inertial and equipped with an orthonormal base  $(e_1^I, e_2^I, e_3^I)$  and an origin  $O$ , forming the  $I$ -system.

The time parameter family of *placements* into the *current configuration*  $\bar{\mathcal{F}}_t \subset \mathbb{E}^3$  is defined as the function  $\kappa : \mathfrak{F} \times \mathbb{R} \rightarrow \bar{\mathcal{F}}_t$  together with its inverse

$$\mathbf{x} = \kappa(\mathfrak{X}, t), \quad \mathfrak{X} = \kappa^{-1}(\mathbf{x}, t), \quad (2.57)$$

where  $\mathfrak{X} \in \mathfrak{B}$  denotes a specific *particle* and  $\mathbf{x}$  its *position vector* in the deformed configuration with respect to  $O$ . This time evolution of placements is called the *motion* of  $\mathfrak{F}$  in the current configuration. The *trajectory*, *velocity* and *acceleration* of a particle  $\mathfrak{X}$  in the deformed configuration then write as, respectively,

$$\mathbf{x}(t) = \kappa(\mathfrak{X}, t), \quad \dot{\mathbf{x}}(t) = \partial_t \kappa(\mathfrak{X}, t), \quad \ddot{\mathbf{x}}(t) = \partial_t^2 \kappa(\mathfrak{X}, t), \quad (2.58)$$

where we use partial time derivatives because the particle  $\mathfrak{X}$  is kept fixed. The region occupied by the image  $\bar{\mathcal{F}}_t = \kappa(\mathfrak{F}, t)$  can be written as the disjoint union  $\bar{\mathcal{F}}_t = \mathcal{F}_t \cup \partial \mathcal{F}_t$  of the *interior*  $\mathcal{F}_t$  and the *boundary*  $\partial \mathcal{F}_t$  of the current configuration, respectively.

Using (2.57)<sub>2</sub> we eliminate the particle  $\mathfrak{X}$  from (2.58)<sub>2</sub> and define the *velocity field* in Eulerian description

$$\dot{\mathbf{x}} = \mathbf{v}(\mathbf{x}, t) := \partial_t \kappa(\underbrace{\kappa^{-1}(\mathbf{x}, t)}_{\mathfrak{X}}, t). \quad (2.59)$$

Applying the chain rule, by keeping the particle  $\mathfrak{X}$  fixed, we derive the *acceleration field*

$$\ddot{\mathbf{x}} = \mathbf{a}^f(\mathbf{x}, t) := \mathcal{D}_t^f \mathbf{v} = \partial_t \mathbf{v} + (\partial_x \mathbf{v}) \dot{\mathbf{x}} = \partial_t \mathbf{v} + (\partial_x \mathbf{v}) \mathbf{v}. \quad (2.60)$$

The operator  $\mathcal{D}_t^f$  operating on  $\mathbf{v}$  formally defines the material derivative for the fluid body.

The rate for deformation in the vicinity of  $\mathbf{x}$  is described by the *spatial velocity gradient*, defined as the tensor

$$\mathbf{l}(\mathbf{x}, t) := \partial_x \mathbf{v}(\mathbf{x}, t). \quad (2.61)$$

The symmetric part of  $\mathbf{l}$  denotes the *spatial strain rate tensor*

$$\mathbf{d}(\mathbf{x}, t) := \text{sym}[\mathbf{l}(\mathbf{x}, t)] = \frac{1}{2}(\mathbf{l} + \mathbf{l}^\top), \quad (2.62)$$

which will be used to describe the constitutive equation for the fluid. The skew-symmetric part of  $\mathbf{l}$  is called the *spatial spin tensor* and is defined by

$$\mathbf{w}(\mathbf{x}, t) := \text{skw}[\mathbf{l}(\mathbf{x}, t)] = \frac{1}{2}(\mathbf{l} - \mathbf{l}^\top). \quad (2.63)$$

Every skew-symmetric second-order tensor in the three-space can be expressed by a corresponding axial vector. We use this fact to define the *vorticity vector*  $\boldsymbol{\eta}(\boldsymbol{x}, t)$  by the relation

$$\boldsymbol{w}c = \frac{1}{2}(\boldsymbol{\eta} \times \boldsymbol{c}) \quad \forall \boldsymbol{c}. \quad (2.64)$$

Forces acting on the fluid body  $\mathfrak{F}$  are generally denoted as  $d\boldsymbol{f}(\boldsymbol{x}, t)$  or  $d\boldsymbol{f}(\boldsymbol{x}, t)$ , depending on whether represented as vector or tensor quantity. We distinguish between *volume body forces*  $\boldsymbol{b} dv$ , *surface traction forces*  $\boldsymbol{t} da$ , *inertia forces*  $(-\rho^f \boldsymbol{a}^f) dv$  and *internal forces*, which we subsequently express in terms of the Cauchy stress contribution  $-\boldsymbol{\sigma} dv$ .

## 2.2.2 Principle of Virtual Power

In §2.1.2 we introduced the concept of virtual displacements, and with this the principle of virtual work for the solid body. In the present section we do the equivalent to derive the equations of motion for the fluid body  $\mathfrak{F}$ . For a fluid, it is more convenient to work on the velocity level instead of the position level. We therefore define virtual velocities and state the governing equation for the fluid formulated by the principle of virtual power.

We adopt the definitions of the *family of virtual placements*  $\boldsymbol{\kappa}(\boldsymbol{x}, t, \varepsilon)$  and the *virtual displacement*  $\delta\boldsymbol{\kappa}(\boldsymbol{x}, t)$  from §2.1.2 also to the fluid body. Furthermore, we denote the *set of all families of virtual placements*  $\mathbb{H}$ , such that

$$\boldsymbol{\kappa}(\boldsymbol{x}, t, \varepsilon) \in \mathbb{H} \quad \Leftrightarrow \quad \delta\boldsymbol{\kappa}(\boldsymbol{x}, t) = \partial_\varepsilon \boldsymbol{\kappa}(\boldsymbol{x}, t, \varepsilon_0) \cdot \delta\varepsilon \quad (2.65)$$

holds. For every time instant  $t_0 \in \mathbb{R}$ , we then define the subset  $\underline{\mathbb{H}}(t_0) \subset \mathbb{H}$  as the families of placements  $\boldsymbol{\kappa}(\boldsymbol{x}, t, \varepsilon)$  where the virtual displacements  $\delta\boldsymbol{\kappa}(\boldsymbol{x}, t_0)$  vanish for  $t_0$ , that is,

$$\underline{\boldsymbol{\kappa}}(\boldsymbol{x}, t_0, \varepsilon) \in \underline{\mathbb{H}}(t_0) := \{\boldsymbol{\kappa}(\boldsymbol{x}, t, \varepsilon) \in \mathbb{H} \mid \partial_\varepsilon \boldsymbol{\kappa}(\boldsymbol{x}, t_0, \varepsilon_0) = \boldsymbol{0}\} \subset \mathbb{H}. \quad (2.66)$$

With the virtual placements of the restricted set  $\underline{\mathbb{H}}(t)$ , marked by an underbar, we define the *virtual velocity* of particle  $\boldsymbol{x}$  as

$$\underline{\delta\boldsymbol{\kappa}}(\boldsymbol{x}, t) := \partial_t \partial_\varepsilon \underline{\boldsymbol{\kappa}}(\boldsymbol{x}, t, \varepsilon_0) \cdot \delta\varepsilon. \quad (2.67)$$

Although we select the virtual displacements from the restricted set  $\underline{\mathbb{H}}(t)$ , the virtual velocities are still arbitrary in direction. We express the virtual



velocity fields in terms of the position fields in the current configuration by

$$\underline{\delta v}(\mathbf{x}, t) := \underline{\delta \dot{\kappa}}(\underbrace{\kappa^{-1}(\mathbf{x}, t)}_{\mathfrak{X}}, t). \quad (2.68)$$

Now, we formulate the *principle of virtual power*, which is equivalent to the principle of virtual work (2.19), but expressed on velocity level: Let  $(d\mathbf{f}_{\text{tot}}, d\mathbf{f}_{\text{tot}})$  be the totality of forces acting on the body expressed in the current configuration  $\mathfrak{F}_t$ . In order that the fluid body  $\mathfrak{F}$  is in dynamical equilibrium, the overall virtual power  $\underline{\delta}P_{\text{tot}}$  performed by  $(d\mathbf{f}_{\text{tot}}, d\mathbf{f}_{\text{tot}})$ , must vanish for all virtual velocities  $\underline{\delta v}$  and gradients thereof, that is,

$$0 = \underline{\delta}P_{\text{tot}} = \int_{\mathfrak{F}_t} \underline{\delta v} \cdot d\mathbf{f}_{\text{tot}} + \int_{\mathfrak{F}_t} (\partial_x \underline{\delta v}) : d\mathbf{f}_{\text{tot}} \quad \forall \underline{\delta v}, \forall t. \quad (2.69)$$

Again, the totality of forces must include all forces, namely the inertia forces, the internal forces, and the external forces. Accordingly, we can write the total virtual power as

$$0 = \underline{\delta}P_{\text{tot}} = \underline{\delta}P^{\text{dyn}} + \underline{\delta}P^{\text{int}} + \underline{\delta}P^{\text{ext}} \quad \forall \underline{\delta v}, \forall t, \quad (2.70)$$

with the virtual power contributions further specified in the following paragraphs. The definition of the virtual velocities via the subset of virtual displacements ensures that the principles of virtual work and power are equivalent.

### Virtual Power Contributions of Inertia Forces

The inertia forces contribute to the virtual power by

$$\underline{\delta}P^{\text{dyn}} := \int_{\mathfrak{F}_t} -\underline{\delta v} \cdot \rho^f [\partial_t \mathbf{v} + (\partial_x \mathbf{v})\mathbf{v}] dv, \quad (2.71)$$

with the acceleration term defined in (2.60).

### Virtual Power Contributions of Internal Forces

Analogous to §2.1.2, we define internal forces with respect to the fluid body  $\mathfrak{F}$  and include the virtual power contribution by the internal forces as

$$\underline{\delta}P^{\text{int}} := \int_{\mathfrak{F}_t} -\underline{\delta d} : \boldsymbol{\sigma} dv, \quad (2.72)$$

with the symmetric Cauchy stress tensor  $\boldsymbol{\sigma}$  and the *variation of the strain rate* defined by

$$\underline{\delta}\mathbf{d}(\mathbf{x}, t) := D\mathbf{d}[\underline{\delta}\mathbf{l}] = \frac{1}{2}(\underline{\delta}\mathbf{l}^T + \underline{\delta}\mathbf{l}). \quad (2.73)$$

Herein, the *variation of the spatial velocity gradient* is given by

$$\underline{\delta}\mathbf{l}(\mathbf{x}, t) := D\mathbf{l}[\underline{\delta}\mathbf{v}] = \partial_x \underline{\delta}\mathbf{v}. \quad (2.74)$$

### Virtual Power Contributions of External Forces

We define external forces with respect to the fluid body  $\bar{\mathfrak{F}}$  analogously to §2.1.2 and include the virtual power contribution by the external forces by

$$\underline{\delta}P^{\text{ext}} := \int_{\mathcal{F}_t} \underline{\delta}\mathbf{v} \cdot \mathbf{b} \, dv + \int_{\partial\mathcal{F}_t} \underline{\delta}\mathbf{v} \cdot \mathbf{t} \, da. \quad (2.75)$$

In summary, we assemble the contributions of the inertia forces (2.71), the internal forces (2.72) and (2.75) and write out the principle of virtual power in the current configuration as

$$\begin{aligned} 0 = \underline{\delta}P_{\text{tot}} &= \int_{\bar{\mathfrak{F}}_t} -\underline{\delta}\mathbf{v} \cdot \rho^f [\partial_t \mathbf{v} + (\partial_x \mathbf{v})\mathbf{v}] \, dv \\ &\quad + \int_{\mathcal{F}_t} -\underline{\delta}\mathbf{d} : \boldsymbol{\sigma} \, dv \\ &\quad + \int_{\mathcal{F}_t} \underline{\delta}\mathbf{v} \cdot \mathbf{b} \, dv + \int_{\partial\mathcal{F}_t} \underline{\delta}\mathbf{v} \cdot \mathbf{t} \, da \quad \forall \underline{\delta}\mathbf{v}, \forall t. \end{aligned} \quad (2.76)$$

### 2.2.3 Perfect Bilateral Constraints

Similar to §2.1.3 we now introduce kinematic constraints on the motion of the fluid body. Perfect bilateral constraints on the velocity field may be equivalently represented in local strong form or in the weak variational form, namely,

$$0 = \gamma^\mu(\mathbf{v}) \quad \Leftrightarrow \quad 0 = \delta\Omega^\mu := \int_{\bar{\mathfrak{F}}_t} \delta\mu \cdot \gamma^\mu(\mathbf{v}) \, dv \quad \forall \delta\mu. \quad (2.77)$$

Therein,  $\gamma^\mu(\mathbf{v})$  is a scalar-valued *constraint function* at the velocity level and  $\delta\mu$  an arbitrary test function called *virtual force*. The forces which ensure the constraint (2.77) are denoted as  $d\mathbf{f}^{\text{con}}$ .

The *principle of Jourdain* is the constitutive law for the constraint forces of perfect bilateral constraints at velocity level and is formulated as follows: The virtual power  $\underline{\delta}P_{\text{adm}}^{\text{con}}$  generated by the constraint forces  $d\mathbf{f}^{\text{con}}$  vanishes for all virtual velocities  $\underline{\delta}\mathbf{v}_{\text{adm}}$  admissible with the constraint, that is

$$0 = \underline{\delta}P_{\text{adm}}^{\text{con}} = \int_{\bar{\mathcal{F}}_t} \underline{\delta}\mathbf{v}_{\text{adm}} \cdot d\mathbf{f}^{\text{con}} \quad \forall \underline{\delta}\mathbf{v}_{\text{adm}}, \forall t, \quad (2.78)$$

or in local form

$$0 = \underline{\delta}p_{\text{adm}}^{\text{con}} = \underline{\delta}\mathbf{v}_{\text{adm}} \cdot d\mathbf{f}^{\text{con}} \quad \forall \underline{\delta}\mathbf{v}_{\text{adm}}, \forall t. \quad (2.79)$$

Furthermore, we find the admissible variations of (2.77) using the Gâteaux derivative (A.1) as

$$\begin{aligned} 0 = \underline{\delta}\gamma_{\text{adm}}^{\mu}(\mathbf{v}) &= D\gamma^{\mu}(\mathbf{v})[\underline{\delta}\mathbf{v}_{\text{adm}}] = [\partial_{\mathbf{v}}\gamma^{\mu}(\mathbf{v})] \cdot \underline{\delta}\mathbf{v}_{\text{adm}} \\ &= \underline{\delta}\mathbf{v}_{\text{adm}} \cdot [\partial_{\mathbf{v}}\gamma^{\mu}(\mathbf{v})] \quad \forall \underline{\delta}\mathbf{v}_{\text{adm}}. \end{aligned} \quad (2.80)$$

A comparison of (2.79) and (2.80), with the fact that both equations hold for all  $\underline{\delta}\mathbf{v}_{\text{adm}}$ , reveals the form of the constraint force

$$d\mathbf{f}^{\text{con}} = \mu[\partial_{\mathbf{v}}\gamma^{\mu}(\mathbf{v})] d\mathbf{v}, \quad (2.81)$$

where  $\partial_{\mathbf{v}}\gamma^{\mu}(\mathbf{v})$  represents the generalized force direction and  $\mu$  is a scalar Lagrange multiplier. The vector-valued force direction, defined as the gradient  $\partial_{\mathbf{v}}\gamma^{\mu}(\mathbf{v})$ , may be found, again, by applying the Gâteaux derivative (A.1) on the constraint function (2.77), that is

$$0 = D\gamma^{\mu}(\mathbf{v})[\tilde{\mathbf{v}}] = [\partial_{\mathbf{v}}\gamma^{\mu}(\mathbf{v})] \cdot \tilde{\mathbf{v}} \quad \forall \tilde{\mathbf{v}}. \quad (2.82)$$

Instead of (2.77) we could also define constraints on the field of the velocity gradient  $\mathbf{I} = \partial_{\mathbf{x}}\mathbf{v}$ , again equivalently in local strong form or in the weak variational form, by

$$0 = \Gamma^{\mu}(\mathbf{I}) \Leftrightarrow 0 = \delta\Pi^{\mu} := \int_{\bar{\mathcal{F}}_t} \delta\mu \cdot \Gamma^{\mu}(\mathbf{I}) d\mathbf{v} \quad \forall \delta\mu. \quad (2.83)$$

The formalism is the same as sketched out above and leads to constraint stresses of the form

$$d\mathbf{f}^{\text{con}} = \mu[\partial_{\mathbf{I}}\Gamma^{\mu}(\mathbf{I})] d\mathbf{v}, \quad (2.84)$$

where the gradient  $\partial_{\mathbf{I}}\Gamma^{\mu}(\mathbf{I})$  represents the tensor-valued stress direction.

### Incompressibility Constraint

We now apply the findings for the perfect constraints to define the incompressibility constraint for the fluid motion. We model the fluid flow as incompressible, that is, a motion with a divergence-free velocity field

$$0 = (\partial_x \mathbf{v}) : \mathbf{I} = \mathbf{1} : \mathbf{I} =: \Gamma^p(\mathbf{1}) \Leftrightarrow 0 = \delta \Pi^p := \int_{\mathcal{F}_t} -\delta p \cdot \Gamma^p(\mathbf{1}) \, dv \quad \forall \delta p, \quad (2.85)$$

where we define the constraint function  $\Gamma^p(\mathbf{1})$  at the velocity level and introduce an arbitrary test function  $\delta p$  called *virtual pressure*. We reconsider (2.72), the virtual power contribution of internal forces,

$$\underline{\delta P}^{\text{int}} = \int_{\mathcal{F}_t} -\underline{\delta \mathbf{d}} : \overbrace{(\boldsymbol{\tau} + \boldsymbol{\varsigma})}^{\boldsymbol{\sigma}} \, dv, \quad (2.86)$$

where we have split the total Cauchy stress  $\boldsymbol{\sigma}$  into an impressed stress  $\boldsymbol{\tau}$  and a constraint stress  $\boldsymbol{\varsigma}$ , which enforces (2.85) to hold.

The principle of Jourdain reveals the specific form of the constraint stress

$$\boldsymbol{\varsigma} = -p(\partial_1 \Gamma^p), \quad (2.87)$$

with the Lagrange multiplier  $p$  recognized as *pressure*. The stress direction  $\partial_1 \Gamma^p$  is found by applying the Gâteaux derivative to (2.85)<sub>1</sub> as

$$D\Gamma^p(\mathbf{1})[\tilde{\mathbf{I}}] = (\partial_1 \Gamma^p) : \tilde{\mathbf{I}} = \lim_{\varepsilon \rightarrow 0} \frac{(\mathbf{1} + \varepsilon \tilde{\mathbf{I}}) : \mathbf{I} - \mathbf{1} : \mathbf{I}}{\varepsilon} = \tilde{\mathbf{I}} : \mathbf{I} = \mathbf{I} : \tilde{\mathbf{I}} \quad \forall \tilde{\mathbf{I}}, \quad (2.88)$$

which yields  $\partial_1 \Gamma^p = \mathbf{I}$  and finally

$$\boldsymbol{\varsigma} = -p\mathbf{I}. \quad (2.89)$$

In accordance to White (2005, p. 66), we model the impressed stress as *Newtonian fluid*

$$\boldsymbol{\tau} = 2\mu^f \mathbf{d} + \lambda^f (\mathbf{d} : \mathbf{I})\mathbf{I}, \quad (2.90)$$

with the *first viscosity*  $\mu^f$  and the *second viscosity*  $\lambda^f$ . For an incompressible flow, where the incompressibility condition (2.85) holds, the second term

vanishes, because  $0 = \Gamma^p(\mathbf{1}) = \mathbf{1} : \mathbf{I} = (\mathbf{d} + \mathbf{w}) : \mathbf{I} = \mathbf{d} : \mathbf{I}$ . We collect the results from (2.85), (2.89) and (2.90) and write out the total stress as

$$\boldsymbol{\sigma} = \boldsymbol{\tau} + \boldsymbol{\zeta} = 2\mu^f \mathbf{d} + \underbrace{\lambda^f(\mathbf{d} : \mathbf{I})}_{0} \mathbf{I} - p(\partial_t \Gamma^p) = 2\mu^f \mathbf{d} - p\mathbf{I}. \quad (2.91)$$

The weak variational equation describing the incompressible flow of a Newtonian fluid then writes as

$$\begin{aligned} 0 = \underline{\delta} P_{\text{tot}} + \delta \Pi^p &= \int_{\bar{\mathcal{F}}_t} -\underline{\delta} \mathbf{v} \cdot \varrho^f [\partial_t \mathbf{v} + (\partial_x \mathbf{v}) \mathbf{v}] \, dv \\ &+ \int_{\bar{\mathcal{F}}_t} -\underline{\delta} \mathbf{d} : (2\mu^f \mathbf{d} - p\mathbf{I}) \, dv \\ &+ \int_{\bar{\mathcal{F}}_t} \underline{\delta} \mathbf{v} \cdot \mathbf{b} \, dv + \int_{\partial \bar{\mathcal{F}}_t} \underline{\delta} \mathbf{v} \cdot \mathbf{t} \, da \\ &+ \int_{\bar{\mathcal{F}}_t} -\delta p (\mathbf{1} : \mathbf{I}) \, dv \quad \forall \underline{\delta} \mathbf{v}, \forall \delta p, \forall t, \end{aligned} \quad (2.92)$$

where the equation of motion (2.76) and the constraint equation (2.85)<sub>2</sub> are combined into one.

### 2.2.4 Linearization

In the same way as in §2.1.4, we linearize the governing equations of the fluid by applying the Gâteaux derivative at the bias solution  $\bar{\mathbf{q}}$  into the direction of the disturbance  $\tilde{\mathbf{q}}$ . We apply the linearization procedure to (2.92) and derive the linearized equations of motion as

$$0 = \underline{\delta} \tilde{P}_{\text{tot}} + \delta \tilde{\Pi}^p = \underline{\delta} \tilde{P}^{\text{dyn}} + \underline{\delta} \tilde{P}^{\text{int}} + \underline{\delta} \tilde{P}^{\text{ext}} + \delta \tilde{\Pi}^p \quad \forall \underline{\delta} \mathbf{v}, \forall \delta p, \forall t, \quad (2.93)$$

with the different contributions given in the following. The *linearized virtual power contribution of the inertia forces* from (2.71) yields

$$\begin{aligned} \underline{\delta} \tilde{P}^{\text{dyn}} &:= D \underline{\delta} P^{\text{dyn}}(\bar{\mathbf{v}})[\tilde{\mathbf{v}}] = \int_{\bar{\mathcal{F}}_t} D \{ -\underline{\delta} \mathbf{v} \cdot \varrho^f [\partial_t \mathbf{v} + (\partial_x \mathbf{v}) \mathbf{v}] \}(\bar{\mathbf{v}})[\tilde{\mathbf{v}}] \, dv \\ &= \int_{\bar{\mathcal{F}}_t} -\underline{\delta} \mathbf{v} \cdot \varrho^f [\partial_t \tilde{\mathbf{v}} + (\partial_x \bar{\mathbf{v}}) \tilde{\mathbf{v}} + (\partial_x \tilde{\mathbf{v}}) \bar{\mathbf{v}}] \, dv. \end{aligned} \quad (2.94)$$

From (2.72), we derive the *linearized virtual power contribution of the internal forces*

$$\begin{aligned}\underline{\delta}\tilde{P}^{\text{int}} &:= D\underline{\delta}P^{\text{int}}(\bar{\mathbf{v}}, \bar{p})[\tilde{\mathbf{v}}, \tilde{p}] = \int_{\mathcal{F}_t} D\{-\underline{\delta}\mathbf{d} : (2\mu^f \mathbf{d} - p\mathbf{I})\}(\bar{\mathbf{v}}, \bar{p})[\tilde{\mathbf{v}}, \tilde{p}] dv \\ &= \int_{\mathcal{F}_t} -\underline{\delta}\mathbf{d} : (2\mu^f \tilde{\mathbf{d}} - \tilde{p}\mathbf{I}) dv\end{aligned}\quad (2.95)$$

with the *perturbation velocity gradient* and the *perturbation strain rate*, respectively, defined as

$$\tilde{\mathbf{I}} := \partial_x \tilde{\mathbf{v}}, \quad \tilde{\mathbf{d}} := \frac{1}{2}(\tilde{\mathbf{I}} + \tilde{\mathbf{I}}^T). \quad (2.96)$$

The *linearized virtual power contribution of the external forces* writes as

$$\begin{aligned}\underline{\delta}\tilde{P}^{\text{ext}} &:= D\underline{\delta}P^{\text{ext}}(\bar{\mathbf{b}}, \bar{\mathbf{t}})[\tilde{\mathbf{b}}, \tilde{\mathbf{t}}] \\ &= \int_{\mathcal{F}_t} D\{\underline{\delta}\mathbf{v} \cdot \mathbf{b}\}(\bar{\mathbf{b}})[\tilde{\mathbf{b}}] dv + \int_{\partial\mathcal{F}_t} D\{\underline{\delta}\mathbf{v} \cdot \mathbf{t}\}(\bar{\mathbf{t}})[\tilde{\mathbf{t}}] da \\ &= \int_{\mathcal{F}_t} \underline{\delta}\mathbf{v} \cdot \tilde{\mathbf{b}} dv + \int_{\partial\mathcal{F}_t} \underline{\delta}\mathbf{v} \cdot \tilde{\mathbf{t}} da,\end{aligned}\quad (2.97)$$

and the *linearized incompressibility constraint* from (2.85) is given by

$$\begin{aligned}\delta\tilde{\Pi}^p &:= D\delta\Pi^p(\bar{\mathbf{v}})[\tilde{\mathbf{v}}] = \int_{\mathcal{F}_t} D\{-\delta p \cdot \Gamma^p(\mathbf{l})\}(\bar{\mathbf{l}})[\tilde{\mathbf{l}}] dv \\ &= \int_{\mathcal{F}_t} -\delta p(\tilde{\mathbf{l}} : \mathbf{I}) dv.\end{aligned}\quad (2.98)$$

Finally, we assemble the linearized contributions (2.94), (2.95), (2.97) and (2.98) of the fluid body to

$$\begin{aligned}0 = \underline{\delta}\tilde{P}_{\text{tot}} + \delta\tilde{\Pi}^p &= \int_{\mathcal{F}_t} -\underline{\delta}\mathbf{v} \cdot \varrho^f [\partial_t \tilde{\mathbf{v}} + (\partial_x \bar{\mathbf{v}})\tilde{\mathbf{v}} + (\partial_x \tilde{\mathbf{v}})\bar{\mathbf{v}}] dv \\ &\quad + \int_{\mathcal{F}_t} -\underline{\delta}\mathbf{d} : (2\mu^f \tilde{\mathbf{d}} - \tilde{p}\mathbf{I}) dv \\ &\quad + \int_{\mathcal{F}_t} \underline{\delta}\mathbf{v} \cdot \tilde{\mathbf{b}} dv + \int_{\partial\mathcal{F}_t} \underline{\delta}\mathbf{v} \cdot \tilde{\mathbf{t}} da \\ &\quad + \int_{\mathcal{F}_t} -\delta p(\tilde{\mathbf{l}} : \mathbf{I}) dv \quad \forall \underline{\delta}\mathbf{v}, \forall \delta p, \forall t\end{aligned}\quad (2.99)$$

## 2.2.5 Boundary Value Problem

Similar to the derivation in §2.1.5 we can rewrite (2.92) as

$$0 = \underline{\delta} P_{\text{tot}} = \int_{\mathcal{F}_t} -\underline{\delta} \mathbf{v} \cdot \{ \partial_x [(2\mu^f \mathbf{d}) - p\mathbf{I}] : \mathbf{I} + \mathbf{b} - \varrho^f [\partial_t \mathbf{v} + (\partial_x \mathbf{v}) \mathbf{v}] \} dv \\ + \int_{\partial \mathcal{F}_t} \underline{\delta} \mathbf{v} \cdot [\mathbf{t} - (2\mu^f \mathbf{d} - p\mathbf{I}) \mathbf{n}] da \quad \forall \underline{\delta} \mathbf{v}, \quad (2.100)$$

where  $\mathbf{n}$  denotes the outward unit vector normal to the boundary surface  $\partial \mathcal{F}_t$ . This leads to the boundary value problem corresponding to (2.92)

$\varrho^f [\partial_t \mathbf{v} + (\partial_x \mathbf{v}) \mathbf{v}] = -\partial_x p + \mu^f [\partial_x (\partial_x \mathbf{v})] : \mathbf{I} + \mathbf{b} \quad \text{in } \mathcal{F}_t$	(2.101)
$\mathbf{t} = (2\mu^f \mathbf{d} - p\mathbf{I}) \mathbf{n} \quad \text{on } \partial \mathcal{F}_t$	

together with the incompressibility condition  $0 = (\partial_x \mathbf{v}) : \mathbf{I}$ . This equation is widely known as Navier–Stokes equation (White, 2005, p. 68).

## 2.3 Coupling of Solid with Fluid

### 2.3.1 Total System

In the preceding sections we considered the equations of motion for a solid body and a fluid body separately. However, our main focus lies on solid–fluid coupled systems and we therefore need to treat the coupling between these two. This section derives the equations of motion for the total system by combining the solid equations of §2.1 and the fluid equations of §2.2. The explicit coupling between solid and fluid is then covered in the subsequent section.

The *total system*  $\mathcal{T} := \mathcal{B} \cup \mathcal{F}$ , formed by the union of the solid and the fluid body, occupies the region  $\mathcal{T}_t := \mathcal{B}_t \cup \mathcal{F}_t$  in the physical space. We call the surface  $\partial \mathcal{T}_t := \partial \mathcal{B}_t \cap \partial \mathcal{F}_t$ , build by the intersection of the solid and fluid boundary, the *interface*. To clearly distinguish between the quantities, we indicate solid quantities with a superscript 's' and fluid quantities with a superscript 'f'.

First, we would like to clarify that the *principle of virtual work* stated in §2.1.2 and the *principle of virtual power* formulated in §2.2.2 can be

regarded as equivalent, that is,

$$0 = \delta W_{\text{tot}} = \int_{\bar{\mathcal{F}}_t} \delta \mathbf{x} \cdot d\mathbf{f}_{\text{tot}} + \int_{\bar{\mathcal{F}}_t} (\partial_x \delta \mathbf{x}) : d\mathbf{f}_{\text{tot}} \quad \forall \delta \mathbf{x} \quad (2.102a)$$

$\Updownarrow$

$$0 = \underline{\delta} P_{\text{tot}} = \int_{\bar{\mathcal{F}}_t} \underline{\delta} \mathbf{v} \cdot d\mathbf{f}_{\text{tot}} + \int_{\bar{\mathcal{F}}_t} (\partial_x \underline{\delta} \mathbf{v}) : d\mathbf{f}_{\text{tot}} \quad \forall \underline{\delta} \mathbf{v}. \quad (2.102b)$$

The principle of virtual power is convenient for a kinematics described at velocity level, what is true for the fluid motion. We therefore apply the principle of virtual power for both solid and fluid, building the total system.

In §2.1.2 and §2.2.2, we introduced the concept of internal and external forces, which are defined as internal or external with respect to a specific system. Considering this, we rewrite the contributions to the virtual power of the external forces. The contribution with respect to the solid body  $\mathfrak{B}$  from (2.30) then writes as

$$\underline{\delta} P^{\text{ext}\mathfrak{B}} = \int_{\mathcal{B}_t} \underline{\delta} \mathbf{v}^s \cdot \mathbf{b}^s dv + \int_{\partial \mathcal{B}_t \setminus \partial \mathcal{J}_t} \underline{\delta} \mathbf{v}^s \cdot \mathbf{t}^s da + \int_{\partial \mathcal{J}_t} \underline{\delta} \mathbf{v}^s \cdot \mathbf{t}^s da, \quad (2.103)$$

the one with respect to the fluid body  $\mathfrak{F}$  from (2.75) writes as

$$\underline{\delta} P^{\text{ext}\mathfrak{F}} = \int_{\mathcal{F}_t} \underline{\delta} \mathbf{v}^f \cdot \mathbf{b}^f dv + \int_{\partial \mathcal{F}_t \setminus \partial \mathcal{J}_t} \underline{\delta} \mathbf{v}^f \cdot \mathbf{t}^f da + \int_{\partial \mathcal{J}_t} \underline{\delta} \mathbf{v}^f \cdot \mathbf{t}^f da. \quad (2.104)$$

Note that we separated the integrals over the interface  $\partial \mathcal{J}_t$  from the integrals over the remaining surface. The integrals over the interface  $\partial \mathcal{J}_t$ —that are *external* with respect to the solid body  $\mathfrak{B}$  or the fluid body  $\mathfrak{F}$ —become *internal* with respect to the total system  $\mathfrak{T}$ . We therefore write out the virtual power contribution of the external forces for the total system as

$$\begin{aligned} \underline{\delta} P^{\text{ext}\mathfrak{T}} := & \int_{\mathcal{B}_t} \underline{\delta} \mathbf{v}^s \cdot \mathbf{b}^s dv + \int_{\partial \mathcal{B}_t \setminus \partial \mathcal{J}_t} \underline{\delta} \mathbf{v}^s \cdot \mathbf{t}^s da \\ & + \int_{\mathcal{F}_t} \underline{\delta} \mathbf{v}^f \cdot \mathbf{b}^f dv + \int_{\partial \mathcal{F}_t \setminus \partial \mathcal{J}_t} \underline{\delta} \mathbf{v}^f \cdot \mathbf{t}^f da, \end{aligned} \quad (2.105)$$

and the virtual power contribution of the internal forces of the total system

$$\begin{aligned} \underline{\delta} P^{\text{int}\mathfrak{T}} := & \int_{\mathcal{B}_t} -\underline{\delta} \mathbf{d}^s : \boldsymbol{\sigma}^s dv + \int_{\partial \mathcal{J}_t} \underline{\delta} \mathbf{v}^s \cdot \mathbf{t}^s da \\ & + \int_{\mathcal{F}_t} -\underline{\delta} \mathbf{d}^f : \boldsymbol{\sigma}^f dv + \int_{\partial \mathcal{J}_t} \underline{\delta} \mathbf{v}^f \cdot \mathbf{t}^f da. \end{aligned} \quad (2.106)$$



At the interface  $\partial\mathcal{J}_t$ , the surface traction force  $\mathbf{t}^s da$  is then exerted from the fluid to the solid and  $\mathbf{t}^f da$  is exerted from the solid to the fluid.

For completeness, we provide the contribution of the inertia forces for the total system as

$$\begin{aligned} \delta P^{\text{dyn}\mathfrak{I}} &:= \delta P^{\text{dyn}\mathfrak{B}} + \delta P^{\text{dyn}\mathfrak{F}} \\ &= \int_{\mathfrak{B}_t} -\delta \mathbf{v}^s \cdot (\rho^s \mathbf{a}^s) dv + \int_{\mathfrak{F}_t} -\delta \mathbf{v}^f \cdot (\rho^f \mathbf{a}^f) dv. \end{aligned} \quad (2.107)$$

### 2.3.2 Interface Condition

This section addresses the conditions on the kinematics and the constraint forces for the coupling between a solid and a fluid body, as depicted in Fig. 2.3. For the fluid to stick at the solid, the velocities of solid and fluid particles must be equal for all particles at the interface  $\partial\mathcal{J}_t$ , that is,

$$\begin{aligned} \mathbf{0} &= \mathbf{v}^s(\mathbf{X}^s, t) - \mathbf{v}^f(\overbrace{\mathbf{x}^s(\mathbf{X}^s, t)}^{\mathbf{x}^f}, t) \\ &= \dot{\mathbf{X}} + \partial_t \mathbf{u}^s(\mathbf{X}^s, t) + [\partial_{\mathbf{X}} \mathbf{u}^s(\mathbf{X}^s, t)] \dot{\mathbf{X}} \\ &\quad - \mathbf{v}^f(\underbrace{\mathbf{X}^s + \mathbf{u}^s(\mathbf{X}^s, t)}_{\mathbf{x}^f}, t) =: \gamma^\mu(\mathbf{u}^s, \mathbf{v}^f), \end{aligned} \quad (2.108)$$

where (2.9) and (2.59) were used to define the vector-valued constraint function  $\gamma^\mu(\mathbf{u}^s, \mathbf{v}^f)$  in terms of the solid displacement  $\mathbf{u}^s(\mathbf{X}^s, t)$  and the fluid velocity  $\mathbf{v}^f(\mathbf{x}^f, t)$ . This perfect bilateral constraint can be equivalently represented in the local strong form or in the weak variational form, that is,

$$\mathbf{0} = \gamma^\mu(\mathbf{u}^s, \mathbf{v}^f) \Leftrightarrow 0 = \delta \Pi^\mu := \int_{\partial\mathcal{J}_t} \delta \boldsymbol{\mu} \cdot \boldsymbol{\gamma}_\mu(\mathbf{u}^s, \mathbf{v}^f) da \quad \forall \delta \boldsymbol{\mu}, \quad (2.109)$$

where  $\delta \boldsymbol{\mu}$  is an arbitrary vector-valued test function that denotes the *virtual traction vector*.

The constraint forces  $\mathbf{t}^s da$  and  $\mathbf{t}^f da$ , acting on the interface  $\partial\mathcal{J}_t$ , are internal forces with respect to the total system  $\mathfrak{I}$  and must therefore satisfy the variational law of interaction. In accordance with Eugster and Glocker (2017), we define the *variational law of interaction* as follows: Let  $d\mathbf{f}^{\text{int},\mathfrak{R}}$  denote the internal forces with respect to a subsystem  $\mathfrak{R} \subseteq \mathfrak{I}$ . Further, let



As this must hold for any subsystem  $\mathcal{K} \subseteq \partial\mathcal{J}_t$ , the expression in the bracket must vanish and we find

$$\boldsymbol{\varphi} = \mathbf{t}^f = -\mathbf{t}^s, \quad (2.114)$$

with the constraint force  $\boldsymbol{\varphi} = (\partial_{\mathbf{v}^f} \boldsymbol{\gamma}^\mu) \boldsymbol{\mu}$  defined by force directions  $\partial_{\mathbf{v}^f} \boldsymbol{\gamma}^\mu$  and the vector-valued Lagrange multiplier  $\boldsymbol{\mu}$ .

### 2.3.3 Linearization

Again, we apply the Gâteaux derivate (A.1) to (2.109) at the bias solution  $\bar{\mathbf{u}}^s$  and  $\bar{\mathbf{v}}^f$  in the direction of the perturbations  $\tilde{\mathbf{u}}^s$  and  $\tilde{\mathbf{v}}^f$  to find the linearized constraint

$$\begin{aligned} 0 &= \delta \tilde{\Pi}^\mu := D\delta\Pi^\mu(\bar{\mathbf{u}}^s, \bar{\mathbf{v}}^f)[\tilde{\mathbf{u}}^s, \tilde{\mathbf{v}}^f] \\ &= \int_{\partial\mathcal{J}_t} D\{\delta\boldsymbol{\mu} \cdot \boldsymbol{\gamma}^\mu(\mathbf{u}^s, \mathbf{v}^f)\}[\tilde{\mathbf{u}}^s, \tilde{\mathbf{v}}^f] da \\ &= \int_{\partial\mathcal{J}_t} \delta\boldsymbol{\mu} \cdot \tilde{\boldsymbol{\gamma}}^\mu da, \end{aligned} \quad (2.115)$$

where

$$\begin{aligned} \tilde{\boldsymbol{\gamma}}^\mu &:= D\boldsymbol{\gamma}^\mu(\bar{\mathbf{u}}^s, \bar{\mathbf{v}}^f)[\tilde{\mathbf{u}}^s, \tilde{\mathbf{v}}^f] \\ &= \partial_t \tilde{\mathbf{u}}^s(\mathbf{X}^s, t) + [\partial_{\mathbf{X}} \tilde{\mathbf{u}}^s(\mathbf{X}^s, t)] \dot{\mathbf{X}}^s \\ &\quad - [\partial_{\mathbf{x}} \bar{\mathbf{v}}^f(\mathbf{X}^s + \bar{\mathbf{u}}^s(\mathbf{X}^s, t), t)] \tilde{\mathbf{u}}^s(\mathbf{X}^s, t) - \bar{\mathbf{v}}^f(\mathbf{X}^s + \bar{\mathbf{u}}^s(\mathbf{X}^s, t), t) \end{aligned} \quad (2.116)$$

defines the linearized constraint function. Note the term  $(\partial_{\mathbf{x}} \bar{\mathbf{v}}^f) \tilde{\mathbf{u}}^s$  characterizing the interaction of the velocity gradient of the fluid bias motion with the displacement of the solid perturbation motion, also found by Benjamin (1960); Landahl (1962); Carpenter and Morris (1990).



# Semi-analytical Model

# 3

The semi-analytical sandwich model presented in this chapter is probably the simplest system of two elastic structures coupled by a viscous liquid. Despite the simplicity, the proposed model features several general phenomena of the liquid coupling (e.g., effects of viscosity or bias motion) and is therefore well suited to study the fundamental vibration mechanisms.

## 3.1 Sandwich Model

### 3.1.1 Model and Assumptions

Fig. 3.1 shows the semi-analytical sandwich model, which is composed of a bottom solid layer of thickness  $h^-$ , a top solid layer of thickness  $h^+$  and a viscous liquid layer filling the gap width  $g$ . We only consider motion in the  $(e_x^I, e_z^I)$ -plane and assume periodicity in the  $e_x^I$ -direction. Whereas the bottom solid layer has no bias motion, we allow a bias velocity  $\hat{v}_x^{s+}$  of the top solid layer. In the liquid layer, a plane Couette flow evolves with the linear velocity profile

$$\bar{v}_x^f(z) = \frac{\bar{v}_x^{s+}}{2} \left( 1 + 2\frac{z}{g} \right), \quad (3.1)$$

which holds for a laminar bias flow (White, 2005, pp. 98).

The bias motion of the solid and liquid shall be disturbed by small, wave-shaped perturbations

$$\tilde{q}(x, z, t) =: \Re\{\hat{q}(z) e^{j(\omega t - kx)}\} = \Re\{\hat{q}(z) e^{j(\omega_r t - kx)} e^{-\delta^t t}\}, \quad (3.2)$$

where  $\tilde{q}(x, z, t)$  denotes an arbitrary perturbation quantity,  $\hat{q}(z)$  its complex amplitude,  $k \in \mathbb{R}$  the longitudinal *wave number* and  $\omega = (\omega^r + j\delta^t) \in \mathbb{C}$

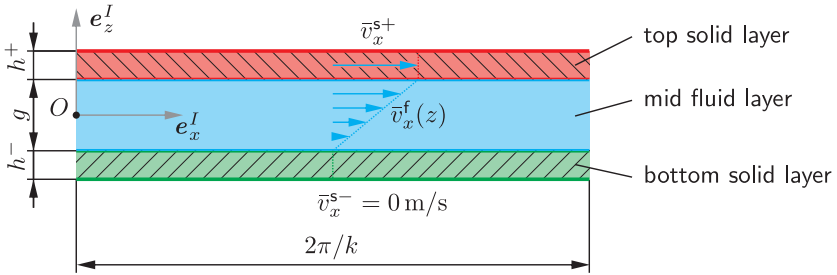


Fig. 3.1: Plane semi-analytical sandwich model.

the *complex angular eigenfrequency*. The real part  $\omega^r := \Re\{\omega\}$  refers to the (real) *angular eigenfrequency* and the imaginary part  $\delta^r := \Im\{\omega\}$  to the *damping factor*.

Note that by choosing a real wave number  $k$  and solving for a complex eigenfrequency  $\omega$ , we are considering the *temporal problem* of spatial-periodic perturbations that oscillate and fade out in time. We could also choose a real frequency  $\omega$  and solve for a complex wave number  $k$ , which would state the spatial problem of time-periodic perturbations that decay in space.

## 3.1.2 Governing Equations

### Solid Layers

The perturbation equations of the solid layers are derived from the boundary value problem (2.56) by linearization about the strain-free bias motion. Thereby, we neglect body forces and apply (2.28) for an isotropic, linear elastic material. The acceleration terms, which include the bias motion  $\bar{v}_x^s$ , are derived in §A.2.5 and given by (A.40). In Cartesian coordinates, the perturbation equations for the displacements  $(\tilde{u}_x^s, \tilde{u}_z^s)$  then read

$$\begin{aligned} \varrho^s (\partial_t^2 + 2\bar{v}_x^s \partial_t \partial_x + \bar{v}_x^{s2} \partial_x^2) \tilde{u}_x^s &= \mu^s (\partial_x^2 + \partial_z^2) \tilde{u}_x^s + (\lambda^s + \mu^s) (\partial_x^2 \tilde{u}_x^s + \partial_z \partial_x \tilde{u}_z^s), \\ \varrho^s (\partial_t^2 + 2\bar{v}_x^s \partial_t \partial_x + \bar{v}_x^{s2} \partial_x^2) \tilde{u}_z^s &= \mu^s (\partial_x^2 + \partial_z^2) \tilde{u}_z^s + (\lambda^s + \mu^s) (\partial_x \partial_z \tilde{u}_x^s + \partial_z^2 \tilde{u}_z^s). \end{aligned} \quad (3.3)$$

We apply the wave ansatz (3.2) and rewrite the equations as

$$\begin{aligned} (-\omega^2 + 2\bar{v}_x^s k\omega - \bar{v}_x^{s2} k^2)\hat{u}_x^s &= c_2^2(\mathcal{D}_z^2 - k^2)\hat{u}_x^s + (c_1^2 - c_2^2)(-k^2\hat{u}_x^s - \text{j}k\mathcal{D}_z\hat{u}_z^s), \\ (-\omega^2 + 2\bar{v}_x^s k\omega - \bar{v}_x^{s2} k^2)\hat{u}_z^s &= c_2^2(\mathcal{D}_z^2 - k^2)\hat{u}_z^s + (c_1^2 - c_2^2)(-\text{j}k\mathcal{D}_z\hat{u}_x^s + \mathcal{D}_z^2\hat{u}_z^s), \end{aligned} \quad (3.4)$$

where  $\mathcal{D}_z := d/dz$  and

$$c_1 = \sqrt{\frac{\lambda^s + 2\mu^s}{\varrho^s}} = \sqrt{\frac{E(1-\nu)}{(1+\nu)(1-2\nu)\varrho^s}}, \quad c_2 = \sqrt{\frac{\mu^s}{\varrho^s}} = \sqrt{\frac{E}{2(1+\nu)\varrho^s}}, \quad (3.5)$$

denote the dilatational and distortional wave speeds, respectively.

### Fluid Layer

The perturbation equation of the liquid layer is derived from the incompressible Navier–Stokes equations (2.101) by linearization about the plane, parallel bias flow  $\bar{v}_x^f(z)$ . After eliminating the perturbation pressure  $\bar{p}$  and the longitudinal perturbation velocity  $\bar{v}_x^f$ , we may write the perturbation equation as

$$0 = \varrho^f(\partial_t + \bar{v}_x^f\partial_x)(\partial_x^2 + \partial_z^2)\bar{v}_z^f - \varrho^f\frac{d^2\bar{v}_x^f}{dz^2}\partial_x\bar{v}_z^f - \mu^f(\partial_x^2 + \partial_z^2)^2\bar{v}_z^f, \quad (3.6)$$

expressed in the transversal perturbation velocity  $\bar{v}_z^f$ . If we apply the wave ansatz (3.2), we find the celebrated Orr–Sommerfeld equation

$$0 = \left[ \varrho^f(\text{j}\omega - \bar{v}_x^f\text{j}k)(\mathcal{D}_z^2 - k^2) + \varrho^f\frac{d^2\bar{v}_x^f}{dz^2}\text{j}k - \mu^f(\mathcal{D}_z^2 - k^2)^2 \right] \hat{v}_z^f, \quad (3.7)$$

where again  $\mathcal{D}_z := d/dz$ . For a discussion of the equation and the details about its derivation, we refer to the textbooks by Drazin and Reid (2004, p. 156), Criminale et al. (2003, p. 13), as well as Schmid and Henningson (2001, p. 57).

### 3.1.3 Implementation

The perturbation equations (3.4) and (3.7), together with conditions for the interfaces and boundaries, can be assembled to a general eigenvalue

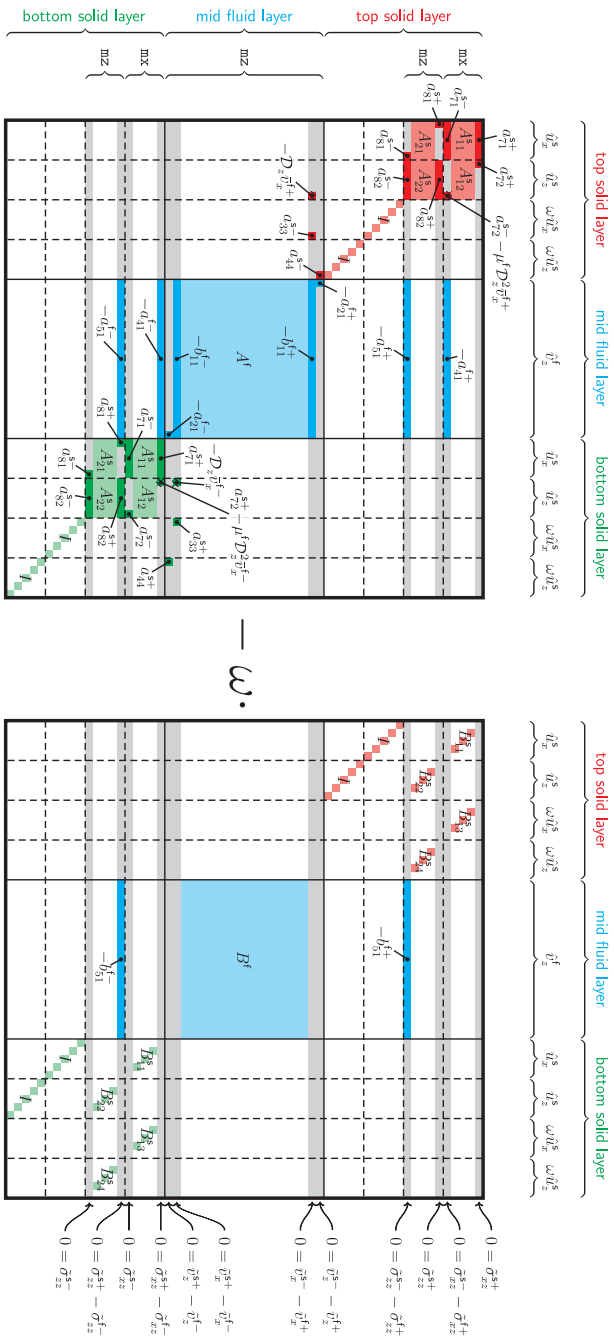


**Fig. 3.2:** Graphical representation of  $\mathbf{A} - \omega \mathbf{B}$  with coefficients defined in §A.3. The gray stripes indicate the matrix rows defining the interface and boundary conditions.



problem. After discretization it takes the form

$$[\mathbf{A} - \omega \mathbf{B}] \hat{\mathbf{q}}, \quad (3.8)$$

where  $\mathbf{A}$  and  $\mathbf{B}$  are coefficient matrices,  $\omega = (\omega^r + j\delta^r) \in \mathbb{C}$  is the eigenvalue and  $\hat{\mathbf{q}}$  the corresponding complex eigenvector containing the discretized forms of  $\hat{u}_x^s$ ,  $\hat{u}_z^s$  and  $\hat{v}_z^f$ . Fig. 3.2 shows the structure of  $\mathbf{A} - \omega \mathbf{B}$  and § A.3 defines its coefficients. We apply the Chebyshev collocation method to discretize the equations at the Gauss–Lobatto points (Malik, 1990; Weder, 2012). Peyret (2002, pp. 50) defines the corresponding discretized representation of the differential operator  $\mathcal{D}_z$ . It is a full matrix reflecting the spectral properties of the collocation method. MATLAB (Mathworks, 2016) together with the Multiprecision Computing Toolbox (Advanpix, 2016) is used to solve the resulting numerical eigenvalue problem in quadruple precision.

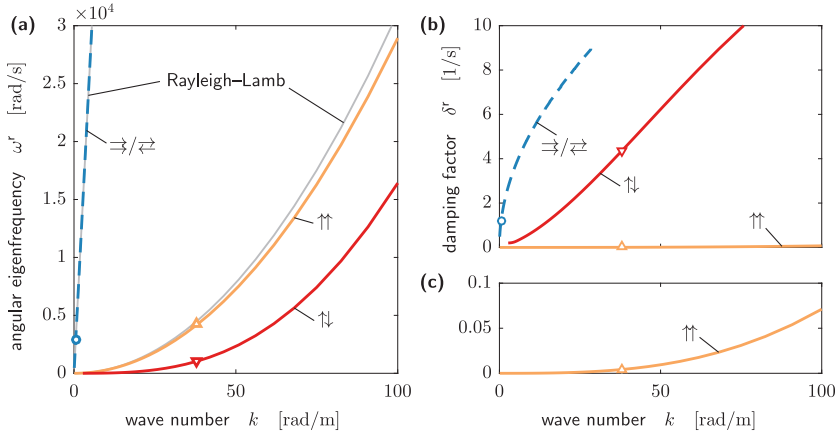


**Fig. 3.3:** Spectrum of (a) angular eigenfrequency  $\omega^r$  and (b,c) damping factor  $\delta^r$  as a function of wave number  $k$  of modes in the low-frequency range. Longitudinal modes ' $\rightarrow$ ' and ' $\leftarrow$ ' (blue dashed line), varicose mode ' $\updownarrow$ ' (red solid line), sinuous mode ' $\uparrow\uparrow$ ' (orange solid line) and Rayleigh–Lamb waves (gray solid lines). Markers indicate the selected parameters for the plotting the mode shapes and velocity profiles in Figs 3.4 and 3.5.

## 3.2 Results

In the present section we show the results of the sandwich model, where we have used  $E = 210 \text{ GPa}$ ,  $\nu = 0.3$ ,  $\rho^s = 7850 \text{ kg/m}^3$ ,  $h^- = h^+ = 2 \text{ mm}$  as parameters for the solid layers (steel) and  $\mu^f = 1.002 \text{ mPa} \cdot \text{s}$ ,  $\rho^f = 998.2 \text{ kg/m}^3$ ,  $g = 5 \text{ mm}$  for the liquid layer (water).

### 3.2.1 Modal Parameters without Bias Motion

We start with the results for the sandwich model without bias motion, this is  $\bar{v}^{s-} = \bar{v}^{s+} = \bar{v}^f(z) = 0 \text{ m/s}$ . Fig. 3.3 shows the spectrum of the angular eigenfrequency  $\omega^r$  and the damping factor  $\delta^r$  as a function of the wave number  $k$ . For comparison, we also plot the Rayleigh–Lamb frequency spectrum of a single solid plate with the same properties (Mindlin, 1960; Graff, 1975, pp. 453). In this low-frequency range, we recognize three modes, which we discuss in more detail by considering the mode shapes  $(\hat{u}_x^s, \hat{u}_z^s)$  in Fig. 3.4 and the profiles of the liquid perturbation velocity  $(\hat{v}_x^f, \hat{v}_z^f)$  in Fig. 3.5.

#### Longitudinal Mode

The longitudinal modes of the sandwich structure are labeled with ' $\rightarrow$ ' or ' $\leftarrow$ ', depending on the relative motion between the top and bottom solid plate. They show a linear  $\omega^r(k)$  relation which nearly coincides with the longitudinal Rayleigh–Lamb spectrum. The motion of the elastic plates is primarily in the  $e_x^l$ -direction. Due to the longitudinal motion of the solid/liquid interface, a Stokes boundary layer is formed in the liquid (White, 2005, pp. 131). Outside of the small viscous boundary layer with frequency dependent thickness  $\delta^f \approx 6.5 \sqrt{\mu^f / (\omega^r \rho^f)}$ , the liquid is at rest. Accordingly, only a small fraction of the liquid mass participates on the longitudinal vibration, and thus, the angular eigenfrequency  $\omega^r$  only insignificantly changes compared to the longitudinal mode of the single plate (less than 0.1% in the plotted range). On the other hand, we found that the boundary layer formed is responsible for the viscous damping. The damping factor  $\delta^r$  increases almost proportionally to  $\sqrt{\omega^r}$ . In the frequency range plotted, we further find a Stokes layer much smaller than the gap width, that is  $\delta^f \ll g$ . The longitudinal modes ' $\rightarrow$ ' and ' $\leftarrow$ ' then become degenerate by sharing the same frequency.

### Sinuous Mode

The sinuous mode, labeled with ‘ $\uparrow\uparrow$ ’, shows a nearly quadratic  $\omega^r(k)$  relation. The mode shape is characterized by a symmetrical deformation of the solid plates with respect to the center axis and by a liquid motion predominantly in the  $e_z^I$ -direction. The angular eigenfrequency of the sandwich structure is reduced by approximately 7.6% compared to the antisymmetric Rayleigh–Lamb mode. We find a similar frequency reduction, when we think of adding the liquid mass to the single solid layers, without changing their stiffness properties. The damping factor of the sinuous mode is low, because there is only a weak boundary layer formed.

### Varicose Mode

The varicose mode, labeled with ‘ $\uparrow\downarrow$ ’, also shows a nearly quadratic  $\omega^r(k)$  relation. The mode shape is characterized by an antisymmetrical deformation of the solid plates with respect to the center axis. This causes a squeezed liquid motion along the  $e_x^I$ -direction, flowing from the narrowing to the widening of the gap. In the low-wavenumber regime, the distance between the narrowing and widening is large ( $\sim \pi/k$ ) and, therefore, the acceleration of the liquid is correspondingly large. This results in a strong reduction of the eigenfrequency  $\omega^r$ , because the liquid is pumped as a bulk along the extensive  $e_x^I$ -direction. A Stokes boundary layer is formed by the bulk motion of the liquid. This is another mechanism than in the longitudinal mode, where the boundary layer is directly formed by the motion of the solid boundary. This viscous boundary is responsible for the large damping factor  $\delta^r$  compared to the sinuous mode.

## 3.2.2 Modal Parameters with Bias Motion

Finally, we discuss the influence of the bias motion on the modal parameters. Fig. 3.6 shows the angular eigenfrequency  ${}_I\omega^r$  and the damping factor  $\delta^r$  of varicose and sinuous modes in function of the bias velocity of the top solid plate  $\bar{v}_x^{s+}$ . We distinguish between right propagating modes with positive wave number  $k^+ > 0$  and left propagating modes with negative wave number  $k^- < 0$ . With increasing bias velocity, we observe that the angular frequency of the right propagating modes increase, whereas the frequency of the left propagating modes decrease. The difference in frequency between left and right propagating modes is nearly proportional to the bias velocity.

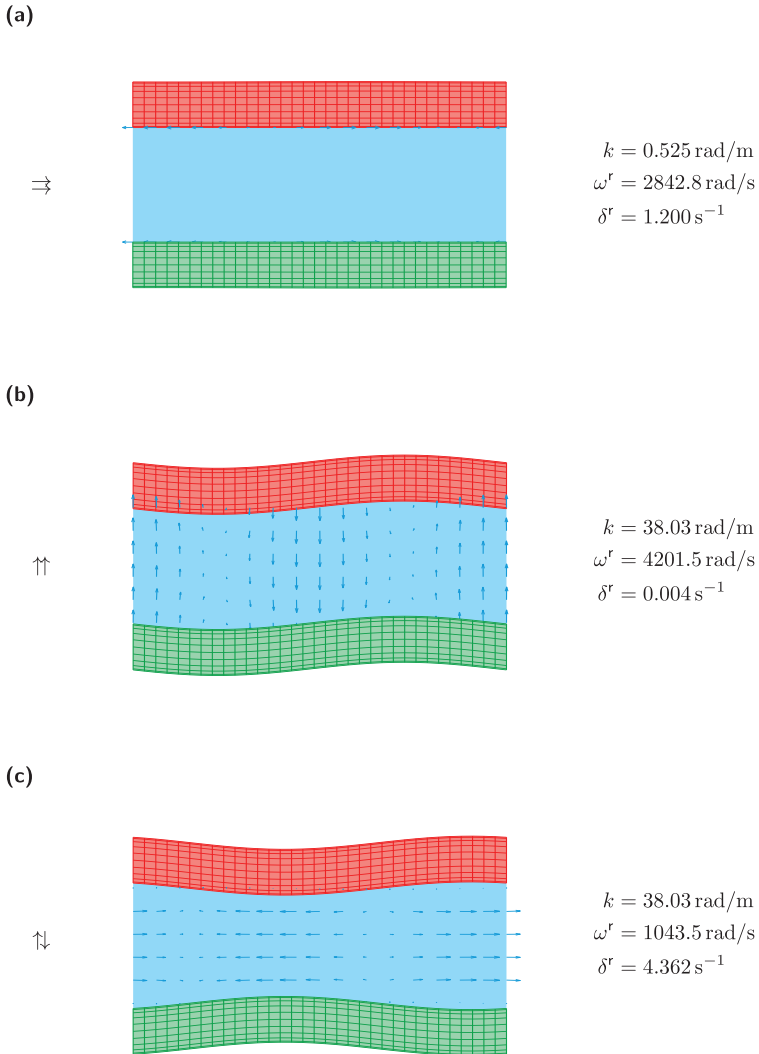


**Fig. 3.4:** Real part of mode shapes of (a) longitudinal mode '⇒', (b) sinusoidal mode '↑↑' and (c) varicose mode '↑↓'. The solid layers are deformed according to the perturbation displacement field  $(\hat{u}_x^s, \hat{u}_z^s)$ . The blue arrows indicate the perturbation velocity field  $(\hat{v}_x^f, \hat{v}_z^f)$  in the fluid.

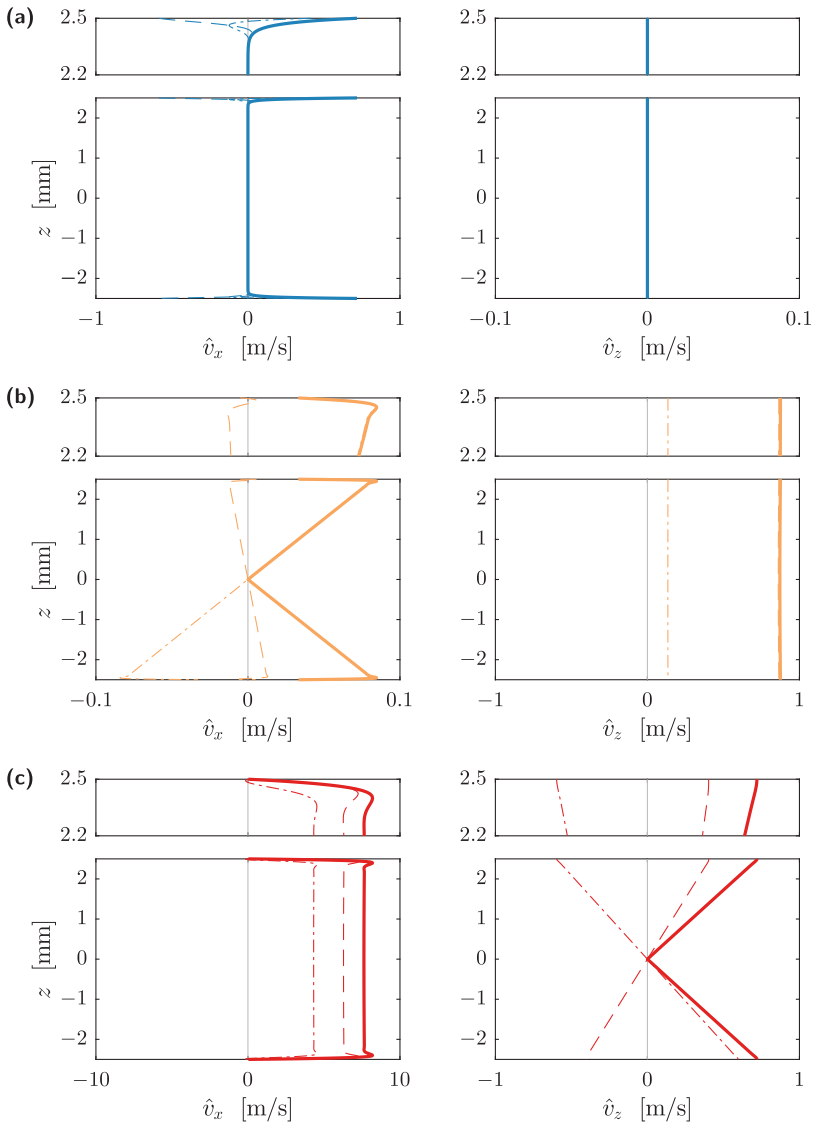


**Fig. 3.5:** Profiles of liquid perturbation velocity components  $\hat{v}_x^f$  and  $\hat{v}_z^f$  of (a) longitudinal mode ' $\Rightarrow$ ', (b) sinuous mode ' $\Uparrow$ ' and (c) varicose mode ' $\Downarrow$ ' for wave numbers  $k$  according to Fig. 3.4. Magnitude (solid lines), real part (dashed lines), imaginary part (dash-dotted lines).

This frequency split effect is due to the average bias velocity to the right direction.

The damping factors of the sinuous modes ' $\uparrow\uparrow^\pm$ ' are nearly independent of the direction of propagation, whereas the varicose modes ' $\uparrow\downarrow^\pm$ ' show different damping factors for right and left propagating modes. We believe that this is a numerical effect, because due to symmetry reasoning, the damping factor should not depend on the direction of propagation.

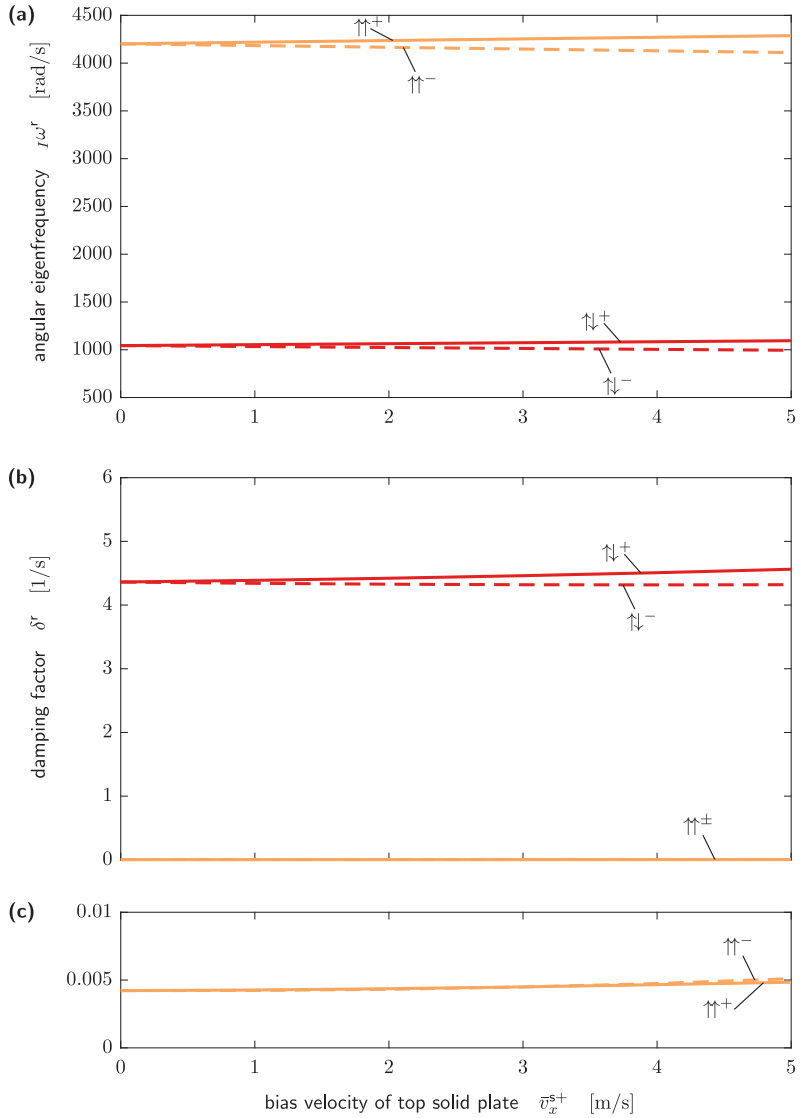


**Fig. 3.6:** Spectrum of (a) angular eigenfrequency  $I\omega^r$  and (b-c) damping factor  $\delta^r$  as a function of the bias velocity of the top solid plate  $\bar{v}_x^{s+}$  for wave numbers  $k^\pm = \pm 38.03$  rad/m for varicose modes ' $\uparrow\downarrow^\pm$ ' and sinuous modes ' $\uparrow\uparrow^\pm$ ', respectively.





# Experimental Test Bench

# 4

This chapter documents the test bench that was engineered to experimentally study the rotor–stator coupling by liquids. As described in §1.4, we investigate the coupling on a strong simplified model, where the rotor and the stator are represented by circular disks.

Following the concepts of design theory, we first formulate the functional requirements for the test bench. We then present the general design concept that meets these requirements and give some reasoning about the chosen measurement techniques. The specific realization of the test bench is discussed in more detail than by Weder et al. (2016). This includes the geometry, the excitation and measurement of the vibrations, as well as the monitoring and operation of the test bench. Thereby, we focus on the polar scan unit for measuring the vibrations on the rotor using self-tracking laser Doppler velocimetry.

## 4.1 Functional Requirements

In the present section, we formulate the functional requirements of the test bench that constitute its design guide lines. As overriding principle we require the design as simple and ideal as possible on one hand, and to be able to sufficiently characterize the vibration on the other. Our intention is to achieve comprehensive and conclusive measurements (Chapter 5) that can be well compared with results of the related simulation models (Chapter 6).

With this principle in mind, we impose the following requirements:

**Small amplitude vibrations** We are interested in small-amplitude vibrations, where a linearized model is expected to be sufficient. We therefore rely on a vibration measurement technique with a high amplitude resolution.

**Mode shapes** To sufficiently characterize the vibration, the test bench must be able to measure the mode shapes of the rotor *and* the stator as well as the correct phase relation between them.

**Boundary conditions** The boundary conditions for the rotor, the stator and the liquid should be designed as ideal as possible. Well defined boundary conditions make the comparison between the results of the experimental test bench and the simulations more conclusive.

**Influence of excitation and measurement** The rotor and the stator are compliant and lightweight structures. The stiffness and mass properties should not be significantly changed by the vibration excitation and the measurement.

**Axially symmetrical geometry** The relevant parts of the test bench shall be designed with axial symmetry. With this, we can use a rotationally symmetric geometry for the simulation model of Chapter 6 which significantly reduces the model complexity and the computation time.

**Automatic measurements** The measurements should be automatized to reduce the influence of the test operator so that we can expect a higher reproducibility and more reliable results.

**Stiff test bench** The test bench stiffness has to be chosen so that its eigenfrequencies are beyond the eigenfrequencies of the rotor–stator system.

**Variation of parameters** The parameters *stator disk thickness*  $h_S$ , *rotor disk thickness*  $h_R$ , *gap width*  $g$  and *rotor angular speed*  $\Omega_R$  must be adjustable. The major parameters and their ranges of variation are listed in Tab. 4.1.

## 4.2 Design Concept and Realization

### 4.2.1 Design Concept

In general, we use *modal analysis* to experimentally characterize the dynamics of the system (Ewins, 2000): The structure under investigation is excited by an external forcing at one point (input) and its dynamical response is

**Tab. 4.1:** Major parameters of the experimental test bench and their ranges of variation.

parameter	variable	range	unit
stator clamping diameter	$D_S$	250	mm
stator disk thickness	$h_S$	{1, 1.5}	mm
gap width	$g$	[1, 15]	mm
rotor disk thickness	$h_R$	{1, 1.5, 2}	mm
rotor clamping diameter	$d_R$	30	mm
rotor outer diameter	$D_R$	200	mm
rotor angular speed	$\Omega_R$	[0, 50]	rad/s
excitation angular frequency	$\varpi$	[0, 5000]	rad/s

then measured at other points (outputs). The resulting frequency response functions (outputs/input) contain the eigenfrequency, damping and mode shapes which characterize the dynamics of the system.

Before we explain the test bench in detail, we briefly sketch the overall design concept. A schematic representation of the design concept is given in Fig. 4.1. The *casing* is a stiff structure acting as a *fluid cavity* and rigid support for the *stator disk* and the rotor assembly. The *rotor disk* is mounted on a stiff *shaft* which itself is supported by a stiff *bearing* and driven by the *main motor*.

We excite the rotor–stator system by an *electromagnetic excitation* of the stator disk (see § 4.3.3). The out-of-plane velocity of the resulting vibrations at the rotor and stator disks is measured using the scanning laser Doppler velocimetry technique. The scanning mechanism allows the placement of the measuring spots at discrete locations so that the vibration shape can be reconstructed by successive measurements. For the non-rotating stator disk we use a standard Cartesian scanning system to measure the vibration (see § 4.3.4). For the rotor disk, we built our own *polar scan unit* that is based on the self-tracking laser Doppler velocimetry, where the laser beam is co-rotating by design. A *glass window* gives optical access to the backside of the rotor disk. The polar scan unit uses a *scanning mirror* to set the radial coordinate and an adjustment mechanism to set the azimuthal coordinate (see § 4.3.5).

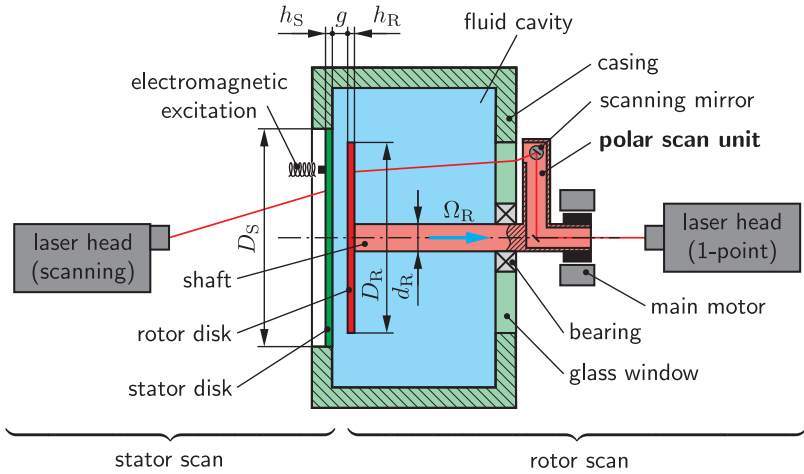


Fig. 4.1: Schematic of the test bench.

The electromagnetic excitation and the laser Doppler velocimetry are both non-contact techniques that only barely influence the mechanical properties of the rotor and the stator. This is an advantage over other transducers like accelerometers or strain gauges that modify the mass and/or stiffness of the structure. Furthermore, the laser Doppler velocimetry provides a high resolution which is necessary for the modal analysis. Finally, no telemetric system or slip rings are needed to transmit measured signals from the rotor to the inertial system.

## 4.2.2 Test Bench Design

This section discusses the specific realization of the test bench design. Fig. 4.2 shows the cutaway drawing of the experimental test bench with the major parts labeled. Tab. 4.2 lists the major components and their manufacturer.

### Casing

The stiff *casing* is composed of a massive cylindrical ring (thickness 30 mm, inner diameter 300 mm) and two thick cover plates (thickness 35 mm). It

forms a *fluid cavity* with a volume of approximately 6.5 l. All metallic components that are in contact with the fluid are made of stainless steel to control corrosion. O-rings are mostly used to create the seal at the non-sliding interfaces. The *glass window* (thickness 29 mm) is made of N-BK7. Its surface is ground, lapped and polished to a flatness of 1  $\mu\text{m}$  to reduce measuring errors. To prevent glass breaking, we glued the glass window at the inner and outer radius to metallic clamping rings using Scotch-Weld 2216 B/A. Six *portholes* distributed around the cylinder provide lateral optical access into the fluid cavity.

### Stator Disk

The *stator disks* are laser cut from ground sheets of hardened steel (1.4034) with thicknesses of 1 mm and 1.5 mm. A single disk is clamped between the massive *stator ring* and the *fastening ring* at the clamping diameter of 250 mm. We seal the contact interface between stator disk and stator ring with the Loctite 574 sealant. The interface between stator ring and casing is sealed using an O-ring. The fastening ring is designed to minimize the bias stress in the disk. Nevertheless, the 36 screws must be tightened carefully with an appropriate tightening sequence and a specified torque to prevent a detuning of the stator disk by in-plane stresses. We use *spacers* of different thicknesses when mounting the stator assembly on the casing. This allows to accurately adjust the gap width  $g$  between rotor and stator disk in the range of 1 to 15 mm in increments of 0.1 mm.

### Rotor Disk

The *rotor disks* are laser cut of the same sheets as the stator disks with thicknesses of 1 mm, 1.5 mm and 2 mm. We bonded the rotor disks to the *rotor hubs* using Loctite Double Bubble epoxy adhesive. This bonding sets the clamping diameter of the rotor disk to 30 mm. We did not use thermal bonding techniques because this leads to residual stresses and a detuning of the rotor. The rotor is mounted on the front side of a stiff *shaft* made of hardened, stainless steel which is supported by four prestressed high-precision *spindle bearings*. These bearings are stiff and provide a very high true-running accuracy of the rotor. We use a *radial shaft seal* to seal off the bearings from the fluid in the cavity.

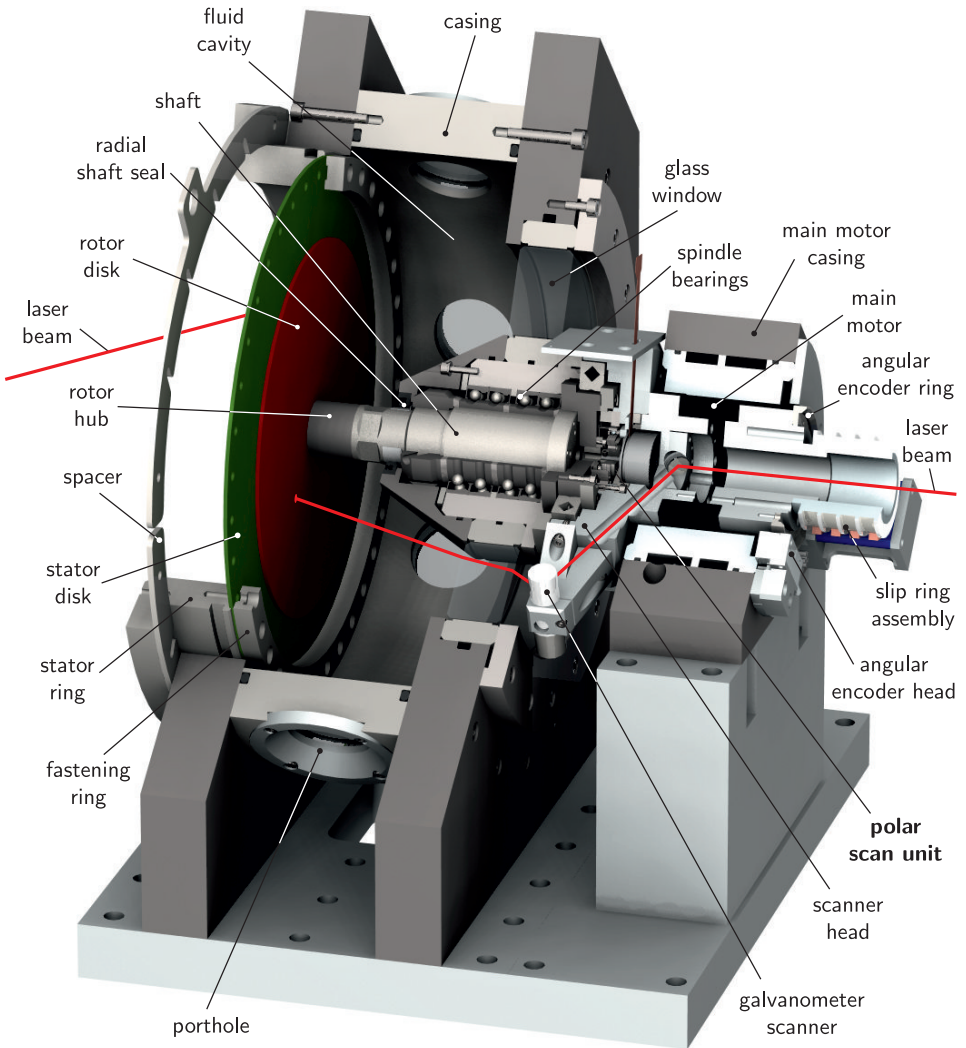


**Fig. 4.2:** Cutaway drawing of the experimental test bench with annotations of the major parts. Selected optical ray paths of the rotor and stator laser Doppler velocimetry systems are plotted as red lines. The detail view of the polar scan unit is shown in Fig. 4.7.

**Tab. 4.2:** List of main components of experimental test bench.

component	manufacturer	model
spindle bearings	SKF	S71908 CDGA/P4A
main motor	Harmonic Drive	TorkDrive-100A-30-AA-C
main motor controller	LTi Drives	ServoOne Junior S022.003
angular encoder ring	Renishaw	RESM-20U-S-B-075
angular encoder head	Renishaw	SR-005-A
angular encoder interface	Renishaw	Si-NN-0001-00-0-0N
slip ring assembly	LTN	SM050-00/04-AG1
cross roller bearing	THK	RE 7013 UU CC0 P2
strain wave gearing	Harmonic Drive	CSD-14-100-2A-R
servo motor	Maxon Motor	EC 32 flat 267121
servo motor controller	Maxon Motor	EPOS2 24/2 380264
galvanometer scanner	SCANLAB	dynAXIS XS
galvanometer amplifier	SCANLAB	microSSV
deflection mirror	TECHSPEC	45754, 400–700 nm
voltage amplifier	Mc Crypt	PA 3000
current sensor	Allegro MicroSystems	ACS712
analog filters	Krohn-Hite	3988
laser head (1-point)	Polytec	OFV-505 SR
laser controller (1-point)	Polytec	OFV-5000 with VD-06
laser head (scanning)	Polytec	PSV-I-400 LR
laser controller (scanning)	Polytec	OFV-5000 with VD-08
data acquisition card	National Instruments	PCI-6110
connector box	National Instruments	BNC-2110
motor interface card	National Instruments	USB-6001

### Polar Scan Unit

The *polar scan unit* is mounted on the back side of the shaft and enables to measure arbitrary points of the rotor disk. In §4.3.5 we describe this unit with a *galvanometer scanner* and an azimuthal adjustment mechanism between shaft and *scanner head* in more detail. The rotor assembly consisting of rotor, shaft and polar scan unit is driven by the *main motor*. This motor allows to control the precise angular position and speed of the rotor with the use of an *angular encoding system*, also mounted on the scanning head. The *slip ring assembly* at the end of the rotor assembly transmits power and positioning signals from the inertial to the rotor system.

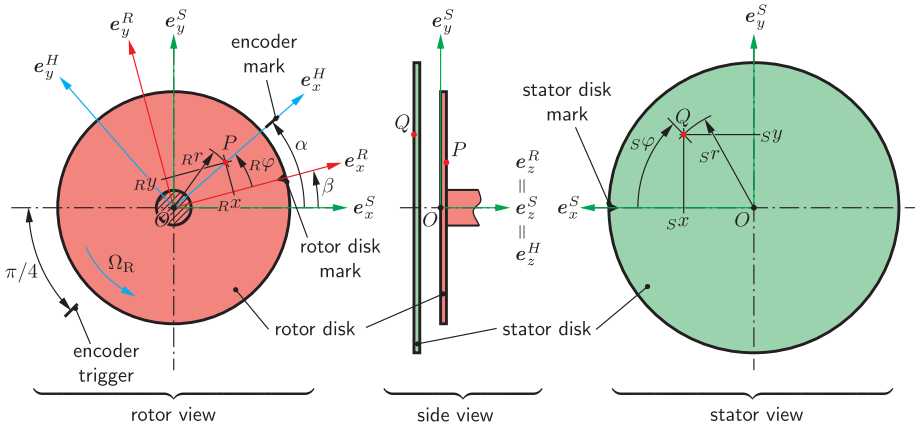


**Fig. 4.3:** Kinematics of the rotor–stator system.  $P$  denotes a measuring point on the rotor disk and  $Q$  a point on the stator disk.

### 4.2.3 Kinematics

In this section we define the kinematics of the rotor–stator system which is important for the correct acquisition and interpretation of the vibration measurements. Fig. 4.3 illustrates the kinematics in rotor, stator and side view, where  $P$  denotes an arbitrary measuring point on the rotor disk and  $Q$  an arbitrary point on the stator disk. The origin  $O$  is placed at the bottom center of the rotor disk. The inertial *stator system* ( $e_x^S, e_y^S, e_z^S$ ), called the  $S$ -system, is a right-handed system formed by unit vectors. Vector  $e_z^S$  is coaxial to the rotation axis of the rotor assembly and  $e_y^S$  is pointing upward in the vertical direction. The body-fixed *rotor system* ( $e_x^R, e_y^R, e_z^R$ ), called the  $R$ -system, is formed by a rotation of the  $S$ -system about the common  $e_z$  axis by the angle  $\beta$ . The *head system* ( $e_x^H, e_y^H, e_z^H$ ), abbreviated as  $H$ -system, is the body-fixed system of the scanner head with the galvanometer scanner lying in the  $(e_x^H, e_z^H)$ -plane. It is formed by a rotation of the  $R$ -system about the common  $e_z$  axis by the angle  ${}_R\varphi$ . The rotation angle between the  $H$ - and the  $S$ -system is then given by  $\alpha := \beta + {}_R\varphi$ . Here,  $\Omega_R := \dot{\beta}$  indicates the angular speed of rotation of the rotor disk.

The galvanometer scanner and the measuring point  $P$  lie both in the  $(e_x^H, e_z^H)$ -plane. We denote the plane polar coordinates of  $P$  in the  $R$ -



system by  $(Rr, R\varphi)$  and the plane Cartesian coordinates by  $(Rx, Ry)$ . The same holds for the point  $Q$  in the  $S$ -system, where we write  $(Sr, S\varphi)$  for the polar coordinates and  $(Sx, Sy)$  for the Cartesian coordinates.

The *encoder mark* is a marker on the encoder ring placed at the  $e_x^H$  axis. The encoder system fires a hardware trigger signal when the encoder mark passes the *encoder trigger*. This happens if  $\alpha = 5\pi/4 + 2\pi n$  with  $n \in \mathbb{Z}$ . We use this trigger to start the vibration measurements at a defined angular position of the rotor disk.

## 4.3 Vibration Excitation and Measurement

### 4.3.1 Measuring Layout and Overview

In the present section we give an overview of the vibration excitation and the measurement. We show the wiring diagram of the experimental test bench in Fig. 4.4 with the main devices listed in Tab. 4.2. The heart of the measuring layout is the *computer* that controls the *main motor* (§ 4.3.2), the *excitation* (§ 4.3.3), the *stator scan* (§ 4.3.4) and the *rotor scan* (§ 4.3.5). All signals are acquired with the *data acquisition card* using the *connector box* (§ 4.3.6). We use LabVIEW by National Instruments (2014) to monitor and control the entire process (§ 4.3.7) and store the measurement data into an HDF5 archive file (§ 4.3.8).

### 4.3.2 Main Motor

The *main motor* consists of a permanent magnet rotor with 11 pole pairs and a stator with the 3 phase windings U, V, and W. PTC and KTY are temperature sensors and function as a thermal controlling of the motor. By the hollow motor design, we can guide the laser beam of the rotor scan system through the motor. The *angular encoding system* provides a high resolution feedback for the *main motor controller* to control the angular position or angular speed of the rotor assembly, depending on the mode of operation. We programmed the main motor controller so that the reference signal (angular position or angular speed) is set by the analog channel A00 of the *motor interface card*, which itself is connected to the computer's USB port. The signals of the angular encoder system are internally forwarded to the data

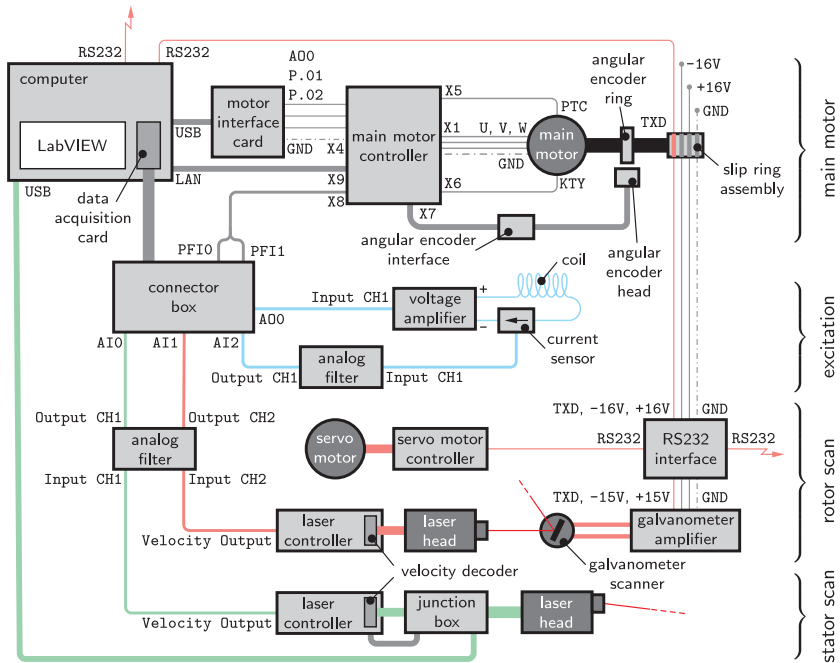
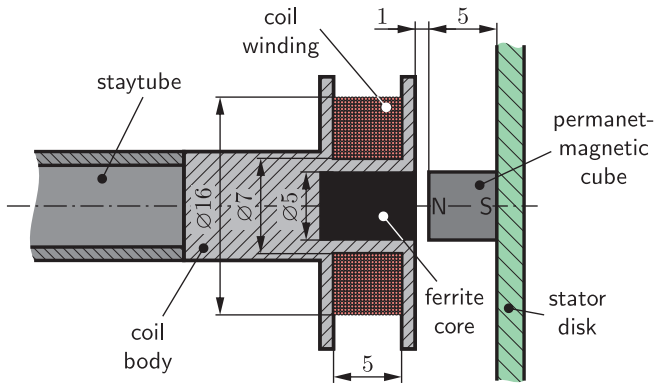


Fig. 4.4: Wiring diagram of the experimental test bench.

acquisition channels PFI0 and PFI1. PFI0 is used to trigger the vibration measurement and PFI1 to measure the actual rotor angular speed.

### 4.3.3 Electromagnetic Excitation

As pointed out before, we use the electromagnetic effect to excite the vibration of the rotor–stator system. The excitation setup in Fig. 4.5 consists of an electromagnetic coil and a permanent magnet. We wound an insulated wire of diameter 0.245 mm on the coil body made of polyether ether ketone to serve as an electromagnetic coil. To reduce the magnetic resistance we placed a soft-magnetic ferrite core in the center of the coil, where the magnetic field is the strongest. The coil has approximately 500 windings, a resistance of  $7.9\ \Omega$  and an inductance of 2.33 mH measured at 1 kHz. We use a permanent-magnetic cube placed on the stator disk to significantly



**Fig. 4.5:** Section view of electromagnetic excitation with electromagnetic coil and permanent magnet.

increase the excitation force that is generated by the magnetic field of the coil and to suppress higher-order excitations that arise with ferromagnets. The cube has an edge length of 5 mm and a mass of 1.05 g, so that the added mass is negligible compared to the modal mass of the vibration.

The electronic controlling of the coil can be seen in the wiring diagram of Fig. 4.4. A *voltage amplifier* feeds the electromagnetic coil, which itself gets its analog input from the analog output channel A00 of the data acquisition card. The excitation force is proportional to the magnetic field and therefore proportional to the current in the coil. To obtain an appropriate input signal for the rotor–stator system, we measure the electric current using a Hall-effect *current sensor*. The current signal from the sensor is low-pass filtered by an *analog filter* to suppress aliasing effects. The signal is then finally acquired by the analog input channel AI2 of the data acquisition card.

#### 4.3.4 Laser Doppler Velocimetry on Stator

For the vibration measurements on the stator disk we used the Polytec PSV-400, a commercially available laser Doppler scanning system. In this section we only explain the working principle of the laser interferometer and sketch the layout of the system. For more detailed information about the PSV-400 system we refer to the manuals (Polytec, 2011a,b).

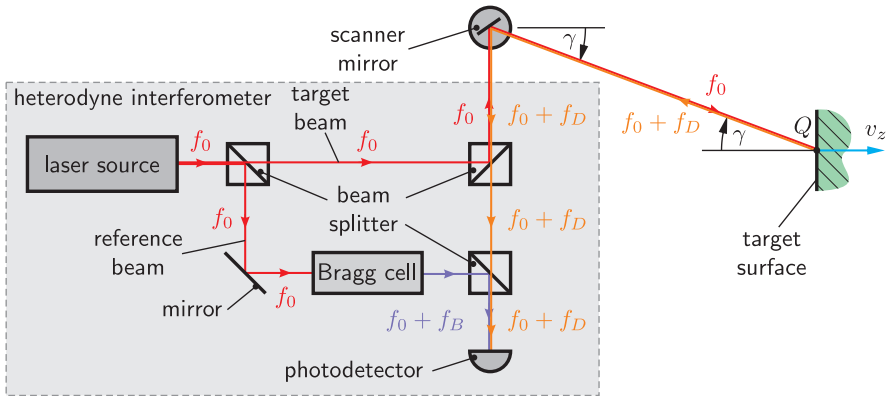


**Fig. 4.6:** Schematic of a heterodyne laser interferometer with scanner mirror and moving target surface.

First, we briefly explain the working principle of the heterodyne laser interferometer with the schematic depicted in Fig. 4.6. Polytec uses a helium-neon laser source to generate the coherent laser beam with a wavelength of  $\lambda = 633 \text{ nm}$  and a frequency  $f_0 = c_0/\lambda \doteq 4.72 \times 10^{14} \text{ Hz}$ , where  $c_0 \doteq 2.99 \times 10^8 \text{ m/s}$  is the speed of light. The first beam splitter divides the laser beam into a reference beam and a target beam. The target beam is routed with splitters and mirrors to the moving target surface, where it gets directly backscattered. According to the Doppler effect, the backscattered beam is frequency shifted by the Doppler frequency  $f_D$ , which is proportional to the velocity component in beam direction. The Doppler shifted beam travels back and interferes with the heterodyned reference beam. Polytec uses a Bragg cell to shift the reference beam's frequency by the heterodyne frequency  $f_B = 40 \text{ MHz}$ . This allows to measure the velocity in the range of  $-10 \text{ m/s}$  to  $+10 \text{ m/s}$  including its sign. The frequency  $f_0$  is filtered out at the photodetector, because of the low-pass characteristics of the sensor. The measured signal is then a modulation of the carrier signal with heterodyne frequency  $f_B$  and the Doppler signal with frequency  $f_D$ .

As can be seen in Fig. 4.4, the PSV-400 consists of a scanning *laser head*, a *junction box*, a *laser controller* with *decoder cards* and a *computer* with a *data acquisition card*. Additionally, the computer runs the Polytec PSV scanning vibrometer software to control the different devices. The laser

scanning head is equipped with a heterodyne laser interferometer together with two galvanometer scanning mirrors to deflect the laser beam. We use the digital *velocity decoder* VD-08 to demodulate the interference signal of the photodetector into a velocity proportional voltage signal. We low-pass filter the velocity signal using an *analog filter* to suppress aliasing effects and digitize the signal. To increase the signal-to-noise ratio, we applied stripes of 3M Scotchlite 7610 reflective sheeting on the stator disk.

Instead of the classical front panel, we use LabVIEW to control the scanning position via the ActiveX interface of the PSV scanning vibrometer software. In LabVIEW we also correct the error resulting from the angle of incidence  $\gamma$  by multiplying the measured signal by the factor  $1/\cos \gamma$ . It is hereby assumed that the in-plane velocity components  $(v_x, v_y)$  at the measuring point  $Q$  are negligible compared to the out-of-plane component  $v_z$ .

### 4.3.5 Self-tracking Laser Doppler Velocimetry on Rotor

In contrast to the vibration measurement on the stator disk, where the disk has no bias motion, the measurement on the rotor disk is more sophisticated. The main problem originates from the speckle pattern backscattered at an optically rough surface—an effect that needs to be taken into account when applying a laser Doppler velocimetry method on rotating parts. In the present section we describe the speckle problem, suggest some possible solutions and present our self-tracking laser Doppler velocimetry system in detail.

#### Speckle Noise Problem

In the previous section we discussed the laser interferometer and saw that the velocity signal can be demodulated from the intensity signal measured by the photodetector. If the target beam is backscattered by an *optically rough surface*, the backscattered image shows a random-phase *speckle pattern* due to constructive and destructive interference. This speckle pattern moves over the photodetector if the target surface moves in the direction normal to the beam and therefore leads to changes in the intensity signal. As described by Rothberg et al. (1989), this effect distorts the velocity measurement. The desired intensity changes due to the motion in beam direction *cannot* be distinguished from the undesired intensity changes due to the speckle pattern resulting from the motion normal to the beam.

When a laser interferometer in the *inertial system* beams on a *space-fixed* measuring spot at a rotating disk, the demodulated velocity signal is then composed of the true vibration part and an erroneous random part caused by the speckle pattern. Note that the random signal part is periodic when measured on a rotor disk with constant angular speed  $\Omega_R$ . That is because the surface roughness at the space-fixed measuring spot repeats for every revolution and so does the speckle pattern. In the Fourier spectrum, this periodic signal manifests in sharp peaks at frequency multiples of  $\Omega_R$  representing the Fourier series of the random speckle signal. This speckle effect strongly reduces the signal-to-noise ratio and makes the direct measurement in the inertial system not applicable.

### Solution Approaches

Several approaches exist to overcome the speckle noise problem in laser Doppler velocimetry. The most common systems use (i) dual mirror scanning, (ii) self-tracking, and (iii) a derotator to reduce the influence of speckles. These three solutions share the idea of measuring the vibration of a *body-fixed* measuring spot in the *rotor system* (instead of measuring a space-fixed point in the inertial system). This helps to minimize the speckle noise.

Bucher et al. (1994) developed the *dual mirror scanning* laser Doppler velocimetry to measure vibrations on rotating parts from the front side. Their system consists of a laser interferometer equipped with a pair of orthogonal mirrors to control the measuring spot that continuously follows a body-fixed point on the rotor. The scanning mirrors must be properly synchronized with the angular position of the rotor. Thereby, the mirror's inertia limits the speed of rotation. Additionally, the continuous scanning laser beam needs unobstructed optical access to the rotor, which is hard to fulfill when measuring from the driving side of the rotor.

The *self-tracking* laser Doppler velocimetry is a method where the laser beam is co-rotating by design. It was initially developed by Lomenzo et al. (1999) and later enhanced by Sever (2004) and Sever et al. (2002, 2006) to measure the vibrations on bladed disks. Considering Fig. 4.1, the beam of the laser interferometer is exactly aligned to the rotation axis of the rotor, where it gets deflected by a rotor-fixed central mirror. After the reflection at the central mirror, the beam rotates in the rotor system and can again be deflected to a body-fixed measuring spot by keeping it self-tracked. A

big advantage of this concept is that the target beam can be guided through a hollow motor while measuring from the driving side (see Fig. 4.1).

The idea of using a *derotator* in combination with a standard scanning vibrometer to measure on rotating parts was initially presented by Boedecker et al. (2006) and led to the commercially PSV-A-440 derotator system by Polytec. A Dove prism is placed between the rotor and the scanning vibrometer, and rotates with half the angular speed of the rotor about their mutual axis. This generates a non-rotating image seen by the scanning vibrometer. This system is expensive and also needs synchronization of the Dove prism rotation speed as well as an unobstructed optical access of the target beam.

Rothberg and Tirabassi (2012) studied the effects of misalignment for the three approaches presented above. They also provide a framework to quantify the misalignment errors in the velocity measurement.

### Realization of our Self-tracking System

We now present our realization of the self-tracking laser Doppler velocimetry system to pointwise measure the vibration on the rotor disk. As illustrated in Fig. 4.1, we enhanced the self-tracking systems by Lomenzo et al. (1999) and Sever (2004) by a radial scanner and an azimuthal positioning mechanism that allows to scan the rotor disk in polar coordinates. We have selected the self-tracking approach since it allows to measure the vibration of the rotor from the driving side by guiding the target beam through the motor. And it is the simplest of the three methods discussed above.

Fig. 4.7 shows a detailed view of the cutaway drawing Fig. 4.2, highlighting the polar scan unit. The central element of the polar scan unit is the *shaft*, where the *rotor disk* is mounted on one end and the *sensor head* on the other end. The *cross roller bearing* connects the sensor head and the shaft and allows a relative rotation between them. We use a *servo motor* together with a *strain wave gear* (gear ratio 1:100, no clearance) to precisely control the polar angle  ${}_R\varphi$  defined in Fig. 4.3. The sensor head supports the *scanner stem* with the *galvanometer scanner* to adjust the radial coordinate  ${}_Rr$  as well as the *deflection mirror* that deflects the target beam from the rotation axis into the direction of the galvanometer scanner. Additionally, the sensor head carries the *servo motor controller*, the *galvanometer amplifier* and the *RS232 interface*. They are supplied by a *slip ring assembly* and communicate (wirelessly) over the RS-232 protocol,

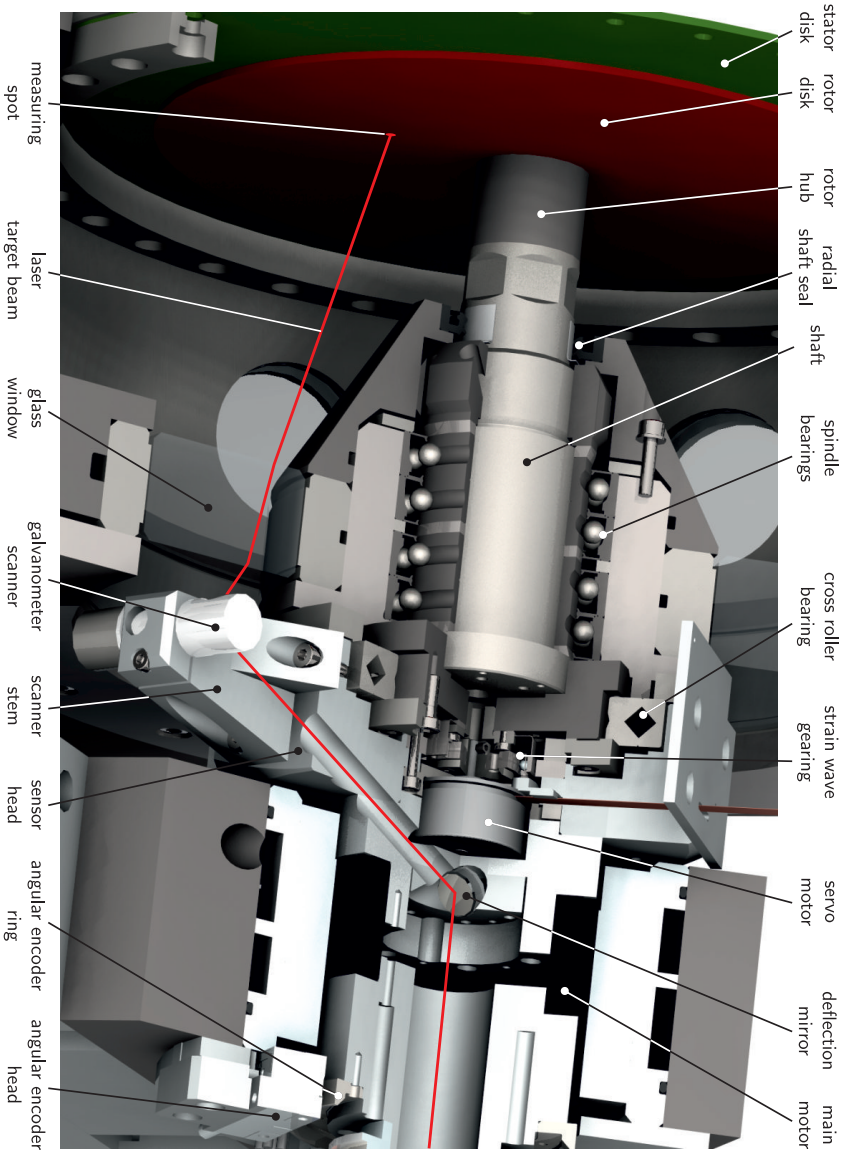


**Fig. 4.7:** Detail of cutaway drawing of Fig. 4.2 highlighting the polar scan unit. The red line indicates a selected beam path of the rotor laser Doppler velocimetry system.



as illustrated in Fig. 4.4. This polar scan unit allows to set the measuring spot at an arbitrary location on the rotor disk, parameterized by the polar coordinates  $(Rr, R\varphi)$ .

A crucial and delicate process is the alignment of the laser target beam to the rotation axis of the polar scan unit. A misalignment leads to a blurred measuring spot and to speckle noise in the velocity signal (Rothberg and Tirabassi, 2012). We designed an alignment unit to adjust the four parameters (2 transversal, 2 tilt) necessary to align the beam. In practice, we tried a combination of monitoring the measuring spot by eye while revolving the rotor (Sever, 2004) and minimizing the speckle noise content in the frequency spectrum (Boedecker et al., 2006).

We use the digital *velocity decoder* VD-06 to demodulate the interference signal into the velocity-proportional voltage signal (see Fig. 4.4). We low-pass filter the velocity signal before digitization to avoid aliasing effects. To increase the backscattering signal at the measuring spot, we apply stripes of 3M Diamond Grade reflective sheeting that also works in water. We compensate for the error by the angle of incidence  $\gamma$  and for the influence of water on the Doppler frequency shift by multiplying the measuring signal with  $1/(n^f \cos \gamma)$ , where  $n^f \doteq 1.333$  is the refraction index of water.

### 4.3.6 Signal Processing and Data Acquisition

From the wiring diagram of Fig. 4.4 we recognize that the analog signals from the current sensor and the laser interferometers are filtered before entering the data acquisition card to prevent aliasing during digitization. In the present section we discuss the relevant parameters of the signal processing and data acquisition of the test bench.

Fig. 4.8 illustrates the relevant frequency parameters of the anti-aliasing procedure that was applied to all analog input signals before digitization. Therein,  $\varpi_s$  denotes the *sampling frequency* of the data acquisition card and  $\varpi_s/2$  the *Nyquist frequency* related to  $\varpi_s$ . We use an 8th-order Bessel-type low-pass filter to attenuate the analog input signal above the *cut-off frequency*  $\varpi_c$  with a roll-off of  $-160$  dB/decade. The data acquisition card simultaneously samples the filtered analog input signals using parallel analog–digital converters with a resolution of 12 bit—that corresponds to 4096 discrete signal levels. The sampling frequency  $\varpi_s$  should be chosen so that the attenuated input signal above the Nyquist frequency  $\varpi_s/2$  is below the threshold of the analog–digital converter. That is the 4096th part of the

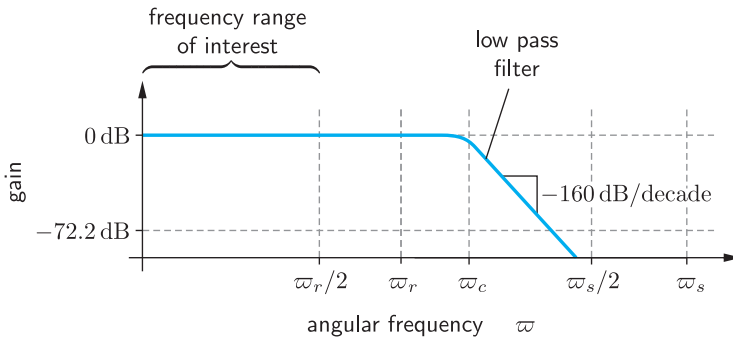


**Fig. 4.8:** Illustration of the relevant frequency parameters of the anti-aliasing procedure.

specified input range or an attenuation of  $-72.2$  dB. With this requirement we make sure that in digitization no high-frequency signal content is mirrored into the frequency range  $[0, \omega_s/2)$ .

After digitization we can apply digital techniques to downsample the signal to a frequency range of interest. Note that again low-pass filtering is necessary to avoid aliasing when resampling. In our case, we Fourier transformed the digital time signal into the frequency domain, cut off the frequency content above  $\omega_r/2$  and then inverse Fourier transformed the signal back into the time domain with the resampling frequency  $\omega_r$ . For this, we used the fast Fourier transform algorithm proposed by Cooley and Tukey (1965). The cut of frequency  $\omega_c$  of the analog low-pass filter should be chosen high enough above  $\omega_r/2$  to avoid a distortion due to the non-ideal filter characteristics.

### 4.3.7 Test Bench Control

As can be seen in Fig. 4.4, we used a computer to control all devices for the experimental test bench. The present section documents the program implemented in LabVIEW (National Instruments, 2014) to operate the test bench, perform the measurements, process the digital signals and store the measurement data. We designed the system as a state machine that can, according to Harel (1987), be represented with the statechart of Fig. 4.9.

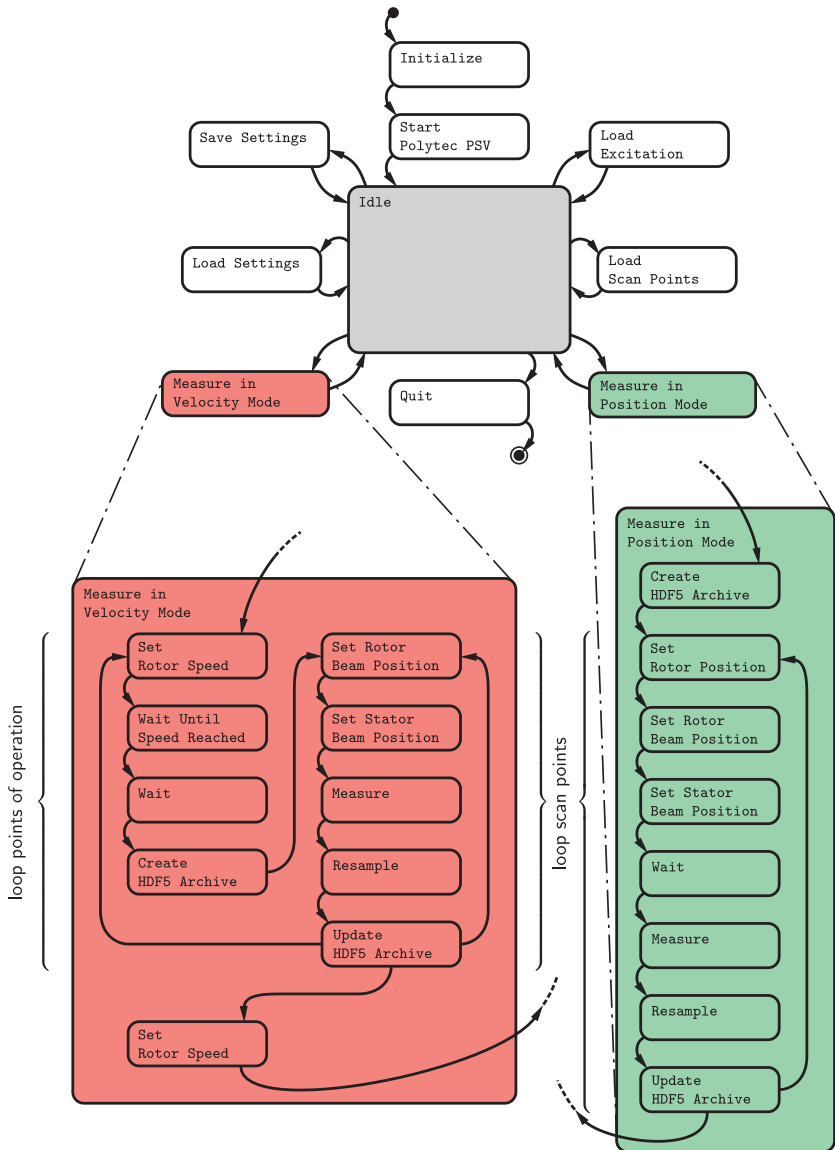


Fig. 4.9: Statechart of the test bench with the states 'Measure in Velocity Mode' and 'Measure in Position Mode' unclustered.

Subsequent to the primary 'Initialize' and 'Start Polytec PSV' states, the machine enters the central 'Idle' state, from which the surrounding states can be reached by user interaction. The most important states are 'Measure in Position Mode' and 'Measure in Velocity Mode', as they define the modal analysis measurements for rotation speeds  $\Omega_R = 0$  and  $\Omega_R > 0$ , respectively. In accordance with Fig. 4.9 we give here a short description of each state:

- Initialize** Initialize the program with the default settings.
- Start Polytec PSV** Start the Polytec PSV ActiveX client to control the galvanometer scanner for the measurements on the stator disk.
- Idle** Default state where the user can enter other states by interaction.
- Load Settings** Load program settings from an XML file.
- Save Settings** Save program settings to an XML file.
- Load Excitation** Load excitation time signal from a text file.
- Load Scan Points** Load polar coordinates of the scan points on the rotor and stator disk from a text file.
- Set Rotor Position** Set the angular position  $\alpha$  of the sensor head by actuating the main motor.
- Set Rotor Speed** Set the rotor angular speed  $\Omega_R$  by actuating the main motor.
- Wait Until Speed Reached** Measure the actual rotor angular speed  $\Omega_R$  and wait until the desired value is reached.
- Wait** Wait for a desired amount of time. This state is used to achieve stationary conditions for a measurement after changing the rotor speed or position.
- Set Rotor Beam Position** Set the polar position  $(R^r, R\varphi)$  of the rotor measuring spot by actuating the galvanometer scanner and the servo motor of the polar scan unit. For the radial position, Snell's law is applied to determine the ray path through air, glass and the fluid.

**Set Stator Beam Position** Set the polar position  $(sr, s\varphi)$  of the stator measuring spot by actuating the galvanometer scanners on the scanning leaser head via ActiveX.

**Measure** Configure the data acquisition card with output, input and trigger channels as well as the timing properties. Acquire the current signal (input) and the velocity signals on stator and rotor (output).

**Resample** Resample the signals acquired with sampling frequency  $\varpi_s$  to the resampling frequency  $\varpi_r$  via fast Fourier transform.

**Create HDF5 Archive** Create an initial HDF5 archive and assign the general attributes.

**Update HDF5 Archive** Update HDF5 archive with the measured signals and the measurement attributes.

**Quit** Shut down the Polytec PSV client and exit the program.

### 4.3.8 Data Storage

We briefly describe the structure of the archive file used to store the measurement data, as it builds the interface between the acquisition and the analysis of the measurements. We use the open-source hierarchical data format HDF5, which was designed by the HDF Group (2018) to store large multidimensional data structures together with metadata. This allows to bundle the measurements with all the additional information into one well-structured HDF5 file.

The major components of a HDF5 are *groups*, *datasets* and *attributes*. Groups are used to structure the data as they can contain other groups and datasets. Datasets are multidimensional arrays of a fixed datatype to store large amount of data. Attributes can be attached to groups or datasets and are used to store metadata related to them. We define the general attributes

- Program Name
- Identifier
- Date
- Medium
- Gap Width [m]
- Stator Thickness [m]
- Rotor Thickness [m]
- Rotor Velocity [rad/s]

which are attached to the default root group '/'. The measurements are bundled into the groups 'Current', 'Rotor' and 'Stator', in which each group contains the resampled time signals stored as datasets. Each dataset is labeled with the index of the measuring point starting with '000' and represents the signal measured at one measuring point. On every dataset we attached the measurement attributes

- Position
- Start Time
- Time Increment [s]
- Unit
- Sensitivity [Unit/V]
- Signal Zero Offset [V]
- Refraction Correction [1]
- Cosine Correction?
- Angle of Incidence [rad]

to define the metadata to the individual measurement. The HDF5-file contains the measurement of one scan and has a size of approximately 44 MB.

# Measurements and Modal Analysis

# 5

In the previous chapter, we were concerned with the experimental test bench to study the rotor–stator coupling by liquids. Now, in the present chapter, we describe the explicit *measuring procedure* to gather the measurement data, explain the *modal analysis* to estimate the modal parameters and show the *experimental results*.

The measuring procedure includes the individual preparation and the reference measurements of the rotor and the stator prior to the actual vibration measurements of the complete rotor–stator system. These are important steps to ensure a well-defined reference state without bias deformation and stress. We further describe a single scan measurement to gather the vibration data for one parameter set. Finally, we describe the measurement series which is a collection of scan measurements with varying parameters.

We estimate the modal parameters of the scan measurement data using modal analysis. This analysis denotes the fitting of a parametrized model to the measured data, usually carried out in the frequency domain. Our system contains rotating solids and a flowing viscous fluid. Therefore, the parametrized model needs to take gyroscopic effects and general damping into account.

## 5.1 Measuring Procedure

### 5.1.1 Sample Preparation

In the present section, we describe the preparation of the rotor and the stator disk for the vibration measurements. The reference state is verified with measurements that we will discuss in the following section.

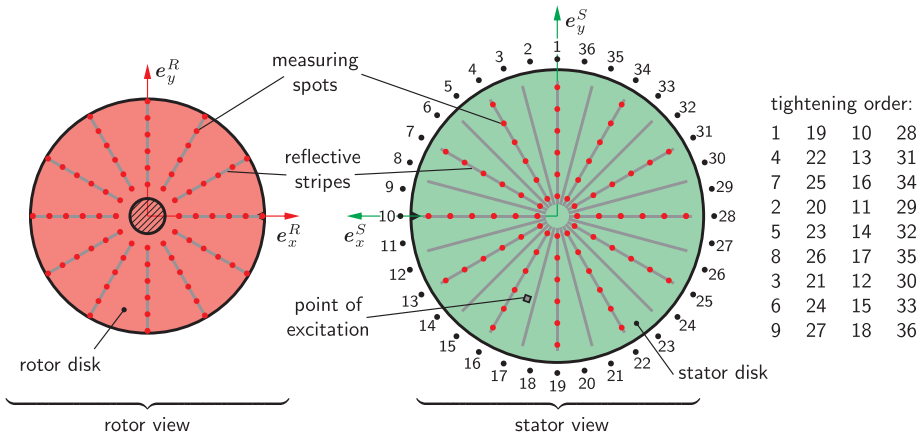


**Fig. 5.1:** Placement of reflective stripes and location of measuring spots on rotor and stator disk. Point of excitation and tightening order for the 36 screws of stator disk.

### Stator

The preparation of the stator includes the placement of the reflective stripes, the clamping of the stator disk and the installation of the electromagnetic excitation. The most important step is the clamping of the stator disk, because this may lead to a detuning of the system.

We will scan the stator disk with 72 measuring spots arranged in a spiderweb array as illustrated in Fig. 5.1. Hence, we arrange 24 stripes (2.5 mm × 105 mm) of 3M Scotchlite 7610 reflective sheeting. These reflective stripes increase the backscattering of the incoming laser beam and thus improve the signal quality of the laser vibrometer considerably. The reflective sheet has a mass density of 340 g/m<sup>2</sup> which yields a total mass of 2.2 g for the 24 stripes. We can therefore neglect the added mass of the reflective sheet compared to the mass of the stator—or even more to the modal mass of the rotor–stator system.

We saw in §4.2.2 that the stator disk is clamped between the massive stator ring and the fastening ring. In the ideal case, the boundary condition at the clamping diameter is rigid and the stator disk is in an undeformed and stress-free reference state. We properly designed the components to



get close to this ideal condition. To this end, we use ground sheets of hardened steel to achieve a high accuracy of flatness for the stator disks. Further we designed the clamping with a large number of screw joints to achieve a uniform force distribution. However, the assembly process has a significant influence on the detuning of the stator. Therefore, we define the tightening procedure for the clamping of the stator disk as follows: We tighten the screws according to the tightening order of Fig. 5.1 and increased the torques in the sequence of 0.4 Nm, 1 Nm and 2 Nm. The reference condition is verified by a comparison of the measured plate vibrations in air with analytical results. If the experimental results deviate significantly from the analytical results, the stator is disassembled and assembled again. The reference measurements and the verification procedure are described in §5.1.2.

Finally, we place the permanent-magnetic cube for the excitation at the polar position  $({}_S r, {}_S \varphi) = (75 \text{ mm}, -7\pi/18)$  with the south pole pointing in the  $+e_z^S$  direction. The electromagnetic coil is mounted with a gap of 1 mm to the magnet cube according to Fig. 4.5.

## Rotor

Consider the assembly of the rotor disk bonded to the rotor hub using Double Bubble epoxy adhesive like described in §4.2.2. To increase the backscattering, we apply 12 stripes ( $2.5 \text{ mm} \times 75 \text{ mm}$ ) of 3M Diamond Grade reflective sheet (see Fig. 5.1). This reflective sheet also works in wet conditions and has a mass density of  $480 \text{ g/m}^2$ , which yields a total mass of 1.1 g for the 12 stripes. Again, the added mass of these stripes is assumed to be negligible. But they have a height of 0.4 mm which may alter the fluid flow over the measuring surface.

## 5.1.2 Reference Measurements and Verification

We measure the eigenfrequencies of the rotor and the stator individually prior to the vibration measurements of the rotor–stator system. With these reference measurements we can document the reference state of our samples. By comparing the measured eigenfrequencies with analytical values, we can further verify the quality of the sample preparation of §5.1.1.

**Tab. 5.1:** Analytical and measured angular frequency  $\omega^r$  in rad/s for the stators of various thicknesses  $h_S$ . The analytic values for a circular disk are calculated according to Leissa (1969). The eigenfrequencies are measured in air.

mode	$h_S = 1.0 \text{ mm}$		$h_S = 1.5 \text{ mm}$	
	analytical	measured	analytical	measured
(0, 0)	1023	989.0	1535	1567
(1, 0)	2130	2076	3195	3211
(2, 0)	3494	3399	5241	5225
(0, 1)	3984	3953	5976	5982
(3, 0)	5112	4995	7668	7638
(1, 1)	6093	6012	9140	9126
(4, 0)	6847	6979	10468	10452
(2, 1)	8393	8473	12709	12674

**Tab. 5.2:** Analytical and measured angular eigenfrequencies  $\omega^r$  in rad/s for the rotors of various thicknesses  $h_R$ . The analytic values for an annular disk are calculated according to Vogel and Skinner (1965). The eigenfrequencies are measured in air.

mode	$h_R = 1.0 \text{ mm}$		$h_R = 1.5 \text{ mm}$		$h_R = 2.0 \text{ mm}$	
	analytical	measured	analytical	measured	analytical	measured
(1, 0)	644.3	630.8	966.5	933.7	1289	1194
(0, 0)	728.5	745.2	1093	1057	1457	1384
(2, 0)	932.8	960.1	1399	1471	1866	1882
(3, 0)	1956	2042	2934	3104	3912	4020
(4, 0)	3418	3563	5127	5388	6837	6999
(0, 1)	4453	4407	6680	6524	8907	—
(1, 1)	4820	4794	7230	7077	9639	9067

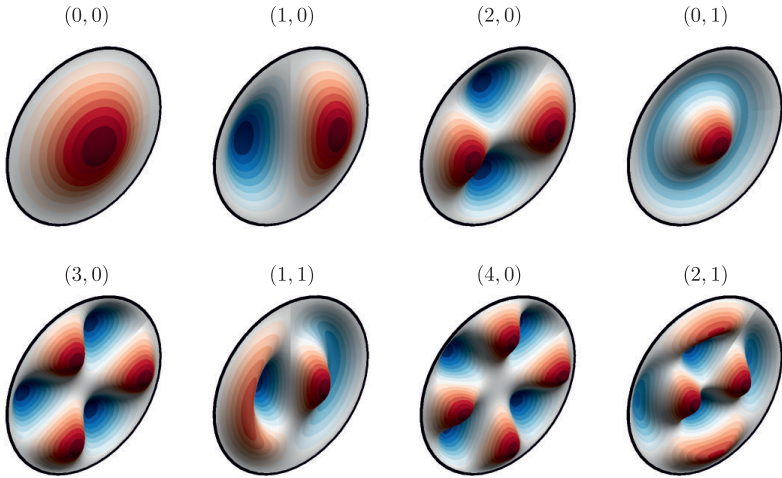


**Fig. 5.2:** Analytical mode shapes of stator according to Leissa (1969).

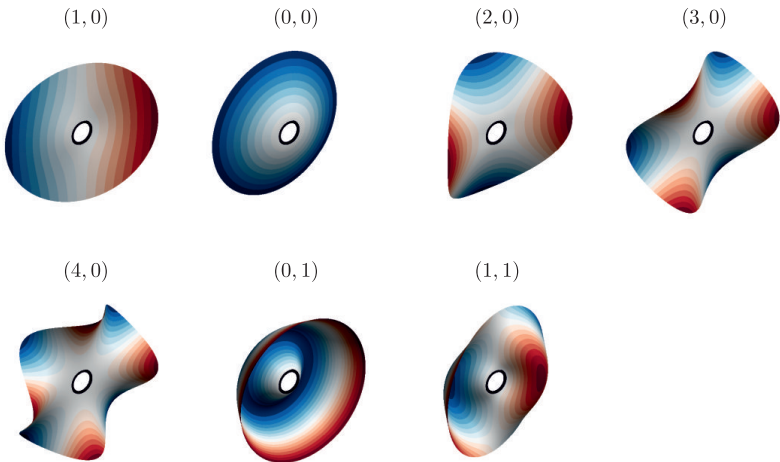


**Fig. 5.3:** Analytical mode shapes of rotor according to Vogel and Skinner (1965).

## Stator

For the reference measurement of the stator, we place the prepared stator assemblies (stator disk, stator ring, fastening ring) on an optical table using foam supports. It is important to choose the gap between stator disk and optical table large enough. Otherwise, the air cavity between disk and table becomes a resonator and alters the eigenfrequencies of the stator. We have found out that the gap must exceed 150 mm to suppress this effect.

We excite the stator vibration with a broad-band periodic chirp signal according to Boyd (1986) using the electromagnetic arrangement of § 4.3.3. We measure the vibration velocity at 72 measuring spots with the scanning vibrometer of § 4.3.4 placed on a tripod. To extract the eigenfrequencies  $\omega^r$ , we simply search for peaks in the frequency spectra of the velocity signals. The eight lowest eigenfrequencies of the stators with thicknesses  $h_S$  of 1.0 mm and 1.5 mm are listed in Tab. 5.1. The table also lists the analytical values for the eigenfrequencies of a disk clamped at the diameter  $D_S = 250$  mm. The values are computed according to Leissa (1969) using  $\rho = 7850$  kg/m<sup>3</sup>,  $E = 210$  GPa and  $\nu = 0.3$  as material parameters. We used the same analytical approach to plot the corresponding mode shapes of Fig. 5.2. The modes are labeled with  $(n, l)$ , where  $n \in \mathbb{N}_0$  denotes the azimuthal wave number (or the number of nodal diameters) and  $l \in \mathbb{N}_0$  its radial index (or the number of nodal circles).

The measured eigenfrequencies are in good agreement with the analytical values. The measured values for the stator thickness  $h_S = 1.0$  mm deviate less than 3.3% and the values for  $h_S = 1.5$  mm less than 2.0% from the analytical solution. We conclude that the prepared stators can be well described with the analytical model of a clamped disk. Hence, the clamping is nearly ideally rigid and the bias stress due to the tightening of the stator disk can be neglected.

## Rotor

Similar to the stator assembly, we performed reference measurements of the rotor assemblies (rotor disk, rotor hub). Accordingly, we mounted a single rotor on the optical table using an intermediate plate to achieve a high stiffness. We used the same equipment for the excitation and the measurement of the vibration as for the stator. Again, the eigenfrequencies

are estimated by locating the peaks in the frequency spectra of the measured velocity signals.

In Tab. 5.2 we list the seven lowest eigenfrequencies  $\omega^r$  for rotors with thicknesses  $h_R$  of 1.0 mm, 1.5 mm and 2.0 mm. The measured eigenfrequencies are compared to the analytical solution by Vogel and Skinner (1965) of an annular disk which is clamped at the diameter  $d_R = 30$  mm and free at the outer diameter  $D_R = 200$  mm, again using  $\rho = 7850$  kg/m<sup>3</sup>,  $E = 210$  GPa and  $\nu = 0.3$  as material parameters. With the same analytical approach, we plot the mode shapes corresponding to the eigenvalues in Fig. 5.3. When we compare the agreement of the measured eigenfrequencies with the analytical results we note some deviations. The measured values of the rotor with thickness  $h_R = 1.0$  mm deviate less than 4.4%, the one with  $h_R = 1.5$  mm less than 5.8% and the one with  $h_R = 2.0$  mm less than 7.4%. This increasing discrepancy suggests that the bonding between rotor disk and rotor hub might not be ideally rigid for the stiff disks.

### 5.1.3 Test Bench Preparation

We assume that the rotor and the stator are well prepared according to §5.1.1. Prior to each scan measurement on the rotor–stator system, we perform the following steps to prepare the test bench:

1. Power on all electric devices so that they can heat up to the thermal equilibrium.
2. Degas the water using the Sonoswiss SW 12 H ultrasonic cleaner. The degassing of the water is necessary, to avoid the formation of air bubbles in the central low-pressure region of the fluid flow. These bubbles would interrupt the target laser path of the rotor scanning vibrometer and disturb the velocity measurement. Further, they might influence the dynamics of the fluid through a change of density and stiffness properties.
3. Clean the optical window carefully using Loctite SF 7063 parts cleaner and Kimtech precision wipes. This is also an important step to ensure the unobstructed optical access of the rotor scanning vibrometer.
4. Fit the rotor onto the shaft and tighten the central screw with a torque of 5 Nm. The relative angular position is arbitrary, as we set the zero reference position in the next step.

5. Move the rotor to the reference position  ${}_R\varphi = 0$  (confer Fig. 4.3). Use the servo motor for this homing movement and set home position to zero.
6. Fit the stator to the casing and use a packet of spacers to adjust the gap width  $g$  between rotor and stator disk. The spacer packet must be assembled to the height

$$a = g + h_S - 1.4 \text{ mm}, \quad (5.1)$$

where  $h_S$  is the thickness of the stator disk. Tighten the 18 screws with a torque of 3 Nm.

7. Carefully flood the fluid cavity with the degassed water until the casing is filled completely. Avoid the building of air pockets at protruding edges.
8. Activate the main motor controller and run the homing procedure to find the angular home position of the scanner head at  $\beta = 5\pi/4$ .

After this preparation, the test bench is ready for the scan measurements described in the following sections.

### 5.1.4 Scan Measurement

We measure the vibration of the rotor–stator system in a pointwise scan. This is a consecutive sequence of repetitive point measurements. For each measurement, we switch the measuring spots on rotor and stator while keeping the point of excitation fixed. In the present section, we specify the scan measurements and the corresponding parameters.

#### Modes of Operation

As depicted in Fig. 4.9, we distinguish two modes of operation: (i) the *position mode* with  $\Omega_R = 0 \text{ rad/s}$  and (ii) the *velocity mode* with  $\Omega_R > 0 \text{ rad/s}$ . The excitation, the location of the measuring spots and the temporal sampling are the same for both modes. Nevertheless, we would like to point out the variations.

In the position mode, we keep the rotor angle fixed at  $\beta = 0$  (confer Fig. 4.3). This yields a static condition with the rotor speed  $\Omega_R = \dot{\beta} =$

0 rad/s and a fluid at rest. Nevertheless, due to the azimuthal adjustment mechanism of our test bench, we need to change both,  ${}_R\varphi$  and  $\alpha$  in order to hold  $\beta = 0$  fixed. This disturbs the fluid slightly, when the azimuthal position of the measuring spot is changed. In that case, we wait for 30 s before starting the single spot measurement so that the disturbance can decay.

In the velocity mode, we run up the rotor to the desired angular rotor speed  $\Omega_R$ . Prior to the actual scan measurement, we wait for 300 s to allow the fluid flow to reach a stationary condition. To ensure consistent initial conditions, we set the triggering so that each point measurement starts when the rotation angle is at  $\beta = 0$ .

### Spatial Sampling

We arrange the 72 measuring spots on the rotor and the stator in a spider-web array according to Fig. 5.1. The spots are equally spaced in azimuthal direction in  $N_\varphi = 12$  azimuthal grid lines. In radial direction, the spots are linearly spaced in  $N_r = 6$  grid circles. The radii of the circles lie between 17 mm and 110 mm for the stator and between 27 mm and 98 mm for the rotor.

### Excitation

We excite the rotor–stator system with an electromagnetic coil at the location  $(s_r, s_\varphi) = (75 \text{ mm}, -7\pi/18)$  (see Fig. 5.1). We use the windowed chirp signal of Fig. 5.4 to drive the electromagnetic coil. The signal is described by the chirped sine function

$$U(t) = U_0 \sin \theta(t), \quad (5.2)$$

where  $\theta(t)$  denotes the instantaneous phase and  $U_0$  the voltage amplitude. For a windowed linear chirp, we define the ramp

$$\varpi(t) = \begin{cases} \varpi_1 + (\varpi_2 - \varpi_1) \frac{t - t_1}{t_2 - t_1} & t_1 \leq t < t_2 \\ 0 & \text{otherwise,} \end{cases} \quad (5.3)$$

for the instantaneous angular frequency  $\varpi(t) = \dot{\theta}(t)$ . Therein,  $\varpi_1$  denotes the frequency at time  $t_1$  and  $\varpi_2$  the one at the end time  $t_2$ . The instanta-

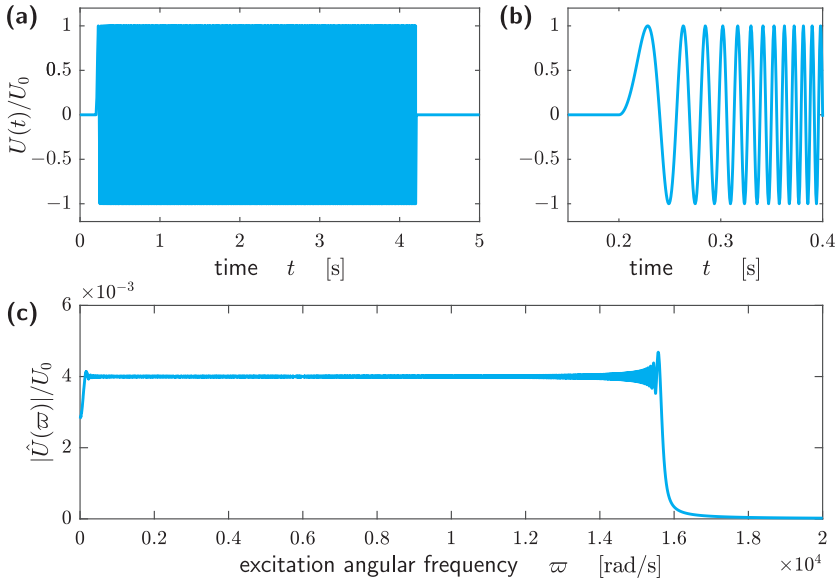


**Fig. 5.4:** (a) Normalized voltage signal  $U(t)/U_0$  in time domain. (b) Detail of  $U(t)/U_0$  around the start time  $t_s$ . (c) Amplitude spectrum of  $\hat{U}(\omega)/U_0$  in the frequency domain.

neous phase is then found by the integration

$$\theta(t) = \int_0^t \varpi(\tau) d\tau. \quad (5.4)$$

Our specific excitation signal has a length of  $T = 5$  s. We sweep the frequency from  $\varpi_1 = 0$  rad/s at  $t_1 = 0.2$  s to the frequency  $\varpi_2 \doteq 15.7 \times 10^3$  rad/s at  $t_2 = 4.2$  s. The excitation terminates at  $t_2 = 4.2$  s such that the vibration decays in the remaining 0.8 s measuring time. Thus, no information is transferred between the subsequent point measurements and they become independent. Further, the windowing is necessary to suppress spectral leakage. As can be seen in the amplitude spectrum of Fig. 5.4, the signal provides a broad-band excitation with a nearly constant amplitude up to  $\varpi_2 \doteq 15.7 \times 10^3$  rad/s.



Note that we defined the voltage signal and not the current signal that drives the electromagnetic coil. It would be more useful to define the current signal directly, because it is proportional to the excitation force of the system. Unfortunately, it is more demanding to use a current controlled amplifier. We therefore use a voltage amplifier to drive the coil but measure the resulting current with a Hall-effect sensor (see Fig. 4.4).

### Temporal Sampling

Here, we specify the sampling parameters based on the principles of §4.3.6. The frequency range of interest ranges up to the maximum excitation frequency of  $\varpi_2 \doteq 15.7 \times 10^3 \text{ rad/s}$ . This determines the resampling rate  $\varpi_r = 2\varpi_2 \doteq 31.4 \times 10^3 \text{ rad/s}$  and the time increment  $\Delta t = 200 \mu\text{s}$ . We set the cut of frequency of the anti-aliasing filter to  $\varpi_c \doteq 188 \times 10^3 \text{ rad/s}$  and the sampling rate of the data acquisition card to  $\varpi_s \doteq 628 \times 10^3 \text{ rad/s}$ .

### Data Storage

We store the data for each scan measurement in a separate HDF5 archive with the structure documented in §4.3.8. The archive file contains the waveforms of the current signal  $I(t)$  as well as the velocity components  $v_z(t)$  of the rotor and the stator for the 72 scan points. The signals are sampled at the resample frequency  $\varpi_r \doteq 31.4 \times 10^3 \text{ rad/s}$ . Further, we attached all information necessary for the subsequent analysis of the data. The naming pattern is

`stator-1.5_rotor-1.0_gap-03.6_0omega-160_00.h5`

for the exemplary parameters  $h_S = 1.5 \text{ mm}$ ,  $h_R = 1.0 \text{ mm}$ ,  $g = 3.6 \text{ mm}$  and  $\Omega_R = 160 \frac{2\pi}{60} \text{ rad/s} \doteq 16.8 \text{ rad/s}$ .

### 5.1.5 Series of Measurements

We perform a series of scan measurements by varying the parameters stator thickness  $h_S$  (2 levels), rotor thickness  $h_R$  (3 levels), gap width  $g$  (8 levels) and angular rotor speed  $\Omega_R$  (7 levels). The parameter levels of the parameters are listed in Tab. 5.3. We do not cover all combinations of the four parameters, but restrict the three geometrical parameters to the  $4 \times 8 = 32$  combinations illustrated in Fig. 5.5. For each geometrical combination we

**Tab. 5.3:** Parameters and level values in the series of measurements.

parameter	symbol	level values	unit
stator thickness	$h_S$	{1.0, 1.5}	mm
rotor thickness	$h_R$	{1.0, 1.5, 2.0}	mm
gap width	$g$	{1.4, 2.2, 2.9, 3.6, 4.4, 6.4, 9.4, 14.4}	mm
angular rotor speed	$\Omega_R$	{0, 8.38, 16.8, 25.1, 33.5, 41.9, 50.3}	rad/s

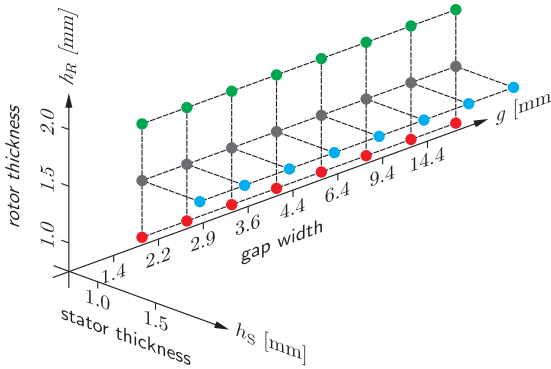


**Fig. 5.5:** Combinations of the geometrical parameters in the series of measurements. On each depicted point, the angular rotor speed  $\Omega_R$  takes the 7 levels {0, 8.38, 16.8, 25.1, 33.5, 41.9, 50.3} rad/s.

run measurements for all 7 levels of the angular rotor speed  $\Omega_R$ . For the complete series, this yields a total of  $32 \times 7 = 224$  scan measurements with a cumulative measuring time of approximately 42 h.

## 5.2 Modal Analysis

Our experiment provides time signals of the excitation (input) and the resulting vibration (output) of the rotor–stator system. The aim of the modal analysis is to estimate the modal parameters from the measurement data. For each mode  $m$ , the modal parameters are the complex eigenvalue

$$\lambda_m = -\delta_m^r + j\omega_m^r, \tag{5.5}$$

composed of the angular eigenfrequency  $\omega_m^r$  and the damping factor  $\delta_m^r$ , as well as the mode shapes  $\mathbf{r}_m$  and  $\mathbf{l}_m$  describing the right and left eigenvectors, respectively. The eigenvalue  $\lambda_m$  determines the temporal evolution of a mode without excitation according to

$$e^{\lambda_m t} = e^{(-\delta_m^r + j\omega_m^r)t} = e^{-\delta_m^r t} e^{j\omega_m^r t}. \quad (5.6)$$

We then see that the angular eigenfrequency  $\omega_m^r$  is assigned to the pseudo angular frequency of the free oscillations and the damping factor  $\delta_m^r$  to its temporal decay rate. The collection of all modes fully describes the dynamics of a linear system.

The fundamentals of modal analysis are well described in the textbooks by Ewins (2000) and Heylen et al. (1997). However, they only partially cover the dynamics of rotating structures which is essential for our rotor–stator system. For the theory of rotor dynamics, we refer to the textbook by Gasch et al. (2012) and the fundamental contributions by Nordmann (1984a,b).

In the following section, we briefly present the basic theory of modal analysis with regard to rotating structures. Subsequently, we utilize rotation symmetries and adapt the formulation to our specific test bench measurements.

## 5.2.1 Theory

### Second-order Form

Consider a linear time-invariant mechanical system with degree of freedom  $N$  formulated in the second-order form as

$$\mathbf{M}\ddot{\mathbf{u}}(t) + (\mathbf{D} + \mathbf{G})\dot{\mathbf{u}}(t) + (\mathbf{K} + \mathbf{N})\mathbf{u}(t) = \tilde{\mathbf{F}}(t), \quad (5.7)$$

where  $\mathbf{u}(t) \in \mathbb{R}^N$  is the displacement vector and  $\tilde{\mathbf{F}}(t) \in \mathbb{R}^N$  the force vector exciting the structure.  $\mathbf{M}$ ,  $\mathbf{D}$ ,  $\mathbf{G}$ ,  $\mathbf{K}$  and  $\mathbf{N}$  denote the mass matrix, the damping matrix, the gyroscopic matrix, the stiffness matrix and the matrix of circulating forces, respectively. They are constant elements of  $\mathbb{R}^{N,N}$  with the properties

$$\mathbf{M} = \mathbf{M}^T \succ 0, \quad \mathbf{D} = \mathbf{D}^T, \quad \mathbf{G} = -\mathbf{G}^T, \quad \mathbf{K} = \mathbf{K}^T, \quad \mathbf{N} = -\mathbf{N}^T. \quad (5.8)$$

The skew-symmetric matrices  $\mathbf{G}$  and  $\mathbf{N}$  take effects due to the rotating structures into account and need to be included in our system.

Associated to the inhomogeneous system (5.7), we can find the homogeneous system

$$\mathbf{M}\ddot{\mathbf{u}}(t) + (\mathbf{D} + \mathbf{G})\dot{\mathbf{u}}(t) + (\mathbf{K} + \mathbf{N})\mathbf{u}(t) = \mathbf{0}. \quad (5.9)$$

by setting  $\tilde{\mathbf{F}}(t) \equiv \mathbf{0}$ . This system describes the free vibrations of the structure without any excitation. If we apply the exponential ansatz

$$\tilde{\mathbf{u}}(t) = \Re\{\mathbf{r}e^{\lambda t}\}, \quad \dot{\tilde{\mathbf{u}}}(t) = \Re\{\lambda \mathbf{r}e^{\lambda t}\}, \quad \ddot{\tilde{\mathbf{u}}}(t) = \Re\{\lambda^2 \mathbf{r}e^{\lambda t}\}, \quad (5.10)$$

this yields the right eigenvalue problem in second-order form

$$[\lambda^2 \mathbf{M} + \lambda(\mathbf{D} + \mathbf{G}) + (\mathbf{K} + \mathbf{N})]\mathbf{r} = \mathbf{0}. \quad (5.11)$$

There are  $2N$  right eigenpairs  $(\lambda_m, \mathbf{r}_m)$  satisfying this equation, with  $\lambda_m \in \mathbb{C}$  denoting the  $m$ -th eigenvalue and  $\mathbf{r}_m \in \mathbb{C}^N$  its associated right eigenvector. We can also formulate the left eigenvalue problem in second-order form

$$\mathbf{l}^T[\lambda^2 \mathbf{M} + \lambda(\mathbf{D} + \mathbf{G}) + (\mathbf{K} + \mathbf{N})] = \mathbf{0}^T, \quad (5.12)$$

with  $2N$  left eigenpairs  $(\lambda_m, \mathbf{l}_m)$ . The left eigenvectors  $\mathbf{l}_m \in \mathbb{C}^N$  are the right eigenvectors of the transposed problem of (5.9) and they therefore share the same eigenvalues  $\lambda_m$ . We concatenate the right and left eigenvectors to the right and left modal matrices

$$\mathbf{R} := (\mathbf{r}_1 \quad \mathbf{r}_2 \quad \cdots \quad \mathbf{r}_{2N}), \quad \mathbf{L} := (\mathbf{l}_1 \quad \mathbf{l}_2 \quad \cdots \quad \mathbf{l}_{2N}), \quad (5.13)$$

respectively. Further, we assume that the  $2N$  eigenvalues are distinct and not real valued so that the eigenvalues and eigenvectors can be ordered in complex conjugate pairs

$$\lambda_{m+N} = \lambda_m^*, \quad \mathbf{r}_{m+N} = \mathbf{r}_m^*, \quad \mathbf{l}_{m+N} = \mathbf{l}_m^*, \quad m = 1, \dots, N. \quad (5.14)$$

### First-order Form

The system in second-order form (5.7), with a general damping matrix  $\mathbf{D}$  and skew-symmetric matrices  $\mathbf{G}$  and  $\mathbf{N}$ , is not diagonalizable (Müller, 1977, p. 58). Nevertheless, we can rewrite (5.7) in the first-order form

$$\underbrace{\begin{pmatrix} \mathbf{K} + \mathbf{N} & \mathbf{0} \\ \mathbf{0} & -\mathbf{M} \end{pmatrix}}_{=: \mathbf{A}} \underbrace{\begin{pmatrix} \tilde{\mathbf{u}}(t) \\ \dot{\tilde{\mathbf{u}}}(t) \end{pmatrix}}_{=: \tilde{\mathbf{x}}(t)} + \underbrace{\begin{pmatrix} \mathbf{D} + \mathbf{G} & \mathbf{M} \\ \mathbf{M} & \mathbf{0} \end{pmatrix}}_{=: -\mathbf{B}} \underbrace{\begin{pmatrix} \tilde{\mathbf{u}}(t) \\ \dot{\tilde{\mathbf{u}}}(t) \end{pmatrix}}_{=: \dot{\tilde{\mathbf{x}}}(t)} = \underbrace{\begin{pmatrix} \tilde{\mathbf{F}}(t) \\ \mathbf{0} \end{pmatrix}}_{=: \tilde{\mathbf{f}}(t)}, \quad (5.15)$$

where we stack the displacement and velocity vector to the state vector  $\tilde{\mathbf{x}}(t) \in \mathbb{R}^{2N}$  and define the general force vector  $\tilde{\mathbf{f}}(t) \in \mathbb{R}^{2N}$ . This first-order form, which writes in short-hand notation as

$$\mathbf{A}\tilde{\mathbf{x}}(t) - \mathbf{B}\dot{\tilde{\mathbf{x}}}(t) = \tilde{\mathbf{f}}(t), \quad (5.16)$$

is diagonalizable with the bi-modal decomposition described below. Accordingly, we need the right and left eigenvectors of the first-order form. Again, we start with the associated homogeneous system

$$\mathbf{A}\tilde{\mathbf{x}}(t) - \mathbf{B}\dot{\tilde{\mathbf{x}}}(t) = \mathbf{0}, \quad (5.17)$$

by setting  $\mathbf{f}(t) \equiv \mathbf{0}$ . Applying the ansatz

$$\tilde{\mathbf{x}}(t) = \Re\{\mathbf{r}e^{\lambda t}\}, \quad \dot{\tilde{\mathbf{x}}}(t) = \Re\{\lambda \mathbf{r}e^{\lambda t}\}, \quad (5.18)$$

yields the right eigenvalue problem in first-order form

$$(\mathbf{A} - \lambda \mathbf{B})\mathbf{r} = \mathbf{0} \quad (5.19)$$

and the related left eigenvalue problem in first-order form is

$$\mathbf{l}^\top (\mathbf{A} - \lambda \mathbf{B}) = \mathbf{0}^\top. \quad (5.20)$$

If we compare the first row of (5.15) with (5.7), we recognize that the eigenvalues of the two forms are equal and that the right and left eigenvectors are interrelated by

$$\mathbf{r}_m := \begin{pmatrix} \mathbf{r}_m \\ \lambda_m \mathbf{r}_m \end{pmatrix}, \quad \mathbf{l}_m := \begin{pmatrix} \mathbf{l}_m \\ \lambda_m \mathbf{l}_m \end{pmatrix}. \quad (5.21)$$

We can again build the right and left modal matrix by concatenation of the eigenvectors

$$\mathfrak{R} := (\mathbf{r}_1 \quad \mathbf{r}_2 \quad \cdots \quad \mathbf{r}_{2N}) = \begin{pmatrix} \mathbf{r}_1 & \mathbf{r}_2 & \cdots & \mathbf{r}_{2N} \\ \lambda_1 \mathbf{r}_1 & \lambda_2 \mathbf{r}_2 & \cdots & \lambda_{2N} \mathbf{r}_{2N} \end{pmatrix}, \quad (5.22)$$

$$\mathfrak{L} := (\mathbf{l}_1 \quad \mathbf{l}_2 \quad \cdots \quad \mathbf{l}_{2N}) = \begin{pmatrix} \mathbf{l}_1 & \mathbf{l}_2 & \cdots & \mathbf{l}_{2N} \\ \lambda_1 \mathbf{l}_1 & \lambda_2 \mathbf{l}_2 & \cdots & \lambda_{2N} \mathbf{l}_{2N} \end{pmatrix}. \quad (5.23)$$

We note that the eigenvalues are distinct and order the eigenvalues and eigenvectors as complex conjugated pairs

$$\lambda_{m+N} = \lambda_m^*, \quad \mathbf{r}_{m+N} = \mathbf{r}_m^*, \quad \mathbf{l}_{m+N} = \mathbf{l}_m^*, \quad m = 1, \dots, N. \quad (5.24)$$

### Bi-modal Decomposition

In §A.4 we show that the left eigenvectors  $\mathbf{l}_n$  and right eigenvectors  $\mathbf{r}_m$  are bi-orthogonal with respect to  $\mathbf{A}$  and  $\mathbf{B}$  for distinct eigenvalues  $\lambda_n$  and  $\lambda_m$ , this is

$$\mathbf{l}_n^T \mathbf{A} \mathbf{r}_m = \begin{cases} 0 & n \neq m \\ a_m & n = m, \end{cases} \quad \mathbf{l}_n^T \mathbf{B} \mathbf{r}_m = \begin{cases} 0 & n \neq m \\ b_m & n = m. \end{cases} \quad (5.25)$$

If all eigenvalues of (5.19) are distinct, the left modal matrix  $\mathfrak{L}$  and the right modal matrix  $\mathfrak{R}$  then diagonalize the matrices  $\mathbf{A}$  and  $\mathbf{B}$  according to

$$\mathbf{a} := \mathfrak{L}^T \mathbf{A} \mathfrak{R} = \mathbf{\Lambda}, \quad \mathbf{b} := \mathfrak{L}^T \mathbf{B} \mathfrak{R} = \mathbf{I}, \quad (5.26)$$

with diagonal matrices  $\mathbf{a}$  and  $\mathbf{b}$ . We further normalize the eigenvectors such that  $\mathbf{l}_n^T \mathbf{B} \mathbf{r}_m = \delta_{nm}$  with  $b_m = 1$ , and  $\mathbf{b}$  therefore equals the identity matrix  $\mathbf{I}$ . In this case, the matrix  $\mathbf{a}$  becomes the matrix  $\mathbf{\Lambda}$  with the  $2N$  eigenvalues  $a_m = b_m \lambda_m = \lambda_m$  on its diagonal.

We multiply  $\mathfrak{L}^T$  to the left of (5.16), use the relation  $\mathfrak{R} \mathfrak{R}^{-1} = \mathbf{I}$  and write the first-order form as

$$(\mathfrak{L}^T \mathbf{A} \mathfrak{R}) \mathfrak{R}^{-1} \tilde{\mathbf{x}}(t) - (\mathfrak{L}^T \mathbf{B} \mathfrak{R}) \mathfrak{R}^{-1} \dot{\tilde{\mathbf{x}}}(t) = \mathfrak{L}^T \tilde{\mathbf{f}}(t) \quad (5.27)$$

Further, we introduce generalized coordinates  $\tilde{\mathbf{q}}(t) \in \mathbb{C}^{2N}$  and generalized forces  $\tilde{\mathbf{g}}(t) \in \mathbb{C}^{2N}$  defined by

$$\tilde{\mathbf{q}}(t) := \mathfrak{R}^{-1} \tilde{\mathbf{x}}(t), \quad \tilde{\mathbf{g}}(t) := \mathfrak{L}^T \tilde{\mathbf{f}}(t) = \mathbf{L}^T \tilde{\mathbf{F}}(t). \quad (5.28)$$

With this variable transformation, we rewrite (5.27) as

$$\mathbf{\Lambda} \tilde{\mathbf{q}}(t) - \mathbf{I} \dot{\tilde{\mathbf{q}}}(t) = \tilde{\mathbf{g}}(t), \quad (5.29)$$

where (5.16) is decomposed into  $2N$  scalar equations of the form

$$\boxed{\lambda_m \tilde{q}_m(t) - \dot{\tilde{q}}_m(t) = \tilde{g}_m(t)} \quad m = 1, \dots, 2N, \quad (5.30)$$

with  $\tilde{g}_m(t) = \mathbf{l}_m^T \tilde{\mathbf{f}}(t) = \mathbf{l}_m^T \tilde{\mathbf{F}}(t)$ . Note that  $\tilde{\mathbf{q}}(t)$  and  $\tilde{\mathbf{g}}(t)$  are complex-valued variables which have no simple physical interpretation. After solving (5.30) we can recast the real-valued physical solution by

$$\tilde{\mathbf{x}}(t) = \mathfrak{R} \tilde{\mathbf{q}}(t) = \sum_{m=1}^{2N} \mathbf{r}_m \tilde{q}_m(t), \quad \tilde{\mathbf{u}}(t) = \mathbf{R} \tilde{\mathbf{q}}(t) = \sum_{m=1}^{2N} \mathbf{r}_m \tilde{q}_m(t). \quad (5.31)$$

### Frequency Response Function

It is convenient to represent (5.30) in the frequency domain. Hence, we take the Fourier transform of the excitation time signal

$$\hat{\mathbf{F}}(\varpi) = \int_{-\infty}^{+\infty} \tilde{\mathbf{F}}(t) e^{-j\varpi t} dt \quad (5.32)$$

to write the Fourier transform of the generalized force as

$$\begin{aligned} \hat{g}_m(\varpi) &= \int_{-\infty}^{+\infty} \tilde{g}_m(t) e^{-j\varpi t} dt = \int_{-\infty}^{+\infty} \mathbf{l}_m^T \tilde{\mathbf{F}}(t) e^{-j\varpi t} dt \\ &= \mathbf{l}_m^T \int_{-\infty}^{+\infty} \tilde{\mathbf{F}}(t) e^{-j\varpi t} dt = \mathbf{l}_m^T \hat{\mathbf{F}}(\varpi). \end{aligned} \quad (5.33)$$

The Fourier transform of the decoupled ordinary differential equations in the time domain (5.30) leads to the algebraic equations in the frequency domain

$$(\lambda_m - j\varpi)\hat{q}_m(\varpi) = \hat{g}_m(\varpi) \quad (5.34)$$

with the solutions

$$\hat{q}_m(\varpi) = \frac{\hat{g}_m(\varpi)}{\lambda_m - j\varpi}. \quad (5.35)$$

Analogous to (5.31), we can recast the solution for the response in the frequency domain by

$$\begin{aligned} \hat{\mathbf{u}}(\varpi) &= \sum_{m=1}^{2N} \mathbf{r}_m \hat{q}_m(\varpi) = \sum_{m=1}^{2N} \frac{\mathbf{r}_m \hat{g}_m(\varpi)}{\lambda_m - j\varpi} \\ &= \sum_{m=1}^{2N} \frac{\mathbf{r}_m \mathbf{l}_m^T}{\lambda_m - j\varpi} \hat{\mathbf{F}}(\varpi) = \underbrace{\sum_{m=1}^N \left[ \frac{\mathbf{r}_m \mathbf{l}_m^T}{\lambda_m - j\varpi} + \frac{\mathbf{r}_m^* \mathbf{l}_m^{*\top}}{\lambda_m^* - j\varpi} \right]}_{=: \mathbf{H}(\varpi)} \hat{\mathbf{F}}(\varpi), \end{aligned} \quad (5.36)$$

where we introduced the frequency response function matrix  $\mathbf{H}(\varpi) \in \mathbb{C}^{N,N}$ . Although  $\mathbf{H}(\varpi)$  is describing the response behaviour of the system, it is entirely formed by the modal parameters  $\lambda_m$ ,  $\mathbf{r}_m$  and  $\mathbf{l}_m$ , which themselves are determined by the homogeneous system (5.9). Equations (5.36) and (5.28) show that the left eigenvectors  $\mathbf{l}_m$  describe the receptivity of the mode  $m$  to the force  $\hat{\mathbf{F}}(\omega)$ .

## 5.2.2 Adaption to Test Bench Measurements

For the modal analysis of the test bench, we assume that the force response of the system can be described by the model (5.7) with degree of freedom  $N$  equal to the number of measuring spots  $N_r \cdot N_\varphi = 6 \cdot 12 = 72$  (see Fig. 5.1). We represent the  $N$  displacement components in  $+e_z^S$  direction by the displacement vector  $\tilde{\mathbf{u}}(t)$ . The force vector  $\tilde{\mathbf{F}}(t)$  models the excitation mapped onto the grid of measuring spots.

In (5.36), we provide the frequency response relation  $\hat{\mathbf{u}}(\varpi) = \mathbf{H}(\varpi)\hat{\mathbf{F}}(\varpi)$  in its general form. It would need  $N^2 = 5184$  measurements (by varying the points of excitation and response individually) to completely determine the frequency response function matrix  $\mathbf{H}(\varpi)$ . Additionally, each individual mode  $m$  is characterized by the complex modal parameters  $\lambda_m$ ,  $\mathbf{r}_m$  and  $\mathbf{l}_m$ , which results in  $2N + 1 = 145$  complex or  $2(2N + 1) = 290$  real scalars. It is not feasible to measure all combinations and to estimate such a large number of parameters. The present section describes how we reduced the complexity to a reasonable level and states the underlying assumptions.

In the present study we focus on the right eigenvectors  $\mathbf{r}_m$  which describe the mode shape of the free vibration without excitation. We therefore disregard the left eigenvectors  $\mathbf{l}_m$  that characterize the receptivity of mode  $m$  to the spatial force distribution of  $\tilde{\mathbf{F}}(t)$ . For this, we assume a decomposition of the force vector according to

$$\tilde{\mathbf{F}}(t) = \boldsymbol{\Gamma}\tilde{F}(t), \quad (5.37)$$

with a constant force distribution  $\boldsymbol{\Gamma} \in \mathbb{R}^N$  and a scalar force magnitude  $\tilde{F}(t)$  proportional to the current signal of the electromagnetic coil. This means that all  $N$  force components mapped to the measuring grid have the same temporal waveform, or, in the frequency domain

$$\hat{\mathbf{F}}(\varpi) = \boldsymbol{\Gamma}\hat{F}(\varpi), \quad (5.38)$$

they all share the phase defined by the Fourier transform  $\hat{F}(\varpi) \in \mathbb{C}$ . This assumption holds for the stator measurements at arbitrary angular rotor speeds  $\Omega_R$ . For the rotor measurements, the assumption is violated for angular rotor speeds  $\Omega_R \neq 0$ , because the stator-fixed excitation is rotating in the rotor system with an angular rotation speed  $\Omega_F = -\Omega_R$ , and hence, the force distribution  $\boldsymbol{\Gamma}$  becomes time dependent. With a constant force distribution  $\boldsymbol{\Gamma}$ , we define an averaged reception factor

$$\bar{\mathbf{l}}_m := \mathbf{l}_m^T \boldsymbol{\Gamma}, \quad (5.39)$$



which is assumed to be nonzero. We are free to normalize the left eigenvector  $\mathbf{l}_m$  and for convenience we choose

$$\bar{\mathbf{l}}_m = \mathbf{l}_m^\top \boldsymbol{\Gamma} = \mathbf{l}_m^{*\top} \boldsymbol{\Gamma} = 1. \quad (5.40)$$

With this normalization, we write the products  $\mathbf{l}_m^\top \hat{\mathbf{F}}(\varpi)$  and  $\mathbf{l}_m^{*\top} \hat{\mathbf{F}}(\varpi)$  appearing in (5.36), as

$$\mathbf{l}_m^\top \hat{\mathbf{F}}(\varpi) = \mathbf{l}_m^\top \boldsymbol{\Gamma} \hat{\mathbf{F}}(\varpi) = \bar{\mathbf{l}}_m \hat{\mathbf{F}}(\varpi) = \hat{F}(\varpi), \quad (5.41)$$

$$\mathbf{l}_m^{*\top} \hat{\mathbf{F}}(\varpi) = \mathbf{l}_m^{*\top} \boldsymbol{\Gamma} \hat{\mathbf{F}}(\varpi) = \bar{\mathbf{l}}_m \hat{\mathbf{F}}(\varpi) = \hat{F}(\varpi), \quad (5.42)$$

and define the averaged frequency response function vector  $\bar{\mathbf{H}}(\varpi) \in \mathbb{C}^N$  as

$$\begin{aligned} \bar{\mathbf{H}}(\varpi) &:= \frac{\hat{\mathbf{u}}(\varpi)}{\hat{F}(\varpi)} = \sum_{m=1}^N \left[ \frac{\mathbf{r}_m \mathbf{l}_m^\top \boldsymbol{\Gamma}}{\lambda_m - j\varpi} + \frac{\mathbf{r}_m^* \mathbf{l}_m^{*\top} \boldsymbol{\Gamma}}{\lambda_m^* - j\varpi} \right] \\ &= \sum_{m=1}^N \left[ \frac{\mathbf{r}_m}{\lambda_m - j\varpi} + \frac{\mathbf{r}_m^*}{\lambda_m^* - j\varpi} \right]. \end{aligned} \quad (5.43)$$

We now present an ansatz for the complex right eigenvector  $\mathbf{r}_m$  which describes the right mode shape. Let  $R_{im}$  denote the elements of the right modal matrix  $\mathbf{R}$  specified in (5.13), with the index  $i = 1, \dots, N$  running over all measuring spots and  $m$  indexing the mode. We utilize the rotation symmetry of the test bench design and suggest a product ansatz for the right mode shapes (see Fig. 5.6)

$$R_{(q-1)N_r+p,m} = \Psi_m(r_p) \Phi_m(\varphi_q), \quad p = 1, \dots, N_r, \quad q = 1, \dots, N_\varphi. \quad (5.44)$$

Therein,  $\Psi_m(r_p) \in \mathbb{R}$  specifies the real-valued radial mode shape and  $\Phi_m(\varphi_q) \in \mathbb{C}$  the complex-valued azimuthal mode shape. The index  $i = 1, \dots, N$  is split up into the radial index  $p = 1, \dots, N_r$  and the azimuthal index  $q = 1, \dots, N_\varphi$ . As the radial mode shape  $\Psi_m(r_p)$  is real, all radial points share the same phase. For the azimuthal mode shape we further propose a Fourier ansatz

$$\Phi_m(\varphi_q) = e^{j(-n_m \varphi_q + \vartheta_m)}, \quad q = 1, \dots, N_\varphi, \quad (5.45)$$

with the azimuthal wave number  $n_m \in \mathbb{Z}$ , the rotation angle  $\vartheta_m \in \mathbb{R}$  and the grid angles  $\varphi_q = (q-1)2\pi/N_\varphi$ . With this ansatz for the right

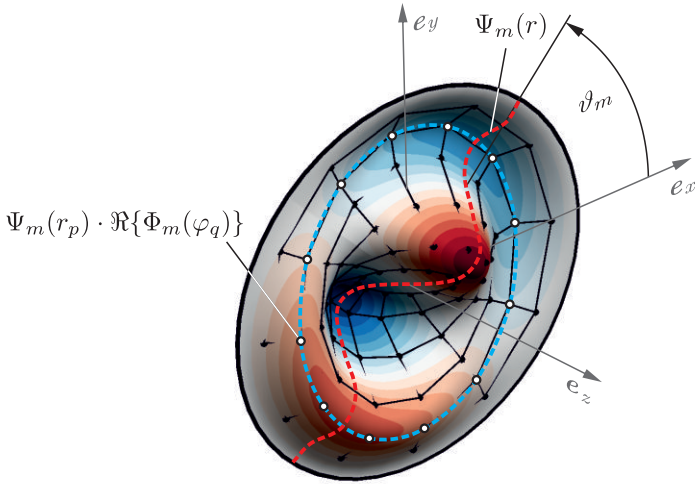


**Fig. 5.6:** Real part of the right mode shape with the product ansatz  $R_{(q-1)N_r+p,m} = \Psi_m(r_p) \Phi_m(\varphi_q) = \Psi_m(r_p) e^{j(-n_m\varphi_q + \vartheta_m)}$ , exemplarily shown for a (1, 1) mode with  $n_m = 1$ .

eigenvector, we write the averaged frequency response function from (5.43) as

$$\begin{aligned}
 \bar{H}_{(q-1)N_r+p}(\varpi) &= \frac{\hat{u}_{(q-1)N_r+p}(\varpi)}{\hat{F}(\varpi)} \quad p = 1, \dots, N_r, \quad q = 1, \dots, N_\varphi \\
 &= \sum_{m=1}^N \left[ \frac{R_{(q-1)N_r+p,m}}{\lambda_m - j\varpi} + \frac{R_{(q-1)N_r+p,m}^*}{\lambda_m^* - j\varpi} \right] \\
 &= \sum_{m=1}^N \left[ \frac{\Psi_m(r_p) \Phi_m(\varphi_q)}{\lambda_m - j\varpi} + \frac{\Psi_m(r_p) \Phi_m^*(\varphi_q)}{\lambda_m^* - j\varpi} \right] \\
 &= \sum_{m=1}^N \Psi_m(r_p) \left[ \frac{e^{j(-n_m\varphi_q + \vartheta_m)}}{(-\delta_m^r + j\omega_m^r) - j\varpi} + \frac{e^{-j(-n_m\varphi_q + \vartheta_m)}}{(-\delta_m^r - j\omega_m^r) - j\varpi} \right], \tag{5.46}
 \end{aligned}$$

where we reintroduced the angular eigenfrequency  $\omega_m^r$  and the damping factor  $\delta_m^r$  from (5.5).

Note that due to the Fourier ansatz (5.45), a single mode  $m$  with azimuthal wave number  $n_m \in \mathbb{Z}$  appears to rotate with an angular frequency  $\Omega_m = \omega_m^r/n_m$ . A standing vibration mode is only formed by a pair of two counter-rotating modes  $m^-$  and  $m^+$  with opposite-signed azimuthal wave numbers  $n_{m^-} = -n_{m^+}$  and equal angular eigenfrequencies  $\omega_{m^-}^r = \omega_{m^+}^r$ . Moreover, it is important to note that the angular eigenfrequency depends on the angular rotation speed of the observer. The relation between the eigenfrequency  ${}_A\omega_m^r$  in system  $A$  and the eigenfrequency  ${}_B\omega_m^r$  in system  $B$  is given by

$${}_B\omega_m^r = {}_A\omega_m^r - n_m\Omega_{AB}, \quad (5.47)$$

where  $\Omega_{AB}$  denotes the angular speed of the  $B$ -system relative to the  $A$ -system. We therefore mark the eigenfrequencies with a preceding subscript indicating the observer system. The damping factor  $\delta_m^r$ , on the other hand, is not affected by a change of observer and we omit the mark. We write the relation between the stator system  $S$  and the rotor system  $R$  explicitly as

$${}_R\omega_m^r = {}_S\omega_m^r - n_m\Omega_R, \quad (5.48)$$

with the rotor angular speed  $\Omega_R$  defining the relative motion  $\Omega_{SR}$ . It follows from (5.47) that we always find an observer system  $M$  where the eigenfrequencies of a mode pair are equal, that is  ${}_M\omega_{m^-}^r = {}_M\omega_{m^+}^r$ .

For each mode  $m$ , we have reduced the number of parameters to  $N_r + 3 = 9$  real variables, namely  $\Psi_m(r_1), \dots, \Psi_m(r_{N_r})$ ,  $\omega_m^r$ ,  $\delta_m^r$  and  $\vartheta_m$ . Additionally, the  $N_r = 6$  variables of the radial mode shape  $\Psi_m(r_p)$  appear linearly in (5.46), which simplifies the parameter fit. To estimate these modal parameters, we measured  $N_r \cdot N_\varphi = 72$  frequency response functions by varying the measuring spot and keeping the excitation fixed.

### 5.2.3 Numerical Implementation

The present section concerns the numerical implementation of the modal parameter estimation. The task is to find modal parameters  $\Psi_m(r_p)$ ,  $\omega_m^r$ ,  $\delta_m^r$  and  $\vartheta_m$  for which the response model (5.46) best fits the measured frequency response functions in the sense of least squares. We used MATLAB for the complete modal-analysis procedure.

First, we transform the measured excitation and response signal into the frequency domain using the fast Fourier algorithm proposed by Cooley and Tukey (1965) and compute the measured frequency response functions.

Fig. 5.7 shows frequency response functions of  $N_r \cdot N_\varphi = 72$  measuring spots acquired on the stator disk for a selected parameter set. Because we measured the vibration velocity instead of the displacement, we work with the mobility  $j\varpi H(\varpi)$  instead of the receptance  $H(\varpi)$  (see Ewins (2000, p. 36) for the terminology). In the frequency response function, we identify the resonance peaks and antiresonance valleys that are important features for the parameter fit.

We employed the following tricks to achieve a robust estimation of the modal parameters:

- We estimate the modal parameters by minimizing the least squares of the error between frequency response function of model and measurement. As the frequency response is a complex function, we split the error up in a real and an imaginary part.
- We separate the linear parameters ( $\Psi_m(r_p)$ ) from the nonlinear parameters ( $\omega_m^r, \delta_m^r, \vartheta_m$ ). In the outer loop, we solve the nonlinear least-squares problem using the MATLAB function `lsqnonlin` with the algorithm by Coleman and Li (1994, 1996). In the inner loop, we solve the linear least-squares problem using the QR algorithm.
- For the initial guess of the nonlinear parameters we used the following data. For the stator analysis at  $\Omega_R = 0 \text{ rad/s}$  the initial guess values are sourced from acoustic finite element simulations. For the rotor analysis and the stator analysis at  $\Omega_R > 0 \text{ rad/s}$  we used already computed results of the stator at lower or equal speeds.
- We do not fit all modes in the measured frequency spectrum at once. Instead, we scan the frequency spectrum in sections from lower to higher frequencies. We used a frequency range width of  $800 \text{ rad/s}$  and only fitted the modes inside this range.
- The frequency response functions of modes outside the frequency range are considered with residual terms. We used the frequency response function of the already computed modes for the residuals of modes below the frequency range. The residuals of modes above the frequency range are approximated by additional terms of the form  $\bar{H}_i^c(\varpi) = \bar{s}_i$ , where  $\bar{c}_i = 1/\bar{s}_i$  denote residual stiffnesses as proposed by (Ewins, 2000, p. 325) and  $i = 1, \dots, N$ .

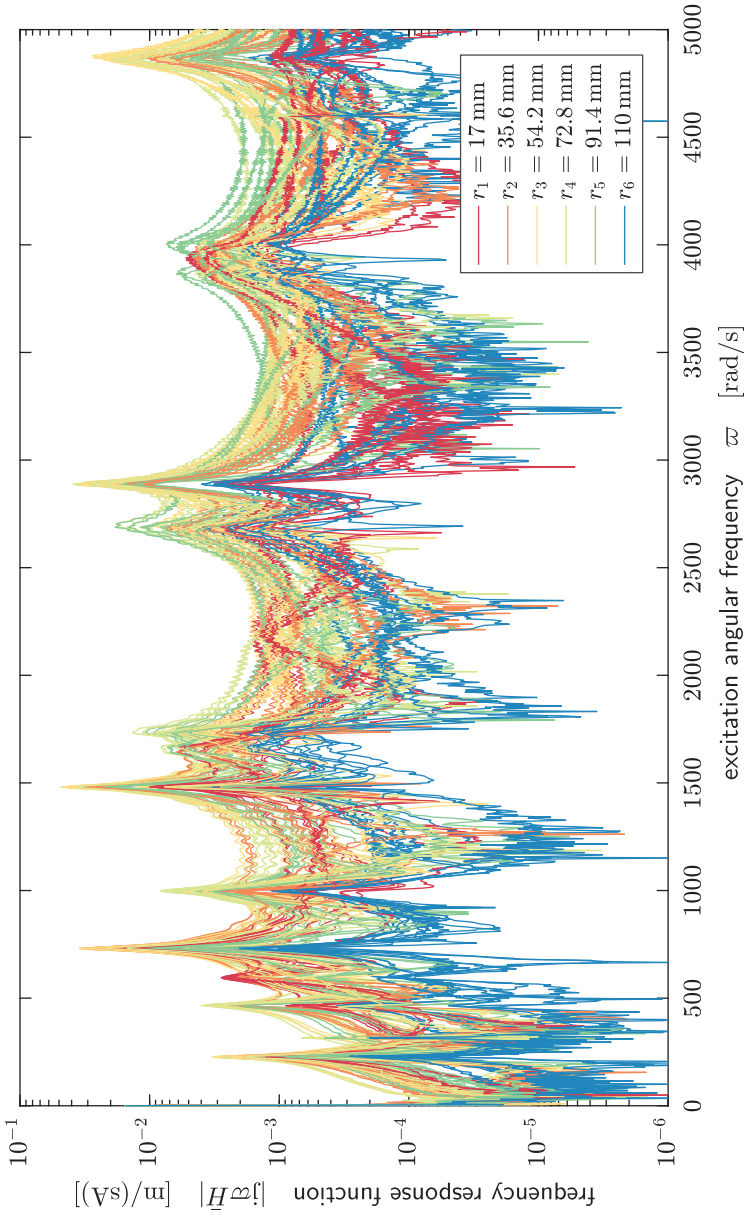


**Fig. 5.7:** Measured frequency response function amplitudes  $|j\varpi\vec{H}|$  at the  $N_r \cdot N_\varphi = 72$  measuring spots on the stator disk for  $h_S = 1.0$  mm,  $h_R = 2.0$  mm,  $g = 2.2$  mm and  $\Omega_R = 0$  rad/s.

- The measurement signals experience a group delay  $\tau$  by passing through the electronic devices. We take the resulting linear phase shift into account by multiplying the frequency response function of the model by  $e^{j\omega\tau}$ .
- For a pair of counter-rotating modes  $m^-$  and  $m^+$  with  $n_{m^-} = -n_{m^+}$ , we couple the damping factors by  $\delta_{m^-}^r = \delta_{m^+}^r$ . At rotor angular speed  $\Omega_R = 0$  rad/s, we also couple the angular eigenfrequencies by  $\omega_{m^-}^r = \omega_{m^+}^r$ .

Fig. 5.8 shows a comparison of the frequency response function of the measurement and the model at different rotor speeds  $\Omega_R$ . It also provides the decomposition of the frequency response function into the individual modes. We see that the resonance peaks of mode pairs, which match at  $\Omega_R = 0$  rad/s, become more and more separated with increasing rotor speed  $\Omega_R$ . This frequency splitting of modes with azimuthal wave number  $n_m \neq 0$  is well described by the model. The next section discusses the experimental results in more detail.

## 5.3 Experimental Results

We now present the experimental results from the modal analysis carried out for the rotor–stator system. In §5.1.5, we defined the set of 224 parameter combinations for the complete series of measurements. It is not reasonable to discuss all results because of the extensive amount of data. For that reason, we show a selection of expressive results, discuss their physical interpretation in detail and provide generalizations. The modal parameters estimated for all measured parameter combinations are tabulated in Appendix B.

### 5.3.1 Eigenfrequency Spectrum and Mode Shapes

In Fig. 5.9 we plot the spectrum of angular eigenfrequencies  $\omega_m^r$  for a selected parameter set and in Fig. 5.10 the corresponding mode shapes. The modes are labeled by  $(n_m, l_m)^{\updownarrow}$  or  $(n_m, l_m)^{\upuparrows}$ , where  $n_m \in \mathbb{Z}$  denotes the azimuthal wave number (or the number of nodal diameters),  $l_m \in \mathbb{N}_0$  is the radial index of the stator (or the number of nodal circles) and the superscripts ‘ $\updownarrow$ ’ and ‘ $\upuparrows$ ’ indicate varicose and sinuous modes, respectively. We

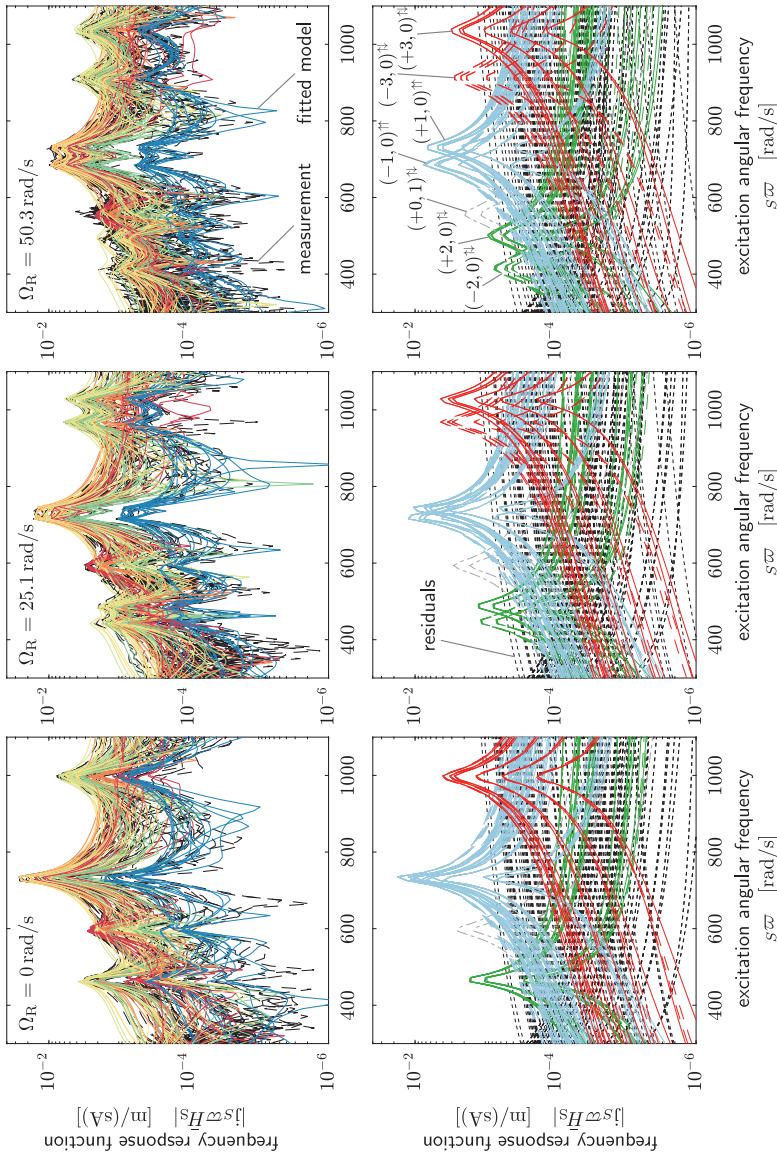


**Fig. 5.8:** Detail of frequency response function amplitudes  $|\hat{j}\varpi\hat{H}|$  of measurement on the stator disk and the fitted model for  $h_S = 1.0$  mm,  $h_R = 2.0$  mm,  $g = 2.2$  mm and varying  $\Omega_R$ . The top row compares the measurement with the fitted model. The bottom row shows the contributions of the fitted modes and residuals.

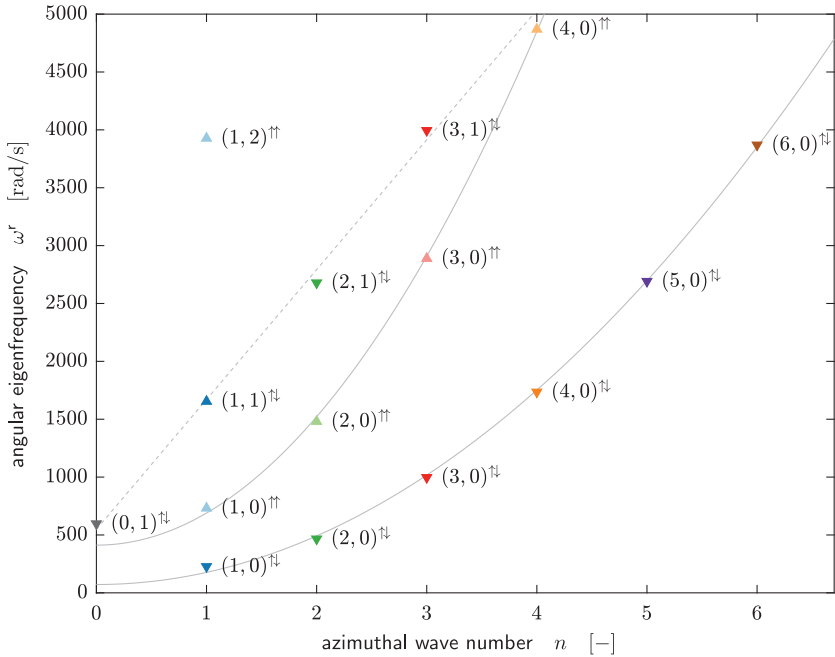


**Fig. 5.9:** Spectrum of angular eigenfrequencies  $\omega^r$  of rotor–stator system for  $h_S = 1.0\text{ mm}$ ,  $h_R = 2.0\text{ mm}$ ,  $g = 2.2\text{ mm}$  and  $\Omega_R = 0\text{ rad/s}$ .

call a mode *varicose* if the motion of the rotor is mainly opposed to the stator and *sinuous* if the motion is mainly synchronous.

From Fig. 5.9, we recognize that the eigenfrequencies can be clustered to branches of equal radial index  $l_m$  and equal type (varicose/sinuous). The branches of the varicose and sinuous modes with radial index  $l_m = 0$  can be well approximated by quadratic functions, whereas the modes with  $l_m = 1$  may be described by a linear relation between eigenfrequency and azimuthal wave number. A comparison of Fig. 5.9 with the frequency spectrum of the semi-analytical model in Fig. 3.3 shows the close resemblance of the behavior—for the varicose modes as well as for the sinuous modes.

Note that in Fig. 5.10 we only visualize the motion of the rotor and the stator, whereas we hide the fluid motion, which indeed contributes to the



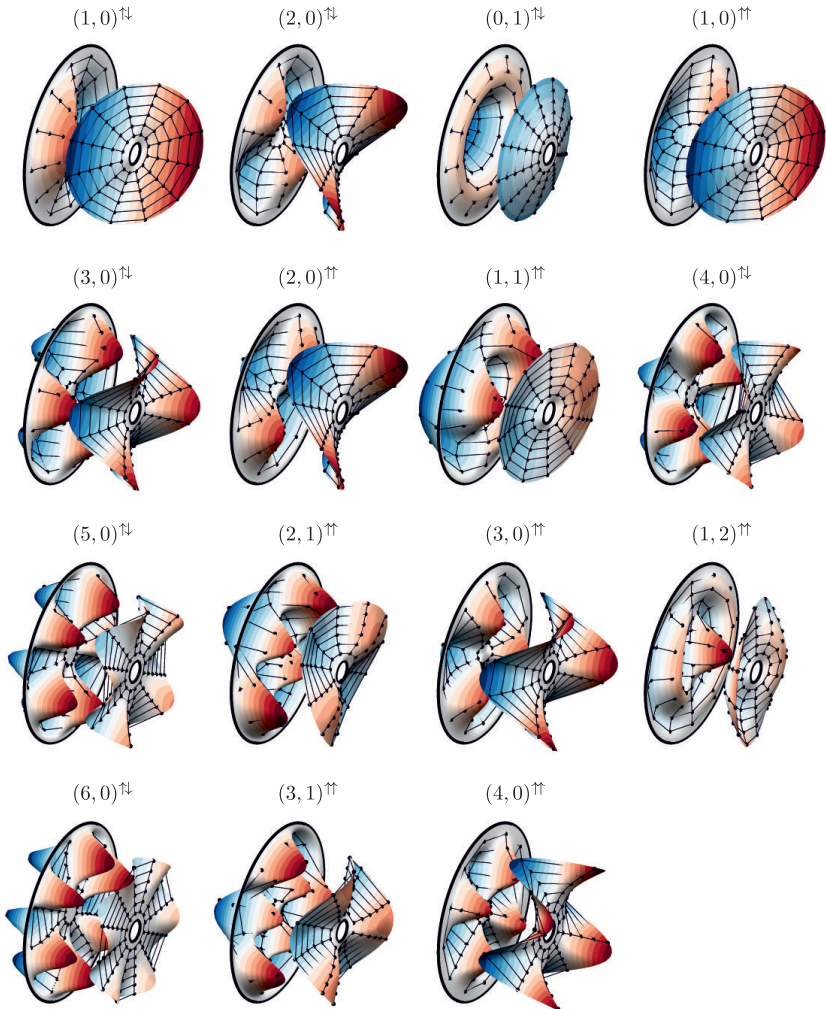


**Fig. 5.10:** Real part of measured right mode shapes of rotor–stator system for  $h_S = 1.0$  mm,  $h_R = 2.0$  mm,  $g = 2.2$  mm and  $\Omega_R = 0$  rad/s. The stator is on the left, the rotor on the right and the spider-web grid indicates the measuring spots.

mode. We can imagine that the fluid motion strongly depends on the mode type. For a varicose mode, where the rotor and the stator are moving in opposite directions, the fluid cavity in between gets strongly squeezed. This leads to large in-plane accelerations of the fluid in the cavity which results in an increased modal mass. For a sinuous mode, on the other hand, the motion of rotor and stator is mainly synchronous and the fluid is only slightly squeezed. The larger modal mass of the varicose mode due to the squeezing is the reason for the lower frequency compared to the sinuous mode (confer varicose and sinuous modes in Fig. 5.9).

The mode shapes in Fig. 5.10 are visualized for one specific parameter set. Nevertheless, these mode shapes are reasonably generic. The major changes can be expressed by the amplitude ratio between rotor and stator defined by

$$\kappa_m := \frac{\max|\Psi_m^R(r)|}{\max|\Psi_m^S(r)|} > 0. \quad (5.49)$$

### 5.3.2 Modal Parameters without Bias Motion

In the present section we discuss the modal parameters for all experiments without bias motion, this is  $\Omega_R = 0 \text{ rad/s}$ . We plot the angular eigenfrequency  $\omega_m^r$ , the damping factor  $\delta_m^r$  and the amplitude ratio  $\kappa_m$  for all geometrical parameter combinations in Figs. 5.11–5.14.

For the presentation of the data we use the color scheme defined in Tab. B.0 of Appendix B. Modes with radial index  $l_m = 0$  are plotted with solid lines and higher order modes with  $l_m > 0$  are plotted with dashed lines. The legend on the right of the plots of Figs. 5.11–5.14 are ordered according to the angular frequency  $\omega^r$ .

#### Angular Eigenfrequency $\omega_m^r$

We observe that the angular eigenfrequencies  $\omega_m^r$  of the varicose  $(*, 0)^{\uparrow\downarrow}$  modes monotonically increase with the gap width  $g$  like a square-root function. In contrast, the eigenfrequencies of the sinuous  $(*, 0)^{\uparrow\uparrow}$  modes only increase up to a gap width of  $g \approx 4 \text{ mm}$  and then remain about constant. Note that the stiffness of the structure is not influenced by a variation of the gap width and the change of the eigenfrequency must therefore be caused by a mass effect. At smaller gap widths, the squeezing effect between rotor and stator becomes more and more dominant, which increases the modal

mass and therefore decreases the eigenfrequency. It seems that for the sinusoidal modes, the fluid gets significantly squeezed only for small gap widths of approximately  $g < 4$  mm, which may be caused by the difference of the radial modes shapes between rotor and stator.

By comparing Fig. 5.11 and Fig. 5.12, where the rotor thickness  $h_R$  varies from 1.0 mm to 1.5 mm, we observe that eigenfrequencies of the varicose  $(*, 0)^{\updownarrow}$  modes increase strongly (approximately 65% per 0.5 mm), whereas the eigenfrequencies of the sinusoidal  $(*, 0)^{\upuparrows}$  modes only increase weakly (approximately 5% per 0.5 mm). This effect gets saturated by a further increase of the rotor thickness  $h_R$  as can be seen in Fig. 5.13. In contrast, a variation of the stator thickness  $h_S$  leads to a slight increase of the eigenfrequencies of the varicose  $(*, 0)^{\updownarrow}$  modes (approximately 5% per 0.5 mm) and a strong increase of the eigenfrequencies of the sinusoidal  $(*, 0)^{\upuparrows}$  modes (approximately 70% per 0.5 mm). This can be seen by comparing Fig. 5.12 with 5.14, where the stator thickness changes from 1.0 mm to 1.5 mm. In summary, we conclude that in the investigated parameter range the eigenfrequencies of the varicose  $(*, 0)^{\updownarrow}$  modes are more sensitive to the rotor thickness  $h_R$  and the eigenfrequencies of the sinusoidal  $(*, 0)^{\upuparrows}$  modes to the stator thickness  $h_S$ .

### Damping Factor $\delta_m^r$

Referring to (5.6), we need to clarify that the damping factor  $\delta_m^r$  is associated to the temporal rate of exponential decay for the system without excitation. If we are interested in a measure for the decay per oscillation, we may introduce the damping ratio defined by

$$D_m := \frac{\delta_m^r}{\omega_m^r}. \quad (5.50)$$

Considering Figs. 5.11–5.14, we notice more variations in the damping factor data compared to the eigenfrequency data. This indicates that the estimation of the damping factor is affected by larger uncertainties.

In general, the damping factor rises with the azimuthal wave number  $|n_m|$ . This is mainly due to the associated eigenfrequency  $\omega_m^r$ , which also rises with the azimuthal wave number, and as a consequence thereof, increases the number of oscillations per time.

We also see that the damping factor drops for small gap widths  $g$  and then levels off. This dependency on the gap width may again be explained

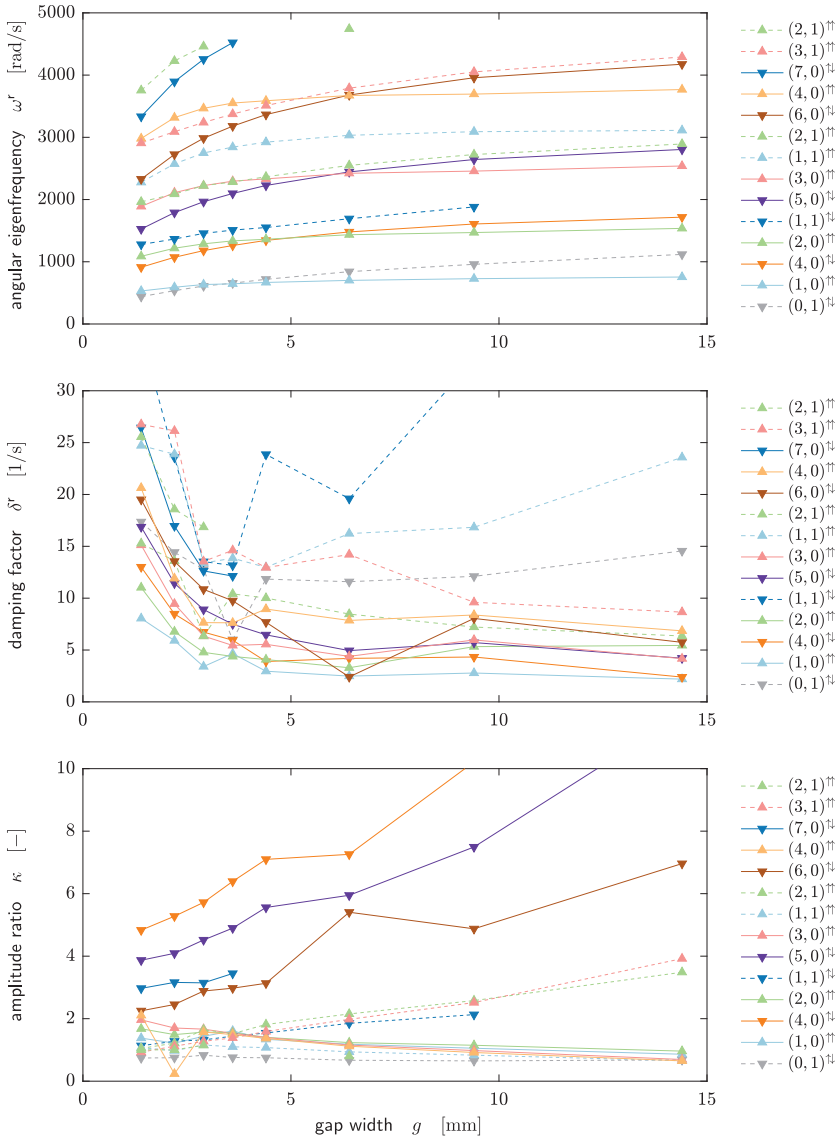


**Fig. 5.11:** Measured angular eigenfrequency  $\omega^r$ , damping factor  $\delta^r$  and amplitude ratio  $\kappa$  as a function of the gap width  $g$  for  $h_S = 1.0$  mm,  $h_R = 1.0$  mm and  $\Omega_R = 0$  rad/s.

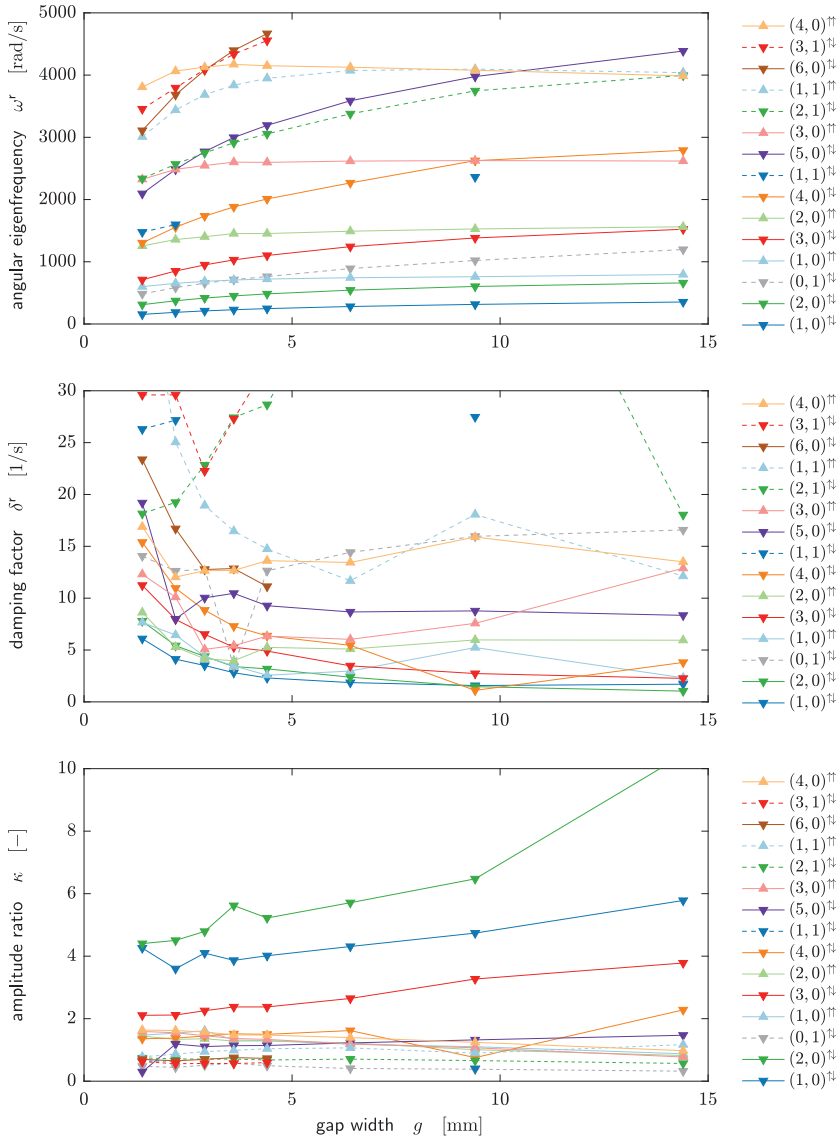


**Fig. 5.12:** Measured angular eigenfrequency  $\omega^r$ , damping factor  $\delta^r$  and amplitude ratio  $\kappa$  as a function of the gap width  $g$  for  $h_S = 1.0$  mm,  $h_R = 1.5$  mm and  $\Omega_R = 0$  rad/s.

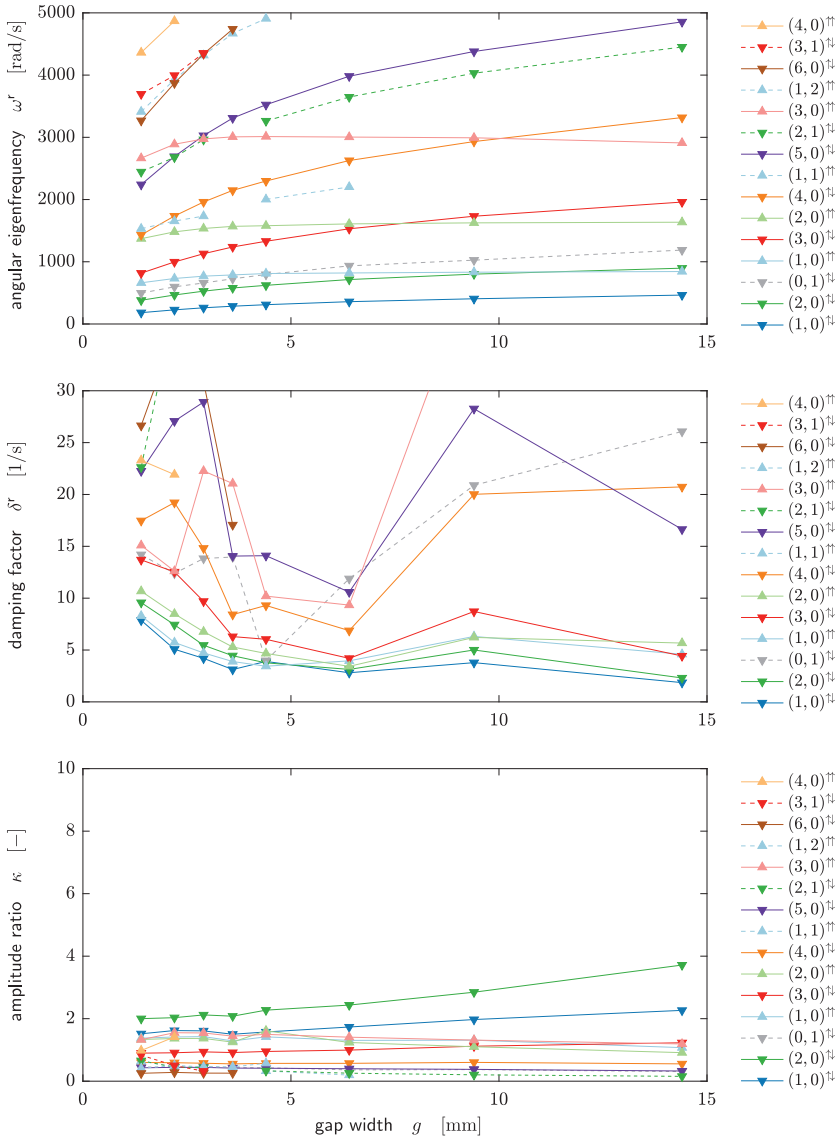


**Fig. 5.13:** Measured angular eigenfrequency  $\omega^r$ , damping factor  $\delta^r$  and amplitude ratio  $\kappa$  as a function of the gap width  $g$  for  $h_S = 1.0$  mm,  $h_R = 2.0$  mm and  $\Omega_R = 0$  rad/s.

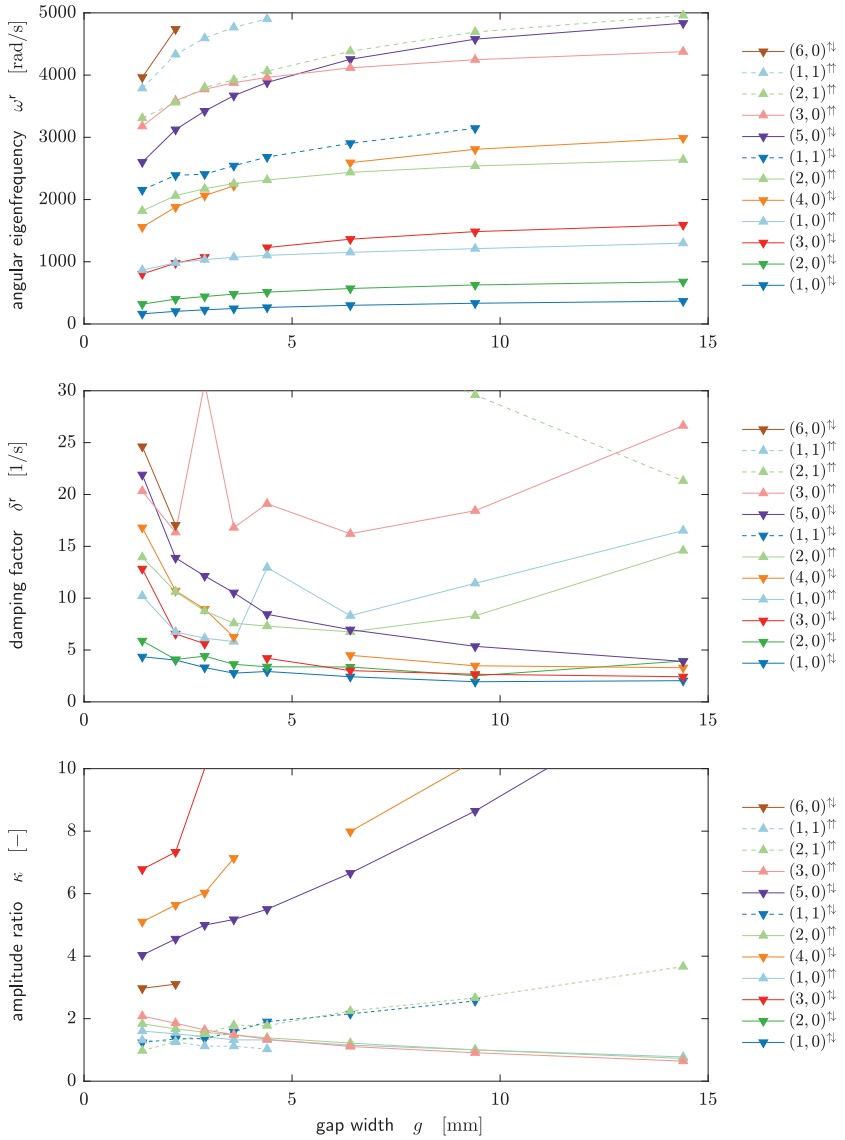


**Fig. 5.14:** Measured angular eigenfrequency  $\omega^r$ , damping factor  $\delta^r$  and amplitude ratio  $\kappa$  as a function of the gap width  $g$  for  $h_S = 1.5$  mm,  $h_R = 1.5$  mm and  $\Omega_R = 0$  rad/s.

by the oscillating squeezing flow between rotor and stator. At smaller gap widths, the in-plane fluid velocity increases, and accordingly, the velocity gradient of the viscous boundary layer too. The larger velocity gradient then raises the viscous dissipation resulting in a larger damping factor, despite the fact that the eigenfrequency also falls with decreasing gap width.

### Amplitude Ratio $\kappa_m$

The amplitude ratio  $\kappa_m$  of the rotor to the stator is defined in (5.49). An amplitude ratio  $\kappa_m > 1$  indicates a mode with dominating rotor vibration and  $\kappa_m < 1$  indicates a mode with dominating stator vibration.

A comparison of Figs. 5.11–5.13 shows a different behaviour of the varicose  $(*, 0)^{\downarrow}$  and sinuous  $(*, 0)^{\uparrow}$  modes. The amplitude ratios of the sinuous  $(*, 0)^{\uparrow}$  modes are nearly unaffected by the azimuthal wave number  $|n_m|$ , especially for gap widths  $g > 4$  mm. The varicose  $(*, 0)^{\downarrow}$  modes, on the other hand, show a strong dependence of the amplitude ratio on the azimuthal wave number. A higher azimuthal wave number  $|n_m|$  generally lowers the amplitude ratio of the varicose modes, except for the  $(1, 0)^{\downarrow}$  and  $(2, 0)^{\downarrow}$  modes, for which the sequence of amplitude ratios are reversed (see Fig. 5.12 and 5.13).

The dependence of the amplitude ratio on the gap width  $g$  is also different for varicose  $(*, 0)^{\downarrow}$  and  $(*, 0)^{\uparrow}$  sinuous modes. Whereas the amplitude ratios of the sinuous modes slightly decline, we observe rising amplitude ratios of the varicose modes for increasing gap widths.

If we compare the amplitude ratios of 5.11 with 5.14, for which the thickness ratios  $h_R/h_S$  are equal, we observe a strong similarity. This provides evidence that the amplitude ratio  $\kappa_m$  is mainly determined by the thickness ratio  $h_R/h_S$ , instead of the individual thickness parameters  $h_R$  and  $h_S$ . With an increasing thickness ratio, the amplitude ratios  $\kappa_m$  of the varicose  $(*, 0)^{\downarrow}$  modes get strongly reduced, whereas the amplitude ratios of the sinuous  $(*, 0)^{\uparrow}$  modes remain nearly constant.

### 5.3.3 Modal Parameters with Bias Motion

We now study the influence of the bias motion on the modal parameters by examining the measurements at angular rotor speeds  $\Omega_R > 0$  rad/s. In Fig. 5.15 we present the angular frequency  ${}_S\omega_m^r$ , the damping factor  $\delta_m^r$



and the amplitude ratio  $\kappa_m$  for a selected parameter set at various angular rotor speeds  $\Omega_R$ .

### Angular Eigenfrequency $\omega_m^r$

Let us first focus on the implications of the angular rotor speed  $\Omega_R$  on the angular eigenfrequency  ${}_S\omega^r$ . Consider Fig. 5.15 and locate a pair of modes  $m^-$  and  $m^+$ , with  $n_{m^-} = -n_{m^+}$ , which have equal eigenfrequencies at  $\Omega_R = 0$  rad/s. We observe that the eigenfrequencies separate for  $\Omega_R > 0$  rad/s when measured in the stator system  $S$ . In the  $S$ -system, the branch with the higher eigenfrequency  ${}_S\omega_{m^+}^r$  is associated with the positive wave number  $n_{m^+} > 0$  and the lower eigenfrequency  ${}_S\omega_{m^-}^r$  with the negative wave number  $n_{m^-} < 0$ . From §5.2.2, we know that the single modes appear to rotate with angular frequency  ${}_S\Omega_m = {}_S\omega_m^r/n_m$ . We therefore denote a mode  $m^+$  as *co-rotating* (rotating in the same direction as the rotor) and  $m^-$  as *counter-rotating* (rotating in the opposite direction as the rotor). The difference

$${}_S\Delta\omega_m^r := {}_S\omega_{m^+}^r - {}_S\omega_{m^-}^r \quad (5.51)$$

is called the *angular frequency split* and plotted in Fig. 5.16 for the selected parameter set. We see that  ${}_S\Delta\omega_m^r$  is approximately proportional to the azimuthal wave number  $|n_m|$  and the angular rotor speed  $\Omega_R$ . In consequence, we do not observe a separation of the eigenfrequency for modes with  $n_m = 0$ .

Note that the eigenfrequencies  $\omega_m^r$ , as well as the reported separation of the eigenfrequencies, depend on the rotation speed of the observer according to relation (5.47). For a given pair of modes, we can therefore always find an observer that does not detect a separation of the eigenfrequencies. The eigenfrequencies in the rotor system  $R$  can be calculated using (5.48). When going from the  $S$  to the  $R$ -system, the eigenfrequencies of a mode pair switch the order. The co-rotating mode  $m^+$  is then associated with the lower eigenfrequency  ${}_R\omega_{m^+}^r$  and the counter-rotating  $m^-$  with the higher eigenfrequency  ${}_R\omega_{m^-}^r$ .

### Damping Factor $\delta_m^r$

Furthermore, we discuss the influence of the angular rotor speed  $\Omega_R$  on the damping factor  $\delta_m^r$ . From Fig. 5.15 we see that some damping factors  $\delta_m^r$

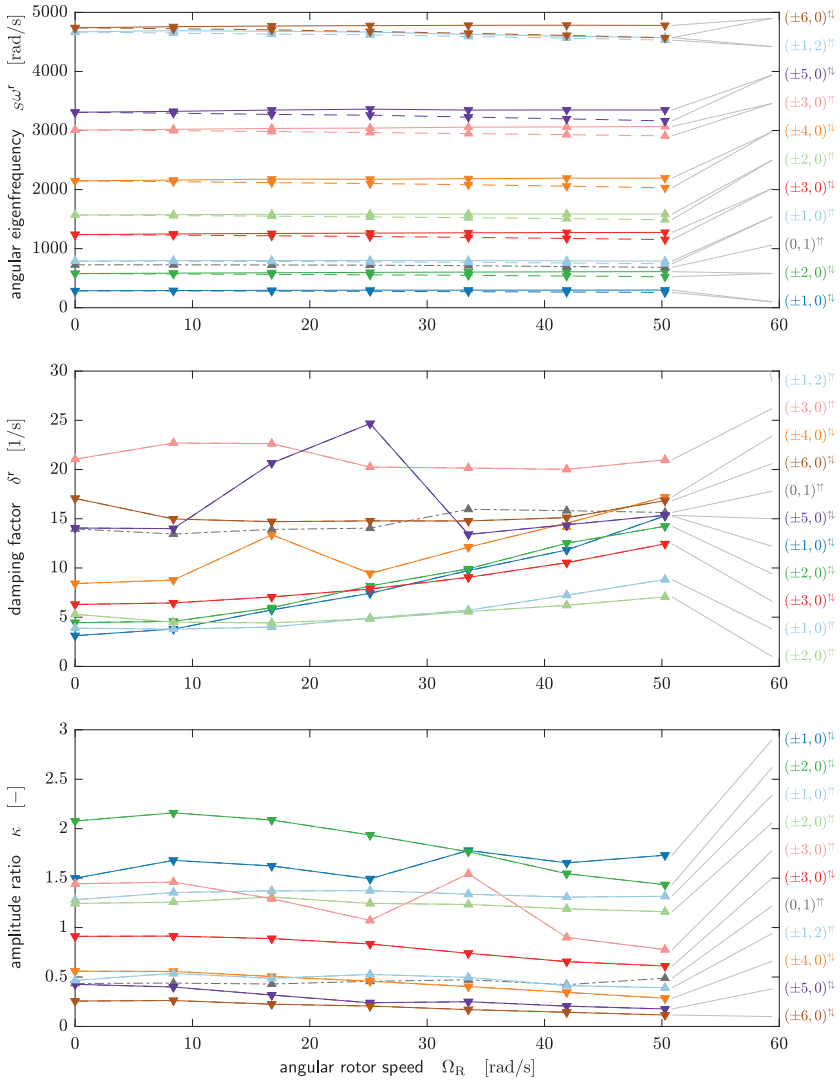


**Fig. 5.15:** Measured angular eigenfrequency  $s\omega^r$ , damping factor  $\delta^r$  and amplitude ratio  $\kappa$  as a function of the angular rotor speed  $\Omega_R$  for  $h_S = 1.0$  mm,  $h_R = 2.0$  mm and  $g = 3.6$  mm. Modes are distinguished by  $n_m > 0$  (solid lines),  $n_m < 0$  (dashed lines) and  $n_m = 0$  (dash-dotted lines).

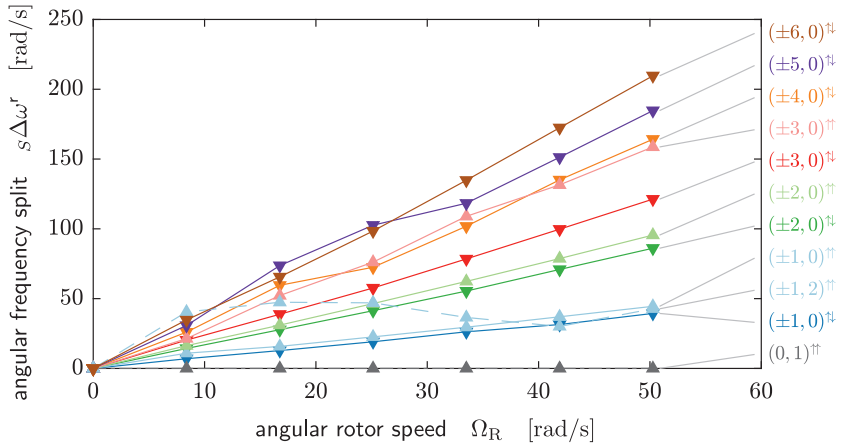


**Fig. 5.16:** Measured angular frequency split  $s\Delta\omega^r$  as a function of the angular rotor speed  $\Omega_R$  for  $h_S = 1.0$  mm,  $h_R = 2.0$  mm and  $g = 3.6$  mm.

fall up to a low point and then increase slightly. The location of the lowest point and its damping factor value seem to depend on the initial damping factor at  $\Omega_R = 0$  rad/s. For larger initial damping values, the lowest point is located at higher angular rotation speeds and has a larger minimum value.

### Amplitude Ratio $\kappa_m$

Finally, we take a look at the angular rotor speed dependency of the amplitude ratio  $\kappa_m$ . In Fig. 5.15 we recognize a slight decline of the amplitude ratio for the vast majority of the modes.



# Finite Element Simulations

# 6

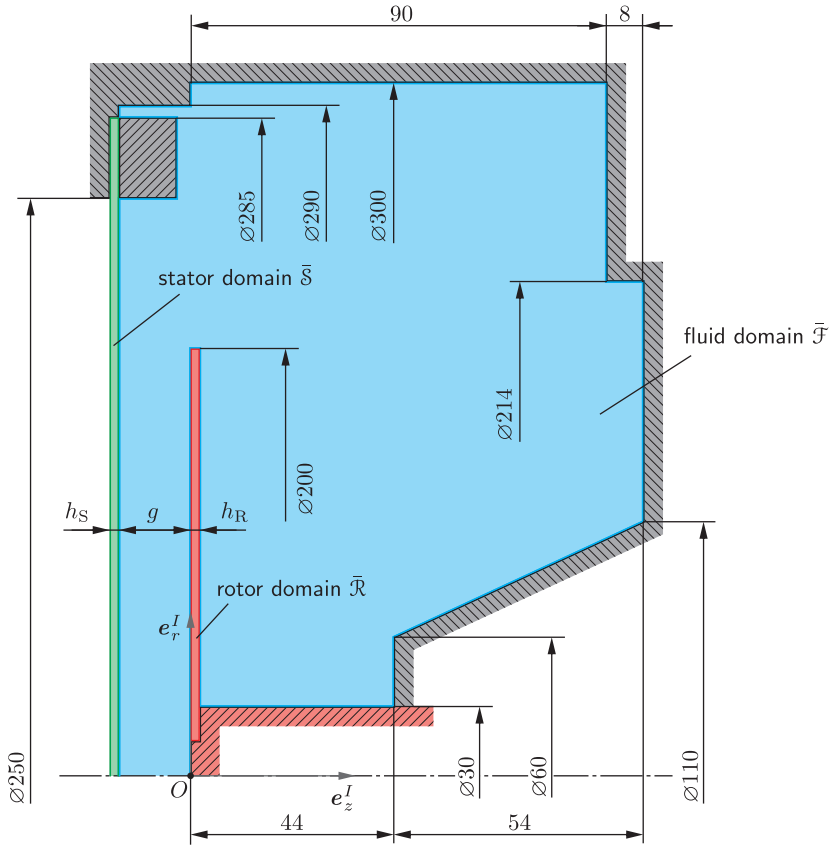
The present chapter covers the numerical modeling of the rotor–stator system coupled by a viscous liquid, which has been experimentally studied in Chapter 5. We use the simulation software COMSOL Multiphysics to compute eigenfrequencies and eigenmodes of the fluid-coupled system with the finite element method. This software allows us to implement user-defined equations in weak variational form, just as we derived them in Chapter 2 by applying the principle of virtual work and power.








We present the simulation model for the test bench described in Chapter 4 and discuss the underlying assumptions. Additionally, we exploit rotation symmetries of the test bench geometry and the vibrational mode shapes to reduce the problem from three to two dimensions. Further, we discuss the implementation in COMSOL Multiphysics with emphasis on the computation of the bias motion and the computational grid. Finally, we present and discuss selected simulation results of the test bench model.

## 6.1 Test Bench Model

### 6.1.1 Model and Assumptions

Fig. 6.1 shows the axisymmetrical geometry of the numerical test bench model. The complete modeling domain is composed of the stator domain  $\bar{S}$ , the rotor domain  $\bar{R}$  and the fluid domain  $\bar{F}$ . These domains are deduced from the nominal geometry of the stator disk, the rotor disk and the fluid cavity, respectively, by omitting non-axisymmetrical features and small-scale details (compare Fig. 6.1 with Fig. 4.2). The gap width  $g$ , the stator thickness  $h_S$  and the rotor thickness  $h_R$  are the geometrical parameters of the model.



- |   |                             |   |   |
|---|-----------------------------|---|---|
|  | $\mathcal{S}$ stator domain |  | $\partial\mathcal{S}^{\text{con}}$ stator-rigid interface             |
|  | $\mathcal{R}$ rotor domain  |  | $\partial\mathcal{R}^{\text{con}}$ rotor-rigid interface              |
|  | $\mathcal{F}$ fluid domain  |  | $\partial\mathcal{F}^{\text{con}}$ fluid-rigid interface              |
|  | static rigid casing         |  | $\partial\mathcal{S}^{\text{amb}}$ stator-ambient interface           |
|  | rotating rigid shaft        |  | $\partial\mathcal{S}^{\text{sym}}$ stator-symmetry interface          |
| $h_S$   | stator thickness            |  | $\partial\mathcal{F}^{\text{sym}}$ fluid-symmetry interface           |
| $h_R$   | rotor thickness             |  | $\partial\mathcal{S} \cap \partial\mathcal{F}$ stator-fluid interface |
| $g$   | gap width                   |  | $\partial\mathcal{R} \cap \partial\mathcal{F}$ rotor-fluid interface  |

**Fig. 6.1:** Geometry of the test bench model with the specification of the domains and interfaces. Dimensions are given in mm.

We refer to §2.1 and model the stator disk  $\mathfrak{S}$  and the rotor disk  $\mathfrak{R}$  as linear elastic solid bodies. For the rotor, we additionally include gyroscopic effects by a rigid-body motion of the reference configuration with angular velocity

$$\mathbf{\Omega} = \Omega_{\text{R}} e_z^I, \quad (6.1)$$

where  $\Omega_{\text{R}}$  denotes the angular rotor speed. As described in §2.2, we model the fluid  $\mathfrak{F}$  as a Newtonian liquid constrained to an incompressible motion.

We decompose the domain boundaries according to their interface conditions. Hence, the stator boundary is subdivided into

$$\partial\mathcal{S} = \partial\mathcal{S}^{\text{con}} \cup \partial\mathcal{S}^{\text{amb}} \cup (\partial\mathcal{S} \cap \partial\mathcal{F}). \quad (6.2)$$

where  $\partial\mathcal{S}^{\text{con}}$  denotes the stator–rigid interface with the displacement constraint to  $\mathbf{u} = \mathbf{0}$ ,  $\partial\mathcal{S}^{\text{amb}}$  refers to the traction-free stator–ambient interface with  $\mathbf{t} = \mathbf{0}$ , and  $\partial\mathcal{S} \cap \partial\mathcal{F}$  indicates the stator–fluid interface with constraint force  $\mathbf{t} = -\boldsymbol{\varphi}$  as traction vector (see §2.3.2). Accordingly, we write

$$\partial\mathcal{R} = \partial\mathcal{R}^{\text{con}} \cup (\partial\mathcal{R} \cap \partial\mathcal{F}) \quad (6.3)$$

for the decomposition of the rotor boundary and

$$\partial\mathcal{F} = \partial\mathcal{F}^{\text{con}} \cup (\partial\mathcal{S} \cap \partial\mathcal{F}) \cup (\partial\mathcal{R} \cap \partial\mathcal{F}), \quad (6.4)$$

for the decomposition of the fluid boundary with the interfaces specified in Fig. 6.1. Note that for three-dimensional domains, we do not include the symmetry interfaces  $\delta\mathcal{S}^{\text{sym}}$  and  $\delta\mathcal{F}^{\text{sym}}$ . We incorporate them later, when we reduce the model from three to two dimensions.

We assume that the vibrations are described by infinitesimal perturbations  $\tilde{\mathbf{q}}$  of the bias motion  $\bar{\mathbf{q}}$  according to §2.1.4. Further, we assume a stationary bias motion  $\bar{\mathbf{q}}$ , or otherwise, an approximation by its time-averaged solution. Additionally, we neglect all external body forces  $\mathbf{B}$  and  $\mathbf{b}$  in the solid and fluid domains, respectively.

## 6.1.2 Perturbation Equations

In the present section, we gather the perturbation equations from Chapter 2 and adapt them to our test bench model. From (2.51), we deduce the

linearized perturbation equation for the stator disk  $\mathfrak{S}$  as

$$\begin{aligned}
 0 = \delta \tilde{W}_{\text{tot}\mathfrak{S}} &= \int_{\tilde{\mathfrak{S}}} -\delta \mathbf{u} \cdot \varrho^s \partial_t^2 \tilde{\mathbf{u}} \, dV \\
 &+ \int_{\tilde{\mathfrak{S}}} -\delta \tilde{\mathbf{E}} : \tilde{\mathbf{S}} \, dV + \int_{\tilde{\mathfrak{S}}} -\delta \tilde{\mathbf{E}} : \bar{\mathbf{S}} \, dV \\
 &+ \int_{\partial \mathfrak{S} \cap \partial \mathcal{F}} -\delta \mathbf{u} \cdot \tilde{\boldsymbol{\varphi}} \, dA \quad \forall \delta \mathbf{u}_{\text{adm}}, \forall t,
 \end{aligned} \tag{6.5}$$

with the perturbation displacement  $\tilde{\mathbf{u}}$ , the virtual displacement  $\delta \mathbf{u}$ , the bias stress  $\bar{\mathbf{S}}$ , the perturbation stress  $\tilde{\mathbf{S}}$ , the bias variation of the Green–Lagrange strain  $\delta \tilde{\mathbf{E}}$ , the perturbation variation of the Green–Lagrange strain  $\delta \tilde{\mathbf{E}}$  and the constraint force  $\tilde{\boldsymbol{\varphi}}$ . Notice that we applied the principle of d’Alembert–Lagrange to eliminate the virtual work contribution of the constraint tractions on the stator–rigid interface  $\partial \mathfrak{S}^{\text{con}}$ . We therefore only allow admissible (virtual) displacement fields which are zero on  $\partial \mathfrak{S}^{\text{con}}$ .

Similarly, we deduce the linearized perturbation equation for the rotor disk  $\mathfrak{R}$  from (2.51) as

$$\begin{aligned}
 0 = \delta \tilde{W}_{\text{tot}\mathfrak{R}} &= \int_{\tilde{\mathfrak{R}}} -\delta \mathbf{u} \cdot \varrho^s \{ \partial_t^2 \tilde{\mathbf{u}} + 2\partial_t (\partial_{\mathbf{X}} \tilde{\mathbf{u}}) \dot{\mathbf{X}} \\
 &+ [(\partial_{\mathbf{X}} \partial_{\mathbf{X}} \tilde{\mathbf{u}}) \dot{\mathbf{X}}] \dot{\mathbf{X}} + (\partial_{\mathbf{X}} \tilde{\mathbf{u}}) \ddot{\mathbf{X}} \} \, dV \\
 &+ \int_{\tilde{\mathfrak{R}}} -\delta \tilde{\mathbf{E}} : \tilde{\mathbf{S}} \, dV + \int_{\tilde{\mathfrak{R}}} -\delta \tilde{\mathbf{E}} : \bar{\mathbf{S}} \, dV \\
 &+ \int_{\partial \mathfrak{R} \cap \partial \mathcal{F}} -\delta \mathbf{u} \cdot \tilde{\boldsymbol{\varphi}} \, dA \quad \forall \delta \mathbf{u}_{\text{adm}}, \forall t,
 \end{aligned} \tag{6.6}$$

where we retained the acceleration terms arising from the motion of the rotor reference configuration. Combining (2.6) and (6.1) with  $P = O$  and  $\mathbf{V}_O = \mathbf{A}_O = \mathbf{0}$  yields the specific velocity and acceleration fields of the reference configuration

$$\dot{\mathbf{X}} = \boldsymbol{\Omega} \times \mathbf{X}, \quad \ddot{\mathbf{X}} = \boldsymbol{\Omega} \times (\boldsymbol{\Omega} \times \mathbf{X}). \tag{6.7}$$

Again, we eliminated the constraint tractions on the rotor–rigid interface  $\partial \mathfrak{R}^{\text{con}}$  by applying the principle of d’Alembert–Lagrange.



From (2.99) we find the linearized perturbation equation for the fluid  $\mathfrak{F}$  as

$$\begin{aligned}
 0 = \delta \tilde{P}_{\text{tot}\mathfrak{F}} &= \int_{\mathfrak{F}} -\underline{\delta}\mathbf{v} \cdot \varrho^f [\partial_t \tilde{\mathbf{v}} + (\partial_x \tilde{\mathbf{v}}) \tilde{\mathbf{v}} + (\partial_x \tilde{\mathbf{v}}) \tilde{\mathbf{v}}] dV \\
 &+ \int_{\mathfrak{F}} -\underline{\delta}\mathbf{d} : (2\mu^f \tilde{\mathbf{d}} - \tilde{p}\mathbf{I}) dV \\
 &+ \int_{\partial\mathcal{S}\cap\partial\mathfrak{F}} \underline{\delta}\mathbf{v} \cdot \tilde{\boldsymbol{\varphi}} dA + \int_{\partial\mathcal{R}\cap\partial\mathfrak{F}} \underline{\delta}\mathbf{v} \cdot \tilde{\boldsymbol{\varphi}} dA \quad \forall \underline{\delta}\mathbf{v}_{\text{adm}}, \forall t,
 \end{aligned} \tag{6.8}$$

where  $\tilde{\mathbf{v}}$  denotes the perturbation velocity,  $\tilde{\mathbf{v}}$  the bias velocity,  $\underline{\delta}\mathbf{v}$  the virtual velocity,  $\tilde{\mathbf{d}}$  the perturbation strain rate,  $\underline{\delta}\mathbf{d}$  the variation of the strain rate and  $\tilde{p}$  the perturbation pressure. The constraint tractions on the fluid–rigid interface  $\partial\mathcal{P}^{\text{con}}$  are eliminated using the principle of Jourdain. Additionally, we enforce a divergence-free velocity field by the incompressibility constraint (2.85), that is,

$$0 = \delta \tilde{\Pi}^p = \int_{\mathfrak{F}} -\delta p (\tilde{\mathbf{I}} : \mathbf{I}) dV \quad \forall \delta p, \forall t, \tag{6.9}$$

where  $\delta p$  denotes the virtual pressure.

Finally, we state the kinematic coupling condition on the rotor–fluid interface  $\partial\mathcal{R} \cap \partial\mathfrak{F}$  and on the stator–fluid interface  $\partial\mathcal{S} \cap \partial\mathfrak{F}$ . The linearized constraint deduced from (2.115) then reads

$$\begin{aligned}
 0 = \delta \tilde{\Pi}^\mu &= \int_{\partial\mathcal{R}\cap\partial\mathfrak{F}} \delta\boldsymbol{\mu} \cdot \{ \partial_t \tilde{\mathbf{u}}^s + (\partial_X \tilde{\mathbf{u}}^s) \dot{\mathbf{X}}^s - (\partial_x \tilde{\mathbf{v}}^f) \tilde{\mathbf{u}}^s - \tilde{\mathbf{v}}^f \} dA \\
 &+ \int_{\partial\mathcal{S}\cap\partial\mathfrak{F}} \delta\boldsymbol{\mu} \cdot \{ \partial_t \tilde{\mathbf{u}}^s - (\partial_x \tilde{\mathbf{v}}^f) \tilde{\mathbf{u}}^s - \tilde{\mathbf{v}}^f \} dA \quad \forall \delta\boldsymbol{\mu}, \forall t,
 \end{aligned} \tag{6.10}$$

where  $\delta\boldsymbol{\mu}$  is the virtual traction vector. Note the superscripts 's' and 'f' to distinguish solid and fluid variables, respectively.

Equations (6.5)–(6.10) fully describe the dynamics of linear perturbations superposed to a bias motion. We can combine them into one single scalar equation in variational form

$$\boxed{0 = \delta \tilde{W}_{\text{tot}\mathfrak{S}} + \delta \tilde{W}_{\text{tot}\mathfrak{R}} + \tau (\delta \tilde{P}_{\text{tot}\mathfrak{F}} + \delta \tilde{\Pi}^p + \delta \tilde{\Pi}^\mu) \quad \forall \delta \mathbf{u}_{\text{adm}}, \forall \underline{\delta} \mathbf{v}_{\text{adm}}, \forall \delta \boldsymbol{\mu}, \forall \delta p, \forall t} \tag{6.11}$$

where the time constant  $\tau$  may be used for a proper scaling.

### 6.1.3 Cylindrical Coordinates and Rotational Symmetry

Notice that the governing equations of the previous section are all written in a coordinate-free tensor form. To evaluate the expressions, we need to introduce a coordinate system appropriate to the given geometry. A natural choice for our axisymmetrical model is a parameterization with cylindrical coordinates  $(r, \varphi, z)$ , where  $r$  refers to the radial coordinate,  $\varphi$  to the azimuthal coordinate and  $z$  to the axial coordinate. Odgen (1984, pp. 1–72) presents a comprehensible introduction to tensor analysis with a focus on the differentiation in curvilinear coordinates. In §A.2 we summarize the necessary ingredients for our situation and evaluate the tensors given in (6.5)–(6.10) using cylindrical coordinates.

We now simplify (6.11) by taking advantage of rotational symmetries. Recall that all terms in (6.11) are integrals of a duality pairing (virtual work, virtual power) between elements of the primal space (virtual displacements, virtual velocities) and the dual space (forces, tractions, stresses). For simplicity, we write  $\delta\tilde{w}$  for the duality pairing,  $\delta u$  for the primal variable and  $\check{F}$  for the dual variable throughout the remaining part of this section. We apply a Fourier ansatz in azimuthal direction for the primal and dual variables according to

$$\delta u(r, \varphi, z) = \Re\{\delta\check{u}(r, z) e^{-jn\varphi}\}, \quad (6.12a)$$

$$\check{F}(r, \varphi, z, t) = \Re\{\check{F}(r, z, t) e^{-jn\varphi}\}, \quad (6.12b)$$

where  $n \in \mathbb{Z}$  denotes the azimuthal wave number. The complex variables  $\delta\check{u} \in \mathbb{C}$  and  $\check{F} \in \mathbb{C}$  specify the azimuthal Fourier coefficients of  $\delta u$  and  $\check{F}$ , respectively. Thus, we can write the duality pairing as

$$\begin{aligned} \delta\tilde{w} &= \delta u(r, \varphi, z) \cdot \check{F}(r, \varphi, z, t) \\ &= \Re\{\delta\check{u}(r, z) e^{-jn\varphi}\} \cdot \Re\{\check{F}(r, z, t) e^{-jn\varphi}\} \\ &= \Re\{|\delta\check{u}| e^{j(\arg \delta\check{u} - n\varphi)}\} \cdot \Re\{|\check{F}| e^{j(\arg \check{F} - n\varphi)}\} \\ &= |\delta\check{u}| |\check{F}| \cos(\arg \delta\check{u} - n\varphi) \cos(\arg \check{F} - n\varphi) \\ &= \frac{1}{2} |\delta\check{u}| |\check{F}| [\cos(\arg \delta\check{u} - \arg \check{F}) + \cos(\arg \delta\check{u} + \arg \check{F} - 2n\varphi)]. \end{aligned} \quad (6.13)$$

Note that the integrals in (6.11) are either volume integrals over a three-dimensional domain, here denoted as  $\mathcal{G}^3$ , or surface integrals over its two-dimensional boundary, here denoted as  $\partial(\mathcal{G}^3)$ . Accordingly, the virtual work

integrals become

$$\int_{\mathcal{G}^3} \delta \tilde{w} \underbrace{r \, d\varphi \, dr \, dz}_{dV} = \int_{\mathcal{G}^2} \left( \int_0^{2\pi} \delta \tilde{W} \, d\varphi \right) r \, dr \, dz, \quad (6.14a)$$

$$\int_{\partial(\mathcal{G}^3)} \delta \tilde{w} \underbrace{r \, d\varphi \, ds}_{dA} = \int_{\partial(\mathcal{G}^2)} \left( \int_0^{2\pi} \delta \tilde{W} \, d\varphi \right) r \, ds, \quad (6.14b)$$

where  $ds := \sqrt{dr^2 + dz^2}$  is an infinitesimal line element. The cyclic virtual work integral in the bracket appears in the volume integral as well as the surface integral. We substitute the duality pairing from (6.13) to evaluate this integral for  $n \neq 0$  as

$$\begin{aligned} \int_0^{2\pi} \delta \tilde{w} \, d\varphi &= \int_0^{2\pi} \delta u \cdot \check{F} \, d\varphi \\ &= \frac{1}{2} |\delta \check{u}| |\check{F}| \int_0^{2\pi} [\cos(\arg \delta \check{u} - \arg \check{F}) \\ &\quad + \cos(\arg \delta \check{u} + \arg \check{F} - 2n\varphi)] \, d\varphi \\ &= \frac{1}{2} |\delta \check{u}| |\check{F}| \left[ \cos(\arg \delta \check{u} - \arg \check{F}) \varphi \right. \\ &\quad \left. - \frac{1}{2n} \sin(\arg \delta \check{u} + \arg \check{F} - 2n\varphi) \right]_0^{2\pi} \\ &= \pi |\delta \check{u}| |\check{F}| \cos(\arg \delta \check{u} - \arg \check{F}) \\ &= \pi \underbrace{\frac{\delta \check{u}^* \cdot \check{F} + \delta \check{u} \cdot \check{F}^*}{2}}_{=: \langle \delta \check{u}, \check{F} \rangle}. \end{aligned} \quad (6.15)$$

The term in (6.13) oscillating with  $\varphi$  does not contribute to the integral over a complete revolution. We abbreviate the relevant expression by  $\langle \delta \check{u}, \check{F} \rangle$ , which measures the phase angle between  $\delta \check{u}$  and  $\check{F}$ .

With (6.15), we reduced the dimension of the integrals (6.14) by one. Hence, the volume integral over  $\mathcal{G}^3$  is replaced by an area integral over the cross section  $\mathcal{G}^2$  and the surface integral over  $\partial(\mathcal{G}^3)$  is replaced by a line integral along the contour  $\partial(\mathcal{G}^2)$ . By doing this, we need to incorporate additional symmetry boundary conditions at the centerline  $r = 0$ . Batchelor

**Tab. 6.1:** Symmetry boundary conditions according to Gloor (2014, p. 10) for the velocity  $\check{v}$ , the pressure  $\check{p}$  and the interface traction  $\check{\varphi}$  at the centerline  $r = 0$ .

	$n = 0$	$n = \pm 1$	$ n  \geq 2$
(i)	$0 = \check{v}_r$	$0 = \check{v}_r \mp j\check{v}_\varphi$	$0 = \check{v}_r$
(ii)	$0 = \check{v}_\varphi$	$0 = \partial_r \check{v}_r$	$0 = \check{v}_\varphi$
(iii)	$0 = \partial_r \check{v}_z$	$0 = \check{v}_z$	$0 = \check{v}_z$
(iv)	$0 = \partial_r \check{p}$	$0 = \check{p}$	$0 = \check{p}$
(v)	$0 = \check{\varphi}_r$	$0 = \check{\varphi}_r \mp j\check{\varphi}_\varphi$	$0 = \check{\varphi}_r$
(vi)	$0 = \check{\varphi}_\varphi$	$0 = \partial_r \check{\varphi}_r$	$0 = \check{\varphi}_\varphi$
(vii)	$0 = \partial_r \check{\varphi}_z$	$0 = \check{\varphi}_z$	$0 = \check{\varphi}_z$

and Gill (1962) initially derived the boundary conditions based on geometric reasoning and Khorrami et al. (1989) have provided its formalized form. In Tab. 6.1 we list the conditions for the velocity  $\check{v}$ , the pressure  $\check{p}$  and the interface traction  $\check{\varphi}$  applied to the interfaces  $\partial\mathcal{S}^{\text{sym}}$  and  $\partial\mathcal{F}^{\text{sym}}$  (confer Fig. 6.1). The same conditions were also successfully applied by Müller (2007, p. 26) and Gloor (2014, p. 10) to investigate the stability of swirling jet flows.

### 6.1.4 Modal Ansatz

The perturbation equations of §6.1.2 are still explicitly depending on time. In accordance with the experimental modal analysis of §5.2, we apply the modal ansatz

$$\begin{aligned}
 \tilde{q}_i(r, \varphi, z, t) &= \Re\left\{ \underbrace{\hat{q}_i(r, z)}_{\check{q}_i(r, z, t)} e^{\lambda t} e^{-jn\varphi} \right\} \quad q_i \in u_r, u_\varphi, u_z, v_r, v_\varphi, v_z, p, \dots \\
 &= \Re\left\{ \hat{q}_i(r, z) e^{-\delta^* t} e^{j(\omega^* t - n\varphi)} \right\}
 \end{aligned} \tag{6.16}$$

to all cylindrical components  $q_i$  of the perturbation variables appearing in (6.11). If we now select an azimuthal wave number  $n \in \mathbb{Z}$  and apply the ansatz (6.16), then (6.11) states an eigenvalue problem with eigen-solutions  $(\lambda, \hat{q}_i(r, z))$ , where  $\lambda \in \mathbb{C}$  refers to the complex eigenvalue and

$\hat{q}_i(r, z)$  to the complex eigenfunctions. Identically to (5.5), we can express the eigenvalue as  $\lambda = -\delta^r + j\omega^r$ , with the damping factor  $\delta^r$  and the angular eigenfrequency  $\omega^r$ . From (6.16), we see that the modes are exponentially decaying with  $e^{-\delta^r t}$  and that they rotate in azimuthal direction with angular frequency  $\Omega = \omega^r/n$ .

## 6.2 Implementation in COMSOL Multiphysics

In the present section, we briefly discuss some aspects regarding the finite element implementation of the test bench model described in §6.1. We used COMSOL 5.2a (build 152) for all simulations and refer to COMSOL (2016a,b) for its documentation. COMSOL Multiphysics takes advantage of the intrinsic modularity of the finite element approach. Consistently, it separates and recombines the key ingredients, which are basically: definition of the physics in weak variational form, mesh generation, definition of basis functions, numerical integration using quadratures, constraint handling either by elimination or by Lagrange multipliers, assembly of equations, numerical solution of equations, and post-processing. Especially the capability to introduce user-defined physics directly in weak form differentiates COMSOL from other finite element codes, where the physics is either hard coded or can only be altered by low-level user subroutines.

In the following, we are concerned with the specific implementation of the test bench model. The simulation is subdivided into the three consecutive solution steps which we explain in more detail in the subsequent sections:

1. **fluid bias motion** (stationary analysis)
2. **solid bias motion** (stationary analysis)
3. **perturbation motions of solid–fluid system** (eigenvalue analysis)

The two initial simulation steps are stationary and define the linearization point for the eigenvalue analysis in the third step. By the separation of the stationary steps 1 and 2, we presume that the fluid bias motion is not influenced by the small deformations of the solid bias motion.

### 6.2.1 Fluid Bias Motion

In the first simulation step, we solve for the bias fluid motion in the domain  $\mathcal{F}$ , about which we linearize the perturbation equations of the fluid.

**Tab. 6.2:** Material properties for the fluid domain  $\bar{\mathcal{F}}$  and the solid domains  $\bar{\mathcal{S}}$  and  $\bar{\mathcal{R}}$ .

domain	parameter	variable	value	
$\bar{\mathcal{F}}$	mass density	$\varrho^f$	998.206 kg/m <sup>3</sup>	} water
$\mathcal{F}$	1st viscosity	$\mu^f$	1.0016 mPa · s	
$\bar{\mathcal{S}}, \bar{\mathcal{R}}$	mass density	$\varrho^s$	7850 kg/m <sup>3</sup>	} steel 1.4034
$\mathcal{S}, \mathcal{R}$	Young's modulus	$E$	210 GPa	
$\mathcal{S}, \mathcal{R}$	Poisson's ratio	$\nu$	0.3	

For this, we use the *turbulent flow* interface of COMSOL's *CFD Module* and model the fluid with the *Reynolds averaged Navier–Stokes equations* (RANS) together with the *k-ε turbulence model* (COMSOL, 2016c). Hence, the model does not resolve the temporal and spatial turbulent fluctuations in the fluid but, in return, calculates the stationary, time-averaged flow. In the domain  $\bar{\mathcal{F}}$ , we solve for the bias velocity  $\bar{\mathbf{v}}$  and the bias pressure  $\bar{p}$ . On the interfaces  $\partial\bar{\mathcal{S}} \cap \partial\mathcal{F}$  and  $\partial\bar{\mathcal{R}} \cap \partial\mathcal{F}$ , we also solve for the bias traction vector  $\bar{\mathbf{t}} = \bar{\boldsymbol{\varphi}}$ . The axisymmetrical model is defined in the  $(\mathbf{e}_r, \mathbf{e}_z)$ -plane, but we allow for vector components in the azimuthal  $\mathbf{e}_\varphi$ -direction by activating *swirl flow*.

We make use of *wall functions* to apply the no-slip boundary condition at the walls. These wall functions approximate the thin boundary layer at the wall without the need to resolve it with finite elements. At the boundaries, where the fluid is in contact with the rotor (rotor disk and rotor shaft), we set the *sliding wall* condition and additionally specify the tangential velocity component as

$$\bar{V}_\varphi = r\Omega_R, \quad (6.17)$$

where  $\Omega_R$  denotes the angular speed of the rotor.

The material properties of the water are set according to Tab. 6.2. These values are derived from the formulations of the IAPWS (2007, 2008) using the reference temperature  $T_0 = 293.15$  K and pressure  $p_0 = 101.4$  kPa.

We use linear shape functions for both the velocity field and the pressure field when discretizing the fluid domain with quadrilateral elements. To enforce convergence of the non-linear equations, we solve them in an *auxiliary sweep* by incrementally increase the angular rotor speed  $\Omega_R$ .

## 6.2.2 Solid Bias Motion

The second simulation step solves for the bias solid motion in the domains  $\bar{\mathcal{S}}$  and  $\bar{\mathcal{R}}$ , about which the perturbation equations for the solid are linearized. We use COMSOL's general *weak form PDE* interface to solve (2.31) for the bias motion  $\bar{\mathbf{u}}$ , which is, in the present stationary case, simply a static deformation. The major quantity that enters the perturbation equations is the bias stress  $\bar{\mathbf{S}}$ , which enables the stress stiffening effect. As boundary conditions, we apply the surface traction  $\bar{\mathbf{T}} = -\bar{\varphi}$  computed in the previous simulation step and constrain the displacements at  $\partial\mathcal{S}^{\text{con}}$  and  $\partial\mathcal{R}^{\text{con}}$  to  $\bar{\mathbf{u}} = \mathbf{0}$ . We include centrifugal effects in the rotor domain  $\bar{\mathcal{R}}$  using the acceleration terms (2.10) evaluated with (6.7) and (6.1). The material properties for the steel disks are provided in Tab. 6.2. We discretize the displacement field using quadrilateral *nodal serendipity* elements with shape functions of quadratic order.

## 6.2.3 Perturbation Motions of Solid–Fluid System

The third simulation step solves the eigenvalue problem for the perturbation equation (6.11). Here, we apply the monolithic approach, where the equations for the solids  $\mathcal{S}$  and  $\mathcal{R}$ , the fluid  $\mathcal{F}$  and their interaction are processed at once. The linearized equations (6.11) with the contributions defined in (6.5)–(6.10) are entered in COMSOL's *weak form PDE* interface. As linearization point, we take the solutions of the bias motion of the preceding simulation steps.

We work with the reduced two-dimensional model and therefore employ the azimuthal ansatz (6.12) as well as the symmetry boundary conditions defined in Tab. 6.1. This implies that the eigenvalue problem of the two-dimensional model becomes dependent on the azimuthal wave number  $n$ , and consequently, the eigenvalue problem can not be solved for all modes at once. Instead, we solve successively for each individual mode and thereby also adapt the mesh to the viscous boundary layer. For more details about the computational grid we refer to the next section.

We discretize the displacement field  $\hat{\mathbf{u}}$  in the solid domains  $\bar{\mathcal{S}}$  and  $\bar{\mathcal{R}}$  using quadrilateral *nodal serendipity* elements with shape functions of quadratic order. In the fluid domain  $\bar{\mathcal{F}}$ , we apply quadrilateral *Lagrange* elements, which are of quadratic order for the velocity field  $\hat{\mathbf{v}}$  and of linear order for the pressure field  $\hat{p}$ .

## 6.2.4 Computational Grid

In the present section, we discuss some aspects of the computational grid generation. We saw in the previous sections that we exclusively use quadrilateral elements for discretization. These elements are accurate, but it is difficult to generate a proper mesh, particularly in an automatic way.

That is why we apply the block grid technique to define a structured mesh of quadrilateral elements. This means that we manually subdivide the computational domain  $\bar{\mathcal{S}} \cap \bar{\mathcal{R}} \cap \bar{\mathcal{F}}$  into quadrilateral blocks, like depicted in Fig. 6.2(a). Each of these blocks can then be meshed with quadrilateral elements using simple direct methods. Indeed, this technique is laborious, but it is also robust and computationally efficient, allows to explicitly specify the mesh density and hence produces high-quality meshes.

In general, we choose the element size according to the gradient of the field variables. In regions with large gradients we define a finer grid than in regions with small gradients. Since we do not know the solution beforehand, we apply physical intuition for the initial meshing. Once, a solution is calculated, the mesh quality is improved by iterative refinement and coarsening.

We discretize the stator disk  $\bar{\mathcal{S}}$  and the rotor disk  $\bar{\mathcal{R}}$  with eight elements equally spaced over the thickness. In the fluid domain  $\mathcal{F}$  we set the default element size to 1.5 mm, which applies to inner regions away from solid boundaries. Special care is required for the mesh at the vibrating fluid–solid interfaces  $\partial\mathcal{S} \cap \partial\mathcal{F}$  and  $\partial\mathcal{R} \cap \partial\mathcal{F}$ . In the fluid’s near-wall region, we expect the formation of a viscous boundary layer due to the relative perturbation motion of solid and fluid. This situation is related to Stokes’ second problem of an infinite plane boundary oscillating at frequency  $\omega^r$ , where an exponentially decaying boundary layer is formed. According to White (2005, pp. 130), the Stokes boundary layer has an approximate thickness of

$$\delta^f = 6.5 \sqrt{\frac{\mu^f}{\omega^r \varrho^f}}, \quad (6.18)$$

and therefore depends on the frequency  $\omega^r$ , the viscosity  $\mu^f$  and the density  $\varrho^f$ . For water it takes the values 292  $\mu\text{m}$  at 500 rad/s and 92  $\mu\text{m}$  at 5000 rad/s. Fig. 6.2(b) shows a detail of the blocking at the near wall regions. To resolve the Stokes layer, we define boundary layer blocks of thickness  $\delta^f$ , which are discretized with fifteen elements geometrically spaced



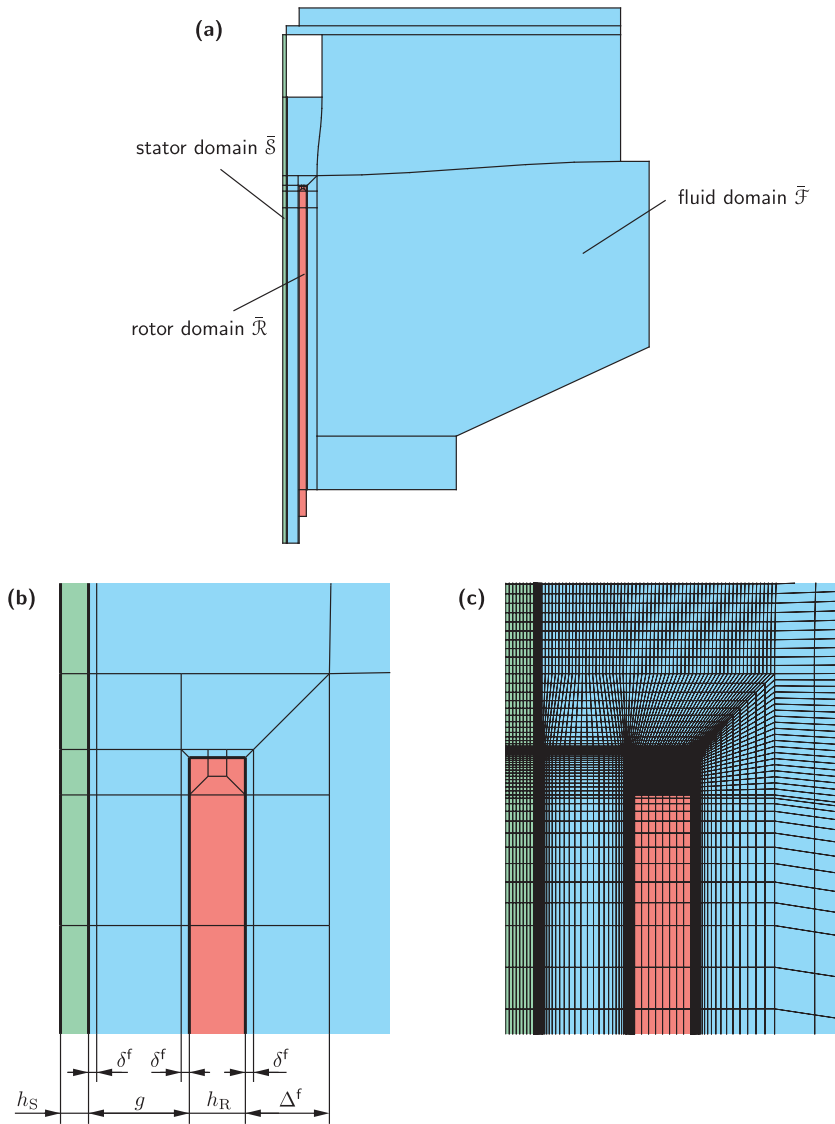


**Fig. 6.2:** (a) Subdivision of computation domain  $\bar{S} \cap \bar{R} \cap \bar{F}$  into quadrilateral blocks. (b) Detail of blocking in the region of the outer diameter of the rotor disk. (c) The same detail with the structured mesh using quadrilateral elements.

over the thickness and adjusted to an estimated frequency of the mode. The additional block of thickness  $\Delta^f = 3 \text{ mm}$  allows a smooth transition from the fine boundary layer to the coarse inner regions.

The blocking and meshing procedure of the computational domain is fully parametrized. We use the same blocking for all simulation steps, except that we adjust the thickness of boundary layer block  $\delta^f$ . In total, the simulation model of the test bench approximately counts 20 000 elements and 250 000 degrees of freedom.

## 6.3 Simulation Results

In the present section, we focus on selected simulation results which are characteristic for the bias motion and the vibration of the rotor–stator configuration. Further results, such as the modal parameters, will be separately presented in the following Chapter 7, where we also compare them with the experimental data.

### 6.3.1 Bias Motion

The (non-zero) solutions of the bias motion for the simulated parameter configurations show high similarities. We therefore exemplarily provide and discuss the results for one selected parameter set. Fig. 6.3 shows the axisymmetrical solution of the stationary Reynolds-averaged Navier–Stokes equations for a selected configuration. The primary bias flow is in the azimuthal  $\varphi$ -direction, which is indicated by a contour plot of the azimuthal velocity component  $\bar{v}_\varphi$ . The bias fluid motion also features secondary flows, which are visualized by a vector plot of the cross-section components  $(\bar{v}_r, \bar{v}_z)$ . Note that the azimuthal velocity component  $\bar{v}_\varphi$  is much larger than the radial component  $\bar{v}_r$  and the axial component  $\bar{v}_z$ . We observe three recirculation regions: (i) The torsional Couette flow between stator disk and rotor disk, (ii) the von Kármán flow above the rotor disk and (iii) a recirculation flow above the fastening ring.

The torsional Couette flow between rotor and stator disk is primarily a shear flow with an azimuthal velocity component increasing from  $\bar{v}_\varphi = 0$  at  $z = -g$  (stator disk) to  $\bar{v}_\varphi = \Omega_R r$  at  $z = 0$  (rotor disk). Boundary layers are formed near the wall due to the turbulent flow regime. The low-velocity secondary flow shows a recirculation pattern with a radial outflow

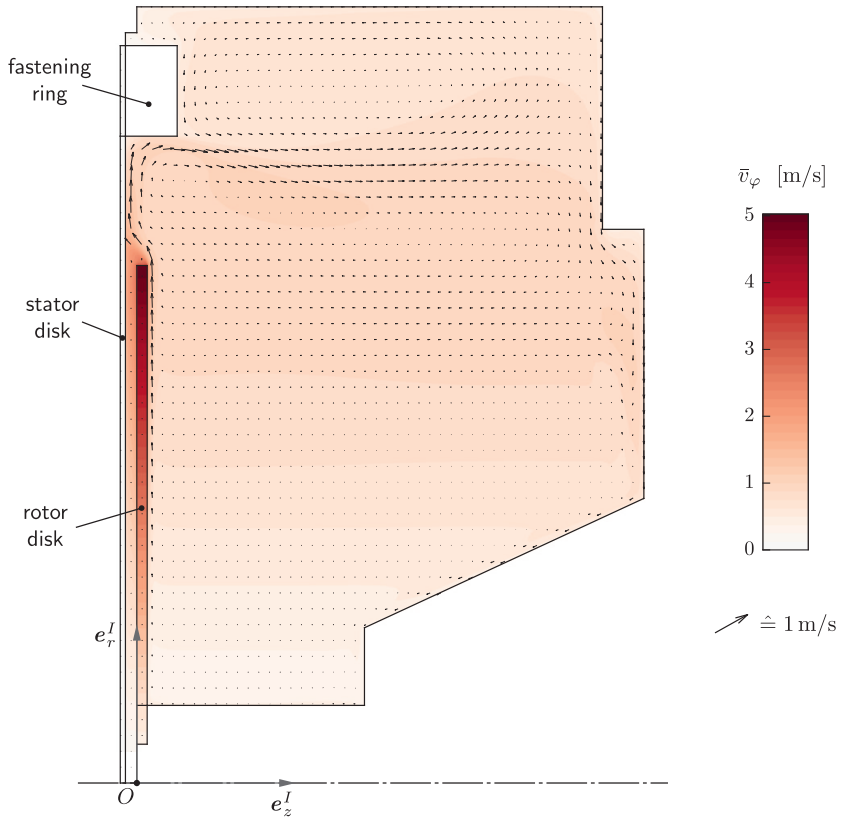


**Fig. 6.3:** Simulated bias velocity field  $\bar{v}$  of test bench model for  $h_S = 1.0$  mm,  $h_R = 2.0$  mm,  $g = 2.2$  mm and  $\Omega_R = 50.3$  rad/s. The color indicates the velocity component  $\bar{v}_\varphi$  and the arrows the cross-section components  $(\bar{v}_r, \bar{v}_z)$ .

near the rotor wall and a radial inflow near the stator wall. The axial flow is negligible except at the center  $r = 0$ , where the axial flow allows an exchange of the radial in- and outflow. The pressure between the rotor and stator disk declines radially towards the center.

The fluid motion above the rotor disk corresponds to the flow described by von Kármán (1921). Again, the flow has a primary component in the azimuthal  $\varphi$ -direction which is superimposed by a secondary flow. The rotation of the disk effects a radial outflow near the wall and this in turn induces a slow axial flow towards the disk. In this way, the rotating disk acts as a centrifugal pump and perpetuates the recirculation of the fluid confined in the cavity. Additionally, the sharp edges at the outer radius of the rotor disk and the inner radius of the fastening ring initiate a flow detachment, and hence, leads to the separation of the flow into the three recirculation regions.

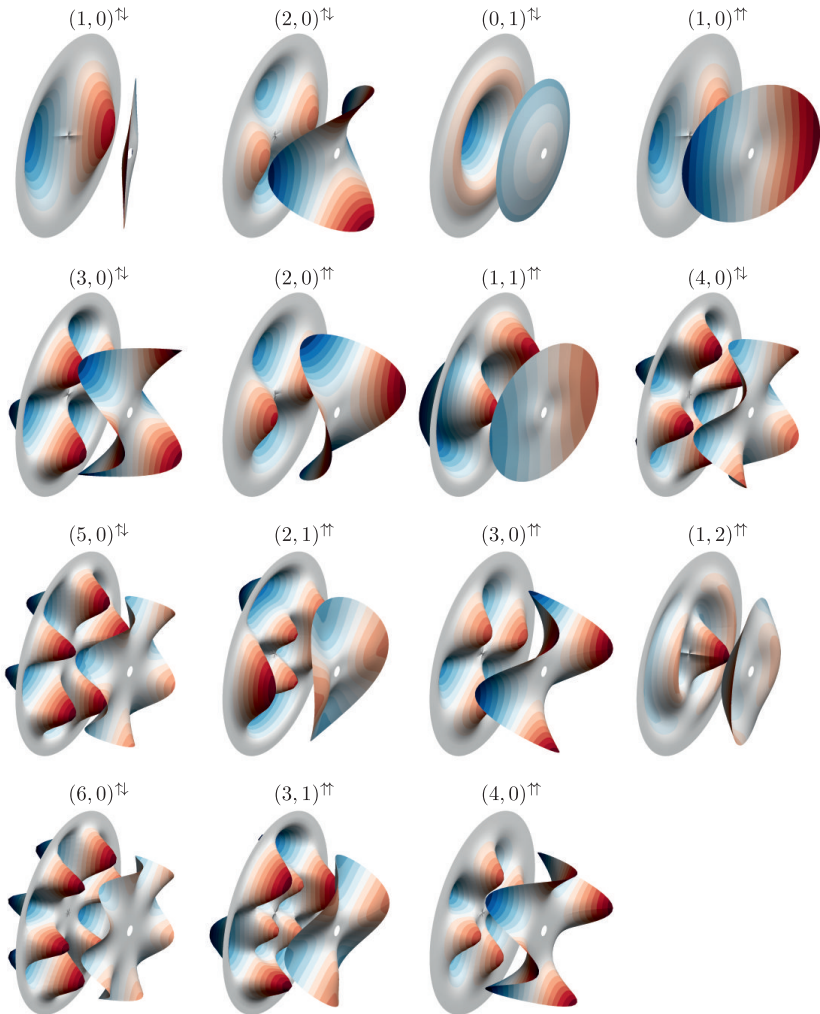
### 6.3.2 Modes Shapes

Fig. 6.4 shows simulated mode shapes for a selected parameter set. The naming convention for the modes is the same as defined in §5.3.1, that is,  $(n, l)^{\downarrow}$  and  $(n, l)^{\uparrow}$  denote varicose and sinuous modes, respectively, with an azimuthal wave number  $n$  and a radial index  $l$ . A qualitative comparison with the measured mode shapes in Fig. 5.10 shows a good agreement between experiment and simulation.

### 6.3.3 Features of Perturbation Motion

#### Perturbation Flow in the Fluid Gap

The perturbation motion of the fluid in the gap between rotor and stator is crucial for the understanding of the coupling mechanism. For that reason, we take the time to study the perturbation motion in the fluid gap in detail. Fig. 6.5 shows profiles for the velocity components  $\hat{v}_r$ ,  $\hat{v}_\varphi$  and  $\hat{v}_z$  at different radial positions in the fluid gap. The profiles are plotted for a varicose  $(+2, 0)^{\downarrow}$  mode and the corresponding sinuous  $(+2, 0)^{\uparrow}$  mode. Notice that the varicose mode has a lower eigenfrequency  $\omega^r$  and a higher damping factor  $\delta^r$  compared to the sinuous mode. Consider Fig. 6.4 to note that these two modes have similar mode shapes of the rotor and the stator, but that for the varicose mode the directions of motion are opposed whereas for



**Fig. 6.4:** Real part of simulated mode shapes of rotor–stator system for  $h_S = 1.0$  mm,  $h_R = 2.0$  mm,  $g = 2.2$  mm and  $\Omega_R = 0$  rad/s. Compare with measured mode shapes in Fig. 5.10.

the sinuous mode the directions are equal. This fact can also be seen in a comparison of the axial velocity component  $\hat{v}_z$ , where the varicose case exhibits a sign change of the nearly linear profile whilst the sinuous case does not.

Due to the no-slip condition at the wall, the perturbation flow of both modes feature a viscous boundary layer, which is most pronounced in the profiles of the components  $\hat{v}_r$  and  $\hat{v}_\varphi$ . The boundary layer is analogous to the one of Stokes' second problem with an approximation of the thickness given in (6.18). Accordingly, the boundary layer thickness is proportional to  $1/\sqrt{\omega^r}$  and we calculate  $\delta^f = 0.30 \text{ mm}$  for the varicose mode and  $\delta^f = 0.17 \text{ mm}$  for the sinuous mode. These analytical values well predict the thickness of the simulated boundary layers. Hence, our simulation model is capable to describe the damping of the system due to viscous effects. For the situation with no bias motion with  $\Omega_R = 0 \text{ rad/s}$ , this is the only mechanism that contributes to the damping. This is because there is in this case no interaction between bias motion and perturbations, and because our model neglects acoustic radiation, damping in the solid bodies and higher-order effects (acoustic streaming).

An inspection of Fig. 6.5 reveals that the in-plane velocity components  $\hat{v}_r$  and  $\hat{v}_\varphi$  are much larger in the varicose case than in the sinuous case. This is due to the relative motion of the rotor and the stator, which is different for the two cases. Characteristic for the varicose mode are velocity components  $\hat{v}_z$  of the rotor and the stator which are opposite in direction. This leads to a squeezing flow in the gap between rotor and stator, where the fluid flows from regions where the gap narrows to regions where the gap widens. This effect is much less pronounced for sinuous modes, where the velocity components  $\hat{v}_z$  of the rotor and the stator are in the same direction. The in-plane flow in sinuous case mainly compensates for the different mode shapes of rotor and stator (due to their different boundary and stiffness conditions).

It is this kinematic effect that leads to larger accelerations of the fluid for the varicose mode and, as a consequence, to an increased added-mass effect. The larger virtual mass results in a lower eigenfrequency of the varicose mode compared to the sinuous mode. Additionally, the squeezing flow also leads to a larger velocity gradient at the boundary layer of the wall, which explains the higher damping factor of the varicose mode (also considering the lower eigenfrequency).

A comparison of the velocity components  $\hat{v}_r$  and  $\hat{v}_z$  in Fig. 6.5 with the components  $\hat{v}_z$  and  $\hat{v}_z$  of the semi-analytical model in Fig. 3.5 show a good

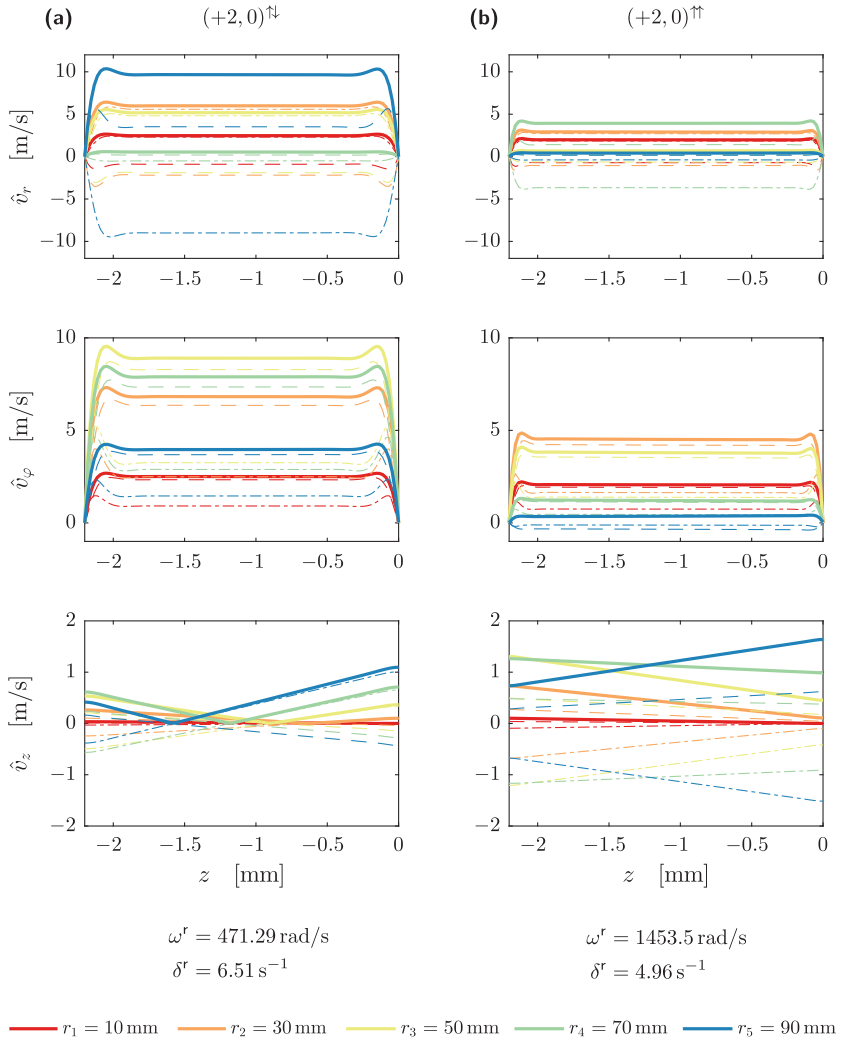


**Fig. 6.5:** Simulated profiles of velocity components  $\hat{v}_r$ ,  $\hat{v}_\varphi$  and  $\hat{v}_z$  at different radial positions in the fluid gap between stator and rotor. (a) varicose mode  $(+2, 0)^\dagger$  and (b) sinuous mode  $(+2, 0)^\ddagger$  for  $h_S = 1.0 \text{ mm}$ ,  $h_R = 2.0 \text{ mm}$ ,  $g = 2.2 \text{ mm}$  and  $\Omega_R = 0 \text{ rad/s}$ . Magnitude (solid lines), real part (dashed lines), imaginary part (dash-dotted lines).

agreement. Many of the effects discussed above have already be discovered in the analysis of the strongly simplified sandwich of Chapter 3.

### Edge Vortices

Fig. 6.6 shows exemplarily the simulated total flow field of a  $(+4, 0)^{\text{tl}}$  mode in the vicinity of the rotor's outer diameter for two different rotor speeds. In the first case with  $\Omega_R = 0 \text{ rad/s}$ , there is no bias motion and the total motion is simply described by the perturbations. We identify two fluid vortices that are located at the sharp edges of the rotor disk which are oriented equally. These vortices are induced by the motion of the rotor disk in the fluid initially at rest. In case with angular rotation  $\Omega_R = 50.3 \text{ rad/s}$ , the underlying bias flow advects the vortices away from the edge and forms a wake of alternating co- and counter-rotating spirals. From Fig. 6.3 we see that the radial velocity of the bias flow at the upper edge is larger and, therefore, the vortices are advected further away. A consequence of this phenomenon is that the vortices of the wake need to be spatially resolved, which demands a finer computational grid in regions away from the walls.



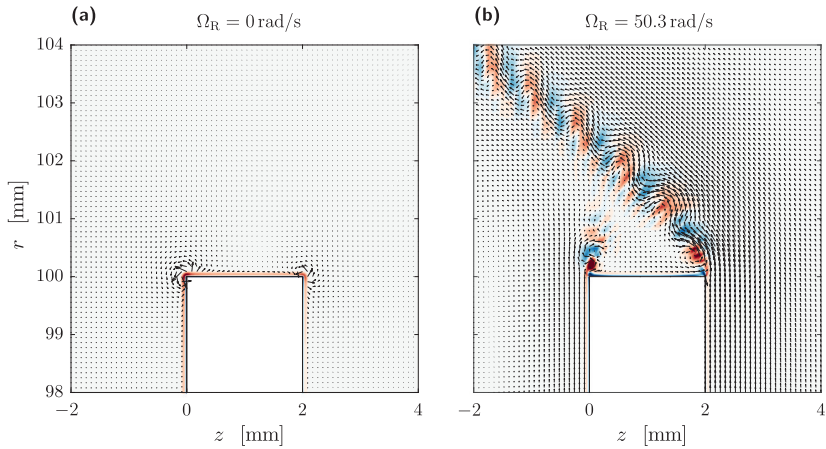


**Fig. 6.6:** Simulated total flow field around the outer diameter of the rotor disk for mode  $(+4, 0)^{\dagger\downarrow}$  at (a)  $\Omega_R = 0 \text{ rad/s}$  and (b)  $\Omega_R = 50.3 \text{ rad/s}$ . The color indicates the total vorticity component  $\bar{\eta}_\varphi + \varepsilon \bar{\eta}'_\varphi$  and the arrows the total velocity cross-section components  $(\bar{v}_r + \varepsilon \bar{v}'_r, \bar{v}_z + \varepsilon \bar{v}'_z)$  for  $h_S = 1.0 \text{ mm}$ ,  $h_R = 2.0 \text{ mm}$  and  $g = 3.6 \text{ mm}$ .



# Comparison of Experiment with Simulation

# 7

We have described the experimental measurements on the test bench in Chapter 5 and simulations of the same configuration in Chapter 6. There, we have already seen the qualitative good agreement between mode shapes from experiments (Fig. 5.10) and from simulations (Fig. 6.4). In the present chapter, we compare the results from experiments and simulation quantitatively and thereby focus on the modal parameters.

## 7.1 Modal Parameters without Bias Motion

In the present section, we compare the modal parameters of experiments and simulations without bias motion, that is  $\Omega_R = 0 \text{ rad/s}$ . Figs. 7.1–7.4 show the angular eigenfrequency  $\omega^r$ , the damping factor  $\delta^r$  and the amplitude ratio  $\kappa$  derived from experimental measurements and from numerical simulations. Complementary to the following comparison, also consider §5.3.2 for an interpretation and discussion of the experimental results.

### Angular Eigenfrequency $\omega^r$

Figs. 7.1–7.4 show a very good agreement between measured and simulated angular eigenfrequencies  $\omega^r$  for the investigated parameter range and for most of the vibration modes. The simulation model also maps the characteristic difference between varicose and sinuous modes, as described in §5.3.2. Nevertheless, we observe discrepancies, especially for the configuration with  $h_S = 1.0 \text{ mm}$  and  $h_R = 1.0 \text{ mm}$  (Fig. 7.1), where the angular eigenfrequencies of some varicose modes  $(n, 0)^{\uparrow\downarrow}$  are slightly underestimated by the simulation. This deviation increases with the azimuthal wave number  $n$ —and therefore with the eigenfrequencies  $\omega^r$ —and particularly manifests

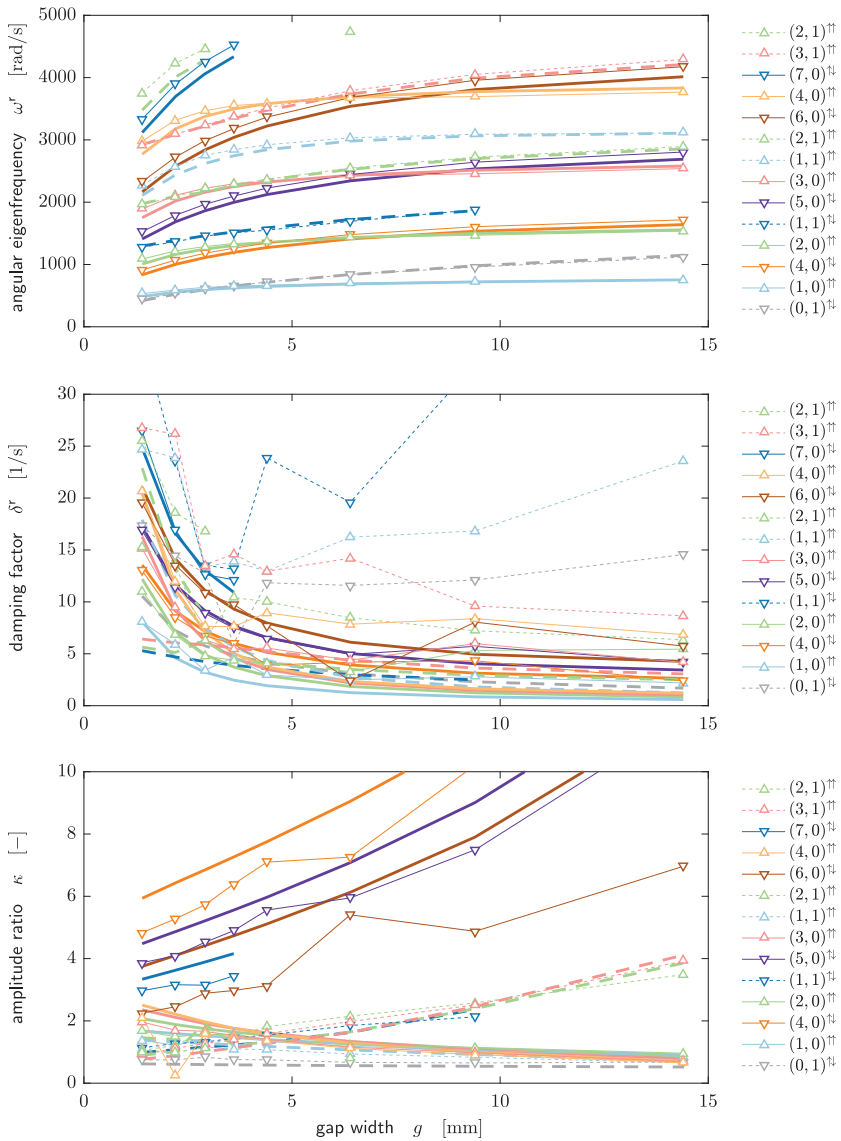


**Fig. 7.1:** Comparison of angular eigenfrequency  $\omega^r$ , damping factor  $\delta^r$  and amplitude ratio  $\kappa$  as a function of the gap width  $g$  for  $h_S = 1.0$  mm,  $h_R = 1.0$  mm and  $\Omega_R = 0$  rad/s. Experiment (thin lines with markers), simulation (thick lines). Modes are distinguished by  $l = 0$  (solid lines) and  $l > 0$  (dashed lines).

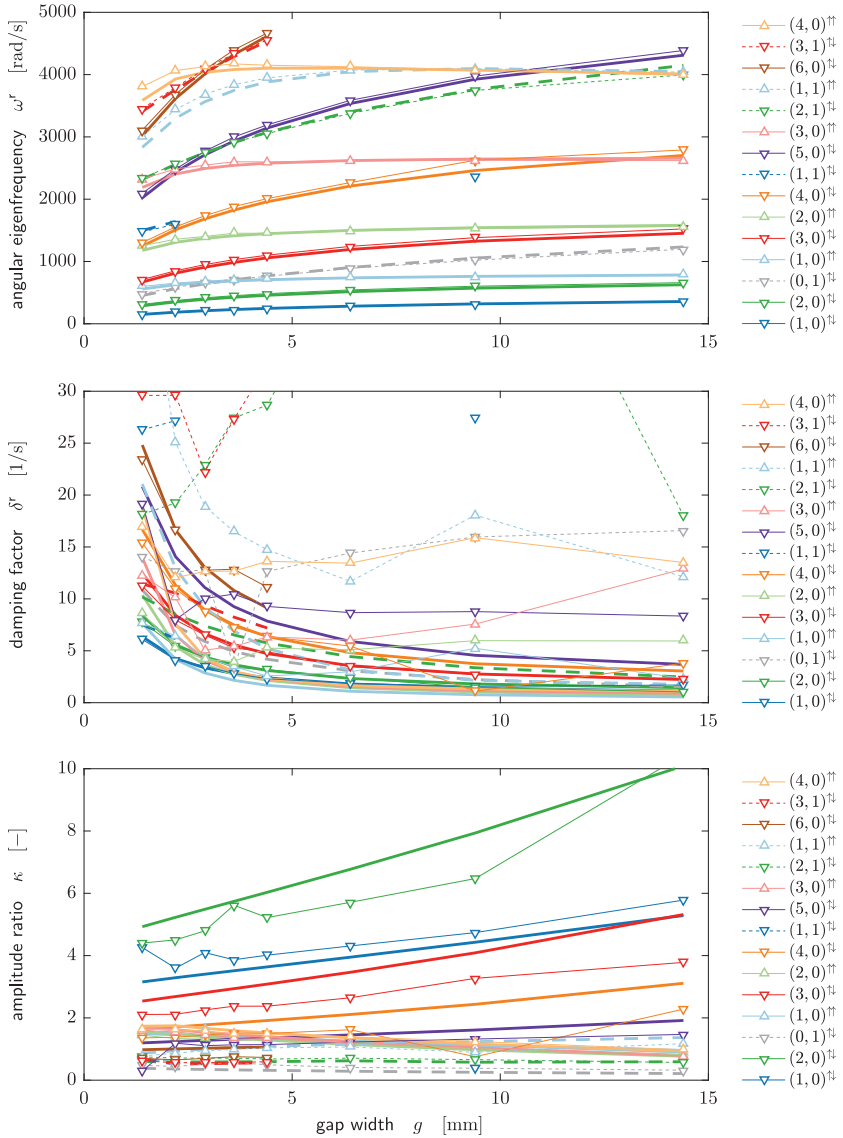


**Fig. 7.2:** Comparison of angular eigenfrequency  $\omega^r$ , damping factor  $\delta^r$  and amplitude ratio  $\kappa$  as a function of the gap width  $g$  for  $h_S = 1.0$  mm,  $h_R = 1.5$  mm and  $\Omega_R = 0$  rad/s. Experiment (thin lines with markers), simulation (thick lines). Modes are distinguished by  $l = 0$  (solid lines) and  $l > 0$  (dashed lines).

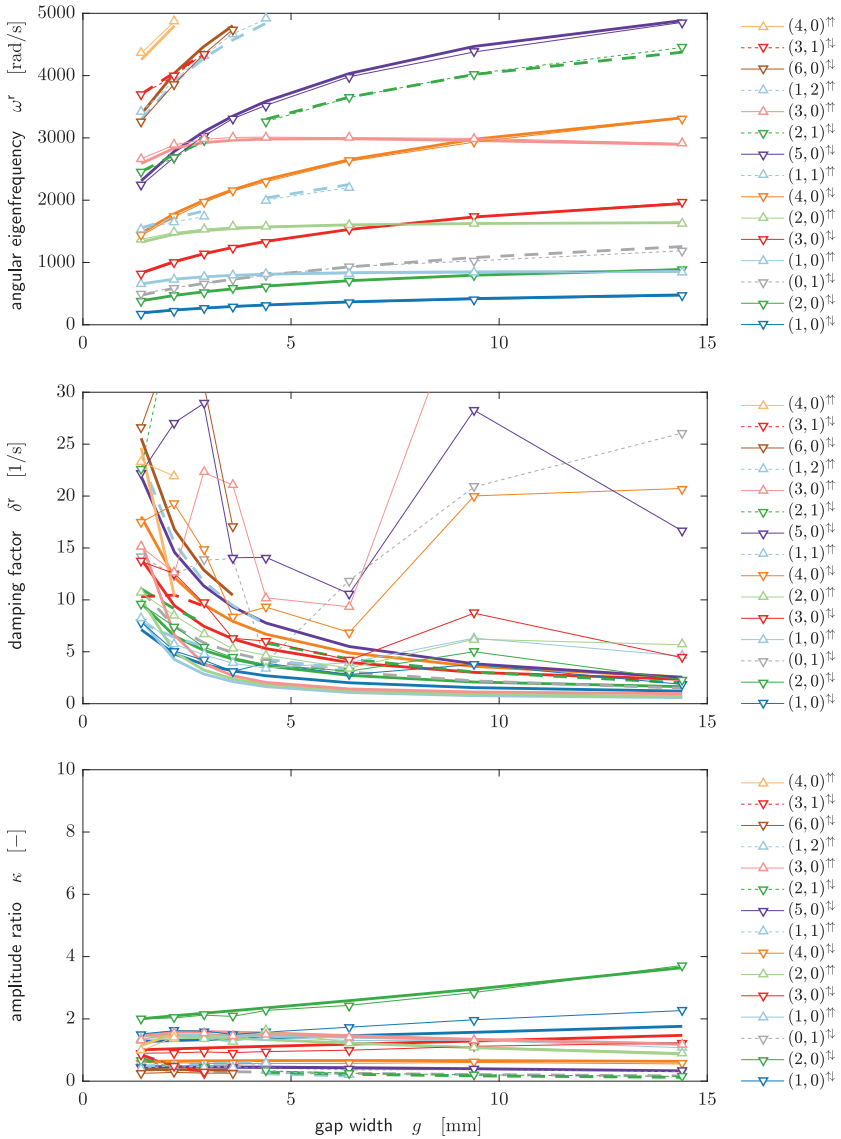


**Fig. 7.3:** Comparison of angular eigenfrequency  $\omega^r$ , damping factor  $\delta^r$  and amplitude ratio  $\kappa$  as a function of the gap width  $g$  for  $h_S = 1.0$  mm,  $h_R = 2.0$  mm and  $\Omega_R = 0$  rad/s. Experiment (thin lines with markers), simulation (thick lines). Modes are distinguished by  $l = 0$  (solid lines) and  $l > 0$  (dashed lines).

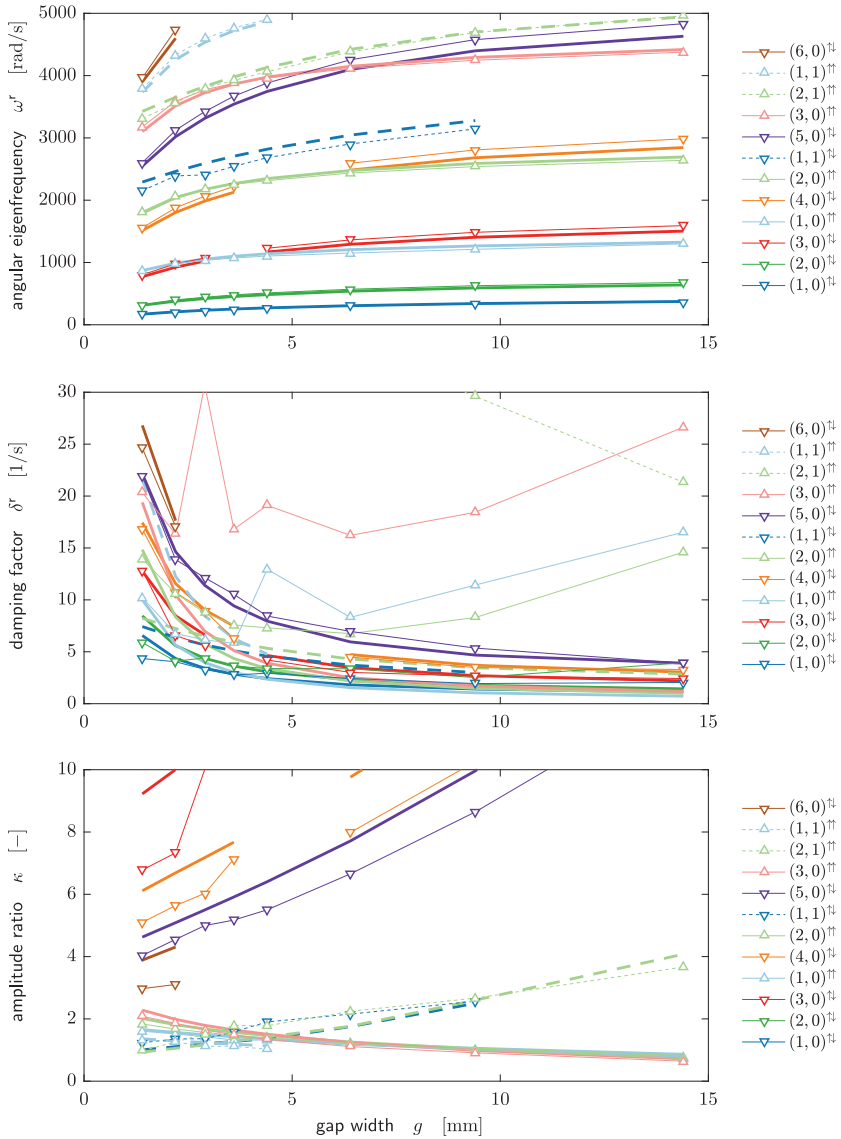


**Fig. 7.4:** Comparison of angular eigenfrequency  $\omega^r$ , damping factor  $\delta^r$  and amplitude ratio  $\kappa$  as a function of the gap width  $g$  for  $h_S = 1.5$  mm,  $h_R = 1.5$  mm and  $\Omega_R = 0$  rad/s. Experiment (thin lines with markers), simulation (thick lines). Modes are distinguished by  $l = 0$  (solid lines) and  $l > 0$  (dashed lines).

for modes of higher order. The deviations may be caused by the compressibility of the water, which is not included in formulation of the fluid in the simulation model.

From the good agreement we conclude that the modal analysis of the measurement data provides reliable eigenfrequencies and that the finite element simulation well predicts the eigenfrequencies of the water coupled system without bias motion.

### Damping Factor $\delta^r$

A comparison of the measured and simulated damping factors  $\delta^r$  in Figs. 7.1–7.4 draws an ambivalent picture. There are modes that show a good agreement between simulation and experiment. For example, the damping factors of the varicose modes  $(n, 0)^{\downarrow}$  are well estimated by the simulation over a large parameter range. However, in some cases with large gap widths ( $g \gtrsim 8\text{ mm}$ ), the simulation estimates smaller damping values compared to the experiment. A similar behavior is observed for the sinuous modes  $(n, 0)^{\uparrow}$ , albeit the range of gap widths with a good agreement is smaller. On the other hand, there is no match between simulation and experiment for varicose modes  $(*, l)^{\downarrow}$  and sinuous modes  $(*, l)^{\uparrow}$  of higher radial order, that is  $l > 0$ .

The reasons for the deviation between simulation and experiment can be manifold. On the simulation side, we neglect, for example, material damping in the solid, damping effects at the clamping, or higher-order effects in the fluid such as streaming. These lead to an underestimation of the damping factor. On the experimental side, we need to consider that the estimation of the damping factor  $\delta^r$ , as described in §§ 5.2.2 and 5.2.3, is a challenging task with uncertainties. Particularly, if the signal-to-noise ratio is low, the experimental modal analysis may overestimate the damping factor.

By considering Figs. 5.1 and 5.10, we see that our point of excitation is not optimally located to excite higher radial-order modes  $(*, l)$ , with  $l > 0$ . For these modes, the excitation is located near the nodal circle of the stator disk, and therefore leads to low vibration amplitudes. We believe that the resultant low signal-to-noise ratio causes an overestimation of the damping factor of these radial modes. For the varicose modes  $(n, 0)^{\downarrow}$  and sinuous modes  $(n, 0)^{\uparrow}$ , which show partially a good agreement of experiment and simulation, it is not clear which effect eventually is responsible for the deviation at larger gap widths.



We conclude that the finite element simulation well predicts the damping factor  $\delta^r$  for varicose modes  $(*,0)^{\downarrow}$  and sinuous modes  $(*,0)^{\uparrow}$  without bias motion and for the gap width range  $g \lesssim 8 \text{ mm}$ . For these modes, the viscous effect is therefore the only relevant damping effect. For the higher-order modes with  $l > 0$  and for configurations with larger gap widths ( $g \gtrsim 8 \text{ mm}$ ), the cause of the deviations between simulation and experiment is not yet determined.

### Amplitude Ratio $\kappa$

The amplitude ratio is defined according to (5.49) as the ratio of the maximum amplitude of the rotor over the maximum amplitude of the stator. Figs. 7.1–7.4 show a qualitative good agreement between measured and simulated amplitude ratio. Especially the different functional dependence on the gap width  $g$  of varicose modes  $(n,l)^{\downarrow}$  and sinuous modes  $(n,l)^{\uparrow}$  is well reproduced by the simulation. Whereas the amplitude ratio increases with  $g$  for the varicose modes, it declines with  $g$  for the sinuous modes. The quantitative agreement of experiment and simulation is particularly well for all the sinuous modes. For the varicose modes, we observe consistent results for the configuration with  $h_S = 1.0 \text{ mm}$  and  $h_R = 2.0 \text{ mm}$  (see Fig. 7.3). For the remaining configurations, the simulated amplitude ratios of the varicose modes are usually higher than the measured values.

## 7.2 Modal Parameters with Bias Motion

Let us now turn to the comparison of experiment and simulation including bias motion. That is the case with  $\Omega_R > 0 \text{ rad/s}$ , where the rotor is in rotation and induces a bias fluid motion. Fig. 7.5 shows the angular eigenfrequency  ${}_S\omega^r$ , the damping factor  $\delta^r$  and the amplitude ratio  $\kappa$  for a selected parameter set at various angular rotor speeds  $\Omega_R$ . The legend entries on the right annotate the experimental data points. We refer to §5.3.2 for a detailed discussion of experimental results for the same configuration.

### Angular Eigenfrequency $\omega^r$

First, we focus on the comparison of the angular eigenfrequency  ${}_S\omega^r$ . Note that we present the frequency results in the stator system  $S$ . For the conversion of the angular frequencies into the rotor system  $R$  we refer to (5.48).

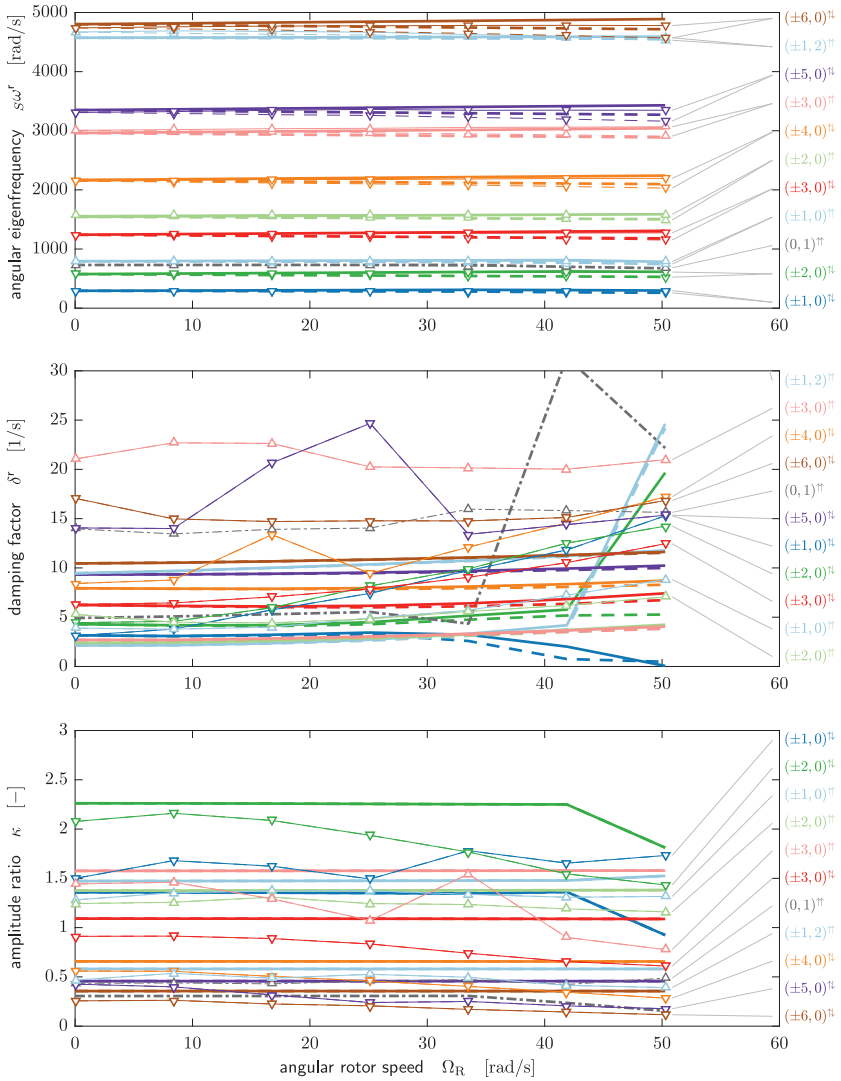


**Fig. 7.5:** Comparison of angular eigenfrequency  $s\omega^f$ , damping factor  $\delta^r$  and amplitude ratio  $\kappa$  as a function of the angular rotor speed  $\Omega_R$  for  $h_S = 1.0$  mm,  $h_R = 2.0$  mm and  $g = 3.6$  mm. Experiment (thin lines with markers), simulation (thick lines). Modes are distinguished by  $n_m > 0$  (solid lines),  $n_m < 0$  (dashed lines) and  $n_m = 0$  (dash-dotted lines).

Fig. 7.5 shows the excellent qualitative and quantitative agreement between measured and simulated angular eigenfrequencies. The simulation model well predicts the frequency splits that arise for pairs of co- and counter-rotating modes with non-zero azimuthal wave number  $n$ . The difference in frequency is roughly proportional to the azimuthal wave number  $|n|$  and the angular rotor frequency  $\Omega_R$ , which is well described by the simulation model. We have included this effect in the finite element model by introducing perturbation equations derived from the linearization about a stationary bias motion (see §§ 2.1.4 and 2.2.4). The stationary bias motion of the fluid has been approximated by the Reynolds-averaged Navier–Stokes equations together with the  $k$ - $\varepsilon$  turbulence model and wall functions (see § 6.2.1). The good agreement suggests that this modeling approach is appropriate for the prediction of the frequency split effect.

### Damping Factor $\delta^r$

Next, we refer to Fig. 7.5 and discuss the comparison of the damping factor  $\delta^r$ . We have already seen in § 7.1 that, even for the non-rotating case with  $\Omega_R = 0$  rad/s, there is only a partial match between experiment and simulation. Therefore, we only qualitatively compare the modes that match for the non-rotating case.

The experimental results show an increase of the damping factor with the angular rotor speed  $\Omega_R$  for most of the modes. This effect is not represented with the simulation model, where the damping factor remains nearly constant. That deviation may be caused by an insufficient modeling of the bias motion near the wall. It is known from hydrodynamic stability theory (Schmid and Henningson, 2001, p. 9; Weder et al., 2015) that the damping factor  $\delta^r$  is influenced by the bias-flow velocity gradient. But, by using wall functions (see § 6.2.1) instead of resolving the bias-flow boundary layer, the interaction between base flow and perturbation flow may not be sufficiently considered in our finite element model. Furthermore, we assumed for the simulation model that the perturbation equations can be derived by the linearization about the stationary Reynolds-averaged bias flow (see § 6.2.1). A violation of this assumption may be an additional reason for the deviation of the damping factor between simulation and experiment.

Another issue is the large variation of the simulated damping factors of the modes  $(\pm 1, 0)^{\updownarrow}$ ,  $(\pm 2, 0)^{\updownarrow}$ ,  $(\pm 0, 1)^{\updownarrow}$  and  $(\pm 1, 0)^{\updownarrow}$ , which appears for  $\Omega_R \gtrsim 30$  rad/s. For a system with bias motion, the eigenvalue prob-

lem becomes non-self-adjoint (non-symmetric) with eigenvectors that are non-orthogonal. Schmid and Henningson (2001, pp. 89) describe that for non-orthogonal eigenvectors, the eigenvalues become sensitive to small disturbance of the governing perturbation equations. This may be the reason for the variation of the addressed modes.

### **Amplitude Ratio $\kappa$**

Finally, we examine the amplitude ratio  $\kappa$  which is also compared in Fig. 7.5. The simulated amplitude ratio is nearly independent of the angular rotor speed  $\Omega_R$ , whereas we observe a slight decline in the measured ratio.

# Conclusions and Outlook

# 8

In this last chapter, we discuss the conclusions of our investigations and provide recommendations for future work.

## 8.1 Conclusions

We have investigated the complex vibration of rotor–stator systems coupled by viscous liquids. The knowledge and understanding of this problem are of particular importance for the design of pump-turbines, in which the elastic structures of the rotor and stator are coupled by the intermediate water (see Fig. 1.1). The challenges of this problem include rotating structures, the deformability of the rotor and stator, as well as various damping mechanisms that are present in the system. Throughout this thesis, we worked with a simplified disk–disk model consisting of a stator disk that is axially separated from a rotor disk, together with a rigid casing that acts as a fluid cavity. The stator disk is clamped to the casing and the rotor disk to a rotating shaft (see Fig. 1.2). We have chosen theoretical, experimental and simulative approaches to address this difficult and explorative problem.

### Major Contributions

Before going into detail, we briefly summarize the major contributions of the present work:

- We have presented a concise theory of linear vibrations of liquid-coupled system including the effects of viscosity and bias motion. The theory is systematically deduced from fundamental principles of continuum mechanics and presented in the weak variational form, which is best suited for its implementation in the finite element framework.

- The especially engineered test bench has enabled conclusive experiments on the vibration of liquid-coupled rotor–stator systems. It particularly has allowed for the measuring of eigenfrequencies, damping factors and mode shapes of rotor and stator on a system with rotating parts. The measurements collected over a wide range of parameters form a substantial and unique experimental database for the current and future work.
- The new physically-based simulation technique has enabled a prediction of modal parameters for rotor–stator systems. The implementation is computationally efficient and includes effects of viscosity and bias motion. A comparison of the simulation results with the experimental data has shown an excellent agreement for the computed eigenfrequencies and a good agreement for the damping factors of the relevant low-frequency modes. By means of the simulation we achieved a deeper understanding of the underlying internal mechanisms of the liquid coupling.

The methodical interplay of theory, experiment and simulation has proven to be particularly fruitful for exploring the current problem and may be seen as a key factor in coping with complexity.

In the following we draw more specific conclusions with respect to the research questions, which we raised in § 1.3 about (i) fundamental mechanisms and features of fluid coupled rotor–stator systems, (ii) the parametric dependency of modal parameters, and (iii) the numerical modeling of such systems.

### **Fundamental Mechanisms and Features**

We draw the following conclusions with regard to the fundamental mechanisms and features of the vibration of elastic rotor–stator systems coupled by viscous liquids:

- From a vibrational point of view, the components rotor, stator and fluid form a system on its own. Therefore, the vibration can, in general, only be analyzed by considering the complete system, and not just its components separately.
- The axial symmetry of the disk–disk model allows to describe linear vibrations by eigenmodes (in an approximate sense), even for the case

with bias motion ( $\Omega_R > 0$  rad/s). Each eigenmode is characterized by an angular eigenfrequency  $\omega^r \in \mathbb{R}$ , a damping factor  $\delta^r \in \mathbb{R}$  and by a (left and right) mode shape (see §5.2.2).

- The mode shapes of the disk–disk model are categorized by the azimuthal wave number  $n \in \mathbb{Z}$  (number of nodal diameters), by the radial index  $l \in \mathbb{N}_0$  (number of nodal circles of the stator), and according to the relative motion between rotor and stator disk (varicose and sinuous modes). We call a mode varicose when the motion of the rotor is mainly opposite to the stator and sinuous when the motion is mainly synchronous (see §§5.3.1 and 6.3.2).
- We have found that varicose modes have lower eigenfrequencies compared to the corresponding sinuous modes (see Fig. 5.9). The finite simulation has revealed that the squeezing flow of the fluid between rotor and stator is more pronounced for the varicose mode and that this added-mass effect is the key cause of the frequency reduction (see §6.3.3).
- For the case without bias motion, we have identified the viscous dissipation as the dominant damping mechanism of the vibration. The dissipation is located in the Stokes boundary layer formed in the near-wall region of the fluid (see §6.3.3).
- The angular eigenfrequency of a vibration mode depends on the rotation speed of the observer. Therefore, the rotor system  $R$  and the stator system  $S$  experience different frequencies in the case of non-zero bias motion (see §5.2.2).
- For the case with bias motion, the system exhibits a frequency split for mode pairs with non-zero azimuthal wave number  $n$  (see Figs. 5.15 and 7.5). For an observer in the stator system  $S$ , the mode with larger eigenfrequency is co-rotating with the rotor bias motion, whereas the corresponding mode with lower eigenfrequency is counter-rotating. The difference in frequency  ${}_S\Delta\omega^r$ , again for the stator observer  $S$ , is roughly proportional to the azimuthal wave number  $n$  and the angular rotor frequency  $\Omega_R$  (see §§5.3.3 and 7.1).

### Parametric Dependency of the Modal Parameters

We draw the following conclusions with regard to the parametric dependency of the systems' modal parameters:

- The specially developed test bench enables highly accurate vibration measurements of a rotor–stator system coupled by liquids. For a disk–disk configuration, the test bench allows a variation of the parameters rotor thickness  $h_R$ , stator thickness  $h_S$ , gap width  $g$  and angular rotor speed  $\Omega_R$  (see Chapter 4).
- We have evaluated the measurement data with the modal analysis approach to estimate the modal parameters eigenfrequency  $\omega^r$ , damping factor  $\delta^r$  and right mode shape. It is necessary to consider the general modal analysis theory via the first-order form (with complex valued left and right mode shapes), to include the gyroscopic effects resulting from the bias motion of the rotor and the fluid (see § 5.2.1).
- The measurement of the vibrations and the subsequent evaluation are largely automated. This has enabled an extensive series of experiments by variation of the configuration parameters (see Chapter 5). We have generated a broad experimental database, which in turn forms a unique basis for the verification of present (and future) simulation models (see Chapter 7).

### Numerical Modeling

We draw the following conclusions with regard to the numerical modeling of rotor–stator systems coupled by viscous liquids:

- We have implemented the linearized perturbation equations of Chapter 2 into the finite element code COMSOL Multiphysics to compute the angular eigenfrequency  $\omega^r$ , the damping factor  $\delta^r$  as well as the (right) mode shape of modes with arbitrary azimuthal wave number  $n \in \mathbb{Z}$ .
- The employed rotational symmetries allowed a reduction to a two-dimensional model, which drastically saves computational cost. Unfortunately, this simplification will not apply for general shaped geometries.



- The finite element model includes the effect of a stationary bias motion of the rotor and the fluid flow. This allows a physically-based and validated prediction of the frequency split, an effect which exists for mode pairs with non-zero azimuthal wave number  $n$  (see §7.2).
- We expect that the angular eigenfrequency does only marginally depend on the (viscous) damping of the system. Therefore, it should be possible to accurately predict the eigenfrequency (and thus the frequency split) by neglecting viscous effects, but by including the convective effects from the bias motion.
- Without bias motion, the finite element model well predicts the damping factor of the fluid coupled system, except for large gap widths and some higher-order modes. We therefore conclude that the viscous damping effect is correctly implemented in the finite element model. But using this direct method, the computational grid must sufficiently resolve the frequency dependent viscous boundary layer.
- With bias motion, the finite element model's prediction of the damping factor is unsatisfactory, because the angular rotor speed  $\Omega_R$  only marginally effects the computed damping factor (see Fig. 7.5). We assume that the interaction of bias motion with the perturbations, which is mainly driven by velocity gradients in the bias flow, is implemented insufficiently. The reason is probably the use of the wall functions in the calculation of the turbulent bias flow.

## 8.2 Outlook

### Fundamental Research on Simplified Models

The present thesis has extensively investigated the vibration of liquid coupled rotor–stator systems on a simplified disk–disk configuration. Notwithstanding, there are still open questions that seem worthwhile to be addressed in future work:

- The presented simulation model does not adequately map the dependence of the damping factor  $\delta^r$  on the angular rotor speed  $\Omega_R$  (see Fig. 7.5). We assume that the applied wall functions do not sufficiently model the bias-flow velocity gradients near the wall and therefore lead

to that deviation. Henceforth, we propose to use low-Reynolds models for the calculation of the bias flow, which resolve the near-wall boundary layer. Low-Reynolds models are, for example, Menter's shear stress transport turbulence model (SST), the low-Reynolds number  $k-\varepsilon$  turbulence model or the Spalart-Allmaras turbulence model (COMSOL, 2016c, pp. 164).

- In this work we focused on the characterization of free vibrations, which are related to the right mode shapes. However, for a system with bias motion, the receptivity of each vibration mode is described by the corresponding left mode shape. Left mode shapes are experimentally measured by moving the point of excitation (Nordmann, 1984b). For the theoretical and simulative investigations of the receptivity, it would be worth to study the adjoint problem (Hill, 1995).
- Weder et al. (2015) proposed a decomposition of the damping factor  $\delta^r$  into terms of dissipation, production and flux of perturbation energy, which has been applied to study damping of perturbations superimposed to compressible parallel bias flow. This technique may be transferred to the present application to provide additional insights about the fundamental mechanisms of damping (or instability).
- Throughout this thesis, we worked with a simplified disk-disk configuration, which represents the interaction between runner crown (rotor) and head cover (stator). By considering Fig. 1.1, we see that this configuration can not be applied to the coupling between runner band (rotor) and discharge ring (stator). It would be interesting to investigate this coupling on a simplified ring-ring configuration.
- For larger vibration amplitudes, nonlinear effects need to be considered, such as additional damping by acoustic streaming (Hahn et al., 2015) or the nonlinear stiffness of the disks.

### Concretization towards Real Turbines

The long-term objectives of this project are tools and methods for the vibrational characterization of real turbines. In Fig. 1.2 we indicate the process of concretization, that is, the transfer of knowledge, tools and methods from

the simplified model to the application on real turbines. This concretization process faces with two major difficulties, for which we suggest solution approaches:

- For the simplified disk model, we have formulated all equations in an inertial frame of reference. The bias motion of the rotor has been taken into account by additional acceleration terms that arise from the motion of the reference configuration (see § 2.1.1). This modeling approach has become possible for the simplified disk model due to the axial symmetry of rotor and stator, and cannot simply be transferred to general geometries. In addition, the perturbation equations for a system with arbitrary shaped rotor and stator are time dependent, so that we can not formulate an eigenvalue problem. To overcome this difficulty, we suggest to formulate the perturbation equations in the rotor frame of reference (rotating with  $+\Omega_R$ ). The stator geometry then needs to be simplified by its axisymmetric representation and modeled with a rotating reference configuration (rotating with  $-\Omega_R$ ).
- In the presented simulation model, we have included viscous terms in the perturbation equations and solved directly for both the eigenfrequency  $\omega^r$  and the damping factor  $\delta^r$ . Using this direct method, the frequency dependent Stokes boundary layer formed near the wall, needs to be sufficiently discretized with finite elements. The direct method has become feasible, because we have reduced the simplified disk model to a two-dimensional problem. In three-dimensional simulations, however, the computational cost is significantly larger. For that case, we propose to compute the damping factor either by (i) introducing wall functions to model the Stokes boundary layer, or, by (ii) calculating the eigenfrequency and the damping factor in two consecutive steps. In the two step procedure, one first solves for the eigenfrequency using the inviscid perturbation equations including bias flow (acoustic equations with convective terms). Secondly, the damping factor can be either computed with analytical methods (Hahn and Dual, 2015), or by numerical means (Monette et al., 2014).



# Mathematical Tools and Evaluations

# A

This appendix gathers the most common mathematical tools used throughout the thesis.

## A.1 Gâteaux Derivative

Let  $f$  be a scalar-, vector-, or tensor-valued function of a vector  $\boldsymbol{x}$ , then

$$Df(\bar{\boldsymbol{x}})[\tilde{\boldsymbol{x}}] := \lim_{\varepsilon \rightarrow 0} \frac{f(\bar{\boldsymbol{x}} + \varepsilon \tilde{\boldsymbol{x}}) - f(\bar{\boldsymbol{x}})}{\varepsilon} = [\partial_{\boldsymbol{x}} f(\bar{\boldsymbol{x}})] \tilde{\boldsymbol{x}} \quad (\text{A.1})$$

defines the *Gâteaux derivative* of  $f$  at  $\bar{\boldsymbol{x}}$  in the direction of  $\tilde{\boldsymbol{x}}$  (see also Odgen, 1984, pp. 48; Marsden and Hughes, 1983, pp. 44; Bonet and Wood, 2008, pp. 47). This equation also introduces the *gradient* of  $f$  at  $\bar{\boldsymbol{x}}$ , denoted as  $\partial_{\boldsymbol{x}} f(\bar{\boldsymbol{x}})$ , if this object is uniquely defined for all  $\tilde{\boldsymbol{x}}$ . We see from (A.1) that the tensor order of the gradient  $\partial_{\boldsymbol{x}} f$  is by one greater than the one of the function  $f$ . Accordingly, let  $F$  be a function of a tensor  $\bar{\mathbf{X}}$ , then we write

$$DF(\bar{\mathbf{X}})[\tilde{\mathbf{X}}] := \lim_{\varepsilon \rightarrow 0} \frac{F(\bar{\mathbf{X}} + \varepsilon \tilde{\mathbf{X}}) - F(\bar{\mathbf{X}})}{\varepsilon} = [\partial_{\mathbf{X}} F(\bar{\mathbf{X}})] : \tilde{\mathbf{X}} \quad (\text{A.2})$$

for the Gâteaux derivative of  $F$  at  $\bar{\mathbf{X}}$  in the direction of  $\tilde{\mathbf{X}}$  and  $\partial_{\mathbf{X}} F(\bar{\mathbf{X}})$  for the gradient of  $F$  at  $\bar{\mathbf{X}}$ . Note that the tensor order of the gradient  $\partial_{\mathbf{X}} F$  is by two greater than of the function  $F$ .

We may further define the second-order Gâteaux derivative of  $f$  at  $\bar{\boldsymbol{x}}$  in the direction of  $\tilde{\boldsymbol{x}}$  by

$$D^2 f(\bar{\boldsymbol{x}})[\tilde{\boldsymbol{x}}] := \lim_{\varepsilon \rightarrow 0} \frac{Df(\bar{\boldsymbol{x}} + \varepsilon \tilde{\boldsymbol{x}})[\tilde{\boldsymbol{x}}] - Df(\bar{\boldsymbol{x}})[\tilde{\boldsymbol{x}}]}{\varepsilon} = \{[\partial_{\boldsymbol{x}} \partial_{\boldsymbol{x}} f(\bar{\boldsymbol{x}})] \tilde{\boldsymbol{x}}\} \tilde{\boldsymbol{x}}, \quad (\text{A.3})$$

which geometrically defines  $\partial_x \partial_x f(\bar{\mathbf{x}})$  as well. Accordingly, for the function  $F$  of a second-order tensor  $\mathbf{X}$ , the second-order Gâteaux derivative at  $\bar{\mathbf{X}}$  in  $\tilde{\mathbf{X}}$  reads

$$D^2 F(\bar{\mathbf{X}})[\tilde{\mathbf{X}}] := \lim_{\varepsilon \rightarrow 0} \frac{DF(\bar{\mathbf{X}} + \varepsilon \tilde{\mathbf{X}})[\tilde{\mathbf{X}}] - DF(\bar{\mathbf{X}})[\tilde{\mathbf{X}}]}{\varepsilon} = \{[\partial_{\mathbf{X}} \partial_{\mathbf{X}} f(\bar{\mathbf{X}})] : \tilde{\mathbf{X}}\} : \tilde{\mathbf{X}}. \quad (\text{A.4})$$

## A.2 Tensor Analysis

The following introduction to tensor analysis in curvilinear coordinates mainly follows the work by Odgen (1984, pp. 33–72). We gather the necessary ingredients for the evaluation of the tensor quantities derived in Chapter 2 in Cartesian and cylindrical coordinates.

### A.2.1 Tensors in Curvilinear Coordinates

We define a bijective *coordinate mapping*  $\boldsymbol{\Pi} : \mathbb{E}^3 \rightarrow \mathbb{R}^3$  together with its inverse  $\boldsymbol{\Pi}^{-1}$  as

$$\boldsymbol{\Pi}(\mathbf{X}) = \begin{pmatrix} \Pi^1(\mathbf{X}) \\ \Pi^2(\mathbf{X}) \\ \Pi^3(\mathbf{X}) \end{pmatrix} = \begin{pmatrix} q^1 \\ q^2 \\ q^3 \end{pmatrix} \in \mathbb{R}^3, \quad \mathbf{X} = \boldsymbol{\Pi}^{-1}(q^1, q^2, q^3), \quad (\text{A.5})$$

with the, in general, curvilinear coordinates  $(q^1, q^2, q^3)$ . The *natural basis*  $(\mathbf{g}_1, \mathbf{g}_2, \mathbf{g}_3)$  associated with the coordinate mapping  $\boldsymbol{\Pi}$  is defined by the tangent vectors on the coordinate curves

$$\mathbf{g}_i := \partial_{q^i} \boldsymbol{\Pi}^{-1}, \quad (i = 1, 2, 3). \quad (\text{A.6})$$

Based on the natural basis,

$$\mathbf{g}^i \cdot \mathbf{g}_j = \delta_j^i = \begin{cases} 1 & \text{if } i = j \\ 0 & \text{otherwise} \end{cases} \quad (i, j = 1, 2, 3), \quad (\text{A.7})$$

uniquely defines the *reciprocal basis*  $(\mathbf{g}^1, \mathbf{g}^2, \mathbf{g}^3)$ , which, as has been proven by Odgen (1984, pp. 56), coincides with the set of normal vectors to the coordinate surfaces

$$\mathbf{g}^i := \partial_{\mathbf{X}} \Pi^i, \quad (i = 1, 2, 3). \quad (\text{A.8})$$

The components of a vector  $\mathbf{a}$  can be either expressed in the natural basis or in the reciprocal basis

$$\mathbf{a} = a^i \mathbf{g}_i = a_i \mathbf{g}^i, \quad (i = 1, 2, 3), \quad (\text{A.9})$$

where we applied Einstein notation for the summation over repeated indices. We call  $(a^1, a^2, a^3)$  the contravariant components of  $\mathbf{a}$  and  $(a_1, a_2, a_3)$  its covariant components. For the spatial differentiation in curvilinear coordinates, it is convenient to introduce the *Christoffel symbols*

$$\Gamma_{ij}^k := (\partial_{q^j} \mathbf{g}_i) \cdot \mathbf{g}^k = -(\partial_{q^j} \mathbf{g}^k) \cdot \mathbf{g}_i, \quad (i, j, k = 1, 2, 3), \quad (\text{A.10})$$

which describe the change of the basis vectors with regard to its coordinates, again expressed in terms of the basis vectors, that is

$$\partial_{q^j} \mathbf{g}_i = \Gamma_{ij}^k \mathbf{g}_k, \quad \partial_{q^j} \mathbf{g}^i = -\Gamma_{jk}^i \mathbf{g}^k, \quad (i, j, k = 1, 2, 3). \quad (\text{A.11})$$

The Christoffel symbols may also be regarded as the contra- and covariant components of the vectors  $\partial_{q^j} \mathbf{g}_i$ .

## A.2.2 Tensors in Cartesian Coordinates

The coordinate mapping for right-handed Cartesian coordinates  $(x, y, z)$  writes

$$\boldsymbol{\Pi}_D(\mathbf{X}) = \begin{pmatrix} q^1 \\ q^2 \\ q^3 \end{pmatrix} := \begin{pmatrix} x \\ y \\ z \end{pmatrix} \in \mathbb{R}^3, \quad \mathbf{X} = \boldsymbol{\Pi}_D^{-1}(x, y, z), \quad (\text{A.12})$$

which form plane, orthogonal and equidistant coordinate surfaces. For Cartesian coordinates, the tangent and gradient vectors are defined as

$$\mathbf{g}_1 = \mathbf{e}_x^D = \mathbf{g}^1, \quad (\text{A.13a})$$

$$\mathbf{g}_2 = \mathbf{e}_y^D = \mathbf{g}^2, \quad (\text{A.13b})$$

$$\mathbf{g}_3 = \mathbf{e}_z^D = \mathbf{g}^3. \quad (\text{A.13c})$$

and coincide with the set of unit vectors  $(\mathbf{e}_x^D, \mathbf{e}_y^D, \mathbf{e}_z^D)$ . We write and define

$${}_D \mathbf{a} := \begin{pmatrix} a_x \\ a_y \\ a_z \end{pmatrix} = \begin{pmatrix} \mathbf{a} \cdot \mathbf{e}_x^D \\ \mathbf{a} \cdot \mathbf{e}_y^D \\ \mathbf{a} \cdot \mathbf{e}_z^D \end{pmatrix} \in \mathbb{R}^3 \quad (\text{A.14})$$

for the mapping of a vector  $\mathbf{a}$  to its Cartesian components  $(a_x, a_y, a_z)$ . Similarly, we write and define

$$\begin{aligned} {}_D\mathbf{A} &:= \begin{pmatrix} A_{xx} & A_{xy} & A_{xz} \\ A_{yx} & A_{yy} & A_{yz} \\ A_{zx} & A_{zy} & A_{zz} \end{pmatrix} \\ &= \begin{pmatrix} (\mathbf{A} \cdot \mathbf{e}_x^D) \cdot \mathbf{e}_x^D & (\mathbf{A} \cdot \mathbf{e}_x^D) \cdot \mathbf{e}_y^D & (\mathbf{A} \cdot \mathbf{e}_x^D) \cdot \mathbf{e}_z^D \\ (\mathbf{A} \cdot \mathbf{e}_y^D) \cdot \mathbf{e}_x^D & (\mathbf{A} \cdot \mathbf{e}_y^D) \cdot \mathbf{e}_y^D & (\mathbf{A} \cdot \mathbf{e}_y^D) \cdot \mathbf{e}_z^D \\ (\mathbf{A} \cdot \mathbf{e}_z^D) \cdot \mathbf{e}_x^D & (\mathbf{A} \cdot \mathbf{e}_z^D) \cdot \mathbf{e}_y^D & (\mathbf{A} \cdot \mathbf{e}_z^D) \cdot \mathbf{e}_z^D \end{pmatrix} \in \mathbb{R}^{3 \times 3} \quad (\text{A.15}) \end{aligned}$$

for the component mapping of a tensor  $\mathbf{A}$ . For the Cartesian coordinates the we find that all Christoffel symbols are identically zero

$$\Gamma_{ij}^k \equiv 0, \quad (i, j, k = 1, 2, 3), \quad (\text{A.16})$$

and, therefore, we write the gradient of a scalar field  $f$ , defined by (A.1), as

$$\begin{aligned} \partial_{\mathbf{X}} f &= \partial_{q^i} f \mathbf{g}^i \\ &= \partial_x f \mathbf{e}_x^D + \partial_y f \mathbf{e}_y^D + \partial_z f \mathbf{e}_z^D, \quad (\text{A.17}) \end{aligned}$$

or, with (A.14), in component form

$${}_D(\partial_{\mathbf{X}} f) = \begin{pmatrix} \partial_x f \\ \partial_y f \\ \partial_z f \end{pmatrix}. \quad (\text{A.18})$$

The gradient of a vector field  $\mathbf{u} = u^i \mathbf{g}_i = u_i \mathbf{g}^i$  with physical components  $(u_x, u_y, u_z) = (u_1, u_2, u_3)$  in Cartesian coordinates writes

$$\begin{aligned} \mathbf{H} &= \partial_{\mathbf{X}} \mathbf{u} = \partial_{q^j} (u_i \mathbf{g}^i) \otimes \mathbf{g}^j = \overbrace{(\partial_{q^j} u_i - \Gamma_{ij}^k u_k)}^{=: H_{ij}} \mathbf{g}^i \otimes \mathbf{g}^j \\ &= \partial_x u_x \mathbf{e}_x^D \otimes \mathbf{e}_x^D + \partial_y u_x \mathbf{e}_x^D \otimes \mathbf{e}_y^D + \partial_z u_x \mathbf{e}_x^D \otimes \mathbf{e}_z^D \\ &\quad + \partial_x u_y \mathbf{e}_y^D \otimes \mathbf{e}_x^D + \partial_y u_y \mathbf{e}_y^D \otimes \mathbf{e}_y^D + \partial_z u_y \mathbf{e}_y^D \otimes \mathbf{e}_z^D \\ &\quad + \partial_x u_z \mathbf{e}_z^D \otimes \mathbf{e}_x^D + \partial_y u_z \mathbf{e}_z^D \otimes \mathbf{e}_y^D + \partial_z u_z \mathbf{e}_z^D \otimes \mathbf{e}_z^D, \quad (\text{A.19}) \end{aligned}$$

or, with (A.15), in component form

$${}_D\mathbf{H} = {}_D(\partial_{\mathbf{X}} \mathbf{u}) = \begin{pmatrix} \partial_x u_x & \partial_y u_x & \partial_z u_x \\ \partial_x u_y & \partial_y u_y & \partial_z u_y \\ \partial_x u_z & \partial_y u_z & \partial_z u_z \end{pmatrix}. \quad (\text{A.20})$$



The divergence of the vector field  $\mathbf{u}$  writes in Cartesian coordinates as

$$(\partial_X \mathbf{u}) : \mathbf{I} = {}_D \mathbf{H} : {}_D \mathbf{I} = \partial_x u_x + \partial_y u_y + \partial_z u_z. \quad (\text{A.21})$$

### A.2.3 Tensors in Cylindrical Coordinates

The coordinate mapping for cylindrical coordinates  $(r, \varphi, z)$  writes

$$\boldsymbol{\Pi}_C(\mathbf{X}) = \begin{pmatrix} q^1 \\ q^2 \\ q^3 \end{pmatrix} := \begin{pmatrix} r \\ \varphi \\ z \end{pmatrix} \in \mathbb{R}^3, \quad \mathbf{X} = \boldsymbol{\Pi}_C^{-1}(r, \varphi, z). \quad (\text{A.22})$$

The tangent and gradient vectors are defined as

$$\mathbf{g}_1 = \mathbf{e}_r^C = \mathbf{g}^1, \quad (\text{A.23a})$$

$$\frac{1}{r} \mathbf{g}_2 = \mathbf{e}_\varphi^C = r \mathbf{g}^2, \quad (\text{A.23b})$$

$$\mathbf{g}_3 = \mathbf{e}_z^C = \mathbf{g}^3, \quad (\text{A.23c})$$

which also defines the set of unit vectors  $(\mathbf{e}_r^C, \mathbf{e}_\varphi^C, \mathbf{e}_z^C)$ . We write and define

$${}_C \mathbf{a} := \begin{pmatrix} a_r \\ a_\varphi \\ a_z \end{pmatrix} = \begin{pmatrix} \mathbf{a} \cdot \mathbf{e}_r^C \\ \mathbf{a} \cdot \mathbf{e}_\varphi^C \\ \mathbf{a} \cdot \mathbf{e}_z^C \end{pmatrix} \in \mathbb{R}^3 \quad (\text{A.24})$$

for the mapping of a vector  $\mathbf{a}$  to its cylindrical components  $(a_r, a_\varphi, a_z)$ . Similarly, we write and define

$$\begin{aligned} {}_C \mathbf{A} &:= \begin{pmatrix} A_{rr} & A_{r\varphi} & A_{rz} \\ A_{\varphi r} & A_{\varphi\varphi} & A_{\varphi z} \\ A_{zr} & A_{z\varphi} & A_{zz} \end{pmatrix} \\ &= \begin{pmatrix} (\mathbf{A} \cdot \mathbf{e}_r^C) \cdot \mathbf{e}_r^C & (\mathbf{A} \cdot \mathbf{e}_r^C) \cdot \mathbf{e}_\varphi^C & (\mathbf{A} \cdot \mathbf{e}_r^C) \cdot \mathbf{e}_z^C \\ (\mathbf{A} \cdot \mathbf{e}_\varphi^C) \cdot \mathbf{e}_r^C & (\mathbf{A} \cdot \mathbf{e}_\varphi^C) \cdot \mathbf{e}_\varphi^C & (\mathbf{A} \cdot \mathbf{e}_\varphi^C) \cdot \mathbf{e}_z^C \\ (\mathbf{A} \cdot \mathbf{e}_z^C) \cdot \mathbf{e}_r^C & (\mathbf{A} \cdot \mathbf{e}_z^C) \cdot \mathbf{e}_\varphi^C & (\mathbf{A} \cdot \mathbf{e}_z^C) \cdot \mathbf{e}_z^C \end{pmatrix} \in \mathbb{R}^{3 \times 3} \end{aligned} \quad (\text{A.25})$$

for the component mapping of a tensor  $\mathbf{A}$ . The non-zero Christoffel symbols of the cylindrical coordinate mapping are

$$\Gamma_{12}^2 = \Gamma_{21}^2 = \frac{1}{r}, \quad \Gamma_{22}^1 = -r, \quad (\text{A.26})$$

and, therefore, we write the gradient of a scalar field  $f$ , defined by (A.1), as

$$\begin{aligned}\partial_{\mathbf{X}}f &= \partial_{q^i}f \mathbf{g}^i \\ &= \partial_r f \mathbf{e}_r^C + \frac{1}{r} \partial_\varphi f \mathbf{e}_\varphi^C + \partial_z f \mathbf{e}_z^C,\end{aligned}\quad (\text{A.27})$$

or, with (A.24), in component form

$${}_C(\partial_{\mathbf{X}}f) = \begin{pmatrix} \partial_r f \\ (\partial_\varphi f)/r \\ \partial_z f \end{pmatrix}.\quad (\text{A.28})$$

The gradient of a vector field  $\mathbf{u} = u^i \mathbf{g}_i = u_i \mathbf{g}^i$  and physical components  $(u_r, u_\varphi, u_z) = (u_1, u_2/r, u_3)$  in cylindrical coordinates writes

$$\begin{aligned}\mathbf{H} = \partial_{\mathbf{X}}\mathbf{u} &= \partial_{q^j}(u_i \mathbf{g}^i) \otimes \mathbf{g}^j = \overbrace{(\partial_{q^j}u_i - \Gamma_{ij}^k u_k)}{=: H_{ij}} \mathbf{g}^i \otimes \mathbf{g}^j \\ &= \partial_r u_r \mathbf{e}_r^C \otimes \mathbf{e}_r^C + \frac{1}{r}(\partial_\varphi u_r - u_\varphi) \mathbf{e}_r^C \otimes \mathbf{e}_\varphi^C + \partial_z u_r \mathbf{e}_r^C \otimes \mathbf{e}_z^C \\ &\quad + \partial_r u_\varphi \mathbf{e}_\varphi^C \otimes \mathbf{e}_r^C + \frac{1}{r}(\partial_\varphi u_\varphi + u_r) \mathbf{e}_\varphi^C \otimes \mathbf{e}_\varphi^C + \partial_z u_\varphi \mathbf{e}_\varphi^C \otimes \mathbf{e}_z^C \\ &\quad + \partial_r u_z \mathbf{e}_z^C \otimes \mathbf{e}_r^C + \frac{1}{r} \partial_\varphi u_z \mathbf{e}_z^C \otimes \mathbf{e}_\varphi^C + \partial_z u_z \mathbf{e}_z^C \otimes \mathbf{e}_z^C,\end{aligned}\quad (\text{A.29})$$

or, with (A.25), in component form

$${}_C\mathbf{H} = {}_C(\partial_{\mathbf{X}}\mathbf{u}) = \begin{pmatrix} \partial_r u_r & (\partial_\varphi u_r - u_\varphi)/r & \partial_z u_r \\ \partial_r u_\varphi & (\partial_\varphi u_\varphi + u_r)/r & \partial_z u_\varphi \\ \partial_r u_z & (\partial_\varphi u_z)/r & \partial_z u_z \end{pmatrix}.\quad (\text{A.30})$$

The divergence of the vector field  $\mathbf{u}$  in cylindrical coordinates writes

$$(\partial_{\mathbf{X}}\mathbf{u}) : \mathbf{I} = {}_C\mathbf{H} : {}_C\mathbf{I} = \partial_r u_r + \frac{1}{r}(\partial_\varphi u_\varphi + u_r) + \partial_z u_z.\quad (\text{A.31})$$

### A.2.4 Evaluations for General Curvilinear Coordinates

The evaluation of the velocity terms in (2.9) for general curvilinear coordinates writes

$$\mathbf{V}^I = \dot{\mathbf{X}} = \dot{X}^i \mathbf{g}_i = \dot{X}_i \mathbf{g}^i, \quad (\text{A.32a})$$

$$\mathbf{V}^{II} = \partial_t \mathbf{u} = \partial_t u^i \mathbf{g}_i = \partial_t u_i \mathbf{g}^i, \quad (\text{A.32b})$$

$$\begin{aligned} \mathbf{V}^{III} &= (\partial_X \mathbf{u}) \dot{\mathbf{X}} = \mathbf{H} \dot{\mathbf{X}} = (H_{ij} \mathbf{g}^i \otimes \mathbf{g}^j) \dot{X}^k \mathbf{g}_k \\ &= H_{ij} \dot{X}^k \delta_k^j \mathbf{g}^i = H_{ij} \dot{X}^j \mathbf{g}^i. \end{aligned} \quad (\text{A.32c})$$

The acceleration terms in (2.10) become

$$\mathbf{A}^I = \ddot{\mathbf{X}} = \ddot{X}^i \mathbf{g}_i = \ddot{X}_i \mathbf{g}^i, \quad (\text{A.33a})$$

$$\mathbf{A}^{II} = \partial_t^2 \mathbf{u} = \partial_t^2 u^i \mathbf{g}_i = \partial_t^2 u_i \mathbf{g}^i, \quad (\text{A.33b})$$

$$\begin{aligned} \mathbf{A}^{III} &= 2\partial_t(\partial_X \mathbf{u}) \dot{\mathbf{X}} = 2\partial_t \mathbf{H} \dot{\mathbf{X}} = 2\partial_t(H_{ij} \mathbf{g}^i \otimes \mathbf{g}^j) \dot{X}^k \mathbf{g}_k \\ &= 2\partial_t H_{ij} \dot{X}^k \delta_k^j \mathbf{g}^i = 2\partial_t H_{ij} \dot{X}^j \mathbf{g}^i, \end{aligned} \quad (\text{A.33c})$$

$$\begin{aligned} \mathbf{A}^{IV} &= [(\partial_X \partial_X \mathbf{u}) \dot{\mathbf{X}}] \dot{\mathbf{X}} = [(\partial_X \mathbf{H}) \dot{\mathbf{X}}] \dot{\mathbf{X}} \\ &= [(\partial_{q^k} \{H_{ij} \mathbf{g}^i \otimes \mathbf{g}^j\}) \otimes \mathbf{g}^k] \dot{X}^m \mathbf{g}_m \dot{X}^n \mathbf{g}_n \\ &= (\partial_{q^k} H_{ij} - \Gamma_{ki}^l H_{lj} - \Gamma_{kj}^l H_{il}) \dot{X}^m \dot{X}^n \delta_m^k \delta_n^j \mathbf{g}^i \\ &= (\partial_{q^k} H_{ij} - \Gamma_{ki}^l H_{lj} - \Gamma_{kj}^l H_{il}) \dot{X}^k \dot{X}^j \mathbf{g}^i, \end{aligned} \quad (\text{A.33d})$$

$$\begin{aligned} \mathbf{A}^V &= (\partial_X \mathbf{u}) \ddot{\mathbf{X}} = \mathbf{H} \ddot{\mathbf{X}} = (H_{ij} \mathbf{g}^i \otimes \mathbf{g}^j) \ddot{X}^k \mathbf{g}_k \\ &= H_{ij} \ddot{X}^k \delta_k^j \mathbf{g}^i = H_{ij} \ddot{X}^j \mathbf{g}^i. \end{aligned} \quad (\text{A.33e})$$

### A.2.5 Evaluations for Plane Periodic Plate

The motion of the reference configuration of a plane periodic plate with velocity  $V_x e_x^D$  is described by

$$\dot{\mathbf{X}} = V_x e_x^D = V_x \mathbf{g}_1 = V_x \mathbf{g}^1 \quad (\text{A.34})$$

$$\ddot{\mathbf{X}} = \mathbf{0}. \quad (\text{A.35})$$

The contra- and covariant components of the velocity and acceleration of the reference configuration, expressed in Cartesian coordinates, are

$$\begin{pmatrix} \dot{X}^1 \\ \dot{X}^2 \\ \dot{X}^3 \end{pmatrix} = \begin{pmatrix} V_x \\ 0 \\ 0 \end{pmatrix} = \begin{pmatrix} \dot{X}_1 \\ \dot{X}_2 \\ \dot{X}_3 \end{pmatrix}, \quad \begin{pmatrix} \ddot{X}^1 \\ \ddot{X}^2 \\ \ddot{X}^3 \end{pmatrix} = \begin{pmatrix} 0 \\ 0 \\ 0 \end{pmatrix} = \begin{pmatrix} \ddot{X}_1 \\ \ddot{X}_2 \\ \ddot{X}_3 \end{pmatrix}. \quad (\text{A.36})$$

For this particular reference motion, we find the terms of the velocity field of the deformed configuration

$$\mathbf{V}^I = \dot{X}_i \mathbf{g}^i = \dot{X}_1 \mathbf{g}^1 = V_x \mathbf{e}_x^D, \quad (\text{A.37a})$$

$$\mathbf{V}^{II} = \partial_t u_i \mathbf{g}^i = \partial_t u_x \mathbf{e}_x^D + \partial_t u_y \mathbf{e}_y^D + \partial_t u_z \mathbf{e}_z^D, \quad (\text{A.37b})$$

$$\begin{aligned} \mathbf{V}^{III} &= H_{ij} \dot{X}^j \mathbf{g}^i = H_{i1} \dot{X}^1 \mathbf{g}^i = \partial_x u_i V_x \mathbf{g}^i \\ &= V_x [\partial_x u_x \mathbf{e}_x^D + \partial_y u_y \mathbf{e}_y^D + \partial_z u_z \mathbf{e}_z^D]. \end{aligned} \quad (\text{A.37c})$$

The corresponding acceleration terms are

$$\mathbf{A}^I = \ddot{X}_i \mathbf{g}^i = \mathbf{0}, \quad (\text{A.38a})$$

$$\mathbf{A}^{II} = \partial_t^2 u_i \mathbf{g}^i = \partial_t^2 u_x \mathbf{e}_x^D + \partial_t^2 u_y \mathbf{e}_y^D + \partial_t^2 u_z \mathbf{e}_z^D, \quad (\text{A.38b})$$

$$\begin{aligned} \mathbf{A}^{III} &= 2\partial_t H_{ij} \dot{X}^j \mathbf{g}^i = 2\partial_t H_{i1} \dot{X}^1 \mathbf{g}^i = 2\partial_t \partial_x u_i V_x \mathbf{g}^i \\ &= 2V_x [\partial_t \partial_x u_x \mathbf{e}_x^D + \partial_t \partial_y u_y \mathbf{e}_y^D + \partial_t \partial_z u_z \mathbf{e}_z^D], \end{aligned} \quad (\text{A.38c})$$

$$\begin{aligned} \mathbf{A}^{IV} &= (\partial_{q^k} H_{ij} - \Gamma_{ki}^l H_{lj} - \Gamma_{kj}^l H_{il}) \dot{X}^k \dot{X}^j \mathbf{g}^i \\ &= \partial_{q^1} H_{i1} \dot{X}^1 \dot{X}^1 \mathbf{g}^i = \partial_x H_{i1} V_x \cdot V_x \mathbf{g}^i = V_x^2 [\partial_x (\partial_x u_i)] \mathbf{g}^i \\ &= V_x^2 [\partial_x^2 u_x \mathbf{e}_x^D + \partial_x^2 u_y \mathbf{e}_y^D + \partial_x^2 u_z \mathbf{e}_z^D], \end{aligned} \quad (\text{A.38d})$$

$$\mathbf{A}^V = H_{ij} \ddot{X}^j \mathbf{g}^i = \mathbf{0}. \quad (\text{A.38e})$$

In component form we write

$$\begin{aligned} {}_D \mathbf{V} &= {}_D (\mathbf{V}^I + \mathbf{V}^{II} + \mathbf{V}^{III}) \\ &= \begin{pmatrix} \partial_t u_x \\ \partial_t u_y \\ \partial_t u_z \end{pmatrix} + V_x \begin{pmatrix} 1 + \partial_x u_x \\ \partial_x u_y \\ \partial_x u_z \end{pmatrix} \end{aligned} \quad (\text{A.39})$$

and

$$\begin{aligned} {}_D\mathbf{A} &= {}_D(\mathbf{A}^{\text{I}} + \mathbf{A}^{\text{II}} + \mathbf{A}^{\text{III}} + \mathbf{A}^{\text{IV}} + \mathbf{A}^{\text{V}}) \\ &= \begin{pmatrix} \partial_t^2 u_x \\ \partial_t^2 u_y \\ \partial_t^2 u_z \end{pmatrix} + 2V_x \begin{pmatrix} \partial_t \partial_x u_x \\ \partial_t \partial_x u_y \\ \partial_t \partial_x u_z \end{pmatrix} + V_x^2 \begin{pmatrix} \partial_x^2 u_x \\ \partial_x^2 u_y \\ \partial_x^2 u_z \end{pmatrix}. \end{aligned} \quad (\text{A.40})$$

### A.2.6 Evaluations for Axisymmetric Disk

The motion of the reference configuration of an axisymmetric disk with angular velocity  $\boldsymbol{\Omega} = \Omega \mathbf{e}_z^C$  is described by

$$\dot{\mathbf{X}} = \boldsymbol{\Omega} \times \mathbf{X} = r\Omega \mathbf{e}_\varphi^C = \Omega \mathbf{g}_2 = r^2 \Omega \mathbf{g}^2 \quad (\text{A.41})$$

$$\ddot{\mathbf{X}} = \boldsymbol{\Omega} \times (\boldsymbol{\Omega} \times \mathbf{X}) = -r\Omega^2 \mathbf{e}_r^C = -r\Omega^2 \mathbf{g}_1 = -r\Omega^2 \mathbf{g}^1 \quad (\text{A.42})$$

The contra- and covariant components of the velocity and acceleration of the reference configuration, expressed in cylindrical coordinates, are

$$\begin{pmatrix} \dot{X}^1 \\ r\dot{X}^2 \\ \dot{X}^3 \end{pmatrix} = \begin{pmatrix} 0 \\ r\Omega \\ 0 \end{pmatrix} = \begin{pmatrix} \dot{X}_1 \\ \dot{X}_2/r \\ \dot{X}_3 \end{pmatrix}, \quad \begin{pmatrix} \ddot{X}^1 \\ r\ddot{X}^2 \\ \ddot{X}^3 \end{pmatrix} = \begin{pmatrix} -r\Omega^2 \\ 0 \\ 0 \end{pmatrix} = \begin{pmatrix} \ddot{X}_1 \\ \ddot{X}_2/r \\ \ddot{X}_3 \end{pmatrix}. \quad (\text{A.43})$$

For this particular reference motion, we find the terms of the velocity field of the deformed configuration

$$\mathbf{V}^{\text{I}} = \dot{X}_i \mathbf{g}^i = \dot{X}_2 \mathbf{g}^2 = r^2 \Omega \mathbf{g}^2 = r\Omega \mathbf{e}_\varphi^C \quad (\text{A.44a})$$

$$\mathbf{V}^{\text{II}} = \partial_t u_i \mathbf{g}^i = \partial_t u_r \mathbf{e}_r^C + \partial_t u_\varphi \mathbf{e}_\varphi^C + \partial_t u_z \mathbf{e}_z^C \quad (\text{A.44b})$$

$$\begin{aligned} \mathbf{V}^{\text{III}} &= H_{ij} \dot{X}^j \mathbf{g}^i = H_{i2} \dot{X}^2 \mathbf{g}^i = (\partial_\varphi u_i - \Gamma_{i2}^k u_k) \Omega \mathbf{g}^i \\ &= \Omega [(\partial_\varphi u_r - u_\varphi) \mathbf{e}_r^C + (\partial_\varphi u_\varphi + \partial_t u_r) \mathbf{e}_\varphi^C + \partial_\varphi u_z \mathbf{e}_z^C]. \end{aligned} \quad (\text{A.44c})$$

The corresponding acceleration terms are

$$\mathbf{A}^I = \ddot{X}_i \mathbf{g}^i = \ddot{X}_1 \mathbf{g}^1 = -r\Omega^2 \mathbf{g}^1 = -r\Omega^2 \mathbf{e}_r^C \quad (\text{A.45a})$$

$$\mathbf{A}^{II} = \partial_t^2 u_i \mathbf{g}^i = \partial_t^2 u_r \mathbf{e}_r^C + \partial_t^2 u_\varphi \mathbf{e}_\varphi^C + \partial_t^2 u_z \mathbf{e}_z^C \quad (\text{A.45b})$$

$$\begin{aligned} \mathbf{A}^{III} &= 2\partial_t H_{ij} \dot{X}^j \mathbf{g}^i = 2\partial_t H_{i2} \dot{X}^2 \mathbf{g}^i = 2\partial_t (\partial_\varphi u_i - \Gamma_{i2}^k u_k) \Omega \mathbf{g}^i \\ &= 2\Omega [(\partial_t \partial_\varphi u_r - \partial_t u_\varphi) \mathbf{e}_r^C + (\partial_t \partial_\varphi u_\varphi + \partial_t u_r) \mathbf{e}_\varphi^C + \partial_t \partial_\varphi u_z \mathbf{e}_z^C] \end{aligned} \quad (\text{A.45c})$$

$$\begin{aligned} \mathbf{A}^{IV} &= (\partial_{q^k} H_{ij} - \Gamma_{ki}^l H_{lj} - \Gamma_{kj}^l H_{il}) \dot{X}^k \dot{X}^j \mathbf{g}^i \\ &= (\partial_{q^2} H_{i2} - \Gamma_{2i}^l H_{l2} - \Gamma_{22}^l H_{il}) \dot{X}^2 \dot{X}^2 \mathbf{g}^i \\ &= (\partial_\varphi H_{i2} - \Gamma_{2i}^l H_{l2} - \Gamma_{22}^l H_{il}) \Omega \cdot \Omega \mathbf{g}^i \\ &= \Omega^2 [\partial_\varphi (\partial_\varphi u_i - \Gamma_{i2}^l u_l) - \Gamma_{2i}^l (\partial_\varphi u_l - \Gamma_{l2}^m u_m) \\ &\quad + r(\partial_r u_i - \Gamma_{i1}^2 u_2)] \mathbf{g}^i \\ &= \Omega^2 [(\partial_\varphi^2 u_r - 2\partial_\varphi u_\varphi - u_r + r\partial_r u_r) \mathbf{e}_r^C \\ &\quad + (\partial_\varphi^2 u_\varphi + 2\partial_\varphi u_r - u_\varphi + r\partial_r u_\varphi) \mathbf{e}_\varphi^C \\ &\quad + (\partial_\varphi^2 u_z + r\partial_r u_z) \mathbf{e}_z^C] \end{aligned} \quad (\text{A.45d})$$

$$\begin{aligned} \mathbf{A}^V &= H_{ij} \ddot{X}^j \mathbf{g}^i = H_{i1} \ddot{X}^1 \mathbf{g}^i = -(\partial_r u_i - \Gamma_{i1}^2 u_2) r \Omega^2 \mathbf{g}^i \\ &= \Omega^2 [-r\partial_r u_r \mathbf{e}_r^C - r\partial_r u_\varphi \mathbf{e}_\varphi^C - r\partial_r u_z \mathbf{e}_z^C]. \end{aligned} \quad (\text{A.45e})$$

In component form we write

$$\begin{aligned} {}_C \mathbf{V} &= {}_C (\mathbf{V}^I + \mathbf{V}^{II} + \mathbf{V}^{III}) \\ &= \begin{pmatrix} \partial_t u_r \\ \partial_t u_\varphi \\ \partial_t u_z \end{pmatrix} + \Omega \begin{pmatrix} \partial_\varphi u_r - u_\varphi \\ \partial_\varphi u_\varphi + u_r + r \\ \partial_\varphi u_z \end{pmatrix} \end{aligned} \quad (\text{A.46})$$

and

$$\begin{aligned} {}_C \mathbf{A} &= {}_C (\mathbf{A}^I + \mathbf{A}^{II} + \mathbf{A}^{III} + \mathbf{A}^{IV} + \mathbf{A}^V) \\ &= \begin{pmatrix} \partial_t^2 u_r \\ \partial_t^2 u_\varphi \\ \partial_t^2 u_z \end{pmatrix} + 2\Omega \begin{pmatrix} \partial_t \partial_\varphi u_r - \partial_t u_\varphi \\ \partial_t \partial_\varphi u_\varphi + \partial_t u_r \\ \partial_t \partial_\varphi u_z \end{pmatrix} + \Omega^2 \begin{pmatrix} \partial_\varphi^2 u_r - 2\partial_\varphi u_\varphi - u_r - r \\ \partial_\varphi^2 u_\varphi + 2\partial_\varphi u_r - u_\varphi \\ \partial_\varphi^2 u_z \end{pmatrix}. \end{aligned} \quad (\text{A.47})$$

### A.3 Implementation of Semi-analytical Model

For the eigenvalue problem (3.8) we express the solid perturbation equations (3.4) as

$$0 = \left[ \begin{pmatrix} A_{11}^s & A_{12}^s & 0 & 0 \\ A_{21}^s & A_{22}^s & 0 & 0 \\ 0 & 0 & 1 & 0 \\ 0 & 0 & 0 & 1 \end{pmatrix} - \omega \begin{pmatrix} B_{11}^s & 0 & B_{13}^s & 0 \\ 0 & B_{22}^s & 0 & B_{24}^s \\ 1 & 0 & 0 & 0 \\ 0 & 1 & 0 & 0 \end{pmatrix} \right] \begin{pmatrix} \hat{u}_x^s \\ \hat{u}_z^s \\ \omega \hat{u}_x^s \\ \omega \hat{u}_z^s \end{pmatrix}, \quad (\text{A.48})$$

with the coefficients

$$\begin{aligned} A_{11}^s &:= c_2^2 \mathcal{D}_z^2 + k^2 (\bar{v}_x^{s2} - c_1^2), & A_{12}^s &:= -jk(c_1^2 - c_2^2) \mathcal{D}_z, \\ B_{11}^s &:= 2k\bar{v}_x, & B_{13}^s &:= -1, \\ A_{21}^s &:= -jk(c_1^2 - c_2^2) \mathcal{D}_z, & A_{22}^s &:= c_1^2 \mathcal{D}_z^2 + k^2 (\bar{v}_x^{s2} - c_2^2), \\ B_{22}^s &:= 2k\bar{v}_x, & B_{24}^s &:= -1. \end{aligned} \quad (\text{A.49})$$

For the definition of the boundary and interface conditions we introduce the auxiliary variables of the form

$$\begin{pmatrix} \hat{u}_x \\ \hat{u}_z \\ \hat{v}_x \\ \hat{v}_z \\ \hat{a}_x \\ \hat{a}_z \\ \hat{\sigma}_{xz} \\ \hat{\sigma}_{zz} \end{pmatrix} = \left[ \begin{pmatrix} a_{11}^s & 0 & 0 & 0 \\ 0 & a_{22}^s & 0 & 0 \\ 0 & 0 & a_{33}^s & 0 \\ 0 & 0 & 0 & a_{44}^s \\ 0 & 0 & 0 & 0 \\ 0 & 0 & 0 & 0 \\ a_{71}^s & a_{72}^s & 0 & 0 \\ a_{81}^s & a_{82}^s & 0 & 0 \end{pmatrix} - \omega \begin{pmatrix} 0 & 0 & 0 & 0 \\ 0 & 0 & 0 & 0 \\ 0 & 0 & 0 & 0 \\ 0 & 0 & 0 & 0 \\ 0 & 0 & b_{53}^s & 0 \\ 0 & 0 & 0 & b_{64}^s \\ 0 & 0 & 0 & 0 \\ 0 & 0 & 0 & 0 \end{pmatrix} \right] \begin{pmatrix} \hat{u}_x \\ \hat{u}_z \\ \omega \hat{u}_x \\ \omega \hat{u}_z \end{pmatrix}, \quad (\text{A.50})$$

with the coefficients

$$\begin{aligned} a_{11}^s &:= 1, & a_{22}^s &:= 1, \\ a_{33}^s &:= j, & a_{44}^s &:= j, \\ b_{53}^s &:= 1, & b_{64}^s &:= 1, \\ a_{71}^s &:= \mu^s \mathcal{D}_z, & a_{72}^s &:= -jk\mu^s, \\ a_{81}^s &:= -jk\lambda^s, & a_{82}^s &:= (\lambda^s + 2\mu^s) \mathcal{D}_z. \end{aligned} \quad (\text{A.51})$$

Similarly, we express the fluid perturbation equation (3.7) as

$$0 = [(A_{11}^f) - \omega (B_{11}^f)] (\hat{v}_z^f) \quad (\text{A.52})$$

with the coefficients

$$\begin{aligned} A_{11}^f &:= jk\varrho^f \left[ \frac{d^2 \bar{v}_x^f}{dz^2} - \bar{v}_x^f (\mathcal{D}_z^2 - k^2) \right] - \mu^f (\mathcal{D}_z^2 - k^2)^2, \\ B_{11}^f &:= -j\varrho^f (\mathcal{D}_z^2 - k^2). \end{aligned} \quad (\text{A.53})$$

The auxiliary variables then write

$$\begin{pmatrix} \hat{v}_x^f \\ \hat{v}_z^f \\ \hat{p} \\ \hat{\sigma}_{xz}^f \\ \hat{\sigma}_{zz}^f \end{pmatrix} = \left[ \begin{pmatrix} a_{11}^f \\ a_{21}^f \\ a_{31}^f \\ a_{41}^f \\ a_{51}^f \end{pmatrix} - \omega \begin{pmatrix} 0 \\ 0 \\ b_{31}^f \\ 0 \\ b_{51}^f \end{pmatrix} \right] (\hat{v}_z^f), \quad (\text{A.54})$$

with the coefficients

$$\begin{aligned} a_{11}^f &:= -\frac{j}{k} \mathcal{D}_z, \\ a_{21}^f &:= 1, \\ a_{31}^f &:= \frac{\mu^f}{k^2} (\mathcal{D}_z^2 - k^2) \mathcal{D}_z + j \frac{\varrho^f}{k} \left( \bar{v}_x^f \mathcal{D}_z - \frac{d\bar{v}_z^f}{dz} \right), \quad b_{31}^f := j \frac{\varrho^f}{k^2} \mathcal{D}_z, \\ a_{41}^f &:= \mu^f (a_{11}^f \mathcal{D}_z - jk), \\ a_{51}^f &:= -a_{31}^f + 2\mu^f \mathcal{D}_z, \quad b_{51}^f := -b_{31}^f. \end{aligned} \quad (\text{A.55})$$

## A.4 Bi-orthogonality of Eigenvectors

In the present section we follow Gasch et al. (2012, pp. 231) and Nordmann (1984a, pp. 20) to prove the bi-orthogonality of left and right eigenvectors, used in §5.2.1. Let  $\mathbf{A} \in \mathbb{R}^{2N \times 2N}$  and  $\mathbf{B} \in \mathbb{R}^{2N \times 2N}$  be real square non-symmetric matrices describing the general right and left eigenvalue problems

$$(\mathbf{A} - \lambda_m \mathbf{B}) \mathbf{r}_m = \mathbf{0}, \quad (\text{A.56a})$$

$$\mathbf{l}_n^T (\mathbf{A} - \lambda_n \mathbf{B}) = \mathbf{0}^T, \quad (\text{A.56b})$$

where  $(\lambda_m, \mathbf{r}_m)$  denotes the  $m$ th right eigenpair and  $(\lambda_n, \mathbf{l}_n)$  the  $n$ th left eigenpair. Note that the left and right eigenvalue problem share its eigenvalues. We multiply  $\mathbf{l}_n^T$  to the left of (A.56a) and  $\mathbf{r}_m$  to the right of (A.56b)



to find

$$\mathbf{l}_n^\top (\mathbf{A} - \lambda_m \mathbf{B}) \mathbf{r}_m = 0, \quad (\text{A.57a})$$

$$\mathbf{l}_n^\top (\mathbf{A} - \lambda_n \mathbf{B}) \mathbf{r}_m = 0. \quad (\text{A.57b})$$

We subtract (A.57a) from (A.57b) and get

$$(\lambda_m - \lambda_n) \mathbf{l}_n^\top \mathbf{B} \mathbf{r}_m = 0. \quad (\text{A.58})$$

We assume that the eigenvalues are distinct and find the first orthogonality condition

$$\mathbf{l}_n^\top \mathbf{B} \mathbf{r}_m = \begin{cases} 0 & n \neq m, \\ b_m & n = m. \end{cases} \quad (\text{A.59})$$

Combining (A.59) with say (A.57a) we find the second orthogonality condition

$$\mathbf{l}_n^\top \mathbf{A} \mathbf{r}_m = \begin{cases} 0 & n \neq m, \\ a_m = b_m \lambda_m & n = m. \end{cases} \quad (\text{A.60})$$

We are free to normalize the eigenvectors to achieve  $b_m = 1$  and hence  $a_m = \lambda_m$ , so that  $\mathfrak{L} := (\mathbf{l}_1 \ \mathbf{l}_2 \ \cdots \ \mathbf{l}_{2N})$  and  $\mathfrak{R} := (\mathbf{r}_1 \ \mathbf{r}_2 \ \cdots \ \mathbf{r}_{2N})$  diagonalize  $\mathbf{A}$  and  $\mathbf{B}$  according to

$$\mathfrak{L}^\top \mathbf{A} \mathfrak{R} = \mathbf{\Lambda}, \quad (\text{A.61a})$$

$$\mathfrak{L}^\top \mathbf{B} \mathfrak{R} = \mathbf{I}. \quad (\text{A.61b})$$



# Measurement Data

# B

## B.1 Measured Modal Parameters

In the following pages we tabulate the modal parameters which have been estimated from the measurements as discussed in Chapter 5. The modal parameters are the *average angular frequency*  $\bar{\omega}^r$ , the *angular frequency split*  ${}_S\Delta\omega^r$ , the *damping factor*  $\delta^r$  and the dimensionless *amplitude ratio*  $\kappa$ . They are defined as

$$\bar{\omega}_m^r := \frac{1}{2}(s\omega_{m+}^r + s\omega_{m-}^r) \quad \text{in rad/s,} \quad (\text{B.1})$$

$${}_S\Delta\omega_m^r := s\omega_{m+}^r - s\omega_{m-}^r \quad \text{in rad/s,} \quad (\text{B.2})$$

$$\delta_m^r := +\omega_{m+}^i = +\omega_{m-}^i \quad \text{in s}^{-1}, \quad (\text{B.3})$$

$$\kappa_m := \frac{\max|\Psi_{m+}^R(r)|}{\max|\Psi_{m+}^S(r)|} = \frac{\max|\Psi_{m-}^R(r)|}{\max|\Psi_{m-}^S(r)|}, \quad (\text{B.4})$$

where  $m^+$  and  $m^-$  indicates a pair of co- and counter-rotating modes with  $n_{m+} \geq 0$  and  $n_{m-} \leq 0$ . See §§5.2.2 and 5.2.3 for details.

Throughout the thesis as well as for the following tables we apply the color scheme of Tab. B.0 for the coloring of the different modes.

**Tab. B.0:** Color scheme used throughout the thesis to differentiate varicose modes (dark) from sinuous modes (bright) along with their azimuthal mode number  $n$ , according to Brewer et al. (2003).

$n$	0	$\pm 1$	$\pm 2$	$\pm 3$	$\pm 4$	$\pm 5$	$\pm 6$
varicose $\Downarrow$	■	■	■	■	■	■	■
sinuous $\Uparrow$	■	■	■	■	■	■	■

**Tab. B.1:** Measured modal parameters  $(\bar{\omega}^r, {}_S\Delta\omega^r, \delta^r, \kappa)^T$  for  $h_S = 1.0$  mm,  $h_R = 1.0$  mm and  $g = 1.4$  mm.

mode	angular rotor speed $\Omega_R$ in rad/s						
	0	8.38	16.8	25.1	33.5	41.9	50.3
$(0, 1)^{\downarrow}$	439.53	439.39	434.28	431.17	417.16	407.41	384.68
	0.00	0.00	0.00	0.00	0.00	0.00	0.00
	17.36	15.45	17.71	17.70	20.46	17.65	18.86
	0.74	0.70	0.78	0.84	0.59	0.89	0.58
$(\pm 1, 0)^{\uparrow}$	530.96	527.84	526.03	521.02	510.65	497.05	480.31
	0.00	6.25	12.71	19.06	25.82	33.32	40.58
	8.05	7.72	8.93	11.54	12.77	14.51	17.45
	1.40	1.57	1.55	1.53	1.53	1.41	1.46
$(\pm 4, 0)^{\downarrow}$	912.32	909.06	906.69	902.00	889.12	870.86	859.43
	0.00	31.17	60.83	90.17	122.71	155.33	200.19
	13.01	12.19	13.17	15.49	18.48	24.66	36.31
	4.71	4.63	3.75	3.19	2.23	2.04	1.13
$(\pm 2, 0)^{\uparrow}$	1087.59	1082.76	1078.29	1071.64	1056.94	1036.76	1008.47
	0.00	14.20	27.19	40.69	54.97	70.02	85.54
	11.03	10.57	11.04	12.50	14.66	17.80	20.57
	1.68	1.68	1.66	1.53	1.45	1.32	1.23
$(\pm 1, 1)^{\downarrow}$	1277.63	1265.53	1256.77	1258.36	1247.41	1241.06	1223.73
	0.00	31.77	44.15	41.70	48.42	49.10	45.74
	35.50	26.70	23.63	23.11	22.22	21.62	20.10
	1.14	1.10	1.04	1.03	1.02	0.96	0.96
$(\pm 5, 0)^{\downarrow}$	1526.04	1521.94	1515.75	1506.31	1486.40	1456.36	1413.32
	0.00	39.83	77.39	112.96	154.41	198.38	239.45
	16.87	15.62	16.07	17.67	19.84	24.50	28.71
	3.88	3.50	2.83	2.37	1.66	1.23	0.76
$(\pm 3, 0)^{\uparrow}$	1889.73	1885.09	1876.82	1865.40	1843.74	1811.51	1767.22
	0.00	20.27	41.72	62.72	84.19	108.45	132.17
	15.12	14.20	14.81	14.96	16.52	18.62	23.05
	1.95	1.99	1.71	1.49	1.38	1.31	0.93
$(\pm 2, 1)^{\downarrow}$	1963.39	1963.35	1959.93	1954.12	1943.10	1927.89	1908.47
	0.00	14.33	23.97	35.47	47.59	59.93	73.42
	15.28	12.43	11.81	12.06	11.91	12.27	12.26
	1.05	1.01	0.98	0.94	0.89	0.82	0.77
$(\pm 1, 1)^{\uparrow}$	2277.07	2282.79	2269.56	2247.50	2214.22	2173.54	2125.86
	0.00	6.21	15.33	18.05	22.06	28.63	33.47
	24.71	20.67	22.25	21.10	22.64	26.24	26.82
	1.10	1.30	1.23	1.22	1.11	1.11	1.08
$(\pm 6, 0)^{\downarrow}$	2328.26	2326.01	2315.89	2299.74	2266.28	2220.97	2157.26
	0.00	48.28	93.09	136.50	186.33	237.14	293.64
	19.51	19.78	18.67	20.14	21.68	24.75	29.07
	2.25	2.70	1.71	1.86	1.38	0.76	0.30
$(\pm 4, 0)^{\uparrow}$	2980.68	2980.79	2966.95	2951.92	2918.56	2864.37	2796.15
	0.00	29.97	56.57	89.44	129.78	150.95	175.25
	20.63	22.03	19.15	17.03	18.48	17.47	22.98
	2.14	2.18	1.73	1.63	1.47	1.24	0.97

**Tab. B.2:** Measured modal parameters  $(\bar{\omega}^r, {}_S\Delta\omega^r, \delta^r, \kappa)^T$  for  $h_S = 1.0$  mm,  $h_R = 1.0$  mm and  $g = 2.2$  mm.

mode	angular rotor speed $\Omega_R$ in rad/s						
	0	8.38	16.8	25.1	33.5	41.9	50.3
$(0, 1)^\uparrow$	535.61	535.26	531.80	528.16	518.59	506.27	490.73
	0.00	0.00	0.00	0.00	0.00	0.00	0.00
	14.42	13.20	14.11	13.56	20.39	16.84	25.86
	0.75	0.62	0.73	0.75	0.73	0.69	0.51
$(\pm 1, 0)^\uparrow$	590.66	590.38	589.88	586.35	579.43	569.67	557.73
	0.00	7.46	13.84	19.37	24.95	31.27	38.00
	5.91	5.32	5.90	7.62	9.43	11.34	13.34
	1.29	1.42	1.47	1.49	1.40	1.41	1.32
$(\pm 4, 0)^\uparrow$	1071.77	1071.18	1070.87	1069.95	1065.44	1057.98	1049.12
	0.00	31.20	60.53	89.25	116.15	150.92	189.88
	8.48	8.55	9.68	11.91	14.43	18.84	20.22
	4.99	4.73	4.50	3.93	3.23	2.65	1.53
$(\pm 2, 0)^\uparrow$	1217.51	1216.07	1213.01	1208.46	1200.98	1189.49	1175.04
	0.00	13.43	27.10	39.95	53.20	67.35	82.50
	6.77	6.72	7.11	7.74	9.61	12.08	14.75
	1.49	1.55	1.55	1.55	1.43	1.36	1.21
$(\pm 1, 1)^\uparrow$	1365.29	1362.97	1367.70	1341.43	1336.59	1329.07	1319.54
	0.00	-14.49	-20.71	24.91	30.78	33.52	40.95
	23.57	26.78	29.52	26.86	28.76	25.69	27.77
	1.26	1.22	1.10	1.07	0.99	0.95	0.88
$(\pm 5, 0)^\uparrow$	1789.73	1788.14	1785.73	1784.76	1772.04	1758.59	1738.26
	0.00	39.54	76.37	121.13	150.87	192.13	230.84
	11.43	11.52	11.56	16.13	14.60	19.15	22.81
	4.08	3.82	3.32	2.66	2.37	1.63	0.94
$(\pm 2, 1)^\uparrow$	2088.14	2087.85	2084.19	2078.55	2069.56	2057.15	2042.43
	0.00	16.26	26.26	38.95	52.10	65.15	76.37
	13.60	11.67	10.35	10.48	10.20	11.12	12.57
	1.21	1.19	1.14	1.09	1.04	0.93	0.87
$(\pm 3, 0)^\uparrow$	2110.59	2111.54	2108.69	2101.52	2091.22	2076.66	2056.47
	0.00	21.15	42.82	65.42	88.27	110.07	129.39
	9.45	9.03	10.33	11.16	11.53	12.70	14.92
	1.68	1.82	1.72	1.62	1.45	1.41	1.25
$(\pm 1, 1)^\uparrow$	2573.34	2568.70	2558.53	2552.80	2536.48	2510.34	2478.26
	0.00	10.91	21.32	26.52	30.03	36.95	45.93
	23.88	20.91	18.85	18.98	17.61	18.22	20.43
	1.02	1.15	1.13	1.12	1.06	1.08	0.91
$(\pm 6, 0)^\uparrow$	2724.85	2722.53	2717.99	2709.34	2694.17	2670.73	2639.42
	0.00	48.29	92.79	136.92	183.59	231.91	282.76
	13.55	14.06	13.82	14.94	15.78	17.65	20.10
	2.45	3.06	1.36	2.24	2.00	1.43	0.61
$(\pm 3, 1)^\uparrow$	3089.80	3088.79	3085.08	3078.60	3067.26	3051.54	3032.16
	0.00	18.99	37.56	56.38	75.08	93.85	114.33
	26.13	24.58	24.34	23.63	23.59	23.58	22.99
	1.12	1.06	0.92	0.79	0.69	0.59	0.52

**Tab. B.3:** Measured modal parameters  $(\bar{\omega}^r, {}_S\Delta\omega^r, \delta^r, \kappa)^T$  for  $h_S = 1.0$  mm,  $h_R = 1.0$  mm and  $g = 2.9$  mm.

mode	angular rotor speed $\Omega_R$ in rad/s						
	0	8.38	16.8	25.1	33.5	41.9	50.3
$(0, 1)^{\downarrow}$	610.22	609.01	629.77	631.18	616.32	587.22	562.09
	0.00	0.00	0.00	0.00	0.00	0.00	0.00
	12.78	11.97	16.48	8.59	18.68	36.70	30.38
	0.83	0.79	0.82	0.93	0.80	0.51	0.52
$(\pm 1, 0)^{\uparrow\uparrow}$	634.02	634.56	626.90	623.81	616.89	608.19	597.02
	0.00	1.88	15.67	19.63	25.65	33.52	39.87
	3.41	3.94	4.30	5.92	7.32	9.47	11.04
	1.44	1.37	1.48	1.34	1.40	1.31	1.33
$(\pm 4, 0)^{\downarrow}$	1179.16	1178.87	1179.03	1178.71	1177.05	1165.68	1164.57
	0.00	31.51	61.01	90.27	122.78	142.04	178.50
	6.73	6.90	8.19	9.76	12.38	15.64	21.97
	5.65	5.50	5.04	4.49	3.95	2.67	1.94
$(\pm 2, 0)^{\uparrow\uparrow}$	1288.04	1288.35	1286.15	1282.08	1275.96	1267.02	1254.89
	0.00	13.17	26.13	39.14	52.41	66.84	80.80
	4.78	4.84	5.27	5.81	6.96	9.24	11.64
	1.57	1.49	1.52	1.40	1.45	1.33	1.21
$(\pm 1, 1)^{\downarrow}$	1456.02	1452.16	1450.33	1447.45	1441.50	1410.26	1407.75
	0.00	-6.57	-8.48	-6.91	-7.75	-9.15	6.31
	13.52	13.75	14.54	15.81	17.18	33.59	46.60
	1.33	1.33	1.36	1.31	1.27	1.08	0.88
$(\pm 5, 0)^{\downarrow}$	1964.77	1963.72	1961.95	1958.93	1952.78	1940.31	1927.05
	0.00	40.08	77.68	114.52	153.92	196.39	236.87
	8.90	9.06	9.22	10.57	11.89	15.00	18.91
	4.52	4.21	3.95	3.29	2.82	1.92	1.26
$(\pm 3, 0)^{\uparrow\uparrow}$	2223.42	2225.19	2223.51	2219.34	2211.69	2200.44	2185.80
	0.00	20.67	40.85	59.90	83.17	103.95	127.24
	6.34	6.51	6.92	7.71	9.03	10.98	12.52
	1.66	1.64	1.55	1.39	1.38	1.23	0.67
$(\pm 1, 1)^{\uparrow\uparrow}$	2748.78	2745.19	2741.98	2726.99	2711.84	2681.49	2656.71
	0.00	10.16	10.04	24.31	31.52	40.21	45.66
	13.39	12.65	13.38	13.61	14.35	22.00	22.59
	1.16	1.11	1.08	0.91	1.07	0.97	1.02
$(\pm 6, 0)^{\downarrow}$	2984.95	2981.94	2978.67	2972.50	2961.26	2938.66	2916.86
	0.00	47.98	92.63	137.52	186.90	238.54	289.40
	10.85	10.76	10.96	11.58	13.05	15.48	17.18
	2.88	3.42	3.74	2.38	1.99	1.64	1.19
$(\pm 3, 1)^{\downarrow}$	3238.90	3238.82	3235.38	3228.76	3224.70	3201.82	3182.12
	0.00	19.87	37.05	56.11	88.14	97.08	117.72
	13.54	12.23	12.24	13.14	16.92	25.80	24.95
	1.27	1.22	1.14	1.04	0.93	0.61	0.50
$(\pm 4, 0)^{\uparrow\uparrow}$	3465.92	3468.66	3465.82	3461.10	3452.96	3442.82	3425.97
	0.00	26.82	54.49	80.39	109.53	140.54	170.64
	7.64	8.45	8.36	8.36	9.42	13.79	13.94
	1.58	1.57	1.48	1.28	1.28	0.99	0.89

**Tab. B.4:** Measured modal parameters  $(\bar{\omega}^r, {}_S\Delta\omega^r, \delta^r, \kappa)^T$  for  $h_S = 1.0$  mm,  $h_R = 1.0$  mm and  $g = 3.6$  mm.

mode	angular rotor speed $\Omega_R$ in rad/s						
	0	8.38	16.8	25.1	33.5	41.9	50.3
$(\pm 1, 0)^{\uparrow\uparrow}$	645.82	651.06	650.82	647.78	642.48	634.33	625.14
	0.00	14.86	16.51	21.49	25.93	32.11	38.09
	4.66	4.34	3.93	5.26	6.68	8.36	9.78
	1.50	1.49	1.43	1.39	1.41	1.32	1.33
$(0, 1)^{\downarrow\downarrow}$	655.93	657.61	659.04	656.81	651.69	644.27	635.53
	0.00	0.00	0.00	0.00	0.00	0.00	0.00
	6.01	6.05	5.92	4.64	8.99	9.51	12.72
	0.76	0.65	0.68	0.67	0.75	0.63	0.70
$(\pm 4, 0)^{\downarrow\downarrow}$	1261.36	1261.74	1262.30	1261.80	1261.89	1260.28	1242.94
	0.00	31.42	61.46	89.74	124.78	151.71	174.17
	5.95	5.92	6.96	9.09	10.68	9.79	17.06
	6.08	5.37	5.51	4.95	3.97	2.93	3.42
$(\pm 2, 0)^{\uparrow\uparrow}$	1335.81	1337.27	1335.94	1332.85	1327.75	1320.86	1311.92
	0.00	13.08	25.44	38.38	51.36	65.38	79.19
	4.38	4.07	4.48	4.85	5.68	7.10	8.97
	1.53	1.44	1.47	1.46	1.41	1.36	1.26
$(\pm 1, 1)^{\downarrow\downarrow}$	1508.65	1506.96	1505.90	1505.39	1502.23	1503.87	1498.76
	0.00	-2.45	-2.95	2.91	5.67	22.29	31.58
	13.16	12.64	12.87	14.87	15.82	18.81	20.44
	1.43	1.42	1.42	1.37	1.33	1.24	1.24
$(\pm 5, 0)^{\downarrow\downarrow}$	2097.29	2097.40	2096.43	2094.89	2092.82	2086.10	2075.13
	0.00	39.71	77.37	115.59	161.37	201.49	239.75
	7.49	7.61	8.01	9.60	12.91	14.07	16.55
	4.87	4.63	4.21	3.66	3.03	2.65	1.44
$(\pm 2, 1)^{\downarrow\downarrow}$	2282.14	2278.57	2275.34	2270.08	2263.62	2253.49	2241.66
	0.00	10.79	12.73	38.22	50.46	63.20	76.55
	10.42	8.29	8.15	8.05	7.31	7.64	8.65
	1.52	1.51	1.48	1.41	1.37	1.31	1.24
$(\pm 3, 0)^{\uparrow\uparrow}$	2295.01	2296.87	2294.17	2292.42	2286.40	2278.54	2269.20
	0.00	15.14	36.47	59.19	78.87	99.24	121.82
	5.44	7.51	9.87	7.33	8.74	9.31	10.20
	1.53	1.50	1.41	1.38	1.28	1.21	1.14
$(\pm 1, 1)^{\uparrow\uparrow}$	2842.25	2839.09	2838.00	2830.26	2815.01	2798.33	2783.10
	0.00	16.09	20.43	38.57	32.53	36.83	44.43
	13.85	11.44	12.48	20.41	17.39	17.29	17.41
	1.11	1.11	1.05	0.97	1.05	1.02	0.98
$(\pm 6, 0)^{\downarrow\downarrow}$	3179.72	3178.80	3176.70	3172.68	3164.13	3152.16	3136.90
	0.00	48.37	94.36	141.20	190.85	240.31	293.80
	9.75	9.15	9.37	10.48	11.53	12.65	15.92
	2.98	4.12	2.84	3.10	2.57	1.80	1.32
$(\pm 3, 1)^{\downarrow\downarrow}$	3373.77	3372.91	3370.94	3371.05	3358.26	3345.52	3328.71
	0.00	18.92	37.03	58.43	78.33	100.45	121.27
	14.62	14.11	16.33	16.33	16.58	16.56	17.27
	1.39	1.36	1.21	1.09	0.98	0.86	0.74

**Tab. B.5:** Measured modal parameters  $(\bar{\omega}^r, {}_S\Delta\omega^r, \delta^r, \kappa)^T$  for  $h_S = 1.0$  mm,  $h_R = 1.0$  mm and  $g = 4.4$  mm.

mode	angular rotor speed $\Omega_R$ in rad/s						
	0	8.38	16.8	25.1	33.5	41.9	50.3
$(\pm 1, 0)^{\uparrow\uparrow}$	667.57	667.37	662.30	658.86	652.76	644.33	636.66
	0.00	7.47	13.85	18.75	23.92	29.54	35.78
	2.96	2.83	3.19	4.26	5.49	6.86	8.15
	1.34	1.31	1.33	1.34	1.30	1.26	1.25
$(0, 1)^{\downarrow\downarrow}$	718.18	717.74	713.96	708.79	699.13	685.58	672.91
	0.00	0.00	0.00	0.00	0.00	0.00	0.00
	11.84	11.24	11.93	14.56	14.55	17.31	15.78
	0.75	0.66	0.67	0.66	0.70	0.67	0.64
$(\pm 4, 0)^{\downarrow\downarrow}$	1343.60	1339.45	1340.93	1336.48	1327.25	1342.52	1340.13
	0.00	31.28	61.02	78.91	101.20	163.71	191.18
	3.89	4.28	3.19	4.36	6.52	14.21	13.61
	6.68	6.18	4.77	5.14	3.99	3.60	3.99
$(\pm 2, 0)^{\uparrow\uparrow}$	1361.77	1370.83	1365.10	1361.50	1356.07	1349.12	1343.24
	0.00	12.53	24.58	36.84	49.34	63.44	77.21
	4.08	3.50	4.03	4.31	4.77	5.88	7.32
	1.41	1.45	1.40	1.42	1.34	1.30	1.21
$(\pm 1, 1)^{\downarrow\downarrow}$	1550.48	1551.26	1554.52	1563.65	1568.35	1564.47	1556.94
	0.00	-11.88	-10.90	5.17	28.37	34.09	39.12
	23.86	18.13	15.41	15.94	17.00	17.84	18.77
	1.55	1.64	1.63	1.51	1.46	1.39	1.32
$(\pm 5, 0)^{\downarrow\downarrow}$	2226.41	2223.01	2222.76	2222.21	2220.45	2215.76	2210.00
	0.00	40.54	78.31	117.04	163.14	201.93	243.85
	6.46	6.87	8.55	9.10	11.56	11.40	12.42
	5.28	4.94	4.45	4.05	3.69	2.99	2.15
$(\pm 3, 0)^{\uparrow\uparrow}$	2332.68	2343.89	2338.79	2335.74	2331.70	2324.44	2318.22
	0.00	17.63	38.01	56.15	81.17	100.35	117.40
	5.55	5.03	4.84	5.11	6.77	7.86	7.11
	1.39	1.46	1.34	1.31	1.29	1.16	1.13
$(\pm 2, 1)^{\downarrow\downarrow}$	2365.93	2367.95	2367.20	2359.28	2343.10	2337.79	2330.10
	0.00	14.46	23.35	12.45	54.30	71.07	78.89
	10.01	7.51	7.37	16.14	18.28	16.94	10.74
	1.77	1.72	1.67	1.46	1.40	1.27	1.32
$(\pm 1, 1)^{\uparrow\uparrow}$	2922.48	2921.65	2911.13	2902.67	2888.90	2875.41	2861.63
	0.00	7.61	19.60	26.61	30.66	37.00	43.69
	12.97	12.90	11.81	11.68	13.71	13.79	14.37
	1.07	1.07	1.04	0.99	0.98	0.99	0.94
$(\pm 6, 0)^{\downarrow\downarrow}$	3365.12	3361.33	3358.78	3355.06	3356.38	3341.55	3333.19
	0.00	49.58	96.14	143.62	206.47	247.15	303.48
	7.68	8.23	8.77	9.45	10.82	12.23	12.60
	3.13	4.40	4.61	3.29	3.49	1.84	1.65
$(\pm 3, 1)^{\downarrow\downarrow}$	3510.66	3510.03	3504.08	3499.20	3489.22	3486.84	3466.37
	0.00	19.61	40.71	59.79	78.44	115.48	128.53
	12.95	12.30	12.85	11.92	16.14	18.66	15.12
	1.59	1.54	1.45	1.31	1.15	1.13	0.91



**Tab. B.6:** Measured modal parameters  $(\bar{\omega}^r, {}_S\Delta\omega^r, \delta^r, \kappa)^T$  for  $h_S = 1.0$  mm,  $h_R = 1.0$  mm and  $g = 6.4$  mm.

mode	angular rotor speed $\Omega_R$ in rad/s						
	0	8.38	16.8	25.1	33.5	41.9	50.3
$(\pm 1, 0)^{\uparrow\uparrow}$	700.74	702.23	703.18	699.63	694.42	686.62	677.69
	0.00	4.96	13.64	17.81	23.10	28.39	34.21
	2.49	3.97	2.58	3.14	4.17	4.90	5.76
	1.20	1.31	1.20	1.20	1.22	1.17	1.16
$(0, 1)^{\downarrow\downarrow}$	841.24	841.17	838.44	834.96	828.67	817.04	805.93
	0.00	0.00	0.00	0.00	0.00	0.00	0.00
	11.59	11.55	11.49	12.28	14.19	16.45	16.85
	0.67	0.70	0.69	0.66	0.74	0.69	0.62
$(\pm 2, 0)^{\uparrow\uparrow}$	1435.03	1435.63	1434.01	1431.12	1426.82	1420.94	1413.58
	0.00	11.61	23.07	34.94	46.79	60.08	72.93
	3.29	3.07	3.27	3.40	3.62	4.40	5.09
	1.25	1.23	1.21	1.23	1.18	1.19	1.12
$(\pm 4, 0)^{\downarrow\downarrow}$	1479.69	1480.47	1480.22	1476.01	1479.62	1479.27	1478.30
	0.00	31.71	66.17	107.62	134.47	174.48	199.54
	4.19	4.38	6.03	8.66	8.18	5.03	3.15
	7.31	7.71	7.05	5.52	5.53	4.45	5.38
$(\pm 1, 1)^{\downarrow\downarrow}$	1691.57	1687.51	1687.68	1689.54	1702.19	1698.73	1693.33
	0.00	-6.08	-6.84	-2.07	26.97	35.11	41.35
	19.60	19.67	17.73	17.77	18.57	17.89	18.77
	1.89	1.90	1.95	1.91	1.74	1.62	1.58
$(\pm 3, 0)^{\uparrow\uparrow}$	2422.06	2424.49	2423.48	2422.29	2420.29	2411.32	2405.79
	0.00	17.62	34.45	50.34	77.70	88.32	107.82
	4.39	4.14	4.70	5.19	7.08	4.91	5.36
	1.16	1.11	1.09	1.05	1.01	1.00	1.00
$(\pm 5, 0)^{\downarrow\downarrow}$	2444.15	2442.89	2446.54	2447.67	2448.76	2446.22	2443.66
	0.00	46.46	81.06	121.02	161.09	205.56	252.75
	4.94	3.42	2.46	4.50	6.31	7.28	10.14
	6.20	7.16	7.15	5.92	5.46	4.85	3.25
$(\pm 2, 1)^{\downarrow\downarrow}$	2549.16	2545.69	2545.89	2544.55	2535.07	2529.70	2522.43
	0.00	14.45	28.11	42.30	56.08	72.35	89.71
	8.47	7.75	7.83	8.38	9.44	9.94	9.79
	2.14	2.04	2.01	1.91	1.88	1.72	1.73
$(\pm 1, 1)^{\uparrow\uparrow}$	3032.70	3031.54	3028.34	3023.14	3011.47	2998.73	2985.91
	0.00	9.76	15.99	21.00	53.65	40.44	44.63
	16.23	14.79	14.17	13.76	37.57	20.07	18.34
	0.94	0.93	0.88	0.87	0.82	0.87	0.83
$(\pm 4, 0)^{\uparrow\uparrow}$	3672.33	3677.27	3675.73	3674.57	3673.11	3667.79	3667.56
	0.00	21.01	43.72	67.29	89.93	116.30	148.33
	7.85	9.33	8.12	7.94	8.00	10.34	11.97
	1.12	1.10	1.03	0.95	0.89	0.79	0.71
$(\pm 6, 0)^{\downarrow\downarrow}$	3679.96	3684.18	3684.33	3683.91	3681.81	3676.53	3673.38
	0.00	49.48	98.98	149.83	198.16	250.97	301.02
	2.41	3.02	4.72	6.08	7.83	8.40	9.53
	5.41	4.77	5.53	4.68	3.73	2.97	2.42

**Tab. B.7:** Measured modal parameters  $(\bar{\omega}^r, {}_S\Delta\omega^r, \delta^r, \kappa)^T$  for  $h_S = 1.0$  mm,  $h_R = 1.0$  mm and  $g = 9.4$  mm.

mode	angular rotor speed $\Omega_R$ in rad/s						
	0	8.38	16.8	25.1	33.5	41.9	50.3
$(\pm 1, 0)^{\uparrow\uparrow}$	728.32	725.71	723.85	720.61	714.91	707.00	698.34
	0.00	14.64	17.23	21.14	25.13	30.10	34.90
	2.78	2.86	2.58	2.67	3.36	3.77	4.62
	1.05	0.98	1.01	1.12	1.00	1.01	0.96
$(0, 1)^{\downarrow\downarrow}$	959.19	959.95	958.01	956.41	949.10	937.55	925.06
	0.00	0.00	0.00	0.00	0.00	0.00	0.00
	12.11	11.69	11.74	11.78	12.94	14.03	17.89
	0.65	0.65	0.64	0.64	0.65	0.72	0.62
$(\pm 2, 0)^{\uparrow\uparrow}$	1469.64	1479.08	1476.91	1476.75	1469.65	1463.09	1456.47
	0.00	14.03	22.66	36.41	44.14	55.97	68.52
	5.33	3.46	3.12	5.20	3.17	3.42	3.79
	1.15	1.00	1.04	1.05	1.03	0.99	0.94
$(\pm 4, 0)^{\downarrow\downarrow}$	1606.87	1606.87	1609.08	1610.92	1613.16	1617.04	1617.81
	0.00	32.68	64.34	96.98	130.49	165.21	202.40
	4.33	3.91	4.22	5.82	6.97	12.35	16.36
	9.75	9.20	8.94	8.07	7.45	5.19	3.69
$(\pm 1, 1)^{\downarrow\downarrow}$	1881.13	1917.62	1928.18	1844.44	1843.11	1839.89	1837.05
	0.00	-56.19	-74.10	25.61	29.74	35.86	44.05
	32.94	42.06	43.94	15.94	14.73	14.71	16.11
	2.11	2.53	2.13	2.48	2.44	2.27	2.23
$(\pm 3, 0)^{\uparrow\uparrow}$	2457.09	2476.14	2474.85	2473.46	2465.72	2460.61	2455.80
	0.00	15.89	30.54	54.85	63.92	81.89	99.81
	5.97	3.64	3.85	8.71	3.89	4.03	4.68
	0.99	0.92	0.93	0.86	0.87	0.86	0.78
$(\pm 5, 0)^{\downarrow\downarrow}$	2643.08	2641.69	2643.10	2644.07	2646.60	2645.43	2651.14
	0.00	42.01	83.49	127.38	169.63	218.69	255.46
	5.72	5.01	4.64	5.20	6.97	7.85	9.18
	7.86	7.59	7.15	6.69	5.68	4.82	4.22
$(\pm 2, 1)^{\downarrow\downarrow}$	2723.45	2723.71	2722.82	2721.34	2715.82	2711.60	2707.47
	0.00	14.64	29.25	44.90	61.94	78.37	94.33
	7.22	6.90	6.35	9.36	7.67	9.06	10.20
	2.63	2.58	2.56	2.38	2.37	2.26	2.07
$(\pm 1, 1)^{\uparrow\uparrow}$	3090.40	3097.76	3096.96	3098.30	3041.88	3036.61	3027.57
	0.00	-5.57	-7.20	-2.70	37.26	41.57	44.11
	16.83	15.61	16.71	16.77	23.80	18.90	19.32
	0.83	0.82	0.79	0.72	0.69	0.68	0.69
$(\pm 4, 0)^{\uparrow\uparrow}$	3694.84	3716.37	3715.37	3712.87	3709.72	3706.02	3701.64
	0.00	19.16	39.52	60.52	81.94	106.82	127.48
	8.38	6.49	6.54	6.40	6.50	8.82	6.65
	0.91	0.92	0.87	0.81	0.73	0.67	0.65
$(\pm 6, 0)^{\downarrow\downarrow}$	3957.49	3955.52	3957.21	3957.35	3958.06	3958.82	3958.57
	0.00	50.87	99.79	155.06	209.65	263.87	321.65
	8.05	7.72	7.71	6.67	6.93	9.32	11.47
	4.88	6.25	6.44	5.13	3.97	3.55	2.59

**Tab. B.8:** Measured modal parameters  $(\bar{\omega}^r, {}_S\Delta\omega^r, \delta^r, \kappa)^T$  for  $h_S = 1.0$  mm,  $h_R = 1.0$  mm and  $g = 14.4$  mm.

mode	angular rotor speed $\Omega_R$ in rad/s						
	0	8.38	16.8	25.1	33.5	41.9	50.3
$(\pm 1, 0)^{\uparrow\uparrow}$	754.73	755.96	754.17	750.29	745.15	737.63	728.18
	0.00	0.40	-0.20	-0.06	0.02	-0.45	-0.70
	2.19	2.04	2.10	2.48	2.57	3.07	3.60
	0.87	0.81	0.88	0.86	0.81	0.85	0.45
$(0, 1)^{\downarrow\downarrow}$	1118.55	1119.56	1118.61	1116.12	1114.94	1106.73	1096.42
	0.00	0.00	0.00	0.00	0.00	0.00	0.00
	14.55	14.15	14.29	14.51	15.60	16.15	17.65
	0.68	0.57	0.61	0.50	0.62	0.59	0.63
$(\pm 2, 0)^{\uparrow\uparrow}$	1536.47	1540.27	1538.72	1537.16	1536.30	1531.92	1526.64
	0.00	10.92	18.74	27.81	38.26	48.60	60.27
	5.44	3.77	3.36	3.40	2.96	3.01	3.47
	1.12	0.76	0.75	0.81	0.75	0.74	0.73
$(\pm 4, 0)^{\downarrow\downarrow}$	1716.73	1718.19	1720.19	1720.93	1723.54	1727.89	1731.71
	0.00	32.54	64.41	95.90	132.15	168.08	195.90
	2.39	2.92	3.87	4.76	6.62	9.42	10.41
	15.86	12.54	12.42	12.59	10.56	7.49	9.45
$(\pm 3, 0)^{\uparrow\uparrow}$	2539.24	2543.26	2543.26	2541.61	2536.93	2534.18	2530.10
	0.00	13.83	26.40	39.52	55.04	69.60	86.31
	4.17	3.88	4.00	3.78	9.14	4.88	5.63
	0.70	0.64	0.67	0.65	0.61	0.54	0.59
$(\pm 5, 0)^{\downarrow\downarrow}$	2804.87	2805.53	2806.39	2808.69	2809.00	2813.21	2818.88
	0.00	43.29	85.18	127.93	172.31	218.74	261.56
	4.21	3.62	3.94	5.75	5.68	7.18	9.33
	11.75	10.41	10.79	9.37	9.13	7.57	4.51
$(\pm 2, 1)^{\downarrow\downarrow}$	2892.82	2891.11	2891.30	2891.00	2890.16	2885.97	2884.44
	0.00	14.36	31.74	48.22	64.83	83.57	102.22
	6.36	5.71	6.08	5.88	8.87	10.42	11.84
	3.63	3.64	3.55	3.48	3.25	3.15	2.91
$(\pm 1, 1)^{\uparrow\uparrow}$	3111.88	3103.20	3103.41	3102.92	3125.98	3072.88	3063.61
	0.00	27.77	31.74	33.24	-5.12	18.86	18.90
	23.58	19.85	20.56	20.10	25.82	40.79	41.34
	0.65	0.57	0.55	0.54	0.52	0.43	0.39
$(\pm 4, 0)^{\uparrow\uparrow}$	3767.58	3772.96	3776.82	3772.80	3773.89	3769.17	3767.19
	0.00	16.64	40.68	50.01	67.01	88.17	108.93
	6.85	7.47	9.28	7.76	9.33	9.58	9.34
	0.65	0.60	0.58	0.58	0.50	0.45	0.42
$(\pm 6, 0)^{\downarrow\downarrow}$	4174.66	4174.57	4175.06	4176.77	4178.13	4182.05	4184.74
	0.00	52.71	106.23	157.34	214.94	269.82	326.33
	5.74	5.16	5.15	5.60	6.45	8.12	9.93
	6.96	8.94	8.38	8.29	7.92	5.46	4.38
$(\pm 3, 1)^{\downarrow\downarrow}$	4290.83	4290.92	4291.13	4291.31	4290.87	4288.82	4286.60
	0.00	25.09	50.89	76.81	104.61	133.06	159.58
	8.66	8.10	8.76	8.28	10.16	9.65	10.73
	3.95	3.73	3.33	3.37	2.95	2.95	2.61

**Tab. B.9:** Measured modal parameters  $(\bar{\omega}^r, {}_S\Delta\omega^r, \delta^r, \kappa)^T$  for  $h_S = 1.0$  mm,  $h_R = 1.5$  mm and  $g = 1.4$  mm.

mode	angular rotor speed $\Omega_R$ in rad/s						
	0	8.38	16.8	25.1	33.5	41.9	50.3
$(\pm 1, 0)^{\updownarrow}$	154.19	156.36	155.83	153.42	150.70	146.22	146.02
	0.00	9.47	15.93	23.47	28.30	35.40	80.60
	6.09	7.55	9.34	9.71	12.22	14.58	6.73
	3.56	2.99	3.32	3.47	3.60	4.11	11.39
$(\pm 2, 0)^{\updownarrow}$	310.89	311.32	311.17	310.41	305.92	302.26	299.46
	0.00	15.58	29.95	43.15	57.91	77.11	79.61
	7.79	8.23	10.29	12.62	14.44	16.89	19.71
	4.40	4.43	4.02	4.06	3.23	3.18	3.22
$(0, 1)^{\updownarrow}$	483.26	481.77	478.96	473.51	463.07	451.43	433.38
	0.00	0.00	0.00	0.00	0.00	0.00	0.00
	14.06	13.97	14.71	15.99	17.15	16.95	18.19
	0.47	0.41	0.46	0.49	0.59	0.44	0.57
$(\pm 1, 0)^{\uparrow\uparrow}$	599.92	601.28	598.45	593.79	586.01	575.19	562.59
	0.00	9.30	14.68	20.65	27.00	33.42	40.87
	7.67	6.92	7.53	8.52	9.84	11.39	12.95
	1.50	1.40	1.43	1.41	1.39	1.33	1.30
$(\pm 3, 0)^{\updownarrow}$	710.76	709.99	708.40	704.99	698.77	688.78	675.72
	0.00	22.61	44.01	64.97	86.99	111.62	135.14
	11.24	11.62	12.44	14.29	16.69	18.40	20.53
	2.12	2.02	1.88	1.67	1.57	1.13	1.09
$(\pm 2, 0)^{\uparrow\uparrow}$	1253.87	1253.39	1249.84	1243.95	1233.29	1219.86	1200.55
	0.00	14.51	27.88	42.65	56.66	73.97	88.18
	8.62	8.61	9.12	9.58	10.64	12.28	14.18
	1.45	1.41	1.37	1.33	1.25	1.18	1.08
$(\pm 4, 0)^{\updownarrow}$	1303.24	1302.59	1296.50	1292.14	1275.00	1264.11	1237.59
	0.00	33.03	56.16	88.70	114.66	154.55	178.55
	15.39	16.75	16.90	17.14	20.11	19.97	21.05
	1.35	1.23	1.00	0.91	0.83	0.65	0.53
$(\pm 1, 1)^{\updownarrow}$	1476.11	1474.21	1471.74	1484.95	1484.99	1462.64	1446.61
	0.00	-15.71	-13.98	-7.60	10.65	-6.75	-9.08
	26.29	23.93	22.70	30.59	33.60	33.47	36.91
	0.64	0.66	0.65	0.63	0.60	0.57	0.50
$(\pm 5, 0)^{\updownarrow}$	2094.74	2092.86	2086.47	2074.09	2055.86	2030.50	1996.73
	0.00	49.64	80.31	106.31	142.75	182.35	223.17
	19.19	17.36	20.01	20.00	21.07	22.88	24.26
	0.21	1.41	0.71	0.59	0.47	0.33	0.21
$(\pm 3, 0)^{\uparrow\uparrow}$	2325.01	2323.01	2317.86	2308.55	2293.39	2272.52	2246.34
	0.00	20.23	45.88	70.89	96.05	122.14	147.92
	12.30	11.43	11.45	12.50	13.46	14.40	15.72
	1.58	1.55	1.44	1.31	1.17	1.04	0.90
$(\pm 2, 1)^{\updownarrow}$	2335.65	2334.00	2329.13	2320.50	2307.77	2288.70	2268.50
	0.00	10.28	25.52	42.23	55.63	67.56	85.51
	18.15	16.86	17.07	16.59	16.59	17.46	25.61
	0.74	0.70	0.67	0.64	0.60	0.55	0.46

**Tab. B.10:** Measured modal parameters  $(\bar{\omega}^r, {}_S\Delta\omega^r, \delta^r, \kappa)^T$  for  $h_S = 1.0$  mm,  $h_R = 1.5$  mm and  $g = 2.2$  mm.

mode	angular rotor speed $\Omega_R$ in rad/s						
	0	8.38	16.8	25.1	33.5	41.9	50.3
$(\pm 1, 0)^{\downarrow}$	187.26	187.96	190.56	189.42	189.34	186.06	187.48
	0.00	6.69	11.73	17.41	26.39	35.28	37.99
	4.12	5.35	8.96	11.27	14.31	15.45	14.89
	3.42	1.96	3.44	3.43	4.05	3.86	4.53
$(\pm 2, 0)^{\downarrow}$	372.89	373.22	374.33	374.49	374.54	370.74	367.50
	0.00	15.86	28.70	41.65	57.42	72.55	87.23
	5.42	6.70	8.37	10.82	14.05	16.70	16.67
	4.48	4.65	4.17	4.10	3.79	3.21	2.61
$(0, 1)^{\downarrow}$	584.87	582.54	580.81	575.68	568.74	558.79	546.91
	0.00	0.00	0.00	0.00	0.00	0.00	0.00
	12.62	13.36	14.60	15.49	17.29	15.31	19.19
	0.44	0.45	0.42	0.52	0.43	0.54	0.38
$(\pm 1, 0)^{\uparrow}$	653.87	652.78	653.17	650.86	646.03	638.76	629.81
	0.00	11.45	16.59	22.00	27.28	33.84	40.72
	6.44	5.61	5.58	6.29	7.23	9.01	10.83
	1.52	1.36	1.36	1.38	1.36	1.32	1.26
$(\pm 3, 0)^{\downarrow}$	850.65	850.50	850.49	849.27	845.87	841.02	833.56
	0.00	21.80	41.93	61.31	82.53	104.37	128.06
	7.96	8.24	9.26	11.03	12.96	16.21	18.39
	2.12	2.12	1.97	1.86	1.64	1.40	1.15
$(\pm 2, 0)^{\uparrow}$	1356.96	1353.85	1352.56	1349.48	1343.61	1335.08	1325.31
	0.00	14.42	28.18	41.63	56.15	70.96	85.90
	5.30	5.46	5.52	6.47	6.82	7.86	9.05
	1.34	1.35	1.33	1.30	1.26	1.22	1.14
$(\pm 4, 0)^{\downarrow}$	1556.09	1555.50	1553.61	1550.58	1543.81	1533.81	1522.63
	0.00	29.14	55.16	79.97	108.47	137.67	166.69
	10.96	10.61	11.24	12.51	13.34	15.10	16.95
	1.38	1.33	1.16	1.08	0.92	0.77	0.67
$(\pm 1, 1)^{\downarrow}$	1597.99	1609.42	1615.95	1613.55	1607.36	1597.81	1586.35
	0.00	13.21	19.01	19.95	23.68	28.99	32.10
	27.16	36.43	26.24	25.02	27.45	24.66	23.91
	0.64	0.60	0.59	0.57	0.54	0.52	0.50
$(\pm 5, 0)^{\downarrow}$	2484.15	2501.62	2496.71	2494.71	2484.46	2468.64	2451.61
	0.00	56.92	80.89	112.08	145.62	185.86	227.10
	7.99	8.79	9.81	11.65	14.76	17.01	20.75
	0.94	1.26	1.07	0.89	0.74	0.54	0.34
$(\pm 3, 0)^{\uparrow}$	2485.69	2489.56	2488.56	2484.54	2478.17	2468.63	2457.61
	0.00	17.23	38.17	61.32	84.90	109.99	135.05
	10.10	11.49	9.63	9.44	8.79	9.79	10.44
	1.55	1.47	1.39	1.31	1.24	1.17	1.09
$(\pm 2, 1)^{\downarrow}$	2566.89	2561.86	2556.81	2550.38	2540.61	2522.37	2503.71
	0.00	14.88	24.62	31.50	38.80	54.99	65.90
	19.24	17.92	16.95	15.75	17.33	16.93	16.01
	0.71	0.69	0.66	0.62	0.55	0.51	0.50

**Tab. B.11:** Measured modal parameters  $(\bar{\omega}^r, {}_S\Delta\omega^r, \delta^r, \kappa)^T$  for  $h_S = 1.0$  mm,  $h_R = 1.5$  mm and  $g = 2.9$  mm.

mode	angular rotor speed $\Omega_R$ in rad/s						
	0	8.38	16.8	25.1	33.5	41.9	50.3
$(\pm 1, 0)^{\updownarrow}$	210.48	211.61	212.37	211.58	209.77	208.09	200.28
	0.00	7.29	13.62	22.96	26.18	36.08	41.04
	3.51	4.34	6.82	9.79	13.21	15.06	17.99
	3.68	3.64	3.63	3.24	3.60	3.36	3.85
$(\pm 2, 0)^{\updownarrow}$	416.85	416.99	417.70	418.65	419.19	417.15	415.00
	0.00	14.85	28.09	41.53	56.35	71.51	87.16
	4.38	4.92	6.70	9.37	12.73	15.43	17.45
	4.77	4.71	4.53	4.35	3.86	3.41	2.72
$(0, 1)^{\updownarrow}$	656.21	653.71	653.19	645.24	652.33	628.84	617.13
	0.00	0.00	0.00	0.00	0.00	0.00	0.00
	12.78	20.12	26.50	24.70	34.49	20.92	24.91
	0.51	0.44	0.46	0.42	0.45	0.41	0.51
$(\pm 1, 0)^{\uparrow\uparrow}$	684.16	687.68	685.21	682.45	678.00	672.10	664.50
	0.00	8.96	14.24	19.80	26.06	32.77	39.56
	4.37	3.87	4.12	4.76	5.62	6.83	8.80
	2.17	1.16	1.37	1.34	1.37	1.32	1.31
$(\pm 3, 0)^{\updownarrow}$	949.53	949.63	949.66	949.02	946.91	943.13	938.27
	0.00	21.73	41.75	61.44	82.55	104.32	126.61
	6.52	6.71	7.54	9.23	10.69	12.65	15.90
	2.25	2.22	2.05	1.98	1.74	1.59	1.35
$(\pm 2, 0)^{\uparrow\uparrow}$	1402.43	1401.62	1401.03	1398.43	1394.12	1387.76	1380.33
	0.00	13.91	27.38	41.07	54.88	69.74	84.49
	4.15	3.99	4.34	4.64	5.31	5.81	6.77
	1.36	1.33	1.33	1.30	1.26	1.24	1.19
$(\pm 4, 0)^{\updownarrow}$	1733.96	1734.19	1733.45	1731.54	1726.60	1719.26	1710.15
	0.00	28.02	53.89	78.10	105.92	136.40	165.91
	8.84	8.70	8.85	10.06	11.61	12.91	14.70
	1.45	1.38	1.28	1.16	1.00	0.86	0.46
$(\pm 3, 0)^{\uparrow\uparrow}$	2546.62	2549.90	2549.80	2547.32	2543.44	2538.12	2531.80
	0.00	21.44	43.68	68.36	90.79	111.75	134.56
	5.06	5.93	5.51	9.32	10.02	7.04	7.55
	1.46	1.46	1.38	1.27	1.20	1.21	1.15
$(\pm 2, 1)^{\updownarrow}$	2749.79	2745.50	2744.64	2766.29	2757.70	2713.91	2696.99
	0.00	17.18	24.58	30.73	46.86	52.57	65.44
	22.84	24.73	20.95	25.84	24.22	17.94	18.07
	0.70	0.70	0.64	0.55	0.40	0.53	0.49
$(\pm 5, 0)^{\updownarrow}$	2770.62	2770.46	2768.22	2763.99	2755.86	2745.57	2730.94
	0.00	34.82	64.44	96.33	131.16	165.28	202.22
	10.04	10.44	10.89	11.43	11.89	13.78	15.13
	1.11	1.03	0.93	0.81	0.71	0.55	0.45
$(\pm 1, 1)^{\uparrow\uparrow}$	3685.36	3683.35	3681.56	3676.14	3664.78	3638.58	3617.82
	0.00	0.47	8.45	18.05	26.42	35.26	43.37
	18.94	19.33	19.33	22.16	23.78	29.06	28.51
	0.95	0.97	0.95	0.93	0.89	0.84	0.73

**Tab. B.12:** Measured modal parameters  $(\bar{\omega}^r, {}_S\Delta\omega^r, \delta^r, \kappa)^T$  for  $h_S = 1.0$  mm,  $h_R = 1.5$  mm and  $g = 3.6$  mm.

mode	angular rotor speed $\Omega_R$ in rad/s						
	0	8.38	16.8	25.1	33.5	41.9	50.3
$(\pm 1, 0)^{\updownarrow}$	228.75	230.00	231.95	233.23	232.57	231.83	228.20
	0.00	7.11	13.29	22.74	31.41	37.14	45.06
	2.82	3.87	6.40	11.99	13.46	17.83	16.01
	3.84	3.86	3.84	3.50	3.55	3.08	3.62
$(\pm 2, 0)^{\updownarrow}$	450.79	451.65	452.39	452.75	453.14	453.23	448.99
	0.00	14.40	33.92	42.29	58.47	71.84	86.53
	3.40	3.75	6.38	8.87	11.63	15.08	20.72
	5.69	5.26	4.98	4.49	4.07	3.91	3.16
$(\pm 1, 0)^{\uparrow\uparrow}$	707.06	706.71	711.16	709.25	705.36	700.16	693.58
	0.00	1.71	16.52	22.34	27.89	33.80	40.43
	3.47	3.66	4.21	4.68	5.02	6.11	7.91
	1.32	1.31	1.32	1.27	1.33	1.33	1.26
$(0, 1)^{\updownarrow}$	712.29	713.32	716.13	714.74	710.49	704.86	693.89
	0.00	0.00	0.00	0.00	0.00	0.00	0.00
	3.41	4.37	6.45	6.93	9.17	11.07	14.64
	0.58	0.43	0.51	0.71	0.54	0.37	0.51
$(\pm 3, 0)^{\updownarrow}$	1029.69	1029.91	1029.93	1029.39	1027.52	1025.05	1021.31
	0.00	22.04	42.30	62.00	83.53	106.02	128.99
	5.27	5.60	6.57	8.09	9.38	11.53	13.34
	2.38	2.35	2.27	2.04	1.95	1.72	1.47
$(\pm 2, 0)^{\uparrow\uparrow}$	1452.93	1449.89	1448.56	1446.46	1442.09	1436.80	1430.06
	0.00	14.72	27.26	40.78	54.49	68.96	83.51
	3.97	3.83	3.80	4.09	4.40	5.13	5.75
	1.29	1.28	1.28	1.21	1.23	1.19	1.18
$(\pm 4, 0)^{\updownarrow}$	1880.98	1880.91	1879.45	1877.54	1873.77	1867.84	1860.35
	0.00	28.44	53.97	79.61	107.97	137.17	167.49
	7.29	7.37	7.98	8.74	9.92	11.42	13.22
	1.51	1.45	1.36	1.17	1.12	0.97	0.79
$(\pm 3, 0)^{\uparrow\uparrow}$	2600.79	2603.84	2603.11	2597.47	2594.47	2592.05	2586.91
	0.00	21.17	42.40	64.45	86.57	109.42	133.05
	5.42	5.18	7.83	8.08	7.37	6.76	7.65
	1.37	1.36	1.28	1.17	1.19	1.14	1.09
$(\pm 2, 1)^{\updownarrow}$	2912.39	2912.81	2906.65	2898.80	2893.82	2876.72	2862.07
	0.00	11.70	31.16	47.64	52.14	54.42	64.57
	27.42	23.94	22.84	28.71	29.37	24.52	23.69
	0.71	0.67	0.52	0.48	0.47	0.48	0.44
$(\pm 5, 0)^{\updownarrow}$	2997.54	2997.29	2997.56	2991.05	2984.66	2975.92	2964.53
	0.00	34.27	76.88	95.90	130.02	165.37	202.30
	10.46	9.57	14.68	10.31	10.72	11.39	13.28
	1.14	1.07	0.93	0.83	0.77	0.66	0.52
$(\pm 1, 1)^{\uparrow\uparrow}$	3836.87	3836.66	3833.06	3829.94	3817.29	3803.95	3786.85
	0.00	4.46	12.84	20.51	28.32	37.56	45.34
	16.47	16.61	17.75	18.33	20.20	21.91	23.71
	0.99	1.00	1.01	0.78	0.92	0.87	0.83

**Tab. B.13:** Measured modal parameters  $(\bar{\omega}^r, {}_S\Delta\omega^r, \delta^r, \kappa)^T$  for  $h_S = 1.0$  mm,  $h_R = 1.5$  mm and  $g = 4.4$  mm.

mode	angular rotor speed $\Omega_R$ in rad/s						
	0	8.38	16.8	25.1	33.5	41.9	50.3
$(\pm 1, 0)^{\updownarrow}$	247.25	248.02	247.92	247.74	244.68	242.22	238.50
	0.00	7.02	13.24	19.20	26.86	31.93	44.14
	2.31	3.30	5.48	10.34	11.59	16.39	18.82
	3.89	3.95	1.96	4.13	4.26	3.31	3.97
$(\pm 2, 0)^{\updownarrow}$	483.58	483.44	483.97	484.76	485.71	487.52	487.22
	0.00	14.51	28.76	41.74	57.40	74.32	85.83
	3.19	3.55	5.97	7.26	10.34	15.07	19.07
	5.10	5.20	2.20	4.96	4.63	4.19	2.82
$(\pm 1, 0)^{\uparrow\uparrow}$	722.61	724.60	720.65	717.10	712.27	706.58	699.55
	0.00	5.48	13.45	19.29	25.28	31.93	38.45
	2.57	3.14	3.42	3.80	4.44	5.28	7.15
	1.30	1.01	1.28	1.31	1.28	1.27	1.24
$(0, 1)^{\updownarrow}$	762.31	761.29	759.46	752.83	735.99	733.55	728.11
	0.00	0.00	0.00	0.00	0.00	0.00	0.00
	12.64	11.44	11.23	11.42	10.55	9.66	9.25
	0.49	0.42	0.43	0.42	0.33	0.35	0.41
$(\pm 3, 0)^{\updownarrow}$	1101.04	1101.79	1101.86	1101.08	1099.71	1097.31	1094.59
	0.00	21.32	42.80	62.04	85.34	107.48	130.48
	4.90	5.00	7.68	7.82	9.50	11.00	13.22
	2.39	2.43	2.31	2.19	2.02	1.76	1.55
$(\pm 2, 0)^{\uparrow\uparrow}$	1453.52	1464.20	1462.50	1459.29	1454.36	1448.25	1441.66
	0.00	12.86	26.16	39.04	53.11	67.07	81.92
	5.25	3.59	3.46	3.70	4.15	4.50	4.95
	1.27	1.28	1.26	1.22	1.20	1.18	1.15
$(\pm 4, 0)^{\updownarrow}$	2009.03	2010.85	2009.12	2006.97	2003.47	1998.37	1991.62
	0.00	28.34	54.09	80.07	108.79	138.14	168.13
	6.36	6.39	6.84	7.51	8.46	9.94	11.23
	1.50	1.49	1.42	1.30	1.19	1.05	0.92
$(\pm 3, 0)^{\uparrow\uparrow}$	2597.53	2610.90	2609.94	2607.33	2602.89	2600.35	2598.36
	0.00	20.53	41.80	63.07	84.53	110.95	137.86
	6.34	5.34	5.37	4.98	6.05	7.55	8.63
	1.33	1.34	1.27	1.23	1.18	1.11	1.03
$(\pm 2, 1)^{\updownarrow}$	3054.31	3056.64	3052.61	3046.98	3038.42	3026.54	3010.76
	0.00	23.50	30.78	36.89	52.92	57.82	65.67
	28.66	31.48	29.72	27.68	30.74	29.34	29.35
	0.68	0.69	0.61	0.55	0.48	0.43	0.40
$(\pm 5, 0)^{\updownarrow}$	3192.75	3196.75	3194.40	3191.28	3184.50	3177.13	3166.76
	0.00	33.41	64.16	96.04	130.32	165.33	201.82
	9.27	8.21	8.53	9.17	9.58	10.47	11.91
	1.14	1.11	1.00	0.91	0.80	0.69	0.59
$(\pm 1, 1)^{\uparrow\uparrow}$	3947.76	3953.07	3948.93	3940.65	3929.66	3919.52	3902.81
	0.00	11.05	19.41	29.45	33.09	39.16	50.34
	14.74	13.48	15.51	20.52	21.00	24.34	22.10
	1.05	1.07	1.04	0.98	0.97	0.88	0.92



**Tab. B.14:** Measured modal parameters  $(\bar{\omega}^r, {}_S\Delta\omega^r, \delta^r, \kappa)^T$  for  $h_S = 1.0$  mm,  $h_R = 1.5$  mm and  $g = 6.4$  mm.

mode	angular rotor speed $\Omega_R$ in rad/s						
	0	8.38	16.8	25.1	33.5	41.9	50.3
$(\pm 1, 0)^{\updownarrow}$	280.80	281.60	282.13	280.89	279.60	277.75	277.73
	0.00	6.68	13.21	19.00	26.70	34.74	43.32
	1.86	2.93	5.03	7.14	10.23	13.43	14.07
	4.20	4.19	1.19	3.66	3.45	3.51	3.09
$(\pm 2, 0)^{\updownarrow}$	543.87	544.12	544.01	544.64	545.66	547.65	547.19
	0.00	14.60	30.48	43.40	58.18	74.55	91.37
	2.38	2.92	5.83	7.16	8.76	12.36	19.15
	5.62	5.70	5.18	4.97	5.34	4.27	4.11
$(\pm 1, 0)^{\uparrow\uparrow}$	743.46	747.76	739.39	736.38	732.34	726.36	719.97
	0.00	6.72	11.73	18.01	23.54	30.48	36.88
	2.97	2.73	2.64	3.08	3.52	4.22	5.54
	1.56	1.01	1.25	1.21	1.23	1.18	1.17
$(0, 1)^{\updownarrow}$	891.10	890.81	886.07	881.67	874.46	861.52	850.45
	0.00	0.00	0.00	0.00	0.00	0.00	0.00
	14.42	14.40	14.33	14.73	14.78	14.56	15.79
	0.41	0.41	0.41	0.42	0.40	0.41	0.39
$(\pm 3, 0)^{\updownarrow}$	1242.98	1243.73	1242.27	1242.65	1241.41	1240.63	1238.37
	0.00	21.96	42.69	63.59	85.62	112.86	132.82
	3.47	3.87	4.70	7.64	7.56	9.19	11.74
	2.65	2.70	2.55	2.45	2.26	2.00	1.80
$(\pm 2, 0)^{\uparrow\uparrow}$	1491.08	1501.65	1492.82	1490.33	1488.58	1481.03	1475.09
	0.00	12.47	24.42	36.79	54.46	63.95	77.90
	5.09	3.46	3.12	3.23	4.88	3.75	4.08
	1.22	1.16	1.14	1.11	1.25	1.06	1.06
$(\pm 4, 0)^{\updownarrow}$	2267.06	2268.94	2266.27	2263.98	2264.47	2264.09	2253.27
	0.00	27.94	54.96	81.21	119.78	152.78	169.79
	5.45	5.43	7.89	6.28	9.89	12.79	9.67
	1.62	1.63	1.49	1.43	1.27	1.07	1.06
$(\pm 3, 0)^{\uparrow\uparrow}$	2618.04	2630.75	2625.14	2623.86	2619.64	2613.69	2610.19
	0.00	19.13	43.97	66.36	85.06	101.24	123.00
	6.03	5.21	6.87	8.97	8.26	5.69	5.86
	1.19	1.18	1.15	1.02	1.02	1.00	0.99
$(\pm 2, 1)^{\updownarrow}$	3377.28	3379.13	3371.71	3384.85	3374.58	3350.72	3337.08
	0.00	27.98	34.33	19.84	20.92	61.53	71.59
	43.14	45.34	40.54	50.02	45.66	35.86	33.97
	0.70	0.59	0.52	0.46	0.36	0.35	0.22
$(\pm 5, 0)^{\updownarrow}$	3587.18	3592.44	3586.45	3583.58	3579.83	3573.80	3566.96
	0.00	33.25	64.10	95.09	127.74	165.79	201.91
	8.67	7.13	7.53	7.98	8.48	8.96	9.92
	1.22	1.13	1.08	0.97	0.86	0.78	0.65
$(\pm 1, 1)^{\uparrow\uparrow}$	4073.15	4077.99	4077.29	4074.63	4064.37	4053.27	4045.95
	0.00	9.99	14.46	23.17	35.94	25.96	41.78
	11.68	11.87	11.58	13.46	15.15	25.11	22.33
	1.04	1.09	1.05	1.09	1.02	0.85	0.90

**Tab. B.15:** Measured modal parameters  $(\bar{\omega}^r, {}_S\Delta\omega^r, \delta^r, \kappa)^T$  for  $h_S = 1.0$  mm,  $h_R = 1.5$  mm and  $g = 9.4$  mm.

mode	angular rotor speed $\Omega_R$ in rad/s						
	0	8.38	16.8	25.1	33.5	41.9	50.3
$(\pm 1, 0)^{\ddagger}$	315.11	316.54	317.65	319.34	320.40	318.97	318.16
	0.00	6.35	13.04	19.44	25.48	33.28	36.83
	1.58	2.51	4.53	7.61	11.58	15.51	17.58
	4.62	4.40	4.44	4.34	4.21	4.04	4.15
$(\pm 2, 0)^{\ddagger}$	603.42	603.38	604.73	605.81	606.65	609.97	611.39
	0.00	14.88	28.96	43.84	59.83	74.87	89.06
	1.47	2.39	3.83	5.51	7.10	10.06	15.42
	6.66	6.29	6.65	6.22	6.03	5.30	4.78
$(\pm 1, 0)^{\dagger\dagger}$	760.00	767.99	766.65	766.17	761.74	755.22	747.24
	0.00	11.67	14.56	19.01	25.03	30.66	36.41
	5.24	2.63	2.16	2.43	3.18	3.50	4.45
	1.07	1.01	1.13	1.01	1.05	1.03	1.04
$(0, 1)^{\ddagger}$	1020.53	1021.14	1018.52	1024.49	1019.37	1007.07	995.16
	0.00	0.00	0.00	0.00	0.00	0.00	0.00
	15.96	15.73	15.98	15.39	15.38	16.31	15.44
	0.38	0.38	0.36	0.37	0.33	0.35	0.33
$(\pm 3, 0)^{\ddagger}$	1382.56	1383.91	1384.53	1385.12	1384.36	1383.82	1382.17
	0.00	21.76	43.68	65.79	88.50	113.27	135.47
	2.73	3.18	3.58	4.82	6.17	8.35	9.96
	3.20	2.99	2.97	2.89	2.64	2.39	2.22
$(\pm 2, 0)^{\dagger\dagger}$	1527.49	1536.71	1534.23	1534.38	1530.85	1524.16	1516.71
	0.00	14.78	24.11	34.06	46.41	59.27	72.13
	5.97	4.41	3.95	3.33	3.12	3.28	3.32
	0.99	0.85	0.98	0.95	0.93	0.92	0.91
$(\pm 1, 1)^{\ddagger}$	2361.06	2375.03	2378.68	2406.67	2312.70	2308.62	2301.06
	0.00	-19.58	-17.80	-15.65	37.85	36.96	37.29
	27.47	26.83	25.65	25.29	34.43	31.47	29.71
	0.42	0.41	0.38	0.39	0.33	0.32	0.31
$(\pm 4, 0)^{\ddagger}$	2624.57	2527.51	2526.78	2526.72	2527.55	2522.39	2519.07
	0.00	27.36	54.65	82.83	117.63	143.65	172.81
	1.11	4.23	4.79	4.65	7.70	7.41	8.13
	1.55	1.84	1.78	1.65	1.42	1.34	1.21
$(\pm 3, 0)^{\dagger\dagger}$	2626.01	2641.48	2640.64	2640.01	2633.53	2629.10	2624.52
	0.00	18.05	36.51	53.43	73.87	93.79	113.76
	7.57	4.88	4.88	4.90	5.99	5.64	5.39
	1.06	0.97	0.97	0.94	0.88	0.86	0.82
$(\pm 2, 1)^{\ddagger}$	3746.50	3753.86	3745.76	3736.16	3736.64	3711.03	3701.06
	0.00	12.63	25.69	39.63	51.24	75.76	81.21
	57.03	56.47	56.02	49.77	59.48	47.38	44.97
	0.64	0.60	0.47	0.39	0.28	0.27	0.26
$(\pm 5, 0)^{\ddagger}$	3976.06	3984.46	3983.66	3982.97	3979.45	3975.44	3969.80
	0.00	32.53	63.73	95.55	126.73	164.07	197.72
	8.77	6.98	7.53	6.79	7.48	8.65	9.18
	1.29	1.23	1.19	1.03	0.96	0.89	0.76

**Tab. B.16:** Measured modal parameters  $(\bar{\omega}^r, {}_S\Delta\omega^r, \delta^r, \kappa)^T$  for  $h_S = 1.0$  mm,  $h_R = 1.5$  mm and  $g = 14.4$  mm.

mode	angular rotor speed $\Omega_R$ in rad/s						
	0	8.38	16.8	25.1	33.5	41.9	50.3
$(\pm 1, 0)^{\downarrow}$	353.54	353.47	353.50	357.00	356.73	355.49	331.88
	0.00	5.71	13.99	19.69	25.54	29.74	66.98
	1.70	2.00	4.37	5.75	8.17	9.88	28.60
	5.60	5.94	1.67	3.36	6.06	6.53	3.24
$(\pm 2, 0)^{\downarrow}$	660.33	662.17	665.00	664.73	668.15	670.88	688.59
	0.00	13.52	30.46	45.42	62.87	81.23	124.15
	1.04	1.62	3.47	5.53	7.99	10.12	9.40
	9.94	10.25	7.37	7.51	7.40	6.06	5.28
$(\pm 1, 0)^{\uparrow}$	795.12	787.85	785.92	782.21	778.20	772.29	766.17
	0.00	16.47	18.61	22.55	24.84	30.50	35.94
	2.33	2.41	2.57	2.54	3.07	2.64	3.71
	0.86	1.02	0.91	0.93	0.88	0.85	0.88
$(0, 1)^{\downarrow}$	1197.03	1193.40	1192.46	1189.48	1185.36	1177.34	1164.50
	0.00	0.00	0.00	0.00	0.00	0.00	0.00
	16.58	17.40	17.54	16.98	17.75	16.98	17.40
	0.32	0.33	0.31	0.34	0.30	0.31	0.31
$(\pm 3, 0)^{\downarrow}$	1522.37	1523.19	1523.50	1525.66	1525.37	1521.51	1516.17
	0.00	22.77	43.77	69.55	92.24	109.09	119.02
	2.27	2.55	3.38	4.24	2.89	4.03	4.15
	3.93	3.83	3.56	3.78	3.73	3.32	3.18
$(\pm 2, 0)^{\uparrow}$	1561.77	1562.07	1560.16	1558.18	1555.45	1548.40	1543.03
	0.00	13.94	23.31	31.96	43.04	49.83	62.36
	5.95	4.30	3.32	3.18	4.06	3.68	3.22
	0.93	0.69	0.78	0.73	0.75	0.72	0.72
$(\pm 3, 0)^{\uparrow}$	2618.95	2624.86	2625.19	2623.89	2636.53	2622.84	2610.52
	0.00	20.70	35.68	53.21	110.05	97.43	99.57
	12.88	9.47	9.44	11.08	13.01	11.47	7.37
	0.77	0.78	0.74	0.66	0.60	0.60	0.60
$(\pm 4, 0)^{\downarrow}$	2790.36	2790.49	2790.97	2791.13	2790.43	2789.57	2788.47
	0.00	29.63	57.43	87.02	116.86	149.19	181.26
	3.80	4.25	4.23	4.58	5.27	6.15	7.68
	2.27	2.22	2.15	2.03	1.98	1.77	1.57
$(\pm 4, 0)^{\uparrow}$	3986.77	3990.58	3990.09	3988.51	3986.11	3985.16	3982.17
	0.00	22.85	46.12	66.87	90.77	119.41	145.28
	13.50	13.29	11.95	11.84	13.42	13.76	14.02
	0.98	0.91	0.86	0.74	0.68	0.59	0.53
$(\pm 1, 1)^{\uparrow}$	4039.71	4042.54	4035.16	4036.37	4030.03	4039.99	4032.70
	0.00	23.42	20.93	25.00	33.20	42.66	82.43
	12.12	11.42	10.17	8.68	9.94	22.00	25.16
	1.12	1.08	1.14	1.14	1.05	1.17	0.33
$(\pm 2, 1)^{\downarrow}$	3994.98	4007.17	4016.76	4024.52	4031.20	4049.32	4056.52
	0.00	31.53	43.52	58.67	48.21	26.51	23.68
	18.04	29.10	26.16	30.89	26.01	21.48	16.30
	0.54	0.54	0.48	0.44	0.37	0.39	0.25

**Tab. B.17:** Measured modal parameters  $(\bar{\omega}^r, {}_S\Delta\omega^r, \delta^r, \kappa)^T$  for  $h_S = 1.0$  mm,  $h_R = 2.0$  mm and  $g = 1.4$  mm.

mode	angular rotor speed $\Omega_R$ in rad/s						
	0	8.38	16.8	25.1	33.5	41.9	50.3
$(\pm 1, 0)^{\updownarrow}$	181.99	184.62	185.27	183.10	180.76	178.13	179.84
	0.00	8.90	16.37	21.08	29.66	37.92	54.41
	7.86	9.06	10.35	9.45	10.63	13.88	3.38
	1.49	1.40	1.60	1.44	1.57	1.69	2.09
$(\pm 2, 0)^{\updownarrow}$	380.99	380.19	378.42	376.24	372.20	367.12	359.31
	0.00	15.00	29.49	43.84	58.52	73.06	87.51
	9.57	9.74	10.71	12.57	12.90	14.80	16.20
	2.00	1.98	1.77	1.50	1.51	1.40	1.33
$(0, 1)^{\updownarrow}$	496.26	496.28	490.40	487.10	474.84	466.90	447.67
	0.00	0.00	0.00	0.00	0.00	0.00	0.00
	14.20	14.13	14.16	15.19	16.16	17.01	17.90
	0.45	0.46	0.53	0.44	0.44	0.37	0.47
$(\pm 1, 0)^{\uparrow\uparrow}$	661.94	659.38	666.01	661.35	653.67	641.90	628.32
	0.00	-4.46	19.43	25.31	32.51	38.21	46.42
	8.29	8.11	8.49	9.48	10.81	12.28	13.55
	1.38	1.40	1.36	1.37	1.35	1.30	1.32
$(\pm 3, 0)^{\updownarrow}$	816.85	816.58	812.60	807.46	799.39	787.47	772.01
	0.00	22.22	43.58	64.16	85.32	107.75	132.96
	13.69	13.81	14.41	15.31	16.74	17.76	19.50
	0.91	0.87	0.80	0.73	0.61	0.53	0.45
$(\pm 2, 0)^{\uparrow\uparrow}$	1371.24	1368.12	1363.05	1355.92	1344.91	1328.96	1311.69
	0.00	15.98	31.11	46.15	62.77	77.63	96.02
	10.67	10.14	10.34	10.56	12.60	12.98	15.17
	1.33	1.31	1.29	1.19	1.10	1.09	0.98
$(\pm 4, 0)^{\updownarrow}$	1430.95	1429.99	1423.47	1415.32	1401.29	1380.71	1362.17
	0.00	29.44	56.15	85.77	111.49	135.38	173.50
	17.47	18.02	17.46	19.85	18.19	21.15	23.83
	0.59	0.55	0.47	0.42	0.29	0.25	0.20
$(\pm 1, 1)^{\uparrow\uparrow}$	1531.39	1527.12	1536.87	1522.65	1521.35	1510.05	1495.84
	0.00	-5.43	19.24	16.20	30.41	36.68	43.33
	33.63	34.53	35.28	36.77	34.38	36.00	38.75
	0.64	0.64	0.62	0.64	0.63	0.60	0.59
$(\pm 5, 0)^{\updownarrow}$	2240.01	2235.47	2227.60	2214.53	2195.31	2168.00	2132.51
	0.00	36.69	71.59	105.18	140.42	179.14	218.71
	22.25	22.36	22.61	23.37	24.26	25.46	26.56
	0.44	0.38	0.30	0.23	0.17	0.12	0.10
$(\pm 2, 1)^{\updownarrow}$	2444.43	2440.75	2433.59	2421.79	2406.07	2382.72	2353.07
	0.00	15.73	26.27	36.64	47.94	59.87	72.94
	22.62	20.25	19.57	19.15	18.72	18.36	18.15
	0.65	0.69	0.64	0.57	0.56	0.55	0.53
$(\pm 3, 0)^{\uparrow\uparrow}$	2665.23	2662.11	2655.59	2642.46	2624.42	2597.98	2561.23
	0.00	23.78	49.70	71.10	94.51	120.00	144.59
	15.09	15.05	16.56	15.91	16.94	18.31	20.21
	1.32	1.28	1.16	1.04	0.91	0.81	0.68

**Tab. B.18:** Measured modal parameters  $(\bar{\omega}^r, {}_S\Delta\omega^r, \delta^r, \kappa)^T$  for  $h_S = 1.0$  mm,  $h_R = 2.0$  mm and  $g = 2.2$  mm.

mode	angular rotor speed $\Omega_R$ in rad/s						
	0	8.38	16.8	25.1	33.5	41.9	50.3
$(\pm 1, 0)^{\downarrow}$	227.17	229.69	229.87	229.05	227.29	223.28	220.28
	0.00	7.12	13.26	19.84	26.24	31.10	40.06
	5.07	5.73	7.98	9.41	11.23	13.30	15.55
	1.58	1.65	1.58	1.65	1.78	1.71	1.15
$(\pm 2, 0)^{\downarrow}$	466.04	467.25	467.13	466.48	463.07	459.34	455.26
	0.00	14.33	27.37	40.45	56.58	71.62	85.45
	7.43	7.04	8.43	10.48	12.22	14.50	15.41
	2.03	2.05	1.93	1.86	1.71	1.57	1.32
$(0, 1)^{\downarrow}$	597.16	598.50	595.16	592.27	582.28	573.60	559.94
	0.00	0.00	0.00	0.00	0.00	0.00	0.00
	12.39	11.85	12.42	12.86	14.95	16.71	17.74
	0.45	0.45	0.46	0.43	0.47	0.44	0.34
$(\pm 1, 0)^{\uparrow}$	731.34	735.77	733.73	730.39	724.24	717.42	708.29
	0.00	9.41	15.57	21.94	28.54	36.24	43.52
	5.73	5.06	5.70	6.64	8.09	9.63	11.79
	1.45	1.39	1.42	1.42	1.40	1.36	1.31
$(\pm 3, 0)^{\downarrow}$	996.90	1001.37	1000.53	997.23	991.43	983.98	974.06
	0.00	20.80	39.49	58.02	80.03	101.76	123.72
	12.53	9.66	10.16	11.37	12.30	14.12	16.39
	0.91	0.91	0.84	0.76	0.67	0.61	0.52
$(\pm 2, 0)^{\uparrow}$	1480.53	1483.05	1480.79	1477.06	1469.73	1461.10	1450.65
	0.00	15.10	31.06	46.76	62.93	79.47	96.36
	8.49	5.78	6.27	6.82	7.40	8.37	9.48
	1.37	1.36	1.34	1.30	1.25	1.18	1.15
$(\pm 1, 1)^{\uparrow}$	1654.01	1647.36	1656.25	1652.30	1642.59	1637.81	1625.27
	0.00	-9.32	2.32	9.31	13.79	26.46	35.36
	48.80	37.67	33.52	33.26	31.88	30.02	26.79
	0.45	0.42	0.42	0.43	0.41	0.42	0.39
$(\pm 4, 0)^{\downarrow}$	1735.19	1745.32	1744.78	1739.69	1730.02	1718.04	1702.73
	0.00	27.04	51.09	74.64	102.90	130.94	159.26
	19.22	12.94	12.43	13.11	13.81	14.98	16.64
	0.55	0.53	0.49	0.44	0.39	0.35	0.27
$(\pm 2, 1)^{\downarrow}$	2678.62	2692.27	2690.34	2680.18	2663.47	2645.30	2623.03
	0.00	29.57	32.39	43.87	46.57	55.94	67.84
	37.99	32.55	27.67	28.54	23.28	23.08	22.47
	0.47	0.44	0.42	0.38	0.36	0.33	0.31
$(\pm 5, 0)^{\downarrow}$	2691.64	2714.67	2715.80	2711.22	2693.57	2675.73	2653.45
	0.00	31.33	60.76	96.33	124.82	161.70	197.67
	27.07	17.30	15.26	19.49	16.67	17.15	18.34
	0.44	0.39	0.34	0.26	0.22	0.21	0.16
$(\pm 3, 0)^{\uparrow}$	2888.68	2894.85	2893.37	2888.13	2880.66	2870.90	2857.99
	0.00	24.87	50.63	75.65	101.14	127.99	154.02
	12.61	9.95	9.60	9.81	9.93	10.90	11.91
	1.55	1.53	1.43	1.35	1.25	1.13	1.02

**Tab. B.19:** Measured modal parameters  $(\bar{\omega}^r, {}_S\Delta\omega^r, \delta^r, \kappa)^T$  for  $h_S = 1.0 \text{ mm}$ ,  $h_R = 2.0 \text{ mm}$  and  $g = 2.9 \text{ mm}$ .

mode	angular rotor speed $\Omega_R$ in rad/s						
	0	8.38	16.8	25.1	33.5	41.9	50.3
$(\pm 1, 0)^{\ddagger}$	260.31	261.43	261.58	261.25	259.66	257.27	253.40
	0.00	7.16	12.95	18.68	25.44	31.57	40.78
	4.20	4.51	6.42	8.34	9.70	12.20	18.29
	1.64	1.66	0.49	1.73	1.52	1.39	1.75
$(\pm 2, 0)^{\ddagger}$	527.57	528.84	529.26	528.21	526.88	523.78	520.97
	0.00	14.64	27.38	40.93	54.97	69.29	85.65
	5.46	5.71	6.82	9.03	10.89	13.09	16.05
	2.10	2.14	2.04	2.03	1.83	1.47	1.43
$(0, 1)^{\ddagger}$	659.28	660.86	658.83	654.24	647.51	635.28	625.64
	0.00	0.00	0.00	0.00	0.00	0.00	0.00
	13.83	12.81	13.36	13.80	16.07	15.82	17.91
	0.47	0.48	0.54	0.47	0.47	0.46	0.44
$(\pm 1, 0)^{\ddagger\dagger}$	768.74	769.41	768.27	765.87	761.59	756.17	749.17
	0.00	6.96	13.98	20.84	28.30	35.48	43.26
	4.72	4.07	4.67	5.61	6.78	8.31	10.16
	1.41	1.41	1.41	1.40	1.35	1.33	1.29
$(\pm 3, 0)^{\ddagger}$	1129.35	1131.89	1132.40	1130.13	1125.57	1120.29	1113.17
	0.00	21.13	38.99	57.84	78.33	99.73	121.63
	9.70	7.94	8.15	9.30	10.40	11.88	14.24
	0.94	0.93	0.89	0.82	0.74	0.66	0.55
$(\pm 2, 0)^{\ddagger\dagger}$	1535.12	1539.45	1538.09	1534.61	1529.70	1523.10	1515.92
	0.00	15.33	30.84	46.24	62.81	78.63	95.93
	6.77	5.33	5.40	5.78	6.58	7.18	8.20
	1.37	1.33	1.35	1.29	1.25	1.19	1.13
$(\pm 1, 1)^{\ddagger\dagger}$	1733.83	1729.52	1742.90	1742.45	1728.98	1723.51	1715.30
	0.00	-14.60	0.16	13.06	21.14	22.08	29.43
	64.70	64.05	56.69	57.09	54.09	48.59	46.91
	0.41	0.36	0.36	0.33	0.30	0.30	0.28
$(\pm 4, 0)^{\ddagger}$	1960.55	1966.25	1968.69	1964.45	1957.30	1948.04	1936.44
	0.00	26.80	49.51	73.09	100.16	127.42	155.48
	14.81	11.43	10.03	10.62	11.45	12.65	13.74
	0.57	0.56	0.50	0.45	0.40	0.35	0.31
$(\pm 2, 1)^{\ddagger}$	2962.16	2946.63	2960.17	2938.27	2929.02	2927.25	2913.18
	0.00	96.14	112.22	141.23	167.57	197.26	234.74
	127.37	103.87	86.42	81.17	78.06	80.84	91.14
	0.49	0.34	0.33	0.39	0.20	0.18	0.12
$(\pm 3, 0)^{\ddagger\dagger}$	2974.08	2979.04	2979.32	2975.03	2971.91	2967.69	2958.44
	0.00	25.73	52.54	80.78	111.14	141.55	169.34
	22.26	22.45	21.18	21.97	21.45	20.79	20.40
	1.55	1.55	1.37	1.14	1.04	0.93	0.85
$(\pm 5, 0)^{\ddagger}$	3028.04	3042.39	3048.84	3042.42	3037.30	3018.98	3001.70
	0.00	36.08	61.52	89.59	134.16	157.47	194.23
	28.91	21.71	15.74	16.13	21.05	18.24	19.03
	0.46	0.39	0.33	0.32	0.22	0.13	0.12

**Tab. B.20:** Measured modal parameters  $(\bar{\omega}^r, {}_S\Delta\omega^r, \delta^r, \kappa)^T$  for  $h_S = 1.0$  mm,  $h_R = 2.0$  mm and  $g = 3.6$  mm.

mode	angular rotor speed $\Omega_R$ in rad/s						
	0	8.38	16.8	25.1	33.5	41.9	50.3
$(\pm 1, 0)^{\downarrow}$	285.86	287.43	287.62	287.11	284.33	281.60	278.67
	0.00	6.95	12.78	19.10	26.24	31.44	39.41
	3.12	3.79	5.74	7.43	9.74	11.83	15.29
	1.50	1.68	1.62	1.49	1.78	1.65	1.73
$(\pm 2, 0)^{\downarrow}$	578.27	578.06	578.19	577.54	575.65	572.19	567.52
	0.00	14.31	27.74	41.36	55.42	70.90	86.11
	4.45	4.58	5.96	8.18	9.91	12.51	14.24
	2.08	2.16	2.09	1.94	1.77	1.55	1.43
$(0, 1)^{\downarrow}$	726.28	726.12	723.70	720.20	711.18	696.73	683.63
	0.00	0.00	0.00	0.00	0.00	0.00	0.00
	13.97	13.45	13.91	14.05	15.96	15.82	15.63
	0.43	0.44	0.43	0.46	0.47	0.42	0.49
$(\pm 1, 0)^{\uparrow}$	788.52	792.77	791.28	786.93	782.17	775.03	766.89
	0.00	10.91	15.77	22.60	29.54	36.99	44.50
	3.89	3.78	4.00	4.91	5.71	7.23	8.82
	1.28	1.35	1.37	1.37	1.34	1.31	1.32
$(\pm 3, 0)^{\downarrow}$	1237.86	1238.52	1237.70	1233.99	1229.31	1222.83	1214.05
	0.00	20.28	38.80	57.63	78.45	99.74	121.28
	6.30	6.45	7.06	7.86	9.05	10.54	12.45
	0.91	0.91	0.89	0.83	0.74	0.66	0.61
$(\pm 2, 0)^{\uparrow}$	1568.99	1566.87	1565.79	1560.05	1555.01	1547.49	1538.86
	0.00	16.31	31.01	46.46	62.35	78.71	95.52
	5.29	4.49	4.42	4.83	5.58	6.21	7.06
	1.24	1.26	1.31	1.24	1.23	1.19	1.16
$(\pm 4, 0)^{\downarrow}$	2147.15	2147.19	2147.32	2138.83	2133.08	2125.51	2112.43
	0.00	25.98	59.55	72.48	101.86	135.07	164.19
	8.42	8.78	13.37	9.44	12.11	14.55	17.22
	0.56	0.56	0.51	0.46	0.40	0.34	0.28
$(\pm 3, 0)^{\uparrow}$	3007.46	3008.97	3009.27	3003.08	3002.21	2995.06	2988.58
	0.00	21.39	52.22	76.13	108.96	131.50	158.65
	21.06	22.70	22.63	20.25	20.15	20.02	20.98
	1.44	1.46	1.29	1.07	1.54	0.90	0.78
$(\pm 5, 0)^{\downarrow}$	3309.02	3308.88	3309.45	3310.65	3287.06	3272.60	3255.00
	0.00	30.76	73.67	102.60	118.34	151.27	184.70
	14.06	14.00	20.65	24.67	13.41	14.39	15.35
	0.43	0.40	0.32	0.24	0.25	0.21	0.18
$(\pm 1, 2)^{\downarrow}$	4669.22	4669.82	4656.34	4643.41	4609.75	4580.10	4552.19
	0.00	40.47	47.41	46.98	36.52	30.08	42.71
	62.36	62.71	66.70	60.19	70.99	76.90	65.14
	0.47	0.54	0.49	0.53	0.50	0.41	0.39
$(\pm 6, 0)^{\downarrow}$	4739.34	4740.98	4737.31	4726.03	4713.86	4696.68	4674.62
	0.00	34.73	65.58	98.42	134.79	172.41	209.65
	17.06	14.98	14.70	14.78	14.77	15.12	16.84
	0.26	0.26	0.23	0.21	0.17	0.14	0.12

**Tab. B.21:** Measured modal parameters  $(\bar{\omega}^r, {}_S\Delta\omega^r, \delta^r, \kappa)^T$  for  $h_S = 1.0$  mm,  $h_R = 2.0$  mm and  $g = 4.4$  mm.

mode	angular rotor speed $\Omega_R$ in rad/s						
	0	8.38	16.8	25.1	33.5	41.9	50.3
$(\pm 1, 0)^{\updownarrow}$	310.15	308.50	309.48	309.50	309.26	307.96	303.56
	0.00	9.19	13.72	19.69	26.86	31.54	39.15
	3.90	3.69	5.36	7.20	9.10	12.03	14.81
	1.70	1.67	1.01	1.55	1.35	1.51	1.23
$(\pm 2, 0)^{\updownarrow}$	621.34	622.10	623.76	622.79	621.61	620.15	618.22
	0.00	14.41	28.46	40.94	55.62	70.38	84.10
	3.76	4.05	5.13	6.73	8.52	10.23	12.80
	2.27	2.23	2.21	2.11	1.92	1.86	1.65
$(0, 1)^{\updownarrow}$	794.49	797.28	796.40	795.53	783.42	782.65	767.63
	0.00	0.00	0.00	0.00	0.00	0.00	0.00
	3.98	8.49	5.07	12.02	11.16	16.47	14.26
	0.43	0.31	0.87	0.32	0.34	0.29	0.43
$(\pm 1, 0)^{\uparrow\uparrow}$	811.04	814.76	818.89	819.45	822.80	822.54	824.03
	0.00	-6.19	-12.74	-10.04	-17.64	-18.21	-24.37
	3.44	4.58	7.40	5.74	6.65	7.60	9.47
	1.40	1.41	1.30	1.18	1.17	1.19	1.28
$(\pm 3, 0)^{\updownarrow}$	1329.57	1333.55	1333.61	1333.21	1329.46	1324.91	1320.50
	0.00	20.24	40.97	60.47	78.01	98.65	120.28
	6.03	5.64	8.54	11.17	9.79	10.16	11.73
	0.95	0.94	0.91	0.85	0.76	0.73	0.63
$(\pm 2, 0)^{\uparrow\uparrow}$	1579.42	1583.04	1582.99	1581.63	1577.98	1573.58	1568.55
	0.00	14.68	30.23	45.46	61.38	77.53	94.34
	4.67	3.52	4.10	4.25	4.58	5.19	6.00
	1.49	1.31	1.30	1.28	1.26	1.21	1.17
$(\pm 1, 1)^{\updownarrow}$	2002.68	1999.55	1999.03	2002.88	2003.41	1984.93	1925.70
	0.00	12.33	9.69	4.92	0.58	-1.59	44.90
	36.35	30.45	32.12	32.74	39.57	51.04	38.24
	0.35	0.29	0.34	0.17	0.33	0.16	0.19
$(\pm 4, 0)^{\updownarrow}$	2297.64	2306.03	2305.49	2303.28	2298.15	2291.98	2283.92
	0.00	24.67	47.63	70.87	96.66	123.13	150.82
	9.30	7.49	7.51	8.00	8.43	9.33	10.38
	0.57	0.56	0.52	0.49	0.44	0.40	0.36
$(\pm 3, 0)^{\uparrow\uparrow}$	3012.10	3018.19	3018.46	3018.06	3015.44	3013.45	3012.29
	0.00	25.31	51.07	78.08	103.90	130.84	157.72
	10.20	9.11	10.98	10.44	10.51	10.10	10.69
	1.50	1.46	1.37	1.28	1.18	1.11	1.04
$(\pm 2, 1)^{\updownarrow}$	3262.62	3273.80	3272.58	3266.54	3259.07	3244.55	3225.54
	0.00	16.67	27.46	34.71	43.96	51.78	62.21
	37.78	36.95	38.21	37.29	36.73	37.32	37.91
	0.33	0.32	0.27	0.23	0.21	0.18	0.15
$(\pm 5, 0)^{\updownarrow}$	3523.11	3538.62	3537.97	3534.68	3527.73	3518.79	3508.41
	0.00	30.22	57.25	82.70	114.04	145.21	177.58
	14.10	9.37	15.33	9.79	11.04	11.46	11.89
	0.42	0.40	0.34	0.32	0.27	0.25	0.20



**Tab. B.22:** Measured modal parameters  $(\bar{\omega}^r, {}_S\Delta\omega^r, \delta^r, \kappa)^T$  for  $h_S = 1.0$  mm,  $h_R = 2.0$  mm and  $g = 6.4$  mm.

mode	angular rotor speed $\Omega_R$ in rad/s						
	0	8.38	16.8	25.1	33.5	41.9	50.3
$(\pm 1, 0)^{\downarrow}$	358.49	359.45	360.75	360.64	360.34	358.16	354.96
	0.00	7.50	13.37	19.93	26.08	32.69	37.41
	2.81	3.05	4.47	6.29	8.12	10.40	13.73
	1.70	1.65	1.69	1.66	1.61	1.68	1.60
$(\pm 2, 0)^{\downarrow}$	714.26	713.62	714.45	714.51	713.97	712.85	712.58
	0.00	14.33	28.12	41.37	56.80	71.04	88.57
	3.13	3.13	3.97	5.55	7.29	9.21	12.42
	2.42	2.38	2.43	2.32	2.09	2.00	1.83
$(\pm 1, 0)^{\uparrow}$	820.06	821.36	827.54	825.83	822.59	817.61	811.98
	0.00	2.98	21.00	26.15	32.08	38.13	44.73
	3.96	7.91	3.55	3.98	4.58	5.22	6.57
	1.31	1.44	1.31	1.31	1.31	1.28	1.25
$(0, 1)^{\downarrow}$	934.18	933.46	930.91	927.26	921.16	911.41	897.89
	0.00	0.00	0.00	0.00	0.00	0.00	0.00
	11.88	11.85	12.13	12.51	12.70	13.92	16.00
	0.36	0.38	0.36	0.36	0.48	0.36	0.37
$(\pm 3, 0)^{\downarrow}$	1530.00	1531.08	1531.49	1529.92	1526.80	1524.47	1520.14
	0.00	19.67	35.65	56.35	75.71	98.05	118.75
	4.20	4.45	6.27	5.38	7.36	7.01	8.50
	1.00	0.97	0.94	0.90	0.84	0.82	0.74
$(\pm 2, 0)^{\uparrow}$	1608.67	1608.31	1607.73	1606.05	1602.67	1598.08	1592.51
	0.00	14.06	28.80	43.77	59.19	74.83	91.14
	3.43	3.10	3.58	3.38	3.95	4.15	5.02
	1.24	1.22	1.19	1.19	1.19	1.12	1.13
$(\pm 1, 1)^{\downarrow}$	2202.28	2197.48	2188.98	2178.42	2192.44	2184.49	2176.39
	0.00	30.92	34.70	42.71	31.13	32.87	34.07
	43.43	40.53	43.26	41.06	34.02	34.51	35.32
	0.21	0.20	0.19	0.16	0.19	0.17	0.17
$(\pm 4, 0)^{\downarrow}$	2626.94	2628.05	2627.79	2624.92	2622.13	2616.37	2609.86
	0.00	23.68	45.50	67.96	92.26	118.86	144.52
	6.87	7.11	7.14	7.51	7.38	8.13	9.04
	0.57	0.55	0.52	0.48	0.46	0.42	0.38
$(\pm 3, 0)^{\uparrow}$	3004.07	3007.35	3010.06	3009.74	3006.58	3006.28	3002.25
	0.00	22.24	50.65	74.14	100.89	132.27	154.97
	9.33	10.89	12.95	11.58	9.05	9.53	9.95
	1.41	1.35	1.26	1.17	1.17	1.11	1.01
$(\pm 2, 1)^{\downarrow}$	3647.10	3644.27	3653.86	3640.88	3612.56	3601.05	3583.83
	0.00	-48.02	-1.13	56.22	33.21	59.29	69.88
	40.10	52.53	48.29	42.06	61.51	50.77	48.38
	0.26	0.23	0.21	0.20	0.15	0.11	0.09
$(\pm 5, 0)^{\downarrow}$	3981.61	3986.19	3985.24	3982.41	3977.85	3974.83	3966.43
	0.00	27.77	51.95	77.88	106.09	143.61	171.80
	10.59	9.58	9.14	9.47	9.04	13.01	13.59
	0.40	0.38	0.34	0.31	0.28	0.23	0.19

**Tab. B.23:** Measured modal parameters  $(\bar{\omega}^r, {}_S\Delta\omega^r, \delta^r, \kappa)^T$  for  $h_S = 1.0$  mm,  $h_R = 2.0$  mm and  $g = 9.4$  mm.

mode	angular rotor speed $\Omega_R$ in rad/s						
	0	8.38	16.8	25.1	33.5	41.9	50.3
$(\pm 1, 0)^{\ddagger}$	405.34	407.67	409.34	409.31	408.29	406.64	403.51
	0.00	7.28	13.47	19.98	26.48	31.94	40.60
	3.78	2.66	3.97	5.60	7.68	10.18	12.88
	1.89	1.89	1.90	1.93	1.82	1.75	1.65
$(\pm 2, 0)^{\ddagger}$	801.48	801.72	803.46	803.70	803.46	802.44	800.01
	0.00	14.64	29.82	43.79	59.25	75.23	84.45
	5.00	2.99	3.67	4.13	6.03	5.90	7.58
	2.80	1.73	2.73	2.76	2.59	2.38	2.12
$(\pm 1, 0)^{\ddagger\dagger}$	832.55	832.65	839.05	837.47	833.91	828.62	820.04
	0.00	2.65	19.68	24.90	31.61	37.98	40.68
	6.31	4.90	4.53	5.41	5.07	6.60	7.24
	1.28	1.20	1.26	1.25	1.21	1.19	1.21
$(0, 1)^{\ddagger}$	1025.87	1021.55	1016.66	1012.31	1015.78	1005.08	989.76
	0.00	0.00	0.00	0.00	0.00	0.00	0.00
	20.88	21.12	20.86	20.34	20.15	20.13	19.27
	0.37	0.38	0.39	0.39	0.36	0.36	0.29
$(\pm 2, 0)^{\ddagger\dagger}$	1625.28	1627.70	1627.29	1625.29	1622.80	1617.63	1609.82
	0.00	13.66	26.68	39.96	55.44	72.14	84.77
	6.22	6.05	6.33	6.17	6.01	7.72	6.75
	1.10	1.09	1.06	1.04	1.01	0.97	0.95
$(\pm 3, 0)^{\ddagger}$	1731.89	1736.25	1738.28	1737.24	1734.26	1730.21	1724.83
	0.00	20.26	38.37	58.07	78.18	99.15	121.62
	8.72	5.53	4.95	5.16	6.03	6.83	7.35
	1.10	1.10	1.06	1.04	0.97	0.91	0.85
$(\pm 4, 0)^{\ddagger}$	2931.87	2951.50	2959.59	2955.74	2954.28	2942.69	2941.56
	0.00	32.10	51.97	76.91	114.95	123.67	162.29
	20.02	17.23	17.34	18.77	20.96	17.88	20.03
	0.57	0.55	0.46	0.42	0.35	0.32	0.27
$(\pm 3, 0)^{\ddagger\dagger}$	2992.43	3010.73	3017.46	3016.64	3014.52	3005.07	3000.52
	0.00	71.58	96.94	113.93	145.08	163.57	191.35
	41.83	40.47	41.83	42.16	41.55	40.08	41.80
	1.33	1.36	1.11	0.84	0.67	0.49	0.32
$(\pm 2, 1)^{\ddagger}$	4030.39	4062.32	4079.42	4067.78	4056.24	4042.69	4023.38
	0.00	49.45	47.09	39.78	49.01	60.93	69.63
	70.90	64.95	56.57	44.02	45.43	50.51	53.55
	0.21	0.19	0.17	0.30	0.13	0.09	0.09
$(\pm 5, 0)^{\ddagger}$	4379.37	4417.60	4435.66	4433.74	4426.77	4419.91	4410.61
	0.00	27.49	48.60	74.68	101.06	128.88	155.43
	28.27	18.26	13.78	12.81	12.60	14.66	14.48
	0.38	0.34	0.30	0.26	0.22	0.19	0.16

**Tab. B.24:** Measured modal parameters  $(\bar{\omega}^r, {}_S\Delta\omega^r, \delta^r, \kappa)^T$  for  $h_S = 1.0$  mm,  $h_R = 2.0$  mm and  $g = 14.4$  mm.

mode	angular rotor speed $\Omega_R$ in rad/s						
	0	8.38	16.8	25.1	33.5	41.9	50.3
$(\pm 1, 0)^\downarrow$	464.37	466.55	466.43	466.49	466.07	466.06	464.02
	0.00	7.05	12.72	18.76	25.34	33.18	38.70
	1.86	2.22	3.54	5.05	6.89	9.34	13.51
	2.26	2.01	2.23	2.27	2.08	2.05	1.75
$(\pm 1, 0)^\uparrow$	843.04	840.44	836.92	832.25	843.80	839.66	835.19
	0.00	-5.38	-6.34	-6.55	27.50	33.12	39.83
	4.59	4.93	4.83	4.91	4.82	5.20	5.77
	1.08	1.06	1.23	1.13	1.07	1.04	1.09
$(\pm 2, 0)^\downarrow$	896.98	896.93	897.66	898.28	899.23	901.62	902.15
	0.00	14.45	29.58	43.72	58.44	70.76	86.12
	2.31	2.10	2.98	4.05	4.92	8.35	10.98
	3.54	3.68	3.58	3.40	3.30	3.07	2.39
$(0, 1)^\downarrow$	1187.77	1185.92	1183.96	1180.43	1176.81	1169.48	1160.43
	0.00	0.00	0.00	0.00	0.00	0.00	0.00
	26.07	26.40	26.41	26.34	26.45	25.88	25.90
	0.31	0.31	0.29	0.31	0.29	0.31	0.28
$(\pm 2, 0)^\uparrow$	1635.49	1636.97	1637.26	1635.49	1632.66	1628.44	1624.11
	0.00	11.48	23.01	35.64	47.96	61.25	74.67
	5.67	5.57	5.44	5.62	5.35	5.88	5.56
	0.90	0.89	0.87	0.86	0.82	0.80	0.79
$(\pm 3, 0)^\downarrow$	1959.37	1959.68	1960.00	1959.31	1958.30	1956.79	1954.09
	0.00	19.15	37.12	56.05	77.18	98.13	119.44
	4.42	4.85	4.58	5.19	5.74	6.68	7.80
	1.23	1.23	1.16	1.13	1.06	0.98	0.89
$(\pm 3, 0)^\uparrow$	2910.17	2913.89	2916.63	2923.02	2926.30	2924.42	2918.18
	0.00	8.35	31.57	56.61	90.07	125.56	149.76
	30.60	34.57	38.45	38.86	40.27	46.17	43.74
	1.20	1.09	0.87	0.70	0.55	0.35	0.30
$(\pm 4, 0)^\downarrow$	3317.59	3318.61	3319.73	3318.72	3316.07	3313.13	3311.10
	0.00	18.82	38.53	57.39	79.10	102.68	137.91
	20.73	21.23	20.91	19.64	19.98	20.10	23.06
	0.56	0.51	0.41	0.35	0.30	0.24	0.20
$(\pm 2, 1)^\downarrow$	4451.25	4454.74	4452.56	4445.00	4434.94	4426.45	4415.31
	0.00	30.57	41.64	44.11	57.36	64.54	64.95
	68.00	61.81	60.64	47.22	52.04	49.78	50.73
	0.16	0.15	0.12	0.11	0.09	0.07	0.06
$(\pm 5, 0)^\downarrow$	4855.22	4856.92	4856.37	4853.94	4849.24	4846.44	4843.60
	0.00	15.63	38.46	53.71	74.84	101.83	128.38
	16.64	19.53	16.25	15.57	14.88	13.87	13.66
	0.31	0.25	0.22	0.21	0.18	0.15	0.13

**Tab. B.25:** Measured modal parameters  $(\bar{\omega}^r, {}_S\Delta\omega^r, \delta^r, \kappa)^T$  for  $h_S = 1.5 \text{ mm}$ ,  $h_R = 1.5 \text{ mm}$  and  $g = 1.4 \text{ mm}$ .

mode	angular rotor speed $\Omega_R$ in rad/s						
	0	8.38	16.8	25.1	33.5	41.9	50.3
$(\pm 1, 0)^{\ddagger}$	163.24	165.03	167.75	172.47	178.44	180.29	196.35
	0.00	9.08	18.70	28.05	65.32	79.41	67.30
	4.35	6.97	11.13	17.26	38.51	48.47	77.77
	10.59	9.23	10.32	9.78	9.01	12.12	11.74
$(\pm 2, 0)^{\ddagger}$	318.77	321.90	322.18	323.01	326.90	329.39	335.59
	0.00	23.40	45.99	60.81	61.27	77.16	60.86
	5.89	6.95	8.07	12.00	12.73	17.39	29.58
	14.17	32.74	27.96	15.34	17.68	12.58	9.10
$(\pm 3, 0)^{\ddagger}$	803.29	803.42	804.67	806.16	802.32	790.99	782.04
	0.00	26.97	49.57	73.89	90.47	101.68	126.54
	12.83	12.47	14.22	14.53	14.61	14.88	18.17
	7.66	7.42	6.24	5.68	5.26	5.60	4.46
$(\pm 1, 0)^{\ddagger\dagger}$	866.60	860.96	862.23	859.96	855.67	849.73	842.25
	0.00	15.09	16.05	20.66	26.42	32.57	40.31
	10.21	10.54	10.65	11.14	11.78	12.93	14.48
	1.60	1.56	1.54	1.53	1.51	1.45	1.39
$(\pm 4, 0)^{\ddagger}$	1556.96	1555.47	1550.79	1544.34	1536.06	1523.65	1508.71
	0.00	32.26	62.70	93.03	121.84	153.36	183.66
	16.80	16.80	17.56	18.08	19.62	20.56	23.02
	5.09	4.71	4.07	3.38	2.86	2.37	2.00
$(\pm 2, 0)^{\ddagger\dagger}$	1818.67	1818.66	1815.19	1809.61	1801.35	1789.02	1774.07
	0.00	14.30	28.44	41.10	55.63	70.65	86.27
	13.95	14.18	14.59	15.07	15.91	16.43	18.03
	1.84	1.78	1.73	1.61	1.51	1.42	1.29
$(\pm 1, 1)^{\ddagger}$	2153.71	2136.83	2137.28	2139.35	2140.40	2144.84	2122.15
	0.00	14.10	14.83	13.64	13.53	9.76	-15.43
	61.13	47.93	50.75	54.01	66.94	96.95	119.89
	1.25	1.24	1.16	1.07	0.94	0.70	0.60
$(\pm 5, 0)^{\ddagger}$	2601.21	2595.66	2587.55	2578.25	2564.46	2544.12	2518.18
	0.00	40.59	80.62	118.29	157.47	197.87	237.73
	21.90	21.62	21.81	22.49	23.96	25.22	28.43
	4.05	3.57	2.87	2.18	1.59	1.19	0.79
$(\pm 3, 0)^{\ddagger\dagger}$	3178.18	3172.05	3169.33	3158.65	3142.20	3124.75	3098.59
	0.00	24.00	43.21	63.93	89.45	110.72	130.02
	20.33	20.54	20.57	20.62	22.01	23.24	23.73
	2.09	2.01	1.77	1.60	1.42	1.10	0.98
$(\pm 2, 1)^{\ddagger}$	3309.14	3308.80	3301.47	3309.88	3309.80	3297.50	3300.15
	0.00	11.34	13.11	21.23	41.35	47.62	70.77
	56.96	58.55	59.92	66.18	72.08	71.63	71.73
	0.96	0.99	0.84	0.67	0.49	0.40	0.27
$(\pm 1, 1)^{\ddagger\dagger}$	3787.14	3774.39	3762.86	3790.65	3815.50	3762.08	3676.08
	0.00	24.96	51.63	47.85	9.81	30.05	44.13
	59.25	53.11	72.24	98.90	77.27	96.26	71.91
	1.32	1.19	1.10	0.86	0.86	0.66	0.76

**Tab. B.26:** Measured modal parameters  $(\bar{\omega}^r, {}_S\Delta\omega^r, \delta^r, \kappa)^T$  for  $h_S = 1.5$  mm,  $h_R = 1.5$  mm and  $g = 2.2$  mm.

mode	angular rotor speed $\Omega_R$ in rad/s						
	0	8.38	16.8	25.1	33.5	41.9	50.3
$(\pm 1, 0)^\dagger$	203.15	204.15	206.58	210.93	209.57	211.73	225.58
	0.00	9.61	17.53	27.33	34.81	31.11	35.67
	4.04	5.37	8.40	11.15	19.10	26.59	34.74
	11.23	11.16	10.20	9.77	6.57	10.41	9.69
$(\pm 2, 0)^\dagger$	399.83	399.36	398.96	397.91	401.91	403.43	408.74
	0.00	21.37	41.65	58.40	71.28	77.38	88.31
	4.09	5.79	8.43	12.22	15.89	15.57	20.60
	20.41	16.68	16.82	14.24	12.97	12.42	13.58
$(\pm 3, 1)^\dagger$	979.24	973.66	974.12	974.96	970.83	966.76	961.93
	0.00	28.57	48.97	68.59	86.37	110.72	129.57
	6.56	6.61	6.06	8.26	8.52	9.09	9.25
	9.49	12.53	9.77	8.74	7.73	6.85	5.26
$(\pm 1, 0)^\ddagger$	982.89	978.54	979.07	978.33	976.67	973.93	970.73
	0.00	12.38	15.51	19.92	25.23	30.95	36.86
	6.74	6.57	6.88	7.34	7.75	8.56	9.64
	1.53	1.44	1.48	1.44	1.41	1.37	1.39
$(\pm 4, 0)^\dagger$	1878.17	1877.72	1876.24	1875.04	1870.44	1864.44	1857.63
	0.00	31.75	60.41	88.83	118.13	150.26	181.70
	10.71	10.89	10.93	12.14	14.09	14.87	16.47
	5.64	5.19	4.95	4.36	3.60	3.28	2.59
$(\pm 2, 0)^\ddagger$	2062.00	2064.23	2062.61	2060.80	2057.12	2052.81	2046.47
	0.00	14.13	26.13	39.34	52.54	66.71	80.79
	10.63	9.46	9.87	10.06	10.11	10.95	11.50
	1.66	1.64	1.60	1.54	1.47	1.38	1.32
$(\pm 1, 1)^\dagger$	2389.71	2301.56	2323.86	2292.81	2297.37	2315.19	2313.10
	0.00	220.05	212.20	45.27	42.78	37.56	45.54
	184.36	105.15	116.36	70.11	59.40	51.10	53.41
	1.31	1.30	1.36	1.19	1.07	0.83	0.76
$(\pm 5, 0)^\dagger$	3124.40	3120.83	3119.14	3114.62	3107.59	3097.77	3085.00
	0.00	40.05	76.64	111.54	151.53	191.76	231.25
	13.88	14.29	14.53	14.55	15.41	16.33	18.19
	4.56	4.10	3.53	3.01	2.55	2.02	1.54
$(\pm 2, 1)^\dagger$	3559.99	3562.22	3557.94	3555.92	3555.69	3539.19	3535.11
	0.00	-27.60	11.48	4.91	37.27	29.62	59.40
	30.26	35.49	34.35	52.74	35.10	43.25	34.90
	1.27	1.32	1.14	0.99	0.83	0.75	0.64
$(\pm 3, 0)^\ddagger$	3588.92	3591.00	3588.10	3585.80	3577.58	3572.87	3561.19
	0.00	21.59	41.81	59.45	82.24	99.16	127.04
	16.35	14.65	15.37	14.25	16.14	16.17	17.23
	1.85	1.70	1.63	1.46	1.33	1.10	1.05
$(\pm 1, 1)^\ddagger$	4331.23	4334.99	4320.13	4319.94	4305.18	4326.72	4275.01
	0.00	6.10	23.98	21.81	42.51	42.33	56.61
	40.80	43.36	43.72	47.12	64.63	91.05	87.82
	1.25	1.11	1.10	0.84	0.91	0.58	0.63

**Tab. B.27:** Measured modal parameters  $(\bar{\omega}^r, {}_S\Delta\omega^r, \delta^r, \kappa)^T$  for  $h_S = 1.5 \text{ mm}$ ,  $h_R = 1.5 \text{ mm}$  and  $g = 2.9 \text{ mm}$ .

mode	angular rotor speed $\Omega_R$ in rad/s						
	0	8.38	16.8	25.1	33.5	41.9	50.3
$(\pm 1, 0)^{\updownarrow}$	227.69	228.67	230.11	232.32	234.40	241.97	243.98
	0.00	8.77	18.27	29.01	30.92	30.23	31.57
	3.31	5.17	7.62	12.59	18.68	25.67	31.42
	11.82	12.17	11.80	11.40	10.84	9.25	9.64
$(\pm 2, 0)^{\updownarrow}$	441.08	441.84	441.97	442.34	445.41	447.98	451.45
	0.00	20.74	42.34	60.98	77.69	88.81	98.22
	4.41	4.41	6.19	10.33	13.64	14.57	16.98
	36.69	175.15	44.87	24.14	18.28	11.99	14.00
$(\pm 1, 0)^{\uparrow\uparrow}$	1034.80	1038.02	1030.74	1029.98	1028.93	1027.00	1024.40
	0.00	-3.55	15.55	20.31	25.49	31.15	37.31
	6.14	5.91	6.03	6.51	6.95	7.75	8.59
	1.43	1.44	1.40	1.35	1.34	1.33	1.27
$(\pm 3, 0)^{\updownarrow}$	1072.36	1071.94	1070.92	1071.56	1072.95	1073.12	1073.22
	0.00	24.76	50.05	70.90	89.20	111.24	133.46
	5.60	6.81	7.21	7.00	9.21	11.45	12.56
	9.33	8.62	7.88	8.12	8.11	7.27	6.36
$(\pm 4, 0)^{\updownarrow}$	2063.93	2063.30	2062.65	2061.72	2060.35	2055.86	2052.08
	0.00	31.87	61.65	91.94	125.64	155.59	189.31
	8.94	8.93	9.19	10.22	11.37	11.37	17.00
	5.97	5.71	5.34	4.82	3.88	3.26	2.57
$(\pm 2, 0)^{\uparrow\uparrow}$	2174.04	2175.39	2175.53	2174.82	2171.00	2167.49	2163.19
	0.00	12.12	25.83	38.73	52.14	66.21	80.08
	8.76	9.15	9.38	9.58	9.63	10.30	10.73
	1.57	1.55	1.51	1.46	1.39	1.33	1.26
$(\pm 1, 1)^{\updownarrow}$	2406.81	2407.33	2405.40	2408.59	2386.99	2387.17	2396.26
	0.00	28.76	32.91	27.48	34.40	35.11	70.23
	83.14	86.30	77.74	73.42	80.36	76.93	83.81
	1.48	1.45	1.39	1.22	1.17	1.07	0.94
$(\pm 5, 0)^{\updownarrow}$	3421.53	3423.00	3419.31	3416.53	3412.16	3405.28	3396.38
	0.00	46.42	78.10	116.94	157.68	198.22	241.50
	12.14	13.01	11.56	12.40	12.92	14.38	15.91
	4.97	4.46	3.91	3.40	2.96	2.40	1.93
$(\pm 3, 0)^{\uparrow\uparrow}$	3771.97	3775.10	3776.22	3770.84	3767.75	3759.56	3753.28
	0.00	22.61	46.09	65.27	82.70	104.78	125.36
	30.72	30.05	28.56	24.89	25.42	23.92	23.20
	1.62	1.44	1.24	1.08	0.88	0.74	0.61
$(\pm 2, 1)^{\updownarrow}$	3801.83	3799.41	3800.20	3796.94	3794.71	3788.14	3780.91
	0.00	26.06	40.80	55.27	67.72	95.46	108.76
	34.36	32.19	33.87	38.44	40.78	45.86	48.43
	1.48	1.41	1.25	1.10	0.93	0.76	0.59
$(\pm 1, 1)^{\uparrow\uparrow}$	4592.88	4592.88	4588.55	4582.91	4604.76	4599.19	4544.86
	0.00	-4.68	6.23	15.59	18.01	23.27	28.60
	41.08	41.58	47.99	65.83	68.08	75.98	83.01
	1.11	1.07	1.07	0.99	0.84	0.66	0.64

**Tab. B.28:** Measured modal parameters  $(\bar{\omega}^r, {}_S\Delta\omega^r, \delta^r, \kappa)^T$  for  $h_S = 1.5$  mm,  $h_R = 1.5$  mm and  $g = 3.6$  mm.

mode	angular rotor speed $\Omega_R$ in rad/s						
	0	8.38	16.8	25.1	33.5	41.9	50.3
$(\pm 1, 0)^\dagger$	248.49	249.21	250.34	253.70	256.01	259.20	254.27
	0.00	9.21	18.31	29.60	33.76	31.49	36.49
	2.77	4.47	6.46	10.19	17.77	27.05	23.34
	11.68	12.62	3.30	12.48	10.37	8.78	5.71
$(\pm 2, 0)^\dagger$	480.19	480.33	482.07	483.12	483.47	484.43	485.19
	0.00	18.42	29.00	47.92	67.13	82.08	108.28
	3.62	5.36	6.72	8.77	11.62	14.41	17.40
	17.50	15.87	16.75	13.90	13.73	11.93	11.66
$(\pm 1, 0)^\ddagger$	1071.75	1075.51	1074.48	1073.30	1071.90	1070.01	1068.23
	0.00	6.90	11.62	17.23	22.80	28.64	34.72
	5.81	5.29	5.49	5.85	6.16	6.87	7.87
	1.32	1.35	1.35	1.33	1.29	0.93	1.25
$(\pm 4, 0)^\dagger$	2220.33	2219.22	2219.52	2219.67	2217.40	2213.79	2208.19
	0.00	31.90	65.54	96.37	128.40	161.41	191.60
	6.25	7.06	8.83	8.52	7.38	8.47	9.01
	6.63	6.40	5.64	5.50	5.71	5.24	4.22
$(\pm 2, 0)^\ddagger$	2255.74	2263.89	2262.13	2260.04	2257.10	2253.69	2251.56
	0.00	12.65	24.77	37.51	50.37	63.68	77.49
	7.58	7.59	8.68	9.65	10.28	11.46	11.16
	1.47	1.46	1.42	1.37	1.31	1.24	1.19
$(\pm 1, 1)^\dagger$	2542.71	2542.60	2546.92	2500.96	2457.25	2451.65	2474.95
	0.00	18.23	-8.22	6.55	46.59	60.86	87.77
	73.65	85.76	93.47	123.83	144.58	151.34	146.92
	1.60	1.62	1.46	1.24	1.19	1.05	0.79
$(\pm 5, 0)^\dagger$	3669.66	3668.80	3666.70	3665.02	3661.45	3656.22	3652.89
	0.00	41.17	79.35	119.94	160.95	203.88	251.02
	10.53	9.45	12.01	9.67	11.42	11.86	15.00
	5.15	4.90	4.34	3.96	3.40	2.86	2.15
$(\pm 3, 0)^\ddagger$	3877.02	3885.92	3886.65	3888.70	3888.61	3884.61	3882.22
	0.00	25.21	46.01	63.71	79.97	106.01	127.79
	16.81	18.56	24.49	21.86	23.66	24.68	25.62
	1.48	1.34	1.14	1.02	0.88	0.74	0.63
$(\pm 2, 1)^\dagger$	3922.33	3923.47	3927.94	3918.98	3921.10	3918.37	3922.73
	0.00	50.15	50.55	69.23	79.58	98.87	126.03
	33.90	44.17	35.74	30.44	32.52	29.87	36.91
	1.72	1.66	1.37	1.29	1.12	1.08	0.90
$(\pm 1, 1)^\ddagger$	4766.32	4778.78	4773.70	4781.79	4787.49	4776.29	4758.57
	0.00	6.21	3.58	8.62	20.09	36.44	29.53
	71.59	70.58	65.83	72.41	67.85	75.87	65.30
	1.11	1.07	0.99	0.92	0.79	0.63	0.59

**Tab. B.29:** Measured modal parameters  $(\bar{\omega}^r, {}_S\Delta\omega^r, \delta^r, \kappa)^T$  for  $h_S = 1.5$  mm,  $h_R = 1.5$  mm and  $g = 4.4$  mm.

mode	angular rotor speed $\Omega_R$ in rad/s						
	0	8.38	16.8	25.1	33.5	41.9	50.3
$(\pm 1, 0)^{\downarrow}$	265.78	265.70	267.24	269.00	270.74	271.94	272.97
	0.00	8.41	16.90	22.34	31.05	33.86	42.36
	2.93	3.95	6.40	9.09	14.38	14.30	15.07
	13.04	13.21	9.97	12.90	14.82	11.29	9.43
$(\pm 2, 0)^{\downarrow}$	511.55	511.97	512.22	514.56	516.68	517.46	517.24
	0.00	14.50	34.77	42.71	60.78	80.52	103.96
	3.38	4.11	6.48	8.52	10.48	14.12	23.04
	18.09	18.60	17.69	14.79	14.26	16.01	8.81
$(\pm 1, 0)^{\uparrow}$	1103.26	1112.28	1114.45	1115.43	1116.51	1118.07	1120.29
	0.00	-11.07	-11.42	-10.73	-9.80	-10.08	-11.22
	12.95	10.08	9.39	8.72	7.70	7.51	7.74
	1.29	1.31	1.29	1.22	1.17	1.15	1.10
$(\pm 3, 0)^{\downarrow}$	1228.71	1228.58	1229.22	1229.81	1228.94	1226.68	1223.85
	0.00	22.76	44.82	66.70	89.11	112.38	138.43
	4.21	4.55	4.92	6.19	7.74	8.87	12.00
	10.08	9.64	9.58	9.45	8.59	7.69	6.23
$(\pm 2, 0)^{\uparrow}$	2313.82	2322.40	2322.32	2320.30	2319.14	2314.27	2312.15
	0.00	10.49	23.23	35.19	46.31	60.05	72.68
	7.31	7.26	8.06	8.59	12.44	10.14	10.44
	1.38	1.39	1.35	1.31	1.16	1.19	1.12
$(\pm 1, 1)^{\downarrow}$	2682.73	2690.94	2692.69	2688.55	2702.59	2605.21	2554.66
	0.00	-38.48	-43.75	-62.06	-68.68	-25.64	91.48
	60.74	60.88	59.77	67.29	69.82	115.49	121.07
	1.90	1.84	1.58	1.42	1.41	1.31	1.30
$(\pm 5, 0)^{\downarrow}$	3881.84	3880.95	3878.68	3879.09	3875.20	3871.34	3867.65
	0.00	40.36	81.22	120.68	159.74	201.51	244.57
	8.44	9.52	8.00	12.01	9.46	9.67	11.55
	5.76	5.52	4.96	4.10	3.87	3.42	2.61
$(\pm 3, 0)^{\uparrow}$	3962.57	3968.81	3968.94	3976.62	3974.84	3974.17	3972.67
	0.00	18.56	32.94	54.37	71.35	91.78	117.61
	19.10	18.43	20.36	21.18	18.56	21.66	23.28
	1.34	1.25	1.12	0.97	0.95	0.78	0.67
$(\pm 2, 1)^{\downarrow}$	4062.60	4062.45	4069.42	4099.15	4090.03	4090.13	4069.70
	0.00	21.84	37.36	52.24	54.53	59.38	80.23
	37.49	43.07	48.70	47.90	37.07	39.81	43.08
	1.76	1.71	1.47	1.16	1.12	0.77	0.78
$(\pm 1, 1)^{\uparrow}$	4904.01	4919.15	4911.86	4899.57	4907.35	4902.48	4870.48
	0.00	-6.60	12.59	30.31	15.17	5.86	53.51
	56.55	58.96	63.97	66.01	73.63	84.41	68.31
	1.00	0.88	0.99	0.89	0.61	0.52	0.44



**Tab. B.30:** Measured modal parameters  $(\bar{\omega}^r, {}_S\Delta\omega^r, \delta^r, \kappa)^T$  for  $h_S = 1.5$  mm,  $h_R = 1.5$  mm and  $g = 6.4$  mm.

mode	angular rotor speed $\Omega_R$ in rad/s						
	0	8.38	16.8	25.1	33.5	41.9	50.3
$(\pm 1, 0)^{\downarrow}$	299.94	300.72	300.95	301.52	304.37	305.40	305.52
	0.00	6.06	16.51	24.11	33.56	36.75	46.48
	2.43	3.16	5.12	7.87	9.89	12.09	19.07
$(\pm 2, 0)^{\downarrow}$	13.96	13.59	15.39	11.89	20.00	10.82	13.94
	570.55	570.86	571.94	573.07	574.67	578.60	578.22
	0.00	14.30	29.96	42.75	58.50	75.46	92.83
$(\pm 1, 0)^{\uparrow}$	3.36	3.31	5.90	6.15	6.06	10.98	14.81
	20.75	21.25	20.12	18.28	16.58	13.13	13.72
	1151.54	1156.27	1158.18	1161.45	1161.42	1161.07	1159.80
$(\pm 3, 0)^{\downarrow}$	0.00	9.29	13.99	19.80	24.32	28.95	32.77
	8.31	6.76	6.62	6.70	6.58	6.58	6.61
	1.18	1.10	1.16	1.07	1.13	1.09	1.08
$(\pm 2, 0)^{\uparrow}$	1362.64	1361.80	1362.58	1364.21	1364.88	1364.32	1363.45
	0.00	23.61	46.20	68.33	92.44	116.75	141.90
	3.01	3.61	4.17	5.37	6.96	8.55	10.85
$(\pm 4, 0)^{\downarrow}$	11.43	11.15	11.21	10.94	9.99	9.28	7.95
	2436.54	2444.20	2443.96	2445.13	2446.78	2440.58	2439.29
	0.00	9.21	20.91	31.70	42.35	55.50	67.35
$(\pm 1, 1)^{\downarrow}$	6.75	6.93	7.68	7.81	9.26	8.59	8.96
	1.21	1.21	1.18	1.14	1.07	1.06	1.01
	2593.02	2591.58	2591.51	2593.17	2593.25	2593.11	2592.27
$(\pm 3, 0)^{\uparrow}$	0.00	31.72	64.09	95.72	128.24	160.87	195.23
	4.49	4.91	4.94	5.40	6.35	7.53	10.08
	8.04	8.09	7.56	7.14	6.73	5.91	4.97
$(\pm 1, 1)^{\uparrow}$	2902.93	2895.19	2902.90	2926.72	2934.59	2898.42	2901.93
	0.00	-32.12	-36.95	-36.60	-33.74	-43.81	-42.66
	49.25	56.75	51.65	47.89	45.29	69.86	71.24
$(\pm 5, 0)^{\downarrow}$	2.17	2.30	2.04	1.90	1.84	1.26	1.28
	4116.26	4123.84	4125.45	4127.17	4126.84	4127.16	4127.23
	0.00	16.86	33.07	48.11	63.68	81.01	99.72
$(\pm 2, 1)^{\downarrow}$	16.21	17.33	18.82	19.39	21.27	21.59	23.46
	1.11	1.06	0.95	0.84	0.75	0.64	0.50
	4254.14	4252.71	4252.40	4252.78	4251.45	4250.80	4248.75
$(\pm 3, 1)^{\downarrow}$	0.00	43.47	83.26	124.10	167.54	210.96	253.76
	6.96	6.84	6.38	7.13	7.23	7.10	8.64
	6.61	6.26	5.85	5.61	5.28	5.02	3.71
$(\pm 2, 1)^{\uparrow}$	4381.91	4381.17	4382.60	4379.74	4381.12	4382.26	4383.05
	0.00	17.68	30.82	40.26	60.24	75.57	89.14
	34.37	34.10	37.67	41.88	42.12	43.48	45.25
	2.26	2.12	1.82	1.56	1.30	1.09	0.87

**Tab. B.31:** Measured modal parameters  $(\bar{\omega}^r, {}_S\Delta\omega^r, \delta^r, \kappa)^T$  for  $h_S = 1.5$  mm,  $h_R = 1.5$  mm and  $g = 9.4$  mm.

mode	angular rotor speed $\Omega_R$ in rad/s						
	0	8.38	16.8	25.1	33.5	41.9	50.3
$(\pm 1, 0)^{\ddagger}$	333.54	334.10	334.95	336.19	337.95	340.92	344.52
	0.00	8.02	16.31	25.63	33.57	38.75	40.75
	1.94	3.12	4.97	7.33	10.80	16.17	18.01
	16.78	16.32	3.88	18.25	15.82	16.43	6.39
$(\pm 2, 0)^{\ddagger}$	627.18	626.92	627.38	629.80	631.38	633.01	634.14
	0.00	14.65	31.49	45.75	60.84	78.71	100.44
	2.51	2.64	5.09	5.14	7.43	7.48	9.92
	24.82	24.84	23.43	25.18	26.32	23.47	19.47
$(\pm 1, 0)^{\dagger\dagger}$	1211.02	1216.00	1216.72	1216.27	1216.19	1215.95	1215.67
	0.00	10.24	13.09	17.75	21.05	25.98	31.18
	11.43	12.94	12.32	13.61	13.83	14.56	15.15
	1.00	1.01	0.98	0.92	0.91	0.89	0.85
$(\pm 3, 0)^{\ddagger}$	1484.63	1484.43	1485.61	1486.67	1487.62	1487.85	1488.09
	0.00	23.69	47.01	71.75	97.97	122.47	146.82
	2.66	2.66	3.12	3.72	4.92	5.96	7.74
	13.99	13.69	13.90	14.06	13.35	8.44	9.29
$(\pm 2, 0)^{\dagger\dagger}$	2539.65	2548.82	2550.92	2551.21	2547.93	2547.10	2545.84
	0.00	9.38	20.06	29.94	41.58	51.11	62.09
	8.30	8.90	9.22	9.39	9.95	9.66	10.29
	1.00	0.97	0.97	0.93	0.90	0.86	0.81
$(\pm 4, 0)^{\ddagger}$	2807.30	2806.34	2806.80	2807.47	2808.14	2808.16	2809.00
	0.00	34.04	65.92	100.41	136.14	171.01	205.90
	3.48	3.80	4.10	4.00	4.60	5.98	7.06
	10.26	9.61	9.76	9.34	9.05	8.50	7.22
$(\pm 1, 1)^{\dagger\dagger}$	3144.48	3132.41	3141.96	3154.21	3092.36	3111.37	3098.44
	0.00	18.43	19.42	11.62	4.85	1.92	29.24
	78.99	96.60	103.23	94.91	110.88	126.15	140.35
	2.54	2.76	2.59	2.07	2.02	1.52	1.31
$(\pm 3, 0)^{\dagger\dagger}$	4247.38	4254.67	4258.26	4259.31	4262.46	4260.51	4261.84
	0.00	18.65	32.17	41.70	54.13	75.58	95.47
	18.43	19.08	21.41	21.79	21.43	21.57	25.68
	0.91	0.82	0.73	0.65	0.59	0.53	0.43
$(\pm 5, 0)^{\ddagger}$	4577.39	4576.40	4576.72	4576.50	4576.28	4576.53	4576.49
	0.00	44.00	87.03	131.83	176.49	222.51	268.23
	5.35	5.25	5.27	5.48	5.44	5.79	6.86
	8.64	8.30	7.57	6.88	6.75	6.11	5.60
$(\pm 2, 1)^{\ddagger}$	4692.38	4693.39	4694.82	4686.39	4687.41	4689.89	4690.45
	0.00	25.18	38.39	53.96	65.30	80.02	94.76
	29.60	30.02	29.69	29.82	27.27	27.45	29.45
	2.66	2.56	2.40	2.17	2.05	1.81	1.45

**Tab. B.32:** Measured modal parameters  $(\bar{\omega}^r, {}_S\Delta\omega^r, \delta^r, \kappa)^T$  for  $h_S = 1.5$  mm,  $h_R = 1.5$  mm and  $g = 14.4$  mm.

mode	angular rotor speed $\Omega_R$ in rad/s						
	0	8.38	16.8	25.1	33.5	41.9	50.3
$(\pm 1, 0)^\downarrow$	366.91	367.36	368.17	369.03	370.41	372.92	374.63
	0.00	6.74	16.56	23.79	32.84	37.61	46.52
	2.04	2.42	4.21	6.12	8.91	13.69	17.81
	20.17	19.54	21.08	19.61	19.79	20.90	17.63
$(\pm 2, 0)^\downarrow$	678.71	678.78	678.58	677.93	681.20	681.08	686.54
	0.00	15.05	36.21	56.71	63.50	82.52	94.66
	3.94	2.51	4.22	6.57	6.39	9.02	10.05
	30.06	31.08	28.50	35.00	34.09	30.70	30.80
$(\pm 1, 0)^\uparrow$	1298.88	1301.21	1302.99	1305.79	1308.64	1309.50	1310.23
	0.00	-22.41	-22.18	-22.33	-20.18	-21.53	-22.71
	16.52	16.81	16.80	17.14	16.78	16.98	17.16
	0.77	0.79	0.76	0.72	0.67	0.62	0.55
$(\pm 3, 0)^\downarrow$	1592.11	1591.72	1593.13	1594.58	1593.93	1593.00	1593.91
	0.00	24.57	48.79	72.09	97.67	124.00	151.64
	2.42	1.62	2.31	2.68	3.78	5.25	5.70
	18.06	19.30	19.00	22.48	19.54	18.18	16.97
$(\pm 2, 0)^\uparrow$	2639.56	2640.97	2642.02	2646.58	2640.28	2638.49	2636.68
	0.00	7.73	15.66	38.15	37.74	46.09	55.67
	14.60	15.78	17.01	24.92	19.71	19.57	20.96
	0.73	0.73	0.70	0.58	0.66	0.57	0.51
$(\pm 4, 0)^\downarrow$	2985.54	2985.66	2986.28	2986.53	2987.56	2989.50	2989.86
	0.00	34.35	68.93	102.99	139.30	175.80	211.60
	3.29	3.09	3.38	3.81	3.64	4.54	5.70
	14.71	14.58	14.54	13.45	12.96	12.39	11.77
$(\pm 3, 0)^\uparrow$	4376.69	4377.69	4376.06	4377.54	4377.82	4378.00	4378.84
	0.00	15.68	28.92	36.31	52.42	67.65	79.63
	26.63	25.76	26.65	25.18	26.37	28.37	25.64
	0.64	0.57	0.48	0.42	0.36	0.31	0.30
$(\pm 5, 0)^\downarrow$	4833.22	4833.18	4833.58	4833.94	4834.38	4834.84	4836.26
	0.00	45.55	90.13	135.53	182.68	229.97	277.33
	3.90	4.47	4.53	4.62	4.52	4.78	5.51
	12.63	11.72	11.00	10.20	9.54	9.77	8.63
$(\pm 2, 1)^\downarrow$	4958.79	4956.34	4957.78	4956.19	4950.45	4955.42	4957.07
	0.00	21.43	37.34	52.32	73.69	91.37	110.51
	21.32	21.33	21.10	22.47	22.08	24.58	23.57
	3.69	3.80	3.27	3.22	3.04	2.67	2.40



# References

- Advanpix (2016). *Multiprecision Computing Toolbox for MATLAB, version 3.9.9.11048*. Advanpix LLC. §3.1.3
- Amabili, M. (2001). Vibrations of circular plates resting on a sloshing liquid: Solution of the fully coupled problem. *Journal of Sound and Vibration*, 245(2):261–283. §1.2
- Amabili, M., Frosali, G., and Kwak, M. K. (1996). Free vibrations of annular plates coupled with fluids. *Journal of Sound and Vibration*, 191(5):825–846. §1.2
- Amabili, M. and Kwak, M. K. (1996). Free vibrations of circular plates coupled with liquids. *Journal of Fluids and Structures*, 10(7):743–761. §1.2
- Bassio, M., Valentín, D., Presas, A., Martin, D. R., Egusquiza, E., Valero, C., and Egusquiza, M. (2017). Numerical study on the influence of acoustic natural frequencies on the dynamic behaviour of submerged and confined disk-like structures. *Journal of Fluids and Structures*, 73:53–69. §1.2
- Batchelor, G. K. (1951). Note on a class of solutions of the Navier–Stokes equations representing steady rotationally-symmetric flow. *The Quarterly Journal of Mechanics and Applied Mathematics*, 4(1):29–41. §1.2
- Batchelor, G. K. and Gill, A. E. (1962). Analysis of the stability of axisymmetric jets. *Journal of Fluid Mechanics*, 14(4):529–551. §6.1.3
- Benjamin, T. B. (1960). Effects of a flexible boundary on hydrodynamic stability. *Journal of Fluid Mechanics*, 9(4):513–532. §2, §2.3.3

- Boedecker, S., Dräbenstedt, A., Heller, L., Kraft, A., Leonhardt, A., Pape, C., Ristau, S., Reithmeier, E., and Rembe, C. (2006). Optical derotator for scanning vibrometer measurements on rotating objects. In *Seventh International Conference on Vibration Measurements by Laser Techniques: Advances and Applications*, volume 6345, pages 1–11. A.I.VE.LA, Proc. SPIE. §4.3.5, §4.3.5
- Bonet, J. and Wood, R. D. (2008). *Nonlinear Continuum Mechanics for Finite Element Analysis*. Cambridge University Press, 2nd edition. §2, §2.1.4, §A.1
- Boyd, S. P. (1986). Multitone signals with low crest factor. *IEEE Transactions on Circuits and Systems*, 33(10):1018–1022. §5.1.2
- Bremer, H. (1988). *Dynamik und Regelung mechanischer Systeme*, volume 67 of *Leitfäden der angewandten Mathematik und Mechanik*. Vieweg+Teubner. §2.1.4
- Bremer, H. (2008). *Elastic Multibody Dynamics: A Direct Ritz Approach*, volume 35 of *Intelligent Systems, Control, and Automation: Science and Engineering*. Springer Netherlands. §2, §2.1.4
- Bremer, H. and Pfeiffer, F. (1992). *Elastische Mehrkörpersysteme*. Teubner Stuttgart. §2.1.4
- Brewer, C. A., Hatchard, G. W., and Harrower, M. A. (2003). ColorBrewer in print: A catalog of color schemes for maps. *Cartography and Geographic Information Science*, 30(1). §B.0
- Bucher, I., Schmiechen, P., Robb, D. A., and Ewins, D. J. (1994). A laser-based measurement system for measuring the vibration on rotating discs. In *First International Conference on Vibration Measurements by Laser Techniques: Advances and Applications*, volume 2358, pages 398–408. A.I.VE.LA, Proc. SPIE. §4.3.5
- Carpenter, P. W. and Morris, P. J. (1990). The effect of anisotropic wall compliance on boundary-layer stability and transition. *Journal of Fluid Mechanics*, 218:171–223. §2.3.3
- Chadwick, P. (1976). *Continuum Mechanics: Concise Theory and Problems*. George Allen & Unwin, 2nd edition. §2.1.1

- Chiba, M. (1996). Free vibration of a partially liquid-filled and partially submerged, clamped-free circular cylindrical shell. *Journal of the Acoustical Society of America*, 100(4):2170–2180. §1.2
- Coleman, T. F. and Li, Y. (1994). On the convergence of interior-reflective Newton methods for nonlinear minimization subject to bounds. *Mathematical Programming*, 67:189–224. §5.2.3
- Coleman, T. F. and Li, Y. (1996). An interior trust region approach for nonlinear minimization subject to bounds. *SIAM Journal on Optimization*, 6(2man):418–445. §5.2.3
- COMSOL (2016a). *COMSOL Multiphysics Reference Manual*. COMSOL AB. CM020005 (COMSOL 5.2a). §6.2
- COMSOL (2016b). *COMSOL Programming Reference Manual*. COMSOL AB. CM020007 (COMSOL 5.2a). §6.2
- COMSOL (2016c). *CFD Module User's Guide*. COMSOL AB. CM021301 (COMSOL 5.2a). §6.2.1, §8.2
- Cooley, J. W. and Tukey, J. W. (1965). An algorithm for the machine calculation of complex Fourier series. *Mathematics of Computation*, 19:297–301. §4.3.6, §5.2.3
- Cooper, A. J. and Carpenter, P. W. (1997a). The stability of rotating-disc boundary-layer flow over a compliant wall. Part 1. Type I and II instabilities. *Journal of Fluid Mechanics*, 350:231–259. §1.2
- Cooper, A. J. and Carpenter, P. W. (1997b). The stability of rotating-disc boundary-layer flow over a compliant wall. Part 2. Absolute instability. *Journal of Fluid Mechanics*, 350:261–270. §1.2
- Coutu, A., Roy, M. D., Monette, C., and Nennemann, B. (2008). Experience with rotor–stator interactions in high head Francis runner. In *24th IAHR Symposium on Hydraulic Machinery and Systems*. IAHR. §1.2
- Criminale, W. O., Jackson, T. L., and Joslin, R. D. (2003). *Theory and Computation of Hydrodynamic Stability*. Cambridge University Press, 1st edition. §1.2, §2, §3.1.2

- Cros, A., Ali, R., Legal, P., Thomas, P. J., Schouveiler, L., Carpenter, P. W., and Chauve, M. P. (2003). Effects of wall compliance on the laminar-turbulent transition of torsional Couette flow. *Journal of Fluid Mechanics*, 481:177–186. §1.2
- Davis, C. and Carpenter, P. W. (1997). Instabilities in a plane channel flow between compliant walls. *Journal of Fluid Mechanics*, 352:205–243. §1.2
- Dompierre, F. and Sabourin, M. (2010). Determination of turbine runner dynamic behaviour under operating condition by a two-way staggered fluid-structure interaction method. In *Earth and Environmental Science*, volume 12 of *IOP Conference Series*. 25th IAHR Symposium on Hydraulic Machinery and Systems. September 20–24, 2010, Politehnica University of Timișoara, Timișoara, Romania. §1.2
- Drazin, P. D. and Reid, W. H. (2004). *Hydrodynamic Stability*. Cambridge Mathematical Library, 2nd edition. §1.2, §2, §3.1.2
- Dubas, M. (1984). Über die Erregung infolge der Periodizität von Turbomaschinen. *Ingenieur-Archiv*, 54(6):413–426. §1.1
- Dubas, M. and Schuch, M. (1987). Static and dynamic calculation of a Francis turbine runner with some remarks on accuracy. *Computers & Structures*, 27(5):645–655. §1.2
- Eugster, S. R. (2015). *Geometric Continuum Mechanics and Induced Beam Theories*, volume 75 of *Lecture Notes in Applied and Computational Mechanics*. Springer International Publishing. §2.1.2
- Eugster, S. R. and dell'Isola, F. (2017). Exegesis of the Introduction and Sect. I from “Fundamentals of the Mechanics of Continua” by E. Hellinger. *Zeitschrift für Angewandte Mathematik und Mechanik*, 97:477–506. §2
- Eugster, S. R. and dell'Isola, F. (2018a). Exegesis of Sect. II and III.A from “Fundamentals of the Mechanics of Continua” by E. Hellinger. *Zeitschrift für Angewandte Mathematik und Mechanik*, 98(1):31–68. §2
- Eugster, S. R. and dell'Isola, F. (2018b). Exegesis of Sect. III.B from “Fundamentals of the Mechanics of Continua” by E. Hellinger. *Zeitschrift für Angewandte Mathematik und Mechanik*, 98(1):69–105. §2



- Eugster, S. R. and Glocker, Ch. (2017). On the notion of stress in classical continuum mechanics. *Mathematics and Mechanics of Complex Systems*, 5(3–4):299–338. §2.1.1, §2.1.2, §2.1.2, §2.3.2
- Ewins, D. J. (2000). *Modal Testing: Theory, Practice and Application*. Research Studies Press, 2nd edition. §4.2.1, §5.2, §5.2.3
- Gasch, R., Knothe, K., and Liebich, R. (2012). *Strukturdynamik. Diskrete Systeme und Kontinua*. Springer Vieweg, 2nd edition. §5.2, §A.4
- Gloor, M. R. (2014). *Numerical Investigation on Hydrodynamic Stability and Noise Radiation of Coaxial Jet Flows*. Diss. ETH No. 22079, ETH Zurich. §6.1, §6.1.3
- Graff, K. F. (1975). *Wave Motion in Elastic Solids*. Oxford University Press. §3.2.1
- Grosh, K. and Pinsky, P. M. (1994). Complex wave-number dispersion analysis of Galerkin and Galerkin least-squares methods for fluid-loaded plates. *Computer Methods in Applied Mechanics and Engineering*, 113(1–2):67–98. §1.2
- Guaus, A., Airiau, C., Bottaro, A., and Kourta, A. (2009). Effects of wall compliance on the linear stability of Taylor–Couette flow. *Journal of Fluid Mechanics*, 630:331–365. §1.2
- Hagedorn, P. (1994). A note on the vibrations of infinite elastic plates in contact with water. *Journal of Sound and Vibration*, 175(2):233–240. §1.2
- Hahn, P. and Dual, J. (2015). A numerically efficient damping model for acoustic resonances in microfluidic cavities. *Physics of Fluids*, 27(062005):1–27. §8.2
- Hahn, P., Leibacher, I., Baasch, T., and Dual, J. (2015). Numerical simulation of acoustofluidic manipulation by radiation forces and acoustic streaming for complex particles. *Lab on a Chip*, 15:4302–4313. §8.2
- Harel, D. (1987). Statecharts: A visual formalism for complex systems. *Science of Computer Programming*, 8(3):231–274. §4.3.7

- Haupt, P. (2002). *Continuum Mechanics and Theory of Materials*. Advanced Texts in Physics. Springer Berlin Heidelberg, 2nd edition. §2.1.1, §2.1.2
- HDF Group (2018). *Hierarchical Data Format, version 5*. The HDF Group. <http://www.hdfgroup.org/HDF5>. §4.3.8
- Hellinger, E. (1914). Die allgemeinen Ansätze der Mechanik der Kontinua. In Klein, F. and Müller, C., editors, *Enzyklopädie der Mathematischen Wissenschaften mit Einschluss ihrer Anwendungen*, volume IV-4, chapter 30, pages 601–694. Teubner. §2
- Hengstler, J. A. N. (2013). *Influence of the Fluid–Structure Interaction on the Vibrations of Structures*. Diss. ETH No. 21645, ETH Zurich. §1.2
- Heylen, W., Lammens, S., and Sas, P. (1997). *Modal Analysis Theory and Testing*. Katholieke Universiteit Leuven, 2nd edition. §5.2
- Hill, D. C. (1995). Adjoint systems and their role in the receptivity problem for boundary layers. *Journal of Fluid Mechanics*, 292:183–204. §8.2
- Howe, M. S. (2003). *Theory of Vortex Sound*. Cambridge University Press. §2
- IAPWS (2007). Revised Release on the IAPWS Industrial Formulation 1997 for the Thermodynamic Properties of Water and Steam. Technical report, The International Association for the Properties of Water and Steam. <http://www.iapws.org/rellguide/IF97-Rev.html> (accessed March 6, 2015). §6.2.1
- IAPWS (2008). Release on the IAPWS Formulation 2008 for the Viscosity of Ordinary Water Substance. Technical report, The International Association for the Properties of Water and Steam. <http://www.iapws.org/rellguide/viscosity.html> (accessed March 6, 2015). §6.2.1
- Jacquet-Richardet, G. and Dal-Ferro, C. (1996). Reduction method for finite element dynamic analysis of submerged turbomachinery wheels. *Computers & Structures*, 61(6):1025–1036. §1.2
- Jeong, K.-H. (1998). Natural frequencies and mode shapes of two coaxial cylindrical shells coupled with bounded fluid. *Journal of Sound and Vibration*, 215(1):105–124. §1.2

- Jeong, K.-H. (2003). Free vibration of two identical circular plates coupled. *Journal of Sound and Vibration*, 260(4):653–670. §1.2
- Jeong, K.-H. and Kim, K.-J. (2005). Hydroelastic vibration of a circular plate submerged in a bounded compressible fluid. *Journal of Sound and Vibration*, 283(1–2):153–172. §1.2
- Jhung, M. J., Choi, Y. H., and Jeong, K.-H. (2003). Fluid bounding effect on natural frequencies of fluid-coupled circular plates. *KSME International Journal*, 17(9):1297–1315. §1.2
- von Kármán, T. (1921). Über laminare und turbulente Reibung. *Zeitschrift für Angewandte Mathematik und Mechanik*, 1(4):233–252. §1.2, §6.3.1
- Khorrani, M. R., Malik, M. R., and Ash, R. L. (1989). Application of spectral collocation techniques to the stability of swirling flows. *Journal of Computational Physics*, 81(1):206–229. §6.1.3
- Kobayashi, R., Kohama, Y., and Takamada, Ch. (1980). Spiral vortices in boundary layer transition regime on a rotating disk. *Acta Mechanica*, 35(1–2):71–82. §1.2
- Krey, F., Hübner, B., and Seidel, U. (2011). Transient simulation of a pump-turbine using coupled vibro-acoustic finite element analyses to investigate rotor–stator interaction phenomena. In *4th International Meeting on Cavitation and Dynamic Problems in Hydraulic Machinery and Systems*. §1.2
- Kwak, M. K. and Kim, K. C. (1991). Axisymmetric vibration of circular plates in contact with fluid. *Journal of Sound and Vibration*, 146(3):381–389. §1.2
- Lais, S., Liang, Q. W., Henggeler, U., Weiss, T., Escaler, X., and Egusquiza, E. (2009). Dynamic analysis of Francis runners—Experiment and numerical simulation. *International Journal of Fluid Machinery and Systems*, 2(4):303–314. §1.2
- Lamb, H. (1920). On the vibrations of an elastic plate in contact with water. *Proceedings of the Royal Society of London. Series A*, 98:205–216. §1.2
- Lamb, H. and Southwell, R. V. (1921). The vibrations of a spinning disk. *Proceedings of the Royal Society of London. Series A*, 99(699):272–280. §1.2

- Landahl, M. T. (1962). On the stability of a laminar incompressible boundary layer over a flexible surface. *Journal of Fluid Mechanics*, 13(4):609–632. §2.3.3
- Larose, P. G. and Grotberg, J. B. (1997). Flutter and long-wave instabilities in compliant channels conveying developing flows. *Journal of Fluid Mechanics*, 331:37–58. §1.2
- Leissa, A. W. (1969). Vibration of plates. Technical Report NASA SP-160, National Aeronautics and Space Administration. §5.1, §5.2, §5.1.2
- Liang, Q. W., Rodriguez, C. G., Egusquiza, E., Escaler, X., Farhat, M., and Avellan, F. (2007). Numerical simulation of fluid added mass effect on a Francis turbine runner. *Computer & Fluids*, 36(6):1106–1118. §1.2
- Lomenzo, R. A., Barker, A. J., and Wicks, A. L. (1999). Laser vibrometer system for rotating bladed disks. In *17th International Modal Analysis Conference*, pages 277–282. §4.3.5, §4.3.5
- Malik, M. R. (1990). Numerical methods for hypersonic boundary layer stability. *Journal of Computational Physics*, 86(2):376–413. §3.1.3
- Marsden, J. E. and Hughes, T. J. R. (1983). *Mathematical Foundations of Elasticity*. Dover Publications. §A.1
- Mathworks (2016). *MATLAB Release 2016a, version 9.0.0.341360*. The Mathworks Inc. §3.1.3
- McLachlan, N. W. (1932). The accession to inertia of flexible discs vibrating in a fluid. *Proceedings of the Physical Society*, 44(5):546–555. §1.2
- Mindlin, R. D. (1960). Waves and vibrations in isotropic elastic plates. In Goodier, J. N. and Hoff, N. J., editors, *Structural Mechanics*, Proceedings of the First Symposium on Naval Structural Mechanics, pages 199–232. Pergamon Press. §3.2.1
- Monette, C., Nennemann, B., Seeley, C., Coutu, A., and Marmont, H. (2014). Hydro-dynamic damping theory in flowing water. In *Earth and Environmental Science*, volume 22 of *IOP Conference Series*, pages 1–11. 27th IAHR Symposium on Hydraulic Machinery and Systems. §8.2

- Müller, P. C. (1977). *Stabilität und Matrizen*. Springer Berlin Heidelberg. §5.2.1
- Müller, S. (2007). *Numerical Investigations of Compressible Turbulent Swirling Jet Flows*. Diss. ETH No. 17375, ETH Zurich. §6.1.3
- National Instruments (2014). *LabVIEW Release 2014, version 14.0f1*. National Instruments Corporation. §4.3.1, §4.3.7
- Nordmann, R. (1984a). Modal analysis in rotor dynamics. In Mahrenholtz, O., editor, *Dynamics of Rotors*, International Centre for Mechanical Sciences, chapter 1.1, pages 3–27. Springer Vienna. §5.2, §A.4
- Nordmann, R. (1984b). Identification of modal parameters of rotors. In Mahrenholtz, O., editor, *Dynamics of Rotors*, International Centre for Mechanical Sciences, chapter 4.3, pages 371–393. Springer Vienna. §5.2, §8.2
- Odgen, R. W. (1984). *Non-linear Elastic Deformations*. Ellis Horwood Limited. §2.1.1, §6.1.3, §A.1, §A.2, §A.2.1
- Peyret, R. (2002). *Spectral Methods for Incompressible Viscous Flow*, volume 148 of *Applied Mathematical Sciences*. Springer New York. §3.1.3
- Polytec (2011a). *Polytec Scanning Vibrometer PSV-400*. Polytec GmbH. Hardware Manual. §4.3.4
- Polytec (2011b). *Polytec Scanning Vibrometer PSV-400*. Polytec GmbH. Software Manual Version 8.8. §4.3.4
- Presas, A., Valentín, D., Egusquiza, E., Valero, C., Egusquiza, M., and Bossio, M. (2017). Accurate determination of the frequency response function of submerged and confined structures by using PZT-patches. *Sensors*, 17(660):1–26. §1.2
- Presas, A., Valentín, D., Egusquiza, E., Valero, C., and Seidel, U. (2014). Experimental analysis of the dynamic behavior of a rotating disk submerged in water. In *Earth and Environmental Science*, volume 22 of *IOP Conference Series*, pages 1–8. 27th IAHR Symposium on Hydraulic Machinery and Systems. §1.2

- Presas, A., Valentín, D., Egusquiza, E., Valero, C., and Seidel, U. (2015a). Influence of the rotation on the natural frequencies of a submerged-confined disk in water. *Journal of Sound and Vibration*, 337:161–180. §1.2
- Presas, A., Valentín, D., Egusquiza, E., Valero, C., and Seidel, U. (2015b). On the detection of natural frequencies and mode shapes of submerged rotating disk-like structures from the casing. *Mechanical Systems and Signal Processing*, 60–61:547–570. §1.2
- Presas, A., Valentín, D., Egusquiza, E., Valero, C., and Seidel, U. (2015c). On the excitation of a submerged disk-like structure with RSI patterns. In *6th IAHR International Workshop on Cavitation and Dynamic Problems in Hydraulic Machinery*. IAHR. §1.2
- Presas, A., Valentín, D., Egusquiza, E., Valero, C., and Seidel, U. (2016). Dynamic response of a rotating disk submerged and confined. Influence of the axial gap. *Journal of Fluids and Structures*, 62:332–349. §1.2
- Rodriguez, C. G., Egusquiza, E., Escaler, X., Liang, Q. W., and Avellan, F. (2006). Experimental investigation of added mass effects on a Francis turbine runner in still water. *Journal of Fluids and Structures*, 22(5):699–712. §1.2
- Rothberg, S. J., Backer, J. R., and Halliwell, N. A. (1989). Laser vibrometry: Pseudo-vibrations. *Journal of Sound and Vibration*, 135(3):516–522. §4.3.5
- Rothberg, S. J. and Tirabassi, M. (2012). A universal framework for modelling measured velocity in laser vibrometry with applications. *Mechanical Systems and Signal Processing*, 26:141–166. §4.3.5, §4.3.5
- Schmid, P. J. and Henningson, D. S. (2001). *Stability and Transition in Shear Flows*, volume 142 of *Applied Mathematical Sciences*. Springer, 1st edition. §1.2, §2, §3.1.2, §7.2, §7.2
- Schouveiler, L., Le Gal, P., and Chauve, M. P. (2001). Instabilities of the flow between a rotating and a stationary disk. *Journal of Fluid Mechanics*, 443:329–350. §1.2

- Sever, I. A. (2004). *Experimental Validation of Turbomachinery Blade Vibration Predictions*. PhD thesis, Imperial College London. §4.3.5, §4.3.5, §4.3.5
- Sever, I. A., Stanbridge, A. B., and Ewins, D. J. (2002). Vibration measurements in a rotating blisk test rig using an LDV. In *Fifth International Conference on Vibration Measurements by Laser Techniques: Advances and Applications*, volume 4827, pages 1–8. A.I.V.E.LA, Proc. of SPIE. §4.3.5
- Sever, I. A., Stanbridge, A. B., and Ewins, D. J. (2006). Turbomachinery blade vibration measurement with tracking LDV under rotation. In *Seventh International Conference on Vibration Measurements by Laser Techniques: Advances and Applications*, volume 6345, pages 1–10. A.I.V.E.LA, Proc. of SPIE. §4.3.5
- Southwell, R. V. (1922). On the free transverse vibrations of a uniform circular disc clamped at its centre; and on the effects of rotation. *Proceedings of the Royal Society of London A: Mathematical, Physical and Engineering Sciences*, 101(709):133–153. §1.2
- Tobias, S. A. and Arnold, R. N. (1957). The influence of dynamical imperfection on the vibration of rotating disks. *Proceedings of the Institution of Mechanical Engineers*, 171(1):669–690. §1.2
- Valentín, D., Presas, A., Egusquiza, E., and Valero, C. (2015). Influence of non-rigid surfaces on the dynamic response of a submerged and confined disk. In *6th IAHR International Workshop on Cavitation and Dynamic Problems in Hydraulic Machinery*. IAHR. §1.2
- Valentín, D., Presas, A., Egusquiza, E., and Valero, C. (2016). On the capability of structural-acoustical FSI simulations to predict natural frequencies of rotating disk-like structures submerged in a heavy fluid. *Journal of Vibrations and Acoustics*, 138(034502):1–6. §1.2
- Valentín, D., Presas, A., Egusquiza, E., Valero, C., and Egusquiza, M. (2017). Experimental study of a vibrating disk submerged in a fluid-filled tank and confined with a nonrigid cover. *Journal of Vibration and Acoustics*, 139(021005):1–11. §1.2

- Vogel, S. M. and Skinner, D. W. (1965). Natural frequencies of transversely vibrating uniform annular plates. *Journal of Applied Mechanics*, 32(4):936–931. §5.2, §5.3, §5.1.2
- Weder, M. (2012). Linear stability and acoustics of a subsonic plane jet flow. Master's thesis, ETH Zurich. §3.1.3
- Weder, M., Gloor, M. R., and Kleiser, L. (2015). Decomposition of the temporal growth rate in linear instability of compressible gas flows. *Journal of Fluid Mechanics*, 778:120–132. §7.2, §8.2
- Weder, M., Horisberger, B., Monette, C., and Dual, J. (2016). Structure-structure coupling by liquids: Vibration measurements on a rotating disk with self-tracking LDV. In *Twelfth International Conference on Vibration Measurements by Laser Techniques: Advances and Applications*, volume 1740, pages 1–5. A.I.V.E.LA, AIP Conference Proceedings. §4
- White, F. M. (2005). *Viscous Fluid Flow*. McGraw-Hill, 3rd edition. §2.2.3, §2.2.5, §3.1.1, §3.2.1, §6.2.4



# Curriculum Vitae

## Mario Weder

born on November 7, 1981  
citizen of Diepoldsau-Schmitter SG

## Education

- 03/2013 – 03/2018 Doctorate at the Institute for Mechanical Systems, ETH Zurich
- 02/2010 – 12/2012 Master's degree in Mechanical Engineering at ETH Zurich with focus on fluid dynamics and mechanics, graduation as MSc ETH ME (with distinction)
- 10/2001 – 12/2004 Diploma in Mechanical Engineering at Fachhochschule Aargau with focus on energy engineering, graduation as Dipl. Masch.-Ing. FH
- 08/1997 – 06/2001 Apprenticeship as Machine Mechanic at ABB, Baden

## Professional Experience

- 12/2012 – 05/2018 Research and teaching assistant at the Institute for Mechanical Systems, ETH Zurich
- 04/2007 – 05/2010 Development engineer in the division Research and Technology at Kistler Instrumente AG, Winterthur
- 01/2005 – 12/2006 Research assistant at the Institute of Product and Production Engineering, School of Engineering FHNW, Windisch

## Scholarships and Awards

- 05/2013                      ETH Medal for outstanding Master's thesis: *Linear Stability and Acoustics of a Subsonic Plane Jet Flow*
- 02/2011 – 12/2012        Scholarship of the Markus Meier Fund for the Master's degree programme in Mechanical Engineering at ETH Zurich
- 12/2004                      Award for the best Diploma in Mechanical Engineering at Fachhochschule Aargau

## Journal Publications

- Weder, M., Gloor, M., and Kleiser, L. (2015). Decomposition of the temporal growth rate in linear instability of compressible gas flows. *Journal of Fluid Mechanics*, 778:120–132.
- Fritzsche, P., Weder, M., Wyss, I., Hörmann, M., and Müller, J. (2008). A procedure for the simulation of failure in thermoplastic composites. *Composite Structures*, 85(4):337–349.

## Conference Proceedings

- Weder, M., Horisberger, B., Monette, C., and Dual, J. (2016). Structure-structure coupling by liquids: Vibration measurements on a rotating disk with self-tracking LDV. *Proceedings of the 12th A.I.V.E.LA Conference on Vibration Measurements by Laser and Noncontact Techniques: Advances and Applications*, Ancona, Italy.
- Weder, M. and Dual, J. (2016). Damping of waves in a layered structure composed of two elastic plates coupled by a viscous liquid. *Proceedings of the 24th International Congress of Theoretical and Applied Mechanics*, Montréal, Canada.
- Ernst, R., Weder, M. and Dual, J. (2012). Multiple defect detection by applying time reversal principle on dispersive waves in beams. *Proceedings of the 18th World Conference on Non-destructive Testing*, Durban, South Africa.

## **Patent Applications**

Schading, G., Müller, J., Schöllhorn, K., Weder, M., and Gossweiler, Ch. (2008). *Apparatus for Performing Dynamic Strength Measurements and Method for Measuring Strength Values*. Patent WO/2008/086635.